



Rui Francisco Pereira Moital Loureiro da Cruz

**An XFEM element to model intersections between
hydraulic and natural fractures in porous rocks**

TESE DE DOUTORADO

Thesis presented to the Programa de Pós-graduação em Engenharia Civil of PUC-Rio in partial fulfillment of the requirements for the degree of Doutor em Engenharia Civil

Advisor: Prof^a. Deane Roehl

Co-advisor: Prof. Eurípedes Vargas

Rio de Janeiro
March 2018



Rui Francisco Pereira Moital Loureiro da Cruz

**An XFEM element to model intersections between
hydraulic and natural fractures in porous rocks**

Thesis presented to the Programa de Pós-graduação em
Engenharia Civil of PUC-Rio in partial fulfillment of the
requirements for the degree of Doutor em Engenharia Civil.
Approved by the undersigned Examination Committee

Prof^ª. Deane de Mesquita Roehl

Advisor

Departamento de Engenharia Civil e Ambiental – PUC-Rio

Prof. Eurípedes do Amaral Vargas Júnior

Co-Advisor

Departamento de Engenharia Civil e Ambiental – PUC-Rio

Prof. Luis Fernando Campos Ramos Martha

Departamento de Engenharia Civil e Ambiental – PUC-Rio

Prof. Leonardo José do Nascimento Guimarães

Universidade Federal de Pernambuco

Dr. Marcio Arab Murad

Laboratório Nacional de Computação Gráfica

Prof. Paulo Dore Fernandes

CENPES/Petrobras

Prof. Márcio da Silveira Carvalho

Vice Dean of Graduate Studies

Centro Técnico Científico – PUC-Rio

Rio de Janeiro, March 26th, 2018.

All rights reserved.

Rui Francisco Pereira Moital Loureiro da Cruz

Graduated in Civil Engineering from Universidade de Coimbra – Portugal in 2006. Masters in Geotechnical Engineering from Universidade de Coimbra – Portugal in 2008. Consultant for Geotechnical projects in Cenor Engenharia (Portugal) and Geomecanica (Brazil) between 2008 and 2014. Researcher at the Tecgraf Institute – PUC-Rio and visiting student at Cambridge University – United Kingdom during the doctoral programme.

Bibliographic data

Cruz, Rui Francisco Pereira Moital Loureiro da

An XFEM element to model intersections between hydraulic and natural fractures in porous rocks / Rui Francisco Pereira Moital Loureiro da Cruz ; advisor: Deane de Mesquita Roehl ; co-advisor: Eurípedes do Amaral Vargas Júnior. – 2018.
225 f. : il. color. ; 30 cm

Tese (doutorado)–Pontifícia Universidade Católica do Rio de Janeiro, Departamento de Engenharia Civil, 2018.
Inclui bibliografia

1. Engenharia civil – Teses. 2. Método dos elementos finitos. 3. Método dos elementos finitos estendidos. 4. Fraturamento hidráulico. 5. Interseção entre fraturas hidráulicas e naturais. I. Roehl, Deane de Mesquita. II. Vargas Júnior, Eurípedes A. III. Pontifícia Universidade Católica do Rio de Janeiro. Departamento de Engenharia Civil. IV. Título.

CDD: 624

To my parents

Acknowledgements

Many people have contributed to the success of this work. To them, I express my deepest acknowledgement for having shared with me such a memorable and happy period of my life.

To my advisors, Professora Deane Roehl and Professor Eurípedes Vargas, for their availability and openness in the moments I took important technical or personal decisions. Their contributions were precious and I hope this work have reached a level that deserves having their names associated to it. To Professora Deane I must thank the conditions given to me in the Tecgraf Institute.

To my colleagues at Tecgraf Institute, with whom I shared most of the time of this research, I thank for the friendship and fondness. I will always feel part of this group. I must thank Cristian, Nilthson, Luis Fernando and Renato, who were always ready for a technical discussion about the most complex or even idiotic ideas related with my work.

To Tecgraf Institute and all its members, who every day made me feel I was part of a research institute of excellence and international calibre. To Conselho Nacional de Desenvolvimento Científico e Tecnológico, to the program Ciência sem Fronteiras and Shell Brasil for the financial support throughout this years.

To Professor Alberto Sayão for the support and motivation transmitted to apply to the doctoral programme. To Karla, for her support and precious English lessons. To my colleagues and friends at COBA Brasil, namely Guilherme for giving me freedom to conjugate work and study, and Fernando for having being such an important part of this carioca adventure. To my tutors, colleagues and good friends in Cambridge who hosted me so kindly. A special greeting to Nicky, David, Hesham, Sinan and Hani, for their support in fitting me in the group and the local culture. To my friends at the Laboratório de Geotecnia do Departamento de Engenharia Civil da Universidade de Coimbra, for their logistics support and companionship in the final year of the thesis. A special greet to António Quintão, for making me “feel like home”, to João Camões, for being always close, to Patrícia and Hugo, for having host me with such affection.

To my family. To my parents, for having led me to where I am now and for their unconditional support, especially when we returned home. To my sister,

parents in law and sisters in law, who were always there so I could be away. To Inês (or PhD Inês, soon), forever life mate, for becoming an even more spectacular person every day. Her motivation and support is carved in every word of this document. To José Afonso, sweet boy with peaceful sleep, because he was born and gave me the privilege of being his father.

Abstract

Cruz, Rui Francisco Pereira Moital Loureiro da Cruz; Roehl, Deane; Vargas, Eurípedes. **An XFEM element to model intersections between hydraulic and natural fractures in porous rocks**. Rio de Janeiro, 2018. 225p. Tese de Doutorado - Departamento de Engenharia Civil, Pontifícia Universidade Católica do Rio de Janeiro

A large number of hydrocarbon reservoirs are naturally fractured. When subjected to hydraulic fracturing treatments, the natural fractures may influence the propagation of the hydraulic fracture, which can grow in a complicated manner creating complex fracture networks in the reservoir. In order to better understand and simulate such phenomena an element based on the eXtended Finite Element Method is proposed. The element formulation comprises fracture intersection and crossing, fracture frictional behaviour, fully coupled behaviour between displacements, pore and fracture fluid pressure, leak-off from the fracture to the surrounding medium and the eventual loss of pressure due to filter cake. The theoretical background and implementation aspects are presented. A set of analyses is performed in order to validate different features of the implemented element. Finally, the results of four practical applications are analysed and discussed: two laboratory hydraulic fracture tests, hydraulic fracture propagation in a multi-fractured synthetic model and percolation through a dam fractured foundation. It is concluded that the implemented code provides very good predictions of the coupled fluid-rock fracture behaviour and is capable of correctly simulating the interaction between hydraulic and natural fractures. Moreover, it is shown that the hydraulic behaviour of the models and the intersection between fractures are very sensible to parameters such as differential in-situ stresses, angle between fractures, initial hydraulic aperture and fracture face transversal conductivity.

Keywords

Finite Element Method; eXtended Finite Element Method; Hydraulic Fracturing; Intersection between hydraulic and natural fractures

Resumo

Cruz, Rui Francisco Pereira Moital Loureiro da Cruz; Roehl, Deane; Vargas, Eurípedes. **Um elemento XFEM para modelar intersecções entre fraturas hidráulicas e naturais em rochas porosas**. Rio de Janeiro, 2018. 225p. Tese de Doutorado - Departamento de Engenharia Civil, Pontifícia Universidade Católica do Rio de Janeiro.

Um elevado número de reservatórios de hidrocarbonetos é naturalmente fraturado. Quando sujeitos a estimulação hidráulica, as fraturas naturais podem influenciar a propagação da fratura hidráulica, que pode tomar uma forma geométrica complexa, criando redes de fraturas no reservatório. De forma a melhor entender e simular tais fenômenos, um elemento baseado no Método dos Elementos Finitos Estendidos (XFEM) é proposto. A formulação do elemento inclui interseção e cruzamento entre fraturas, atrito entre as faces das fraturas, comportamento acoplado entre deslocamentos, poro-pressões e pressões do fluido da fratura, absorção de fluido da fratura para o meio poroso (leak-off) e a eventual perda de pressão nas faces da fratura (filter cake). Os fundamentos teóricos e os aspectos relevantes da implementação são apresentados. Um conjunto de análises é realizado de forma a validar em separado as diferentes funcionalidades do elemento implementado. Finalmente, os resultados de quatro aplicações práticas são analisados e discutidos: dois conjuntos de ensaios de laboratório de interseção de fratura, propagação de fratura hidráulica num modelo sintético multi-fraturado e percolação na fundação fraturada de uma barragem. Conclui-se que o código implementado fornece previsões muito boas do comportamento acoplado do meio fraturado e tem capacidade de simular corretamente a interação entre fraturas hidráulicas e naturais. Pode também verificar-se que o comportamento hidráulico dos modelos e a propagação e interseção de fraturas são muito influenciados por parâmetros tais como o diferencial de tensões in-situ, ângulo entre fraturas, a abertura hidráulica das fraturas e a condutividade transversal das faces da fratura.

Palavras Chave

Método dos Elementos Finitos; Método dos Elementos Finitos Estendidos; Fraturamento Hidráulico; Interseção entre fraturas hidráulicas e naturais

Table of contents

1	Introduction	20
1.1.	Hydraulic fracturing in naturally fractured formations	20
1.2.	Research motivation	22
1.3.	Research objectives	23
1.4.	Thesis organization	25
2	Basic concepts and literature review	27
2.1.	Hydraulic fracture modelling	27
2.1.1.	Introduction	27
2.1.2.	Analytical models	31
2.1.3.	Numerical models	33
2.2.	Intersection between hydraulic and natural fractures	42
2.2.1.	Introduction	42
2.2.2.	Field and laboratory tests	44
2.2.3.	Analytical models	48
2.2.4.	Numerical models	50
2.3.	The eXtended Finite Element Method	55
2.3.1.	Introduction	55
2.3.2.	Fracture geometry in XFEM	57
2.3.3.	XFEM with coupled problems	58
2.3.4.	XFEM with fracture branching or crossing	59
2.3.5.	Crack tip behaviour in XFEM	60
2.3.6.	Contact problems in XFEM	62
3	XFEM Formulation for Coupled Problems	65
3.1.	Governing equations	65
3.2.	Weak formulation	69
3.3.	Spatial discretization	71
3.3.1.	XFEM discretization	71
3.3.2.	Enrichment functions	73

3.3.3. Intersections	76
3.3.4. Fracture discretization	79
3.3.5. Resulting space discretization	80
3.4. Time discretization	80
3.5. Newton-Raphson algorithm	81
3.6. Fracture constitutive behaviour	83
3.6.1. Contact penalty method	83
3.6.2. Mohr-Coulomb model	85
4 Implementation	88
4.1. Abaqus Software	88
4.1.1. General Description	88
4.1.2. XFEM in Abaqus	90
4.1.3. Abaqus User Subroutines	91
4.2. XFEMHF code	93
4.2.1. Overview	93
4.2.2. Abaqus algorithm	95
4.2.3. Fracture geometry pre-processor	98
4.2.4. UEL algorithm	101
4.2.5. Fracture geometry post-processor	104
4.2.6. Element topology	106
4.2.7. Numerical integration	108
4.2.8. Limitations of the implementation	111
5 Validation tests	113
5.1. KGD analytical solution	113
5.2. Flow in a fractured medium	117
5.2.1. Unidimensional percolation	117
5.2.2. Injection in fracture intersection	121
5.2.3. Percolation through a fractured medium	124
5.2.4. Consolidation in a fractured medium	129
5.3. Contact and friction	137
5.3.1. Single element with horizontal fracture	137
5.3.2. Single element with inclined fracture	144

5.3.3. Multi-fractured medium	147
6 Applications	152
6.1. Comparison with laboratory tests	152
6.1.1. Blanton tests	152
6.1.2. Khoei tests	164
6.2. Propagation of hydraulic fracture in multi-fractured medium	173
6.3. Percolation through a dam foundation	184
7 Conclusions	195
References	199
Annex A Resulting space discretization	213
Annex B Newton-Raphson Algorithm	223

List of figures

Figure 1.1 – Fracture development as function of wellbore orientation (Rahim et al., 2012).	21
Figure 1.2 – Different events of interaction between hydraulic and natural fractures	22
Figure 1.3 – Fracture intersections in a fractured medium	24
Figure 2.1 – Borehole pressure response during hydraulic fracture of a vertical wellbore (Fjaer, 2008). a) Idealized plot of two pressure cycles. b) Realistic plot with distinct breakdown pressure. c) Realistic plot without distinct breakdown pressure	28
Figure 2.2 – Schematic of fracture geometry of analytical solutions: a) Penny shaped. b) KGD. c) PKN (Adachi et al., 2007)	31
Figure 2.3 – Examples of Pseudo 3D (P3D) and Planar 3D (PL3D) models: a) P3D cell based (Settari, 1988). b) P3D cell based (Meyer, 1989). c) P3D cell based (Warpinski and Smith, 1989). d) PL3D with fixed quadrangular mesh (Clifton and Abou-Sayed, 1981). e) PL3D with moving triangular mesh (Clifton and Abou-Sayed, 1981)	34
Figure 2.4 – Bonded particles model (Shimizu, Murata and Ishida, 2011)	40
Figure 2.5 – Domains and flow paths in a bonded assembly of particles (Wang et al., 2014)	41
Figure 2.6 – Breakdown of the interaction process between hydraulic fracture (HF) and natural fracture (NF) (Gu et al., 2012)	44
Figure 2.7 – Leuders Lime model with angle of bearing of 70° (Lamont and Jessen, 1963)	45
Figure 2.8 – Type of interaction observed at different combinations of differential stress and angle of approach (adapted from Blanton (1982))	46
Figure 2.9 – Pictures from the mineback observations (Warpinski and Teufel, 1987)	47
Figure 2.10 – Comparison of laboratory tests with analytical criteria. a) Opening criterion. b) Arresting criterion (Blanton, 1982)	48
Figure 2.11 – Comparison of laboratory tests with Gu's analytical criterion. a) Gu's tests. b) Blanton's tests	49

Figure 2.12 – Comparison of laboratory tests with Cheng's analytical criterion. a) dip vs strike angles space b) dip vs differential stresses space (Cheng <i>et al.</i> (2014))	49
Figure 2.13 – Resultant hydraulic fracture pattern and rose diagram in the case where natural fractures make a 45° angle with the original orientation of the hydraulic fracture (Dahi-Taleghani and Olson, 2011)	51
Figure 2.14 – Hydraulic fracture and natural fracture behaviour as hydraulic fracture is propagating toward the pre-existing natural fracture and intersects with it. Light blue represents the debonded zone of the natural fracture (Keshavarzi, Mohammadi and Bayesteh, 2012)	52
Figure 2.15 – Pore pressures in the model (Nagel <i>et al.</i> , 2011)	54
Figure 2.16 – Fluid pressures in the fracture network (Kresse <i>et al.</i> , 2014)	54
Figure 2.17 – Hydraulic fractures generated in a medium with three pre-existing joints (blue disks are microcracks) (Damjanac <i>et al.</i> , 2013)	55
Figure 2.18 – Discontinuity on a structured mesh (a) and on an unstructured mesh (b). The circled nodes are enriched by the jump function whereas the squared nodes are enriched by the branch tip functions (Moës and Belytschko, 2002)	56
Figure 2.19 – Excess pore pressure field (Sheng <i>et al.</i> , 2015)	59
Figure 2.20 – Enriched nodes represented by circles (Duarte, Reno and Simone, 2007)	60
Figure 2.21 – Modelling of the fracture process zone. (a) Two cohesive laws with the same cohesive strength and fracture energy. (b) The extent of the cohesive zone at a certain moment (Moës and Belytschko, 2002; Wang, 2016)	61
Figure 2.22 – The iterative procedure in the LATIN algorithm (Dolbow, Moës and Belytschko, 2001)	64
Figure 3.1 – Generalized fractured domain. a) Boundary conditions of a fractured body Ω with a geomechanical discontinuity Γ_c . b) Geometry of the fracture domain Ω' (adapted from Khoei <i>et al.</i> (2014))	66
Figure 3.1 – Representation of fracture flow. a) Longitudinal flow. b) Transversal flow	69
Figure 3.2 – Value of shape function in node i for a 4-node element. a) View 0°. b) View 70°. c) View 250°	72
Figure 3.3 – Standard and Enriched degrees of freedom and their positions	73
Figure 3.4 – Pore pressure patterns (section A-A') near a hydraulic fracture. a) Filter cake not considered. b) Filter cake with loss of pressure. c) Filter cake with different top and bottom leak-off conditions	74

Figure 3.5 – Pore pressure patterns (section A-A') near a natural fracture. a) Without loss of pressure through the fracture. b) With loss of pressure in the fracture	75
Figure 3.6 – Value of shape function in node j multiplied by the enrichment shifted function ($H(x)-H_j$) for 4-node element. a) View 0° . b) View 70° . c) View 250°	76
Figure 3.7 – Enrichment function J (adapted from (Daux, Moes and Dolbow, 2000)	77
Figure 3.8 – Value of shape function in node j multiplied by the enrichment shifted function ($J(x)-J_j$) for a 4-node element. a) View 0° . b) View 70° . c) View 250°	77
Figure 3.9 –Intersection enriched degrees of freedom and their positions	78
Figure 3.10 –Secondary fracture enrichment when crossing occurs	78
Figure 3.11 –Fracture pressure degrees of freedom and their positions	80
Figure 3.12 – Zoom of an intersection and fractures integration points. a) Situation with all fractures opened. b) Situation of contact between fractures	85
Figure 3.13 – Mohr Coulomb failure surface	85
Figure 3.14 – Tensile cut-off failure surface	86
Figure 3.15 – Return paths for Mohr Coulomb model. a) vertical return. b) perpendicular return	86
Figure 4.1 – Implementation of the XFEM with “corner” and “edge” phantom nodes (Zielonka <i>et al.</i> , 2014)	91
Figure 4.2 – Calls of user subroutines within the flow in Abaqus	93
Figure 4.3 – Main steps of a simulation	94
Figure 4.4 – Flow of a XFEMHF simulation – dashed outlines represent coded subroutines and continuous represent Abaqus internal routines	97
Figure 4.5 – General flow of a XFEMHF simulation with initial stress state	98
Figure 4.6 – General flow of the general definition stage of the pre-processor	100
Figure 4.7 – General flow of the UEL subroutine	103
Figure 4.8 – General flow of the material constitutive subroutine	103
Figure 4.9 – General flow of the fracture geometry post-processor	104
Figure 4.10 – Examples of regions where propagation is checked	105
Figure 4.11 – Examples of regions close to other fractures	105
Figure 4.12 – Possible positions of fracture pressure degrees of freedom in possible fracture propagation segments	107
Figure 4.13 – Storage of fracture pressure degrees of freedom	108
Figure 4.14 – Difference of element definition between Interface elements and XFEM elements. On the left, black continuous lines represent element borders,	

grey hatches represent continuous elements and green hatches represent interface elements. On the right, black continuous lines represent element borders, grey hatches represent continuous elements and dashed lines represent the fracture inside the element domain	109
Figure 4.15 – Examples of integration points position in sub-regions	110
Figure 4.16 – Examples of integration points position in fractures	111
Figure 5.1 – Geometry of the mesh and boundary conditions	114
Figure 5.2 – Plots for KGD analytical and numerical solution. a) Injection pressure vs time. b) Fracture maximum aperture vs time. c) Fracture length vs time.	116
Figure 5.3 – Two situations of unidimensional fluid percolation in a model with different layers. On the left side, percolation from the bottom to the top of the model. On the right side, percolation from the fracture to the porous medium	117
Figure 5.4 – Geometry and boundary conditions of the mesh	118
Figure 5.5 – Pressure profiles of the model and analytical solution for each calculation	120
Figure 5.6 – Geometry of the mesh and boundary conditions	121
Figure 5.7 – Pore-pressure fields. Note: The colour scales presented are different for each calculation	123
Figure 5.8 – Pore-pressures in sections A-A and B-B	123
Figure 5.9 – Geometry of the mesh and boundary conditions	124
Figure 5.10 – Geometry of the mesh of Abaqus with interface elements model	125
Figure 5.11 – Pore-pressure fields	127
Figure 5.12 – Pore-pressures in sections A-A and B-B	128
Figure 5.13 – Flow vectors along the model	129
Figure 5.14 – Geometry of the mesh and boundary conditions	130
Figure 5.15 – Geometry of the mesh of GeMA with interface elements model	131
Figure 5.16 – Pore-pressure fields at time 95×10^5 s	134
Figure 5.17 – Pore-pressures in sections A-A and B-B at time 95×10^5 s	135
Figure 5.18 – Flow vectors along the model at time 95×10^5 s	136
Figure 5.19 – Vertical displacement in the top border's mid-point for all four analyses with XFEMHF	136
Figure 5.20 – Geometry of the mesh and boundary conditions	137
Figure 5.21 – Prescribed vertical displacement at the top of the model	138
Figure 5.22 – Deformed mesh at the end of 8 increments. a) Time increments represented. b) Model without in-situ stress. c) Model with in-situ stress of 500 kPa	139

Figure 5.23 – Fracture opening (a) and vertical stress in the continuous region (b)	140
Figure 5.24 – Fracture opening vs Normal stress in the fracture for every increment (grey circle points the first increment). a) Simulation without in-situ stress. b) Simulation with in-situ stress	141
Figure 5.25 – Geometry of the mesh and boundary conditions	141
Figure 5.26 – Deformed mesh	143
Figure 5.27 – Horizontal displacement versus shear stress in the fracture	144
Figure 5.28 – Normal stress versus shear stress in the fracture	144
Figure 5.29 – Mesh and boundary conditions	145
Figure 5.30 – Uniaxial strength variation with fracture inclination (assumed rock intact strength is plotted in dashed lines)	147
Figure 5.31 – Fracture stress paths for different fracture inclinations	147
Figure 5.32 – Mesh and boundary conditions	148
Figure 5.33 – Deformed mesh in different increments	149
Figure 5.34 – Prescribed displacement vs reaction at the top of the model	150
Figure 5.35 – Fracture stress state (normal and shear stresses) for every fracture integration points of the model. a) $d = 0,002$ m. b) $d = 0,045$ m. c) $d = 0,15$ m.	151
Figure 6.1 – Models used to simulate the different fracture orientations. a) 30° . b) 45° . c) 60° . d) 90°	154
Figure 6.2 – Comparison of the numerical simulations with the laboratory tests numbered according to Blanton (1982)	156
Figure 6.3 (cont.) – Comparison of deformed models with the laboratory tests (when available)	161
Figure 6.4 – Relative shear stresses in the pre-existing fracture for model 22. Red dashed lines denote the extremities of the fracture represented in the near figure. Orange line represents the level of the intersection.	162
Figure 6.5 – Relative shear stresses in the pre-existing fracture for model 20. Red dashed lines denote the extremities of the fracture represented in the near figure. Orange line represents the level of the intersection.	164
Figure 6.6 – Schematic view of the geometry and boundary conditions of hydraulic fracturing experimental tests	165
Figure 6.7 – Meshes used in the simulations. a) Specimen 1. b) Specimen 2	166
Figure 6.8 – Comparison of crack trajectory between the numerical solution with XFEMHF, laboratory test and numerical solution by Khoei <i>et al.</i> (2015). a) Specimen 1. b) Specimen 2	168

Figure 6.9 – Comparison of displacement fields when junction occurs between numerical solutions (the same colour scale is used in both simulations)	170
Figure 6.10 – Comparison of fracture aperture and normal stress along the natural fracture between numerical solutions for specimen 1	171
Figure 6.11 – Comparison of fracture aperture and normal stress along the natural fracture between numerical solutions for specimen 2	172
Figure 6.12 – Comparison between numerical solutions for specimen 1 of maximum principal stress σ_1 at the right side of the natural fault	173
Figure 6.13 – Fracture patterns obtained in different tests. a) Dominating fracture with multiple branches at large difference of horizontal stress. b) Radial random net-fractures at low difference of horizontal stress (Zhou and Xue, 2011)	174
Figure 6.14 – The relation between fracture geometry and in-situ stress contrast (Zhou and Xue, 2011)	175
Figure 6.15 – Geometry of the model and boundary conditions.	175
Figure 6.16 – Fluid Pressure applied at the hydraulic fracture mouth	178
Figure 6.17 – Deformed models and pore-pressure fields at $t = 100$ s	179
Figure 6.18 – Final fracture network ($t = 100$ s). Initial fractures in light grey and propagated segments in blue	181
Figure 6.19 – Relative fracture opening in the final fracture network ($t = 100$ s).	182
Figure 6.20 – Description of the final fracture network pattern ($t = 100$ s).	183
Figure 6.21 – Schematic model used by (Segura and Carol, 2004)	184
Figure 6.22 – Geometry and boundary conditions for the models: a) Dam0. b) Dam1. c) Dam2. d) Dam3	186
Figure 6.23 – Resulting pore pressures in models Dam1a to Dam1i (colour scale: red is 120 kPa, blue is 60 kPa)	189
Figure 6.24 – Volumetric flow rate in models Dam1a to Dam1i	190
Figure 6.25 – Pore Pressure values in section A-A. a) Models Dam1a, Dam1b and Dam1c – $w_{init}=10^{-4}$ m. b) Models Dam1d, Dam1e and Dam1f – $w_{init}=5 \times 10^{-5}$ m. c) Models Dam1g, Dam1h and Dam1i – $w_{init}=10^{-5}$ m.	191
Figure 6.26 – Volumetric flow rate in models Dam0, Dam1a, Dam2a, Dam2b, Dam3a, Dam3b and Dam 3c	193
Figure 6.27 – Pore Pressure values for model Dam0 (colour scale: red is 120 kPa, blue is 60 kPa)	193
Figure 6.28 – Pore Pressure values for models Dam2a and Dam 2b (colour scale: red is 120 kPa, blue is 60 kPa)	193

Figure 6.29 – Pore Pressure values for models Dam3a, Dam3b and Dam3c (colour scale: red is 120 kPa, blue is 60 kPa)

List of tables

Table 5.1 – Hydraulic properties	115
Table 5.2 – Mechanical properties	115
Table 5.3 – Hydraulic properties	119
Table 5.4 – Model boundary conditions	119
Table 5.5 – Hydraulic properties	122
Table 5.6 – Hydraulic properties	125
Table 5.7 – Hydraulic properties	131
Table 5.8 – Mechanical properties	132
Table 5.9 – Mechanical properties	138
Table 5.10 – Mechanical properties	142
Table 5.11 – Prescribed horizontal displacement and initial vertical stress	143
Table 5.12 – Mechanical properties	146
Table 5.13 – Mechanical properties	148
Table 6.1 – Hydraulic properties	154
Table 6.2 – Mechanical properties	155
Table 6.3 – In-situ Stresses	155
Table 6.4 – Geometry and material properties of the two hydraulic fracturing experiments	166
Table 6.5 – Hydraulic properties	167
Table 6.6 – Mechanical properties	167
Table 6.7 – Hydraulic properties	176
Table 6.8 – Mechanical properties	176
Table 6.9 – In-situ Stresses	177
Table 6.10 – Hydraulic properties	187
Table 6.11 – Hydraulic properties of fractures in the first set of calculations	188
Table 6.12 – Hydraulic properties of fractures in the second set of calculations	188

1

Introduction

1.1. Hydraulic fracturing in naturally fractured formations

Hydraulic fracturing (or hydraulic stimulation) is an operation that consists in the injection of a fluid under high pressures into the reservoir rock to generate tensile stresses in the rock, initiating a fracture. This fracture keeps growing during fluid pumping. Combined with the fracturing fluid, a granular agent (proppant) is injected. When the fracture closes its faces against this agent once the pumping operation stops, a high conductivity channel forms in the fracture for the flux of hydrocarbons from the rock to the well. This is one of the most important activities in hydrocarbons extraction nowadays.

According to Valkó and Economides (1995), 50% oil wells and 70% gas wells were stimulated using this technology during the second half of the 20th century. Considering the huge increase in unconventional reservoirs during the past 15 years, one may assume those numbers have further increased. Nowadays, this technique may be applied for different purposes, such as: (a) the stimulation of rock formations with poor or damaged permeability, mainly in shale gas reservoirs, to increase conductivity between the reservoir and the producing wells, (b) improvement of produced water re-injection where water is injected to replace produced fluids and maintain reservoir pressure or provide enhanced oil recovery, (c) cuttings reinjection where a slurry of drill cuttings is injected into a formation to mitigate the cost and risk of surface disposal, (d) in-situ stress measurement by balancing the fracturing fluid pressure in a hydraulically opened fracture with the geostatic stresses, and (e) wellbore integrity analysis of drilling operations to avoid propagating near-wellbore fractures that could result in drilling fluid losses to the formation and to inability to effectively clean the wellbore (Zielonka *et al.*, 2014).

Hydraulic fracturing may be applied on a wide depth range, being more common in depths between 2000 and 3500 m. Horizontal, vertical or even inclined wells are used to create longitudinal or transversal fractures, and one or multi-stage

of the natural fractures (NF). Figure 1.2 illustrates the events that can occur. As the interaction between fractures depends on several physical parameters, such as in-situ stress and angle between fractures, a realistic simulation of the treatment is needed to improve design and consequently production.

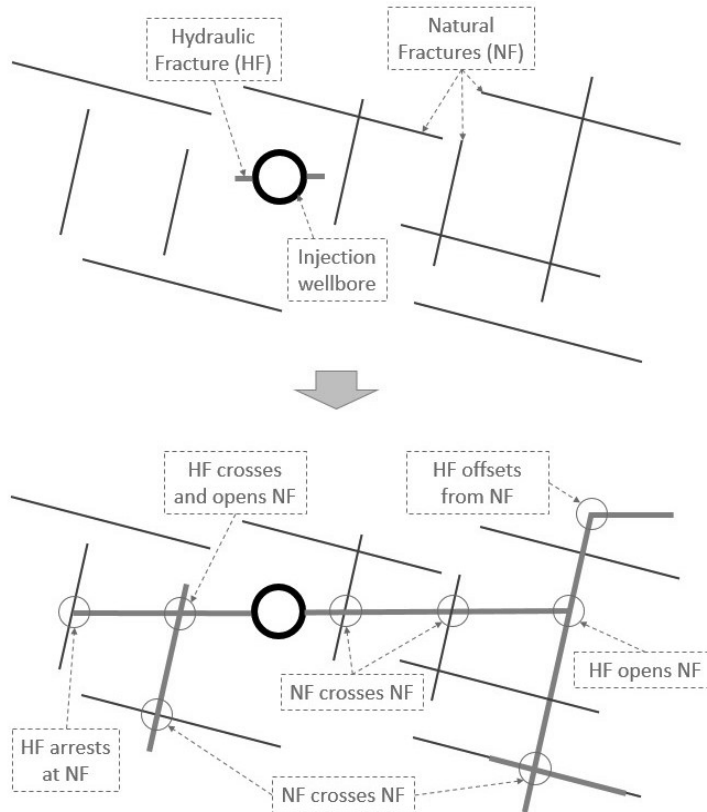


Figure 1.2 – Different events of interaction between hydraulic and natural fractures

1.2. Research motivation

Modern methods of simulation and prediction of hydraulic stimulation of geomaterials are still very limited to academic cases. Most commercial software used by the industry are focused in rapid design and still resort to very simple formulations (Warpinski *et al.*, 1993) that assume planar fractures with simple geometry with one-dimensional decoupled leak-off in linear-elastic impermeable materials.

As stated by Adachi *et al.* (2007) there is a rising tide of evidence from direct monitoring of actual field treatments that suggests that the fracture can grow in a complicated manner, taking advantage of local heterogeneities, layering, and

natural fracture networks in the reservoir. These factors complicate and make the process of treatment design and numerical modelling far more challenging.

Numerical methods have been widely used to simulate hydraulic fracturing treatments. Although many different academic works use techniques such as the Boundary Element Method or the Discrete Element Method, the Finite Element Method takes by far the preference of most researchers. The techniques for modelling fracture propagation within the finite element framework are mainly based on: adaptive meshing, interface or cohesive elements, damage models and enrichment techniques.

One very well-known enrichment technique is the eXtended Finite Element Method (XFEM), which was introduced by Belytschko and Black (1999) and Moës and Dolbow (1999) and later applied to model propagation of hydraulic fractures in quasi-brittle materials by Moës and Belytschko (2002). Even though very interesting results were achieved, there are still many "grey" areas of knowledge, such as the branching and intersection of fractures, fluid flow related to fractures, and the effects of rock heterogeneities (Li *et al.*, 2015).

Considering all the mentioned limitations in the available methods for hydraulic fracture simulation and the many parameters that govern HF behaviour, the motivation for this research is the possibility of using a recent and advanced numerical technique such as the XFEM to bring better insight in the subject of numerical modelling of hydraulic stimulation in naturally fractured reservoirs.

1.3. Research objectives

This research work aims at the development of a finite element to study the interaction between hydraulic and natural fractures. The proposed finite element uses enrichment techniques to represent displacement discontinuities, i.e. fractures. By increasing the number of enriched variables, multiple intersecting fractures may be represented in one single element. Thus, the element is capable of simulating not only multiple fractures in the same model but also fracture intersections, as the ones showed in Figure 1.3.

Other complex phenomena are considered, such as fracture frictional behaviour, fully coupled behaviour with pore and fracture fluid pressure, exchange of fluid between the fracture and the surrounding medium and the consideration of

an eventual loss of pressure between the fracture faces and the porous medium (filter cake). The simulation of the mentioned phenomena is achieved by discretizing the finite element problem with three physical variables: displacements, pore-pressures and fracture pressures.

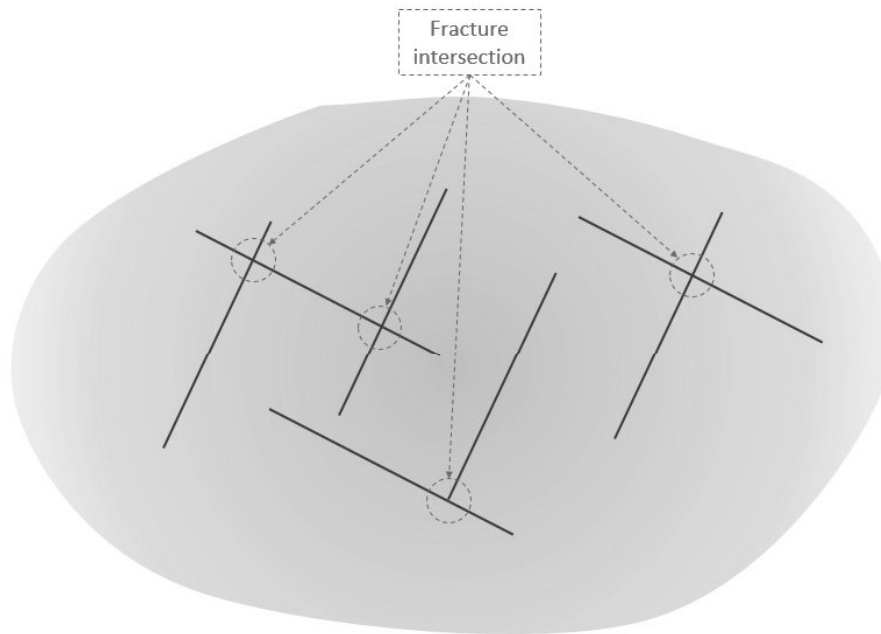


Figure 1.3 – Fracture intersections in a fractured medium

The implementation of an enriched element requires additional procedures that deal with fracture geometry. This is achieved by implementing a pre-processor and a post-processor. The former defines the global location of the fractures, their intersections with each other and intersections between fractures and the element mesh. The latter checks for fracture propagation by computing a propagation criterion based on the stress state.

The element implementation and the mentioned procedures are integrated with the software Abaqus (Simulia, 2014) as user subroutines, together with input and output auxiliary codes, resulting in a numerical simulation suite which is named XFEMHF. This overcomes the limitations of built-in Abaqus XFEM elements, which cannot be intersected by more than one fracture. Similar but simpler implementations of this type were also done by other authors with good results (Giner *et al.*, 2009; Chen, 2013; Silva, 2015).

In addition to the implementation work, a wide variety of numerical applications are computed for validation and to prove the applicability of the numerical tool. In most of the presented models, parametric analyses are run.

Summing up, the objectives of this thesis may be summarized in:

- Formulation and implementation of an XFEM element that is capable of simulating
 - multiple fractures, including intersections;
 - fracture frictional behaviour;
 - fully coupled behaviour with pore and fracture fluid pressure;
 - exchange of fluid between the fracture and the surrounding medium;
 - an eventual loss of pressure between the fracture faces and the porous medium (filter cake);
- Implementation of a pre-processor for definition of fracture geometry;
- Implementation of a post-processor for propagation computing;
- Integration of the implemented code with Abaqus software;
- Validation of the formulation comparing the implemented code with analytical or other software solutions;
- Application to real cases or synthetic models.

Finally, this research work aims at contributing to improve knowledge on the subject of intersection between hydraulic and natural fractures, mainly in unconventional reservoirs. The use of a more advanced numerical tool may bring better prediction of injection pressure, injected volumes, fracture opening and fracture network pattern, resulting in improved treatment design. The application to parametric studies of real cases may also clarify in which scenarios of stimulation the treatment is more effective and the production optimized.

1.4. Thesis organization

This thesis is organized in seven chapters. The first chapter introduces the research, its motivations and objectives. The second chapter presents the basic concepts and the most relevant research works that give support to this research, namely hydraulic fracture modelling, intersection between hydraulic and natural fractures and the eXtended Finite Element Method.

The third chapter presents the theoretical background and develops the formulation of the proposed element, focusing on the special spatial discretization

that the XFEM requires of the governing equations. The constitutive model used to simulate the behaviour of the natural fractures is also presented. Chapter 4 describes the most important aspects and details of the implementation of the XFEMHF algorithm and its components. It also describes the interaction of the implemented code with the software Abaqus and the limitations associated to it.

The fifth chapter presents the comparison between numerical models and analytical solutions or other software, in order to validate the implemented formulation. Finally, tests in three models are used to verify the accuracy of the contact and friction model for natural fractures.

Chapter six presents applications to more realistic cases. It starts by comparing numerical models with two sets of experimental tests by Blanton (1982), and Khoei *et al.* (2015). Then, a synthetic multi-fractured model is subjected to a parametric analysis of the in-situ stresses and initial fracture hydraulic aperture. Finally, a model of percolation under a dam foundation is set and different parameters are tested to study their influence, including a comparison with the results of Segura and Carol (2004).

In the last section, the main conclusions are summarized. Proposals to further develop and improve the implemented algorithm of this research are also presented and discussed.

2

Basic concepts and literature review

Only recently, researchers started applying enrichment techniques to the modelling of interaction between hydraulic and natural fractures. Consequently, the amount of research in this specific subject is limited. Nevertheless, a wide variety of research related to different parts of this subject is available, such as the use of enrichment techniques to simulate multiple fractures in uncoupled problems, or the modelling of single planar hydraulic fractures. To cover all the areas of knowledge that are involved in this thesis, three main subjects were deeply reviewed. The first section presents a review on hydraulic fracture modelling, from its early analytical works based on linear elastic fracture mechanics to modern numerical techniques. Next, studies regarding the interaction between fractures, physical or numerical, are contextualized and presented. The last section approaches the history of the eXtended Finite Element Method and its applications to coupled or branched problems.

2.1.

Hydraulic fracture modelling

2.1.1.

Introduction

An idealized plot of a borehole pressure response against injected volume is represented in Figure 2.1a. The first linear part represents the system elastic deformation, mainly the fracturing fluid compression in the borehole. Fracture initiation is identified by a pressure peak, followed by a drastic pressure drop (breakdown), which means the fracture volume grows at a higher rate than the injected volume. Keeping continuous pumping will lead to stable fracture propagation. In a second pumping cycle (Figure 2.1a), a reduction of the peak pressure is noted. Once the fracture already exists, no tensile strength has to be reached and the in-situ stresses are different from the ones before the first cycle.

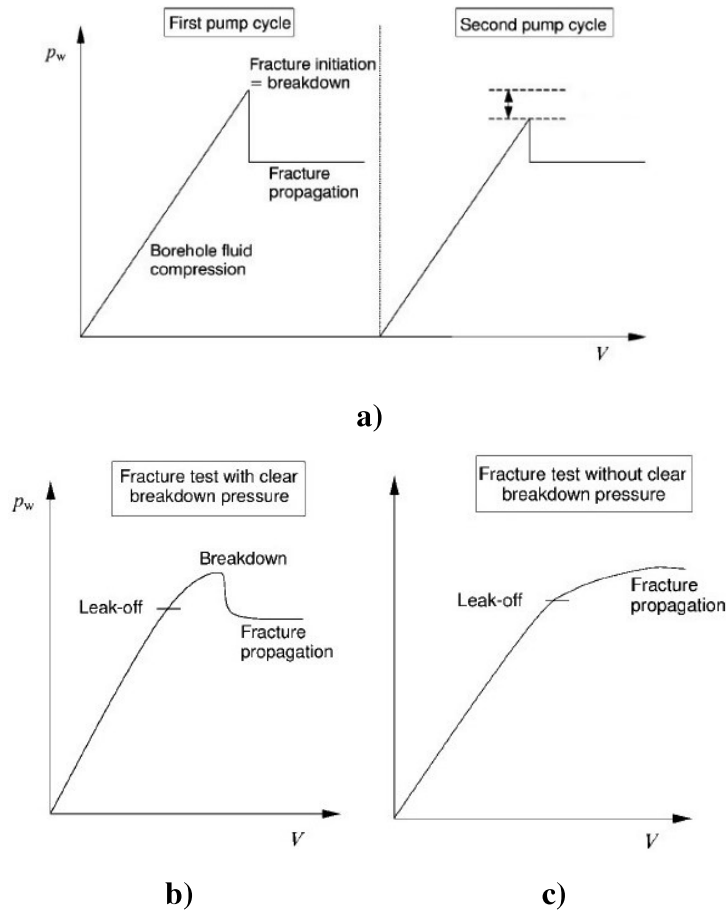


Figure 2.1 – Borehole pressure response during hydraulic fracture of a vertical wellbore (Fjaer, 2008). a) Idealized plot of two pressure cycles. b) Realistic plot with distinct breakdown pressure. c) Realistic plot without distinct breakdown pressure

More realistic plots show this processes occur with smoother transitions which are harder to detect. Figure 2.1b shows a test with clear breakdown pressure, while in Figure 2.1c it is not detectable. According to Fjaer et al. (2008) this can happen due to several reasons, from filter cake efficiency to plastification and stress dependent properties, temperature and leakage.

Hydraulic fracture propagation is mainly based on three physical processes. First, fluid flow within the fracture, which imposes a pressure load on the fracture surfaces. Second, rock mechanical deformation as a result of the flow pressure. Third, fracture propagation when a critical condition is reached. Furthermore, other complex phenomena may be involved, such as:

- leak-off of fracturing fluid from the fracture to the rock matrix;
- transport of suspended proppant particles within the fracture;

- effects of temperature on the fracturing fluid rheology;
- effects of chemical composition of the fluid on rock behaviour.

Hydraulic fracture treatments usually take place in a time-scale of tens of minutes to a few hours, depending upon the designed fracture size and volume of proppant to be placed (Adachi *et al.*, 2007). As the body wave speeds are much larger than the macroscopic propagation velocity of a hydraulically driven fracture, it may be admitted that dynamic effects like wave propagation can be neglected and fracture propagation can be analysed as a succession of equilibrium states. For example, a fracture is driven in the order of 610 m in 5 to 8 hours, while an elastic wave traverses this distance in 200 milliseconds (Hanson, Shaffer and Anderson, 1981).

The first attempts of modelling the hydraulic fracturing process date from more than 50 years. However, it remains a current challenge, not only due to the wide variety of phenomena and scales associated but also because it is so hard to track evidences in the laboratory or in the field. Standing before a large number of models created to model different situations and phenomena, one has to choose which model to use based mainly on experience with the reservoir characteristics.

According to Valkó and Economides (1995), a hydraulic fracturing model should follow three basic principles:

- Fundamental laws such as material and energy balances must be obeyed;
- Complete mathematical formulation of the governing and boundary equations, without resorting to “weighing factors”, should be derived;
- A fracture tip propagation criterion and its interaction with the provided energy must be explicitly stated.

In general, the solution for hydraulic fracture modelling consists of a series of "snapshots" that correspond to unique instances in time and crack shape. From the literature review made throughout this research, two different philosophies of modelling hydraulic fracturing could be differentiated.

The first has its domain in the plane where the fracture grows, with the width of the fracture being perpendicular to the calculation plane. This is a classical approach that assumes a bi-planar fracture, widely used by the industry to design or simulate the process.

The second approach models the continuum space. It can be used in 2D or 3D models, and the fracture is usually simulated in a perpendicular plane to the fracture plane in case of two-dimensional simulations. In these models, the propagation direction does not have to be known at start and can change during its development. These have been used mostly to evaluate the interaction between hydraulic fractures and natural fractures. Although only a few references with employment of these models in the industry were found, those models have high academic interest for the capabilities they present.

The transport and placement of proppant within the fracture is usually modelled by representing the slurry (i.e., the mixture of proppant and fluid) as a two-component, interpenetrating continuum. This implies that the fluid flow equations are solved for the mixture, and not for each individual component. Modelling of the proppant transport then reduces to solving an advective (mass conservation) equation for the proppant volumetric concentration. More complex modelling of this phenomena can be found in the literature, including models used in commercial simulators (Kresse *et al.*, 2014) that assume three layer models (proppant, slurry and clean fluid).

In a different process from the conventional hydraulic fracturing, named Thermally Induced Fracturing (TIF), thermal effects take a major role in the treatment results, especially when there is a large temperature difference between the (cold) injection water and the (hot) reservoir. Typical response is a sudden increase in injectivity after a significant period of stable injection. This reflects that the reservoir rock has been gradually cooled during injection of the cold water. The reservoir rock shrinks due to cooling, and eventually the smallest in situ stress is reduced to a level below the bottom hole injection pressure. This results in the creation of a fracture which provides a much larger contact area with the formation and hence dramatic increase in injectivity (Fjaer, 2008). Cohen, Kresse and Weng (2013) studied the impact of the reservoir temperature on the production for different fracturing fluids with their rheological properties depending on temperature, through the implementation of a model that couples the heat transport equations inside the fracture and the heat exchange with the reservoir.

Chemical effects may also exist in fracturing treatments such as acid fracturing, which is used in very specific cases (shallow carbonates), and consists on using acid instead of proppant. This will react with the rock, creating channels

that improve the permeability of the fracture. In this field, studies exist to predict the influence of chemical solutions on rock properties, such as in Karfakis and Akram (1993).

The research papers presented in this literature review are focused on the phenomena which are considered of main importance to hydraulic fracture modelling, i.e. fluid flow, mechanical behaviour and fracture propagation.

2.1.2. Analytical models

A basic stimulation treatment simulation needs to return parameters which are essential to study the effectiveness of the treatment, as pumping time, pressure in the well and fracture volume (width, height and length). Therefore, the first efforts to model the process tried to couple basic phenomena such as:

- elasticity of the rock medium around the fracture;
- fracturing fluid flow, to relate the injection with pressure inside the fracture;
- material balance, to relate the fracture growth with injected volume;
- proppant propagation.

Three analytical solutions proved to be reliable enough to be used for decades as basis for hydraulic fracturing prediction. First, Sneddon (1946) developed solutions for geometries that conform with a plane strain fracture or a “penny-shaped” fracture with radial flow (see Figure 2.2a). In the “penny-shaped” model, the fracture width is determined by assuming a uniform fracture flow pressure. This solution applies best when the well orientation coincides with the direction of minimum confining stresses, i.e. the fracture evolves around the wellbore.

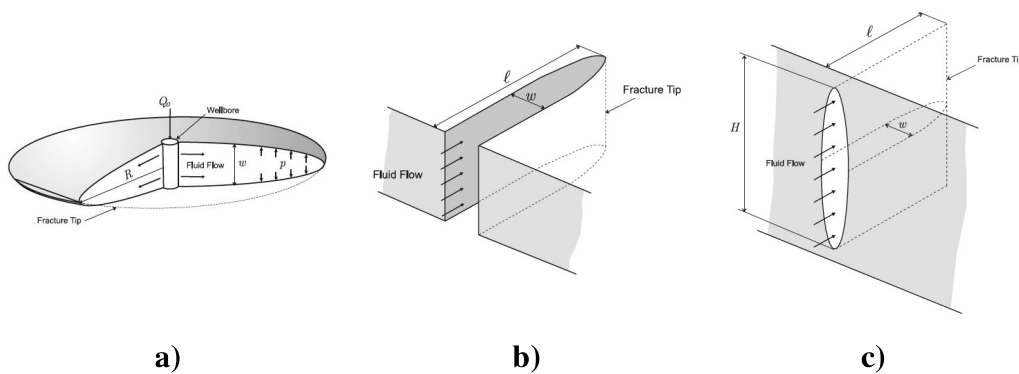


Figure 2.2 – Schematic of fracture geometry of analytical solutions: a) Penny shaped. b) KGD. c) PKN (Adachi et al., 2007)

Khristianvic and Zheltov (1955) and Geertsma and de Klerk (1969) developed the KGD analytical model for hydraulic fracturing, in which a plane strain geometry is admitted in the vertical direction (see Figure 2.2b). This way, the fracture width is constant and the flow channel (from the wellbore to the fracture) is rectangular. Furthermore, the flow rate is constant and all cross sections are independent along the vertical direction. This model shows better applicability to short fractures with large height. However, as pointed by Valkó and Economides (1995) it tends to overestimate the fracture width. Another limitation is that net pressure decreases with time and is independent of injection rate, which contradicts experience.

Perkins and Kern (1961) introduced an analytical model which was improved by Nordgren (1972) to account for the effect of fluid leak-off into the surrounding rock mass, resulting in the PKN model (see Figure 2.2c). In this model, the fracture height is fixed and admitted to be much smaller than the fracture length. For each vertical plane, an elliptical shape is defined and it is assumed that plane strain occurs. However, the stresses and deformations are different in each vertical plane. The flow channel is elliptical and the flow rate is constant, assuming uniform pressure proportional to the fracture width in vertical direction. This method provides good approximations for elongated fractures with shorter heights.

Both PKN and KGD models are based on the assumptions that fracture height is constant while the other dimensions in width and length increase during propagation. The key difference between these methods is the way of considering fracture width variation along vertical and horizontal directions. This difference leads to two different ways of solving the hydraulic fracturing problem. In the PKN model, the effect of the fracture tip is not considered so that the stress concentration is controlled by the effect of viscous fluid flow. In the KGD model, however, the stress concentration at the fracture tip is more important for the fracture propagation (Youn, 2016).

These analytical solutions are limited to analyse very simple geometries in a homogeneous and isotropic medium, but they provide fundamental understanding about the asymptotic behaviour of the fracture tip (Youn, 2016). The strong dependence of the solution on the asymptotic behaviour of the tip led several authors to propose analytical solutions to cover different propagation regimes. Desroches et al. (1993) studied the propagation on zero-toughness and impermeable

formations. Lenoach (1995) suggested the zero-toughness and leak-off dominated case, and Detournay and Garagash (2003) and Bunger, Detournay and Garagash (2005) dealt with toughness-dominated regimes. These studies have showed that hydraulic fractures may be controlled by toughness, viscosity, or fluid leak-off and that the fracture regime may change while the fracture evolves (Detournay, 2004; Adachi and Detournay, 2008).

2.1.3. Numerical models

2.1.3.1. Modelling bi-planar fractures

For a wide variety of treatments and reservoir characteristics, it is common to assume the fracture as planar, perpendicular to the minimum confining stress. As stated by Adachi, et al. (2007) simple computer models were developed using the KGD and PKN geometries with proppant transport. These served as guides in the treatment design and provided a method to show the sensitivity to critical input parameters of injection rate, treatment volumes, fluid viscosity and leak-off, and provided a basis for changing these parameters to increase the propped fracture penetration and also to minimize proppant bridging and screen-outs. One should notice that these models (PKN and KGD) were a base for several variations, such as the introduction of the Carter Equation for leak-off (PKN-C and KGD-C) and the consideration of a power law for non-newtonian fluids (PKN- α and KGD- α), as presented by Valkó and Economides (1995).

Since the 80s, these simpler models have been developed to become more flexible and able to adapt to more realistic problems, such as multi-layer reservoirs, variable injection rates and variation of the three dimensions of the fracture (width, length, height), being usually called Pseudo 3D (P3D) models (Settari, 1988; Meyer, 1989; Warpinski and Smith, 1989). These usually assume the sub-division of the fracture length in cells with different heights, allowing the growth of height and length, computed separately and based on KGD and PKN solutions, respectively. The reservoir elastic properties are considered homogeneous and Linear Elastic Fracture Mechanics governs fracture propagation. Leak-off is generally assumed as unidimensional and in the fracture plane flow is usually computed by the Finite Differences Method in one (length) or two directions.

More complete models were also proposed, such as the Planar 3D (PL3D) model (Clifton and Abou-Sayed, 1981). In this, it is assumed that the fracture footprint and the coupled fluid flow equation are described by a 2D mesh of cells oriented in a vertical plane and full 3D elasticity equations are used to describe width as function of fluid pressure. Figure 2.3 shows some examples of the mentioned models.

2.1.3.2. Modelling in the continuum

There is a rising tide of evidence from direct monitoring of actual field treatments that suggests that fractures grow in a complicated manner, taking advantage of local heterogeneities and layering. These factors complicate the design of treatments and make numerical modelling far more challenging (Adachi *et al.*, 2007). It should be noted as well that many of the current hydraulic fracturing simulators do not predict the correct wellbore fluid pressure even for planar fractures (Carter *et al.*, 2000).

Numerous 2D, pseudo-3D, and planar 3D hydraulic fracturing simulators work relatively well in many cases where the geometry of the fracture is easily defined and constrained to a single plane. However, there are instances where a fully 3D simulator is necessary for more accurate modelling. Furthermore, many hydraulic fracturing operations are performed in soft formations that are prone to non-linear mechanical failure—a real challenge for current models that are based on the principles of Linear Elastic Fracture Mechanics (LEFM). A fully 3D simulation is also essential to understand the behaviour of a hydraulic fracture in a reservoir with natural fractures, as well as the reciprocal influence of fractures when the treatment comprises multiple injections.

In reviewed literature, many different methods to simulate 2D or 3D fracture propagation in the continuum were found, mostly being based on a system of differential equations to be solved applying numerical methods. The transient effect in time is almost always admitted as quasi-static, with the solution obtained in each time step being dependent of the previous time step using Finite Difference or Newmark schemes.

It may be affirmed that the Finite Element Method is the most popular, but other approaches were also successfully applied, such as the Boundary Element Method, the Discrete Element Method or the Finite Differences Method. Although

more often complex assumptions about crack tip behaviour are being made, such as damage and cohesive laws, the LEFM approach is still used in many studies.

Finite Element Method

The Finite Element Method (FEM) is usually applied to either the mechanical deformations, the fluid flow or the coupling of both phenomena. When coupled, it is very common to use Biot's Theory and when applied to fluid flow in separate, the lubrication equation is solved.

For mechanical behaviour and discretization of the fracture, the following groups of element formulations may be highlighted:

- Interface elements with cohesive laws (cohesive elements);
- Models based on concept of damage mechanics;
- Plastic flow models;
- Elements with enriched nodes (eXtended finite element method).

In the first group, the fracture path is an input for the model, as the interface elements have to be placed according to the discontinuity position. In the remaining groups, the crack path is a solution of the problem and complex geometries may be obtained, although it depends on several factors, such as mesh geometry and refinement.

Interface elements with cohesive laws are easy to implement and avoid stress and pressure singularities at crack tip. In addition, the cohesive zone model has the interesting capability of modelling microstructural damage mechanisms inherent to hydraulic fracturing such as initiation of micro cracking and coalescence (Chen *et al.*, 2009). However, Shojaei, Dahi Taleghani and Li (2014) mentioned some limitations of the cohesive models, such as difficulties in situations involving intersecting discontinuities or the inability to predict changes in rock poroelastic properties like Biot coefficient and Biot modulus.

Carrier and Granet (2012) used interface elements with a cohesive law and the hydro-mechanical equations in a fully coupled approach to simulate four limiting propagation regimes: toughness-fracture storage, toughness-leak-off, viscosity-fracture storage and viscosity-leak-off dominated. Similarly, Bendezu *et al.* (2013) used cohesive elements to successfully compare fracture propagation with analytical solutions for toughness-dominated hydraulic fractures in KGD and

Penny-shaped geometries. Chen *et al.* (2009) also compared models with cohesive elements and reported excellent agreement between the finite element results and analytical solutions for the case where the fracture process is dominated by rock fracture toughness. Papanastasiou (1999) used cohesive elements, together with a remeshing scheme was employed with fine mesh near the fracture tip during propagation, to evaluate of the effective fracture toughness of the material, assuming elasto-plastic behaviour for the rock medium.

Yao *et al.* (2010) ran three-dimensional models of a three-layer water injection case to compare with a P3D model, PKN model and analytical solution. Their results showed that, compared with the traditional methods, the models with cohesive elements can predict the hydraulic fracture geometry more accurately. Complex 3D models were also applied to real case studies, such as a staged fracturing process of a horizontal well in the Daqing Oilfield, China (Zhang *et al.*, 2010).

Models based on the concept of damage mechanics were also used to simulate hydraulic fracturing. Shojaei, Dahi Taleghani and Li (2014) pointed some advantages of continuum damage based porous models, such as their capability to capture crack initiation, propagation, interaction and possible branching in an integrated framework, allowing material properties evolution during failure. Another main advantage lies in the fact that common continuum elements are used and there is no need to remesh, once the fractured elements have their properties weakened when fracturing occurs, i.e. once a certain value of damage occurs, the corresponding element is removed from the model by setting a small value for its elastic modulus. Li *et al.* (2012) used the same concept to simulate hydraulic fracturing on a laboratory sample, with the heterogeneity of rock considered by assuming that the mechanical properties conform to the Weibull distribution. Hu *et al.* (2014) simulated injection of water in a wellbore and hydraulic fracture at an arc dam heel. The crack was described by an equivalent anisotropic continuum with degraded material properties in the direction normal to the crack orientation.

The use of elasto-plastic constitutive models is mainly associated to cases of unconsolidated formations, where shear failure seems to be more important than tensile failure during the hydraulic fracturing process (Xu and Wong, 2010). The models used to adjust to this behaviour were Mohr-Coulomb and Drucker-Prager, associated with a tension cut-off. These can simulate not only fracture propagation

due to plastification but also changes in effective stresses in the fracture surroundings due to leak-off, which is high in this kind of permeable mediums. Buseti, Mish and Reches (2012) used an elasto-plastic damage model with pressure-dependent yielding, strain hardening and softening, and strain-based damage evolution to compare a four-point beam test, a dog-bone triaxial test and a hydraulic fracturing event with experimental results. The authors showed that the resolution of the damaged zone equivalent to a discrete fracture is determined by the coarseness of the FE mesh.

The use of enriched degrees of freedom to represent cracks explicitly has been gaining more and more focus by the academic community. Although this technique had been applied previously to mechanical cracks (Belytschko and Black, 1999; Dolbow, Moës and Belytschko, 2001) or simulation of flow in fractured medium (Réthoré, Borst and Abellan, 2006), the incorporation of the capability to propagate the hydraulic fracture has been developed more recently.

Mohammadnejad and Khoei (2013) and Khoei *et al.* (2014) developed a numerical model based on the extended Finite Element Method (XFEM) for the fully coupled hydro-mechanical analysis of deformable, progressively fracturing porous media interacting with the flow of two immiscible, compressible wetting and non-wetting pore fluids. The works point out that by allowing the interaction between various processes, that is, the solid skeleton deformation, the wetting and the non-wetting pore fluid flow and the cohesive crack propagation, the effect of the geomechanical discontinuity can be completely captured.

Zielonka *et al.* (2014) Compared analytical solutions (KGD and “Penny-Shaped”) with interface elements and XFEM elements with cohesive behaviour in two and three dimensional models assuming toughness/storage dominated and viscosity/storage dominated propagation regimes, showing that both methods reproduce accurately the analytical solutions, and converge monotonically as the mesh is refined. Chen (2013) implemented the extended finite element method (XFEM) in Abaqus user subroutines for the solution of hydraulic fracture problems comparing the finite element results with the analytical solutions available in the literature.

Salimzadeh and Khalili (2015) used extended finite element method (XFEM) with the cohesive crack model as fracturing criterion to simulate hydraulic fracturing. Coupling between fracture and pore fluid was captured through a

capillary pressure-saturation relationship, while the identical fluids in fracture and pore are coupled through a so-called leak-off mass transfer term. Model verification follows against analytical solutions available from literature. The authors showed that the results by single-phase flow might underestimate the leak-off.

Remij *et al.* (2015) presented an enhanced local pressure model for modelling fluid pressure driven fractures in porous saturated materials. The authors reconstructed the pressure gradient due to fluid leakage near the fracture surface based on Terzaghi's consolidation solution, ensuring that fluid flow happens exclusively in the fracture and that it is not necessary to use a dense mesh near the fracture to capture the pressure gradient.

Sobhaniaragh, Mansur and Peters (2016) presented a numerical technique based on the Cohesive Segments Method in combination with Phantom Node Method, called CPNM, to simulate 3D non-planar hydraulically driven fracture problem in a quasi-brittle shale medium. The authors used two different key scenarios, including sequentially and simultaneously multiple hydraulic, showing that later stages in sequentially hydraulic fracturing mainly secure larger values of fracture opening than what is achieved with simultaneously hydraulic fracturing. This effect can be attributed to the effect of stress interactions among fractures.

Mohammadnejad and Andrade (2016) modelled pump-in/shut-in tests in order to capture the bottom-hole pressure/time records and extract the confining stress perpendicular to the direction of the hydraulic fracture propagation from the fracture closure pressure.

Youn (2016) presented in his thesis the development and validation of an advanced hydro-mechanical coupled finite element program based on XFEM in order to estimate wellbore bottom-hole pressure during fracture propagation. The same research also considers material heterogeneity to check the effect of random formation property distributions on the hydraulic fracture geometry. The work uses a new stochastic approach combining XFEM and random field which is named eXtended Random Finite Element Method (XRFEM).

Boundary Element Method

In the reviewed works that use the Boundary Element Method (BEM), the method is often applied to simulate the rock mechanical behaviour, with subsequent coupling to the flow solution of a finite element or finite differences method. This

method shows advantages because it only requires discretization along the fracture, demanding less CPU capacity.

Carter *et al.* (2000), Carter, Ingraffea and Engelder (2000), Sousa, Carter and Ingraffea (1993) use a linear elastic boundary element program with special hypersingular integration techniques and provide an elastic influence matrix that relates the unit pressures at the nodes on the crack surface with the elastic displacements. This matrix is then used along with the equilibrium fluid pressures to determine the overall structural response due to both the far field boundary conditions and the fluid pressure in the crack.

Discrete Element Method

Two types of models based on the Discrete Element Method (DEM) were found in the review. The Particle Flow Model and the Distinct Element Method.

The Particle Flow Model simulates the movement and interaction of circular particles. The constitutive behaviour of the rock is simulated by associating a contact model with each contact, as seen Figure 2.4 by Shimizu, Murata and Ishida (2011).

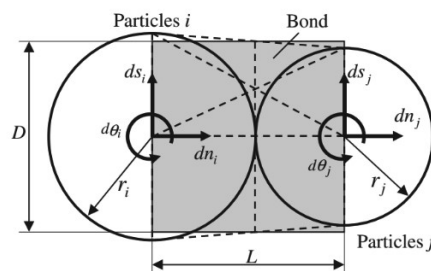


Figure 2.4 – Bonded particles model (Shimizu, Murata and Ishida, 2011)

Thus, HF can be modelled by assuming that a rock is made up of individual particles of specific stiffness bonded with bonds of specific strength. Shimizu, Murata and Ishida (2011) showed that under the applied load, the bonds between the particles can break, and a small crack can form. The crack pattern develops automatically with no need for remeshing. The calculation cycle is a time-stepping algorithm that requires the repeated application of the law of motion for each particle and a force-displacement law for each contact. The seepage effect can be modelled by adopting a fluid "domain" and fluid "pipe" (see Figure 2.5).

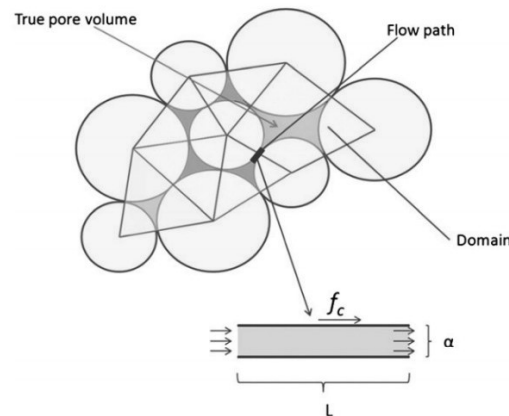


Figure 2.5 – Domains and flow paths in a bonded assembly of particles (Wang et al., 2014)

A "domain" is defined as a closed chain of particles, in which each link in the chain is a bonded contact. Each domain holds a pointer, via which all domains become connected. Meanwhile, a "pipe" is not only a fluid channel in a solid but also a channel connecting "domains", which is considered to be tangential to each bonded contact. The aperture of a "pipe" is proportional to the normal displacement of the contact. It changes when the contact breaks or when the particle moves. The volume of a "domain" is related to the number and aperture of the surrounding pipes. In addition, the water pressure in the "domain" continually changes as the coupling calculation proceeds, and it is applied to each particle as a body force with the flow in the channel being modelled using the Poiseuille equation (Wang *et al.*, 2014).

The second type of model based on DEM is the Distinct Element Method. It refers to the particular discrete-element scheme that uses deformable contacts and an explicit, time-domain solution of the original equations of motion (Nagel *et al.*, 2011). In this method, the rock mass assembly of deformable blocks interfaces a joint network which describes the interaction between distinct blocks. The deformation of each block is modelled by internal discretization. In Nagel *et al.* (2011) and Hamidi and Mortazavi (2014) the deformable rock blocks are modelled with the finite difference method. Considering the interaction of intact blocks and joints, DEM can effectively calculate the mechanical behaviour of block systems under different stress and displacement boundary conditions. Fracture propagation occurs in the bounds between blocks when the stress state reaches a certain limit value. Fluid flow occurs only in the joints and there is no porous flow in the rock

matrix. Also, the numerical resolution of transient flow is done by using the finite difference scheme (Hamidi and Mortazavi, 2014).

Finite Differences Method

The Finite Difference Method (FDM) is commonly associated to other methods, such as the FEM. However, in the works reviewed, three applications use exclusively the FDM. Two of them considered a continuum three-dimensional medium with linear elastic (Zhou and Hou, 2013) or elasto-plastic (Agarwal and Sharma, 2011) behaviour, using Biot's theory to couple the mechanical and flow phenomena, in a similar way as some of the reviewed FEM models.

One additional model used a simplified, and also computationally more efficient version of the particle flow model. A lattice, consisting of point masses (nodes) connected by springs, replaces the particles and contacts (respectively) of the particle flow model. Two springs that represent elasticity of the rock connect the lattice nodes, one representing the normal and the other shear contact stiffness. The solution of the equations of motion (three translations and three rotations) for all nodes in the model adopts a central difference scheme FDM. The relative displacements of the nodes are then used to calculate the force change in the springs. If the force exceeds the calibrated spring strength, the spring breaks and a micro crack forms. Fluid flow occurs through the network of pipes that connect fluid elements, located at the centres of either broken springs or springs that represent pre-existing joints. The model uses the lubrication equation to approximate the flow within a fracture (Damjanac *et al.*, 2013).

2.2.

Intersection between hydraulic and natural fractures

2.2.1.

Introduction

The behaviour of a hydraulic fracture near a natural fault or discontinuity is of great importance for an efficient reservoir simulation, as natural discontinuities can significantly influence the hydraulic fracturing process (Zhang and Ghassemi, 2011).

As proven in laboratory tests, a variety of events may happen when a hydraulic fracture intersects a natural fracture. Gu *et al.* (2012) gives a clear description of the different phenomena that occur:

1. First, the fracture tip reaches the interface (Figure 2.6a), but the fluid front remains behind because of the fluid lag. At this moment, the net fluid pressure (the difference between the fracturing-fluid pressure and the minimum in-situ stress) at the intersection point can be considered zero, but the natural fracture is already under the influence of the stress field generated by the hydraulic fracture. This step can be analysed by the mechanical interaction between the hydraulic fracture and the natural fracture without considering fluid flow. There are two possible outcomes from this interaction:
 - slippage or arrest (Figure 2.6b),
 - crossing (Figure 2.6c).
2. The second step in the process occurs soon thereafter when the fluid front reaches the natural fracture and fluid pressure at the intersection point rises.
 - In the case of slippage, the fluid may flow into the natural fracture and dilate it if the fluid pressure is larger than the normal compressive stress on the natural fracture. If flow continues, the dilated natural fracture becomes part of a hydraulic-fracture network (Figure 2.6d), i.e., the hydraulic fracture turns and propagates along the natural fracture.
 - Two possibilities exist for the case of crossing. In the first case, the natural fracture remains closed if the fluid pressure is less than the normal stress on the natural fracture (Figure 2.6e). In this case, the hydraulic fracture remains planar, and there may be enhanced leak-off if the filling material inside the natural fracture is permeable. The other possibility is that the fluid pressure is greater than the normal stress and the fluid flows into the opened natural fracture. In this case, the hydraulic fracture branches into the natural fracture, multiple fracture fronts propagate, and a complex network forms. As pumping continues, the fracture behaviour continues to evolve. For example, in the case of (Figure 2.6d), the hydraulic fracture may leave the path of the natural fracture and propagate again along the

preferred direction (perpendicular to the minimum horizontal stress). The hydraulic fracture may reinitiate at the intersection point (Figure 2.6f), at some weak points along the natural fracture, or at the end of the natural fracture. In the case of Figure 2.6e, the natural fracture may open later when the fluid pressure at the intersection rises further and overcomes the normal stress on the natural fracture.

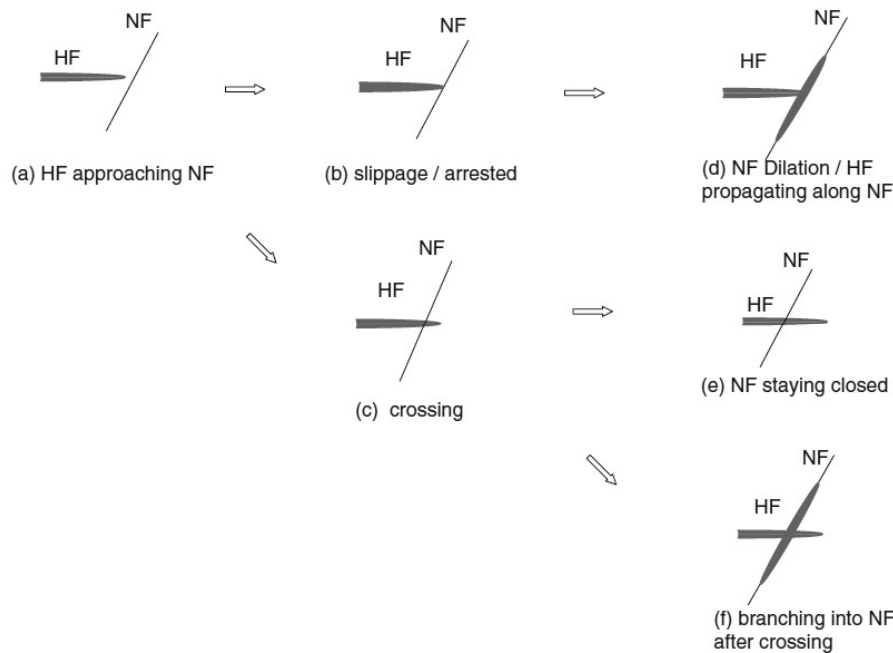


Figure 2.6 – Breakdown of the interaction process between hydraulic fracture (HF) and natural fracture (NF) (Gu et al., 2012)

Both Academia and the Industry put effort in understanding the mentioned phenomena by means of the monitoring of laboratory or field tests. The difficulties associated with the observation of such phenomena gives way to the numerical tools to work as a complement to increase the knowledge around the subject.

2.2.2. Field and laboratory tests

In the early days of research in this subject, Lamont and Jessen (1963) have tested 106 outcrop rock samples under triaxial stress conditions, showing that an existing fracture would have little effect on the hydraulic fracture. They also concluded that in every successful test there was fracture crossing. However, the authors assumed that around 30% of the tests were unsuccessful when the hydraulic

fractures did not cross the existing fractures because of bleed-off of the fracture fluid at the top and bottom faces or at the ends of the existing fracture. In this author's opinion, this may lead to the assumption that in such cases the event of natural fracture opening occurred. Lamont and Jessen (1963) also stated that the lower the angle between fractures, the further the path deviated from the centre line of the model. This deviation was always toward that part of the existing fracture which was closer to the injection end of the model, as Figure 2.7 shows.

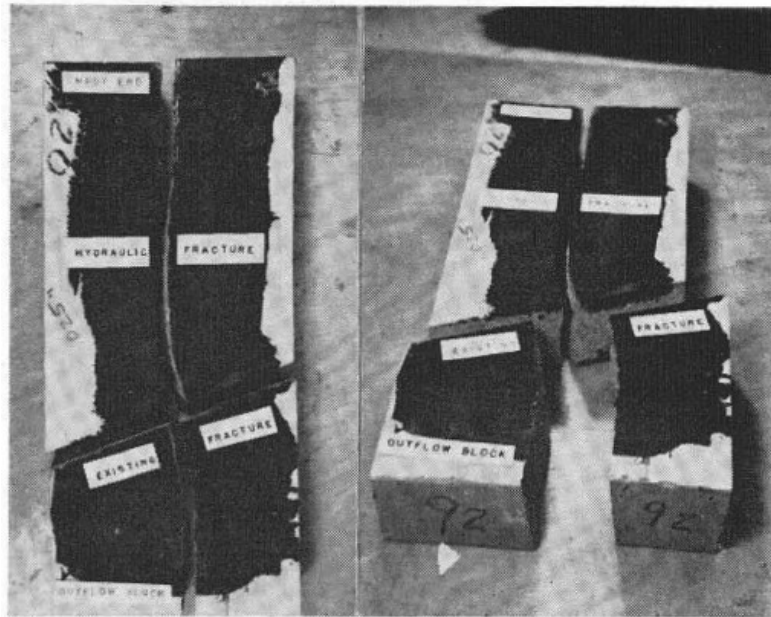


Figure 2.7 – Leuders Lime model with angle of bearing of 70° (Lamont and Jessen, 1963)

Daneshy (1974) performed experiments to study how hydraulic fractures evolved in the presence of natural flaws, observing that crossing occurs when the natural faults are closed and arrest happens in all other situations. Hanson, Shaffer and Anderson (1981) used small-scale laboratory experiments to study the effects of frictional characteristics on hydraulic fracture growth across unbounded interfaces in rocks, concluding that decreasing friction reduces the tendency of the crack crossing the interface.

Blanton (1982) executed laboratory tests on naturally fractured blocks of Devonian shale and hydrostone using different intersection angles under different triaxial states of stress. Figure 2.8 shows that the hydraulic fractures were mostly arrested by the natural fracture or opened the natural fracture, with exception of

cases with high differential stresses and high angles of approach, where crossing occurred.

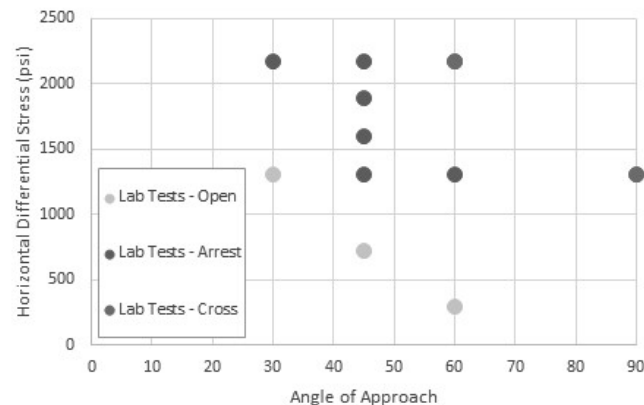


Figure 2.8 – Type of interaction observed at different combinations of differential stress and angle of approach (adapted from Blanton (1982))

Zhou and Xue (2011) carried out six tests on multiple naturally fractured blocks varying the in-situ stresses. Three types of fracture network patterns after propagation resulted. The authors showed that for high in-situ differential stresses the hydraulic fracture tends to dominate. As the differential stresses decrease, the hydraulic fracture propagates with branches. For extreme low differential stresses, natural fractures tend to dominate fracture geometry.

Gu *et al.* (2012) conducted six tests on sandstone samples with varying fracture angles and initial confining stresses, showing that the fracture is more likely to turn and propagate along the interface than to cross it when the angle is less than 90°. Cheng *et al.* (2014) performed 24 tests on cement blocks with variation of confining stresses and three-dimensional angle between fractures (dip and strike angles). The results showed that crossing happens in models with high approaching angles and high horizontal stress differences. The knowledge accumulated by the mentioned tests allowed the authors to make predictions and further comparisons with field microseismic results in a real case study. The same authors also showed that above a critical pump displacement or above a critical viscosity, the hydraulic fracture tends to cross the natural fracture. On the other hand, below the critical values hydraulic fracture propagates along the natural fracture rather than crossing it (Cheng, Jin, Y. Chen, *et al.*, 2014)

Khoei *et al.* (2015) carried out hydraulic fracturing experimental tests in fractured media under plane strain conditions, with the experimental tests being

continued until the hydro-fracture merged with the natural fault. A number of tentative experiments showed that the intersection of hydro-fracture with the natural fault is characterized by an abrupt loss of the water level in the pump fluid tank

As expected, due to the complexity involved, the number of field tests found in the literature is small. Murphy and Fehler (1986) used microseismic observations to claim that the shear slippage along the natural discontinuities can be activated before the conventional tensile failure occurs, especially in the presence of high differences between the minimum and maximum in-situ stresses. Based on their observations, the occurrence of slippage along the natural fracture faces leads to the hydro-fracture branching, or dendritic evolution patterns, which are in agreement with microearthquake locations.

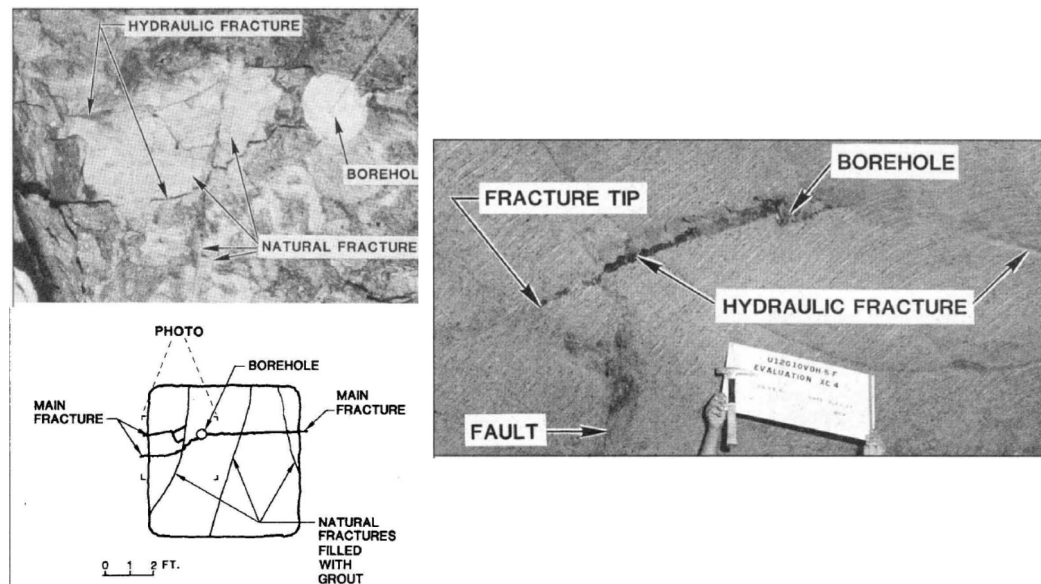


Figure 2.9 – Pictures from the mineback observations (Warpinski and Teufel, 1987)

Warpinski and Teufel (1987) presented perhaps the only field study with large-scale and direct observations in the literature. The authors integrated results from mineback experiments (425 m depth) with laboratory experiments to explain the influence of geologic discontinuities in hydraulic fracturing. Figure 2.9 presents some pictures of the mineback work. This study concluded that geologic discontinuities may influence fracture height, length, leak-off, treatment pressure, and proppant transport. The effect of the discontinuities depends on many parameters, such as the permeability of the joints, frictional properties, in-situ

stresses, joint spacing and orientation, treatment pressure, and fracture fluid leak-off viscosity.

2.2.3. Analytical models

In some of the research works mentioned in Section 2.2.2, the field tests gave empirical support to analytical methods developed by the authors. These methods mainly focus on predicting the intersection behaviour. Most of these criteria depend on the differential in-situ stress, angle of approach, friction in the natural fracture, rock tensile strength and fracture energy.

Blanton (1982) used an equation to compute the fracture stress state, and then define which type of intersection occurs by comparing the stress state with the pressure applied by the fluid. Figure 2.10 shows plotting of the analytical solutions (for different fracture energies) against the laboratory tests.

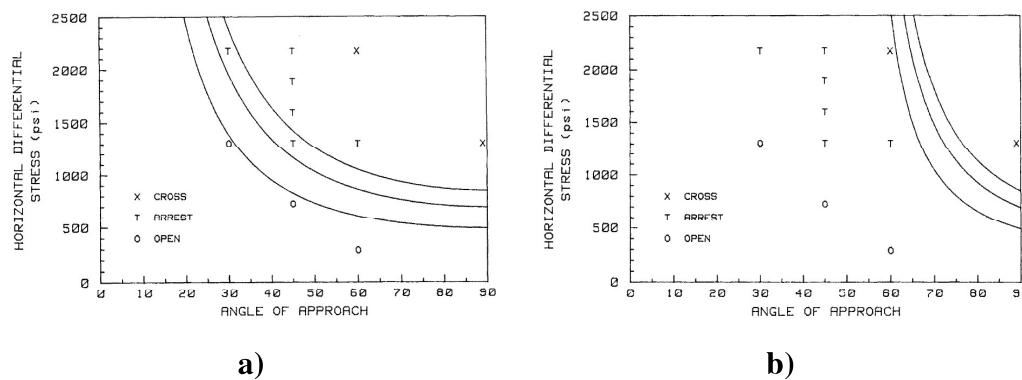


Figure 2.10 – Comparison of laboratory tests with analytical criteria. a) Opening criterion. b) Arresting criterion (Blanton, 1982)

Zhou *et al.* (2008) studied the hydraulic fracture propagation behaviour in naturally fractured reservoirs through a series of triaxial fracturing experiments, operating different values of horizontal stress, angle of approach, and shear strength of pre-existing fracture. The authors observed two hydraulic fracture patterns in different stress regimes. In a normal stress regime, it leads to fractures, with interacting branches because of the pre-existing fracture. Tortuous fractures were found along the fracture height when one of the horizontal stresses is the maximum principle stress.

Gu *et al.* (2012) have developed a criterion to determine if a fracture crosses a frictional pre-existing interface at non-orthogonal angles, validating it with

laboratory tests as stated previously. This criterion is an extension of Renshaw and Pollard (1995) for orthogonal intersections of fractures with material interfaces. Figure 2.11 shows the results obtained in the reference. .

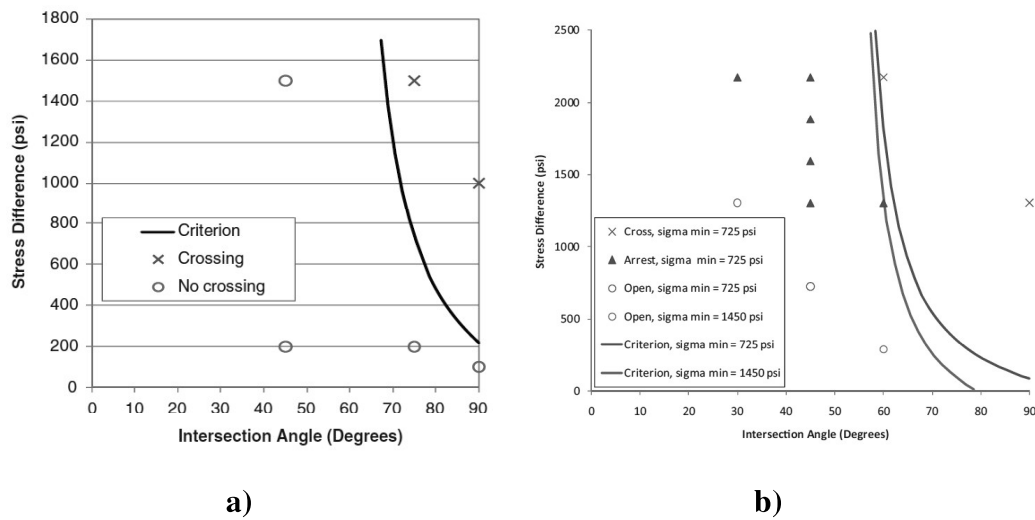


Figure 2.11 – Comparison of laboratory tests with Gu's analytical criterion. a) Gu's tests. b) Blanton's tests

Cheng *et al.* (2014) developed a three-dimensional analytical model to predict crossing which assumed that crossing occurs when two conditions are met: first, the maximum tensile stress at the hydraulic fracture tip is equal to the tensile strength of the rock on the opposite side of the natural fracture; second, no shear slippage occurs on the natural fracture surface. Results of Figure 2.12 show that the criterion fits very well to the laboratory tests for the relations between dip angle, strike angle and differential confining stress.

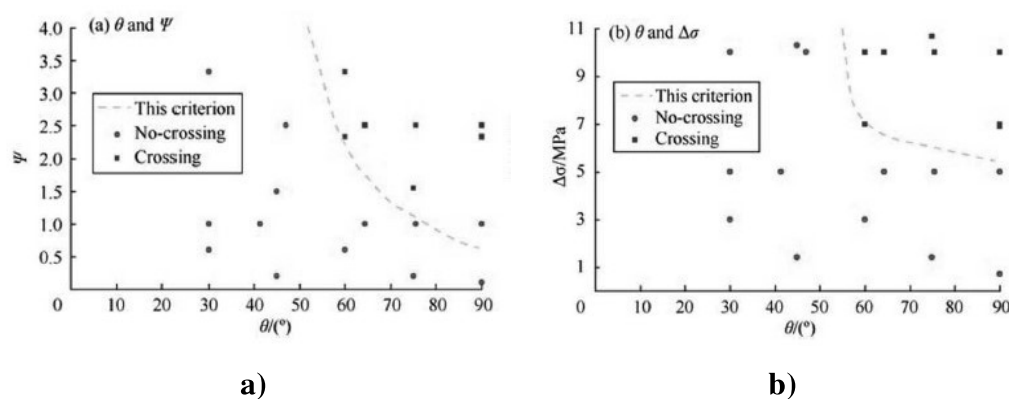


Figure 2.12 – Comparison of laboratory tests with Cheng's analytical criterion. a) dip vs strike angles space b) dip vs differential stresses space (Cheng *et al.* (2014))

2.2.4. Numerical models

Despite the advances in modelling with numerical tools, most models in the literature still assume that the hydraulic fracture is a single planar fracture. This contrasts with the fact that multistranded hydraulic-fracture geometry is a common occurrence (Dahi-Taleghani and Olson, 2011; Zhang and Ghassemi, 2011). Consequently, single-crack models may result in loss of accuracy if fracture interaction with natural fractures is not taken into account.

In the past few years, researchers focused more on this specific subject, resulting in developments in understanding how natural fractures affect a hydraulic fracturing treatment. Similarly to the studies described in Chapter 2.1.3.2, different techniques were used to simulate numerically the interaction between hydraulic and natural fractures.

Finite Element Method

Dyskin and Caballero (2009) investigated the interaction between the hydraulically driven fracture and frictionless natural fault using the finite element method, and illustrated that a relatively long frictionless and cohesionless fault is capable of arresting the hydraulic fracture propagation.

Dahi-Taleghani and Olson (2011) presented a numerical model based on enriched nodes to study fracture intersections by tracking fluid fronts in the network of reactivated fissures, where the hydraulic fracture was arrested by pre-existing natural fractures, and/or was controlled by shear strength and potential slippage at the fracture intersections. The same authors performed analyses in full scale fractured reservoirs (see Figure 2.13) and showed that when natural fractures are perpendicular to the direction of the hydraulic fracture, the largest possible debonded zone may form, which is equivalent to the optimum case to stimulate a reservoir.

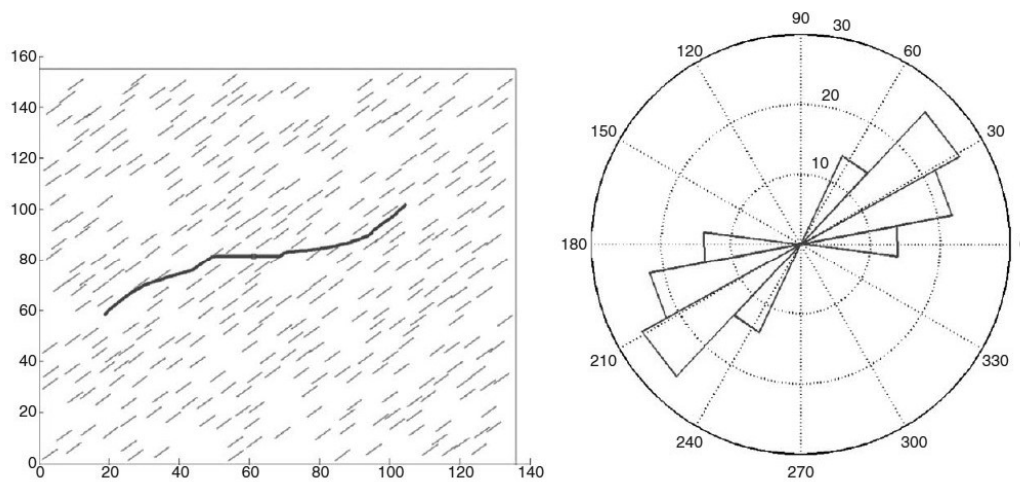


Figure 2.13 – Resultant hydraulic fracture pattern and rose diagram in the case where natural fractures make a 45° angle with the original orientation of the hydraulic fracture (Dahi-Taleghani and Olson, 2011)

Zhang and Ghassemi (2011) performed a comprehensive study on the interaction between the hydraulic fracture and natural fault, and concluded that the fault influence is conditioned by its shear stiffness, its inclination, and its distance from the hydraulic fracture. It was also highlighted that the hydraulic fracture always tends to propagate along the maximum compressive stress direction.

Keshavarzi, Mohammadi and Bayesteh (2012) studied the interaction between hydraulic and natural fractures using the XFEM, considering a constant and uniform net pressure throughout the hydraulic fracture system. They compared numerical simulations with the laboratory tests of Blanton (1982) and showed that natural fractures most probably divert hydraulic fractures at low angles of approach while at high horizontal differential stress and angles of approach of 60 or greater, the hydraulic fracture crosses the natural fracture. Keshavarzi and Jahanbakhshi (2013) compared the XFEM results of fracture interactions studies (see Figure 2.14) with a neural network that was developed based on horizontal differential stress, angle of approach, interfacial coefficient of friction, Young's modulus of the rock and flow rate of the fracturing fluid. The results indicated that the developed Artificial Neural Network was not only feasible but also yields quite accurate outcome.

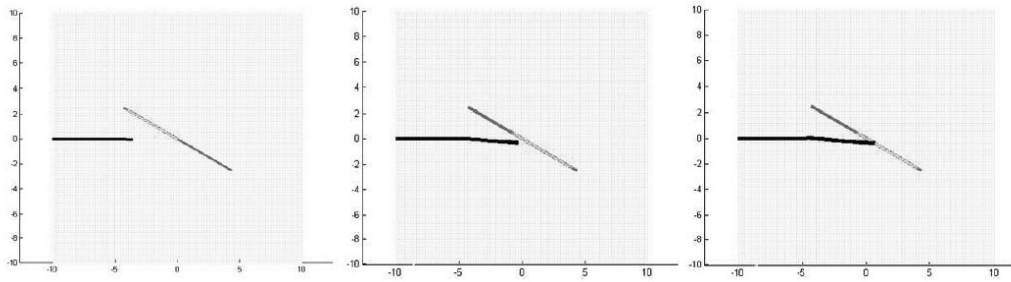


Figure 2.14 – Hydraulic fracture and natural fracture behaviour as hydraulic fracture is propagating toward the pre-existing natural fracture and intersects with it. Light blue represents the debonded zone of the natural fracture (Keshavarzi, Mohammadi and Bayesteh, 2012)

Khoei, Vahab and Hirmand (2016) modelled the interaction between the fluid-driven fracture and frictional natural fault using an enriched-FEM technique based on the partition of unity method. The intersection between two discontinuities was modelled by introducing a junction enrichment function. The medium is considered impermeable and the fluid pressure within the fracture was assumed constant throughout the propagation process. The frictional contact behaviour along the fault faces was modelled using an X-FEM penalty method. The authors showed that a lower value of fault length together with a larger frictional resistance along the natural fault produces a larger vertical tensile stress ahead of the intersection point of two discontinuities, and increases the possibility of penetration of the hydro-fracture through the natural fault. One further conclusion of the work is that the far-field stress conditions have a significant effect on the performance of internal pressure imposed on the hydro-fracture faces, and plays an important role on the mechanism of interaction between the hydro-fracture and natural fault. Moreover, it was concluded that there is a wide range of parameters that may affect the overall behaviour of the interaction mechanism, including the hydraulic fracture/natural fault configuration, the fault inclination angle, far-field stress conditions, and the frictional resistance along the natural fault.

In Khoei *et al.* (2015) the results of two hydraulic fracturing experimental tests performed on impermeable rock blocks with natural discontinuities were compared with those obtained from the X-FEM numerical model, showing very good agreement between the numerical and experimental results. It was shown that the shear strength of the natural fault plays a key role in the mechanism of

interaction, including the arrest, penetration, offset crack propagation, and diversion when the hydro-fracture merges with the natural fault.

Other Methods

Dong and De Pater (2001) used the boundary element method for the simulation of hydraulic fracturing and its interaction with faults. The work was based on the displacement discontinuity method, which was first presented by Crouch and Starfield (1983), and concluded that a fault has an evident effect on the crack propagation.

Zhang and Jeffrey (2006) modelled a fluid-driven fracture intersecting a pre-existing fracture using the displacement discontinuity method and the finite difference method to deal with the coupling mechanism of rock fracture and fluid flow. It was stated that in the presence of pre-existing fractures, the fluid-driven cracks can be arrested or retarded in growth rate as a result of diversion of fluid flow into and frictional sliding along the pre-existing fractures. Frictional behaviour significantly affects the ability of the fluid to enter or penetrate the pre-existing fracture only for those situations where the fluid front is within a certain distance from the intersecting point. The authors also showed that fracture re-initiation from secondary flaws can reduce the injection pressure, but re-initiation is suppressed by large sliding on pre-existing fractures that are frictionally weak.

Nagel *et al.* (2011) used the Distinct Element Method to model discontinuities governed by Mohr Coulomb as boundary interactions between blocks. The deformable blocks were subdivided into a mesh of finite differences elements and the flow model included a system of flow planes. The simulation of injected well with natural fractures was performed and the fracture geometry was defined by means of a Discrete Fracture Network (DFN), as shown in Figure 2.15.

Kresse *et al.* (2014) proposed a tool that, although based on very simple methods, gathered many phenomena that affect hydraulic fracture propagation in fractured reservoirs. The coupled fluid flow and elastic deformation equations were defined with similar assumptions of conventional pseudo-3D fracture models and the stress effects between fractures given by Theory of Dislocations. The interaction with natural fractures is based on an analytical crossing model and the fracture geometry is defined in an unconventional fracture model (UFM), as shown in Figure 2.16. The implemented model solves a system of equations governing

fracture deformation, height growth, fluid flow, and proppant transport in a complex fracture network with multiple propagating fracture tips. Simulation results from the model showed that stress anisotropy, natural fractures, and interfacial friction play critical roles in creating fracture network complexity.

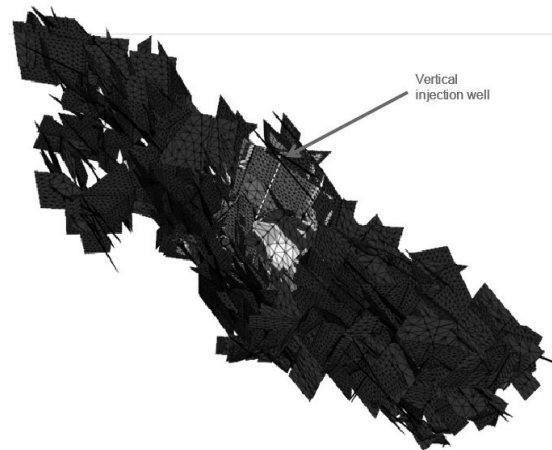


Figure 2.15 – Pore pressures in the model (Nagel et al., 2011)

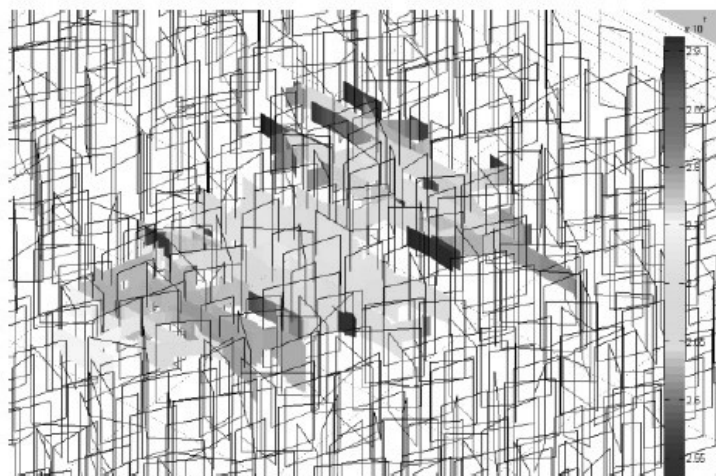


Figure 2.16 – Fluid pressures in the fracture network (Kresse et al., 2014)

Damjanac *et al.* (2013) presented a code that uses a three-dimensional lattice representation of brittle rock consisting of point masses (nodes) connected by springs with the pre-existing joints being derived from a user-specified discrete fracture network (DFN). Non-steady, hydro-mechanically coupled fluid flow and pressure within the network of joint segments and the rock matrix were also considered. The equation of motion is solved for all lattice nodes using the Finite Difference Method. The springs between the nodes break when their strength (in tension) is exceeded, corresponding to the formation of microcracks, which link to

form macro scale fractures. The authors applied the proposed code to the simulation of an injected well with natural fractures, as Figure 2.17 shows.

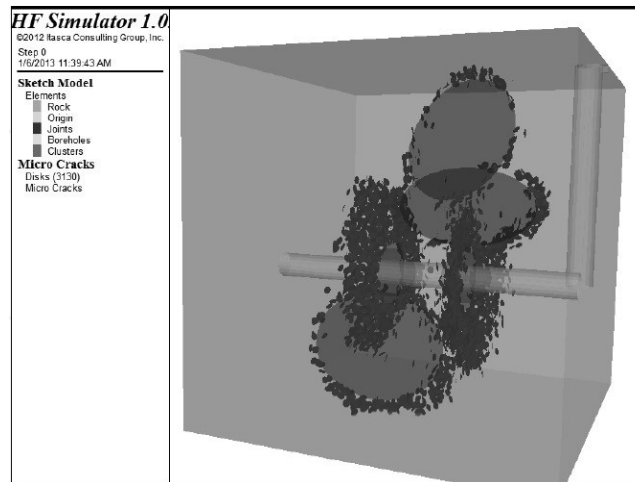


Figure 2.17 – Hydraulic fractures generated in a medium with three pre-existing joints (blue disks are microcracks) (Damjanac et al., 2013)

2.3. The eXtended Finite Element Method

2.3.1. Introduction

The eXtended finite element method (XFEM) is a technique to model strong (displacement) or weak (strain) discontinuities over a conventional finite element model. This technique was first presented by Belytschko and Black (1999), following research on enrichment strategies presented Benzley (1974). It was presented as a minimal remeshing finite element method for crack growth based on setting special enrichment functions to extra degrees of freedom along the fracture tip to capture the field singularities. The authors supported the method in the partition of unity property, presented by Melenk and Babuska (1996), which basically states that the shape functions in any point inside a finite element may be affected of local approximation functions, as its sum is kept equal to one.

Moes and Dolbow (1999) developed the method in order to avoid any type of remeshing, by using the Haar function in the fracture body and tip functions in the fracture tip. Figure 2.18 shows the nodes that are affected by the method, where the circled nodes represent the fracture body and the squared nodes the fracture tip. The method treats the crack as a completely separate geometric entity and the only

interaction with the mesh occurs in the selection of the enriched nodes. The authors highlight how accurately the stress intensity factors can be computed with relatively coarse meshes and how it is readily generalized to other problems such as those in three dimensions and involving nonlinear materials. As the main drawback, it is pointed out that there is the need to account for a variable number of degrees of freedom per node.

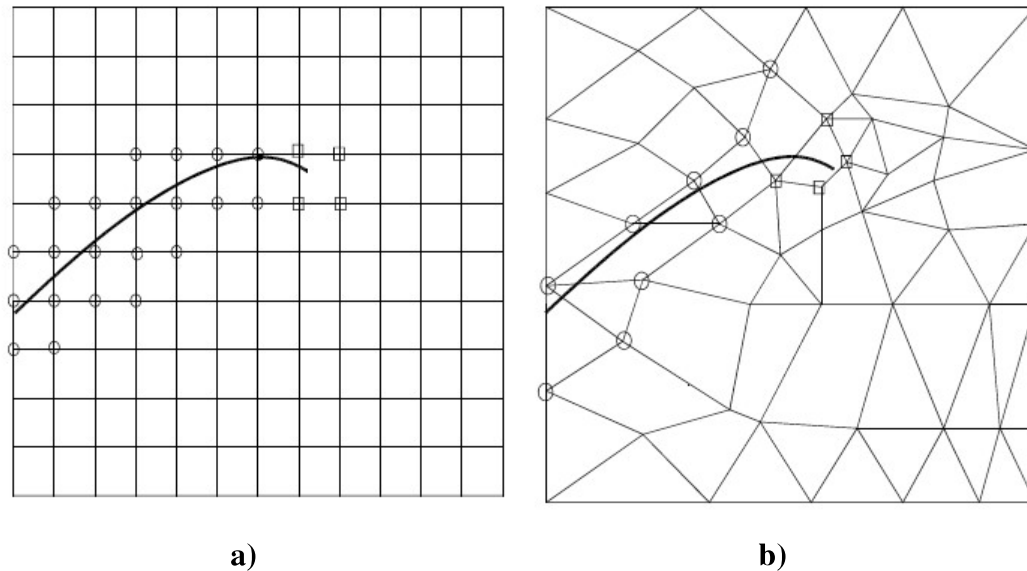


Figure 2.18 – Discontinuity on a structured mesh (a) and on an unstructured mesh (b). The circled nodes are enriched by the jump function whereas the squared nodes are enriched by the branch tip functions (Moës and Belytschko, 2002)

Sukumar *et al.* (2000) scaled the XFEM implementation for three-dimensional problems, comparing the results with penny and elliptical analytical solutions and showing that a good agreement was obtained. Wells and Sluys (2001) and Moës and Belytschko (2002) extended the implementation to quasi-brittle materials, by considering a cohesive zone at the crack tip, showing the effectiveness of the proposed method through simulations of cohesive crack growth in concrete.

The use of the XFEM in quadratic elements was presented by Stazi *et al.* (2003). Lee *et al.* (2004) combined a mesh superposition method with the XFEM to model stationary and growing fractures. The fracture tip field was modelled by superimposed quarter point elements on an overlaid mesh, and the body of the discontinuity was implicitly described by a step function on partition of unity.

Khoei (2008) presents in his book an extensive overview about the theoretical and practical application of the XFEM in continuum mechanics.

Similarly to the present research, different authors have implemented the XFEM using commercial software, such as Abaqus. Giner *et al.* (2009) and Silva (2015) implemented an XFEM element using Abaqus UEL user subroutine to simulate mechanical problems based in linear elastic fracture mechanics and non-linear frictional contact analyses. Chen (2013) also considered fluid pressure degrees of freedom to describe the fluid flow within the crack and its contribution to the crack deformation, thus modelling hydraulic fracture problems.

2.3.2. Fracture geometry in XFEM

In the XFEM, the fracture geometry is independent of the mesh and its presence is taken into account by creating enrichment degrees of freedom and applying local functions to those. In order to correctly and efficiently represent the fracture geometry, different techniques were used.

The level set function (LSF), by Osher and Sethian (1988) is the most frequently used technique with the XFEM to implicitly define the location and geometry of a discontinuity. Basically, two functions are used to represent the fracture at any point of the domain, one for the crack body and the other for the crack tip. Then, the values of the enrichment functions at any degree of freedom may be taken from the LSF, directly (signed distance) or indirectly (tip enrichment functions) (Fries and Baydoun, 2012). This technique may also be used for crack growth as new segments update the LSF when propagation occurs.

More advanced LSF techniques were developed later, such as Ventura, Budyn and Belytschko (2003) who introduced the LSF consisting of vectors to describe a propagating fracture in the element-free Galerkin method. Ji, Chopp and Dolbow (2002) presented a hybrid XFEM-LSF to model the evolution of fluid phase interfaces to represent temperature jump.

Sukumar *et al.* (2008) solved three-dimensional problems by combining the XFEM with the fast marching method, which was originally developed by Sethian (1996) and is characterized by avoiding the need to represent the geometry of the interface during its evolution by tracking the first arrival of the interface as it passes a point.

2.3.3. XFEM with coupled problems

The flow of fluids in deformable porous media has been studied via the XFEM framework to analyse the physical behaviour of many issues in geotechnical and petroleum engineering (Youn, 2016). De Borst, Réthoré and Abellan (2006) analysed a two phase fluid saturated media for a biaxial plane strain case with a discontinuity propagation. Réthoré, de Borst and Abellan (2006) presented a two-scale approach of the XFEM for fluid flow within a deforming unsaturated and progressively fracturing porous medium and Réthoré, de Borst and Abellan (2007) modelled dynamic shear band propagation in a fluid-saturated medium. Gracie and Craig (2010) applied the XFEM for predicting the steady state leakage from layered sedimentary aquifer systems perforated by abandoned wells, showing that for coarse meshes this technique proved to be more than two orders of magnitude more accurate than the standard FEM. Huang *et al.* (2011) proposed an enrichment scheme to compute model fractures and other conduits in porous media flow problems that could capture effects of local heterogeneities introduced by subsurface features of the pressure solution.

Silvestre *et al.* (2015) implemented an enriched element to compare the coupled behaviour of fractured materials with analytical solutions and with examples simulated in other software. Lamb, Gorman and Elsworth (2013) presented a fracture mapping approach combined with the extended finite element method to simulate coupled deformation and fluid flow in fractured porous media using a transfer function to model the flow interaction between the porous matrix and existing fractures. Sheng *et al.* (2015) (see Figure 2.19) presented a numerical framework to simulate coupled deformation and fluid flow in porous media, also addressing problems with arbitrary orientation and intersection of sealed fractures.

As the modelling of hydraulic fractures is also a coupled problem, many other research works in this area are presented in Chapters 2.1.3 and 2.2.4.

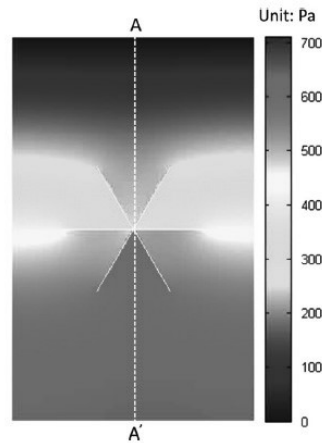


Figure 2.19 – Excess pore pressure field (Sheng et al., 2015)

2.3.4. XFEM with fracture branching or crossing

The consideration of multiple fractures that intersect each other within the XFEM concept was introduced by Daux, Moes and Dolbow (2000), through the concept of an enriched junction function to be used at each intersection. Budyn *et al.* (2004) applied the XFEM technique for multiple fractures growing and interacting within both homogeneous and inhomogeneous brittle materials. Zi *et al.* (2004) provided an approach to model multiple fracture propagation and intersection in a quasi-brittle cell with random minor fractures.

Duarte, Reno and Simone (2007) presented high-order implementations of a generalized finite element method for three-dimensional branched cracks (see Figure 2.20) showing that convergence rates obtained are close to those of problems with smooth solutions.

The same methodology was used by Chen and Lin (2010) to compute the T-Stress in the branch crack problem and Das, Sandha and Narang (2013) to study the behaviour of rock bolts for improvement in ground support.

Siavelis *et al.* (2013) used junction functions to simulate large sliding along branched discontinuities, running several examples, including a 3D geological graben with branching faults.

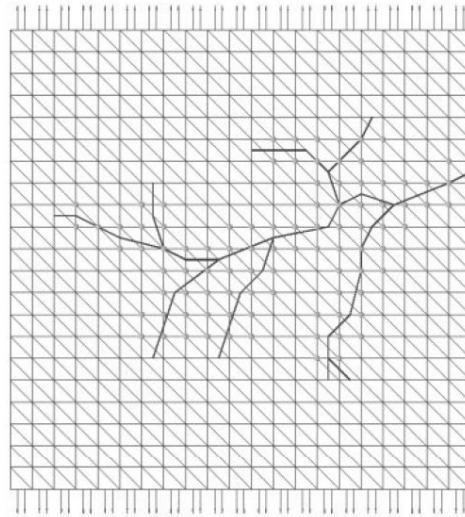


Figure 2.20 – Enriched nodes represented by circles (Duarte, Reno and Simone, 2007)

2.3.5. Crack tip behaviour in XFEM

In the early years of research with XFEM, most academic works (Belytschko and Black, 1999; Sukumar *et al.*, 2000; Belytschko *et al.*, 2001; Ventura, Budyn and Belytschko, 2003; Zi *et al.*, 2004) considered the tip behaviour by using a specific enrichment function based on an asymptotic stress field, following the Linear Elastic Fracture Mechanics (LEFM). Figure 2.18 shows that the tip nodes are considered only near the fracture tip. The asymptotic functions were based in sinusoidal functions and allowed to use propagation criteria based on stress intensity factors. Basically, a new fracture segment is created when the stress intensity factors at fracture tip are reached.

Aware of the relevance of the small-scale processes that occur at the fracture tip, which control the global response of the fracture, and of the complexity involved in constructing solutions for fluid driven factors (Detournay, 2004), Lecampion (2009) presented an XFEM formulation for the solution of hydraulic fracture problems by introducing special tip functions encapsulating tip asymptotic functions that represent the different regimes typically encountered in hydraulic fractures.

However, LEFM is only applicable when the size of the fracture process zone (FPZ) at the crack tip is small compared to the size of the crack and the size of the specimen (Bazant and Planes, 1998). In order to extend the use of XFEM to quasi-

brittle materials, Wells and Sluys (2001) and Moës and Belytschko (2002) applied the cohesive crack concept, where the propagation is governed by a traction–displacement relation (see Figure 2.21a) across the crack faces near the tip. This behaviour is assigned to the region between the real physical tip and the mathematical tip, where the process zone ends (see Figure 2.21b). Moës and Belytschko (2002) considered that, since the stresses at the tip are not singular, non-asymptotic functions should be used for tip enrichment. Other authors used enriched techniques to simulate cohesive crack growth and showed its applicability to problems such as Mode I and Mixed Mode experimental tests (Mariani and Perego, 2003; Cox, 2009) or three and four point beam bending tests (Mergheim, Kuhl and Steinmann, 2005).

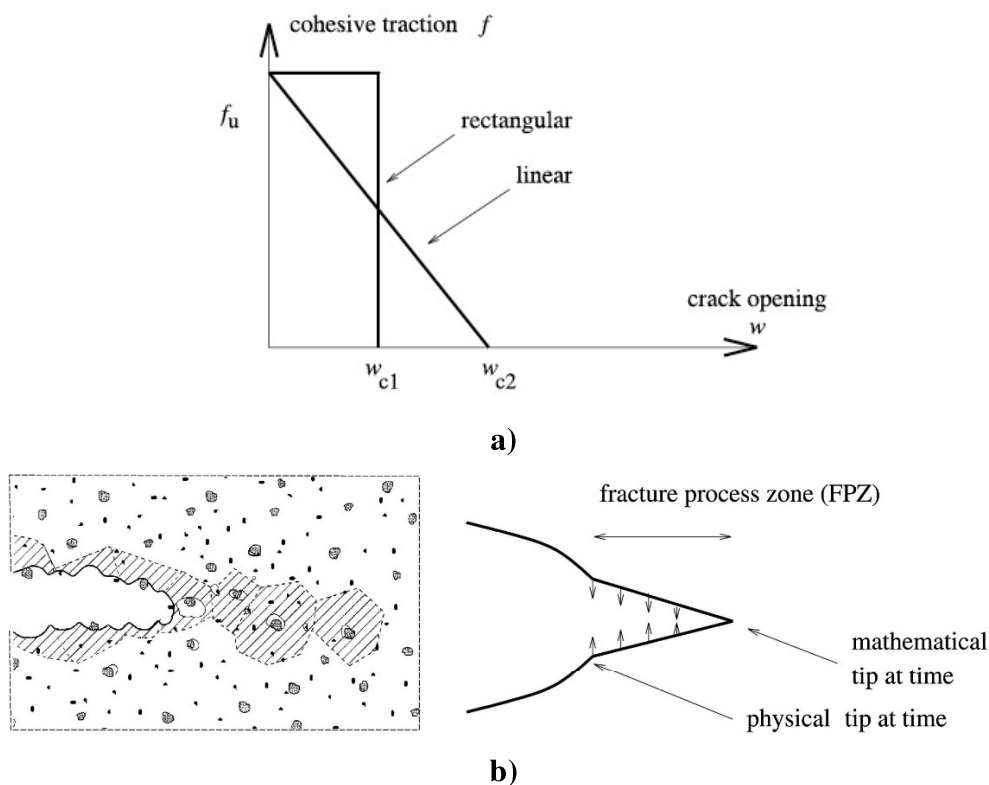


Figure 2.21 – Modelling of the fracture process zone. (a) Two cohesive laws with the same cohesive strength and fracture energy. (b) The extent of the cohesive zone at a certain moment (Moës and Belytschko, 2002; Wang, 2016)

Wells and Sluys (2001) modelled cohesive crack growth by considering only the jump function to represent the fracture and guaranteeing the closure of the tip by deactivating the jump enhancement at the nodes closest to the tip. This facilitates implementations, as only one enrichment function is required and concerns are

avoided, such as the existence of blending elements. However, it must be stated that the fracture tip cannot lie inside one element, but only on its borders. Therefore, a propagation segment must always cross the element totally. Other research works were developed under this premise (Zi and Belytschko, 2003; de Borst, Remmers and Needleman, 2006; Comi and Mariani, 2007; Mougaard, Poulsen and Nielsen, 2007), as well as commercial software (Simulia, 2014).

2.3.6. Contact problems in XFEM

To simulate situations where compressive stresses lead to contact between fracture faces, different types of contact models have been implemented. The literature review identifies the most frequently used contact models in association with XFEM simulations are:

- Penalty Method;
- Lagrange Multipliers;
- Augmented Lagrange Multipliers;
- LATIN method.

The penalty method consists in using a high stiffness (penalty coefficient) between the fracture faces, when the faces are in contact. This way, when under compressive contact, two fracture faces suffer a slight overlap and the stresses obtained from that relative displacement are the normal contact stresses. This method is easy to implemented which does not require the introduction of constraints or degrees of freedom to represent contact. It also does not require the introduction of outer iterative loops for constraint check. On the other hand, the accuracy of satisfying equilibrium highly and overlapping restrictions depends on the magnitude of penalty parameter. The larger the value of the penalty parameter, the more accurate is the solution. However, very large values for the penalty parameter may result in an ill conditioned formulation when the penalty parameter is combined with finite stiffness of bodies in contact. As stated by Grazina (2009), the process may intensify instability problems for paths that impose randomness in the relative displacements evolution. Khoei and Nikbakht (2006) and Liu and Borja (2008) applied this method to simulate frictional contact using standard Coulomb friction. More recently, Khoei and Mousavi (2010) presented a node-to-node

contact algorithm for XFEM to model the large deformation-large sliding contact problem using the penalty approach.

The Lagrange Multipliers Method, considers extra degrees of freedom so the contact forces are computed as primary unknowns. The restriction of null relative displacement of the faces in contact is enforced exactly. The major limitation of this method is that it requires extra variables in the model, affecting the dimension and sparsity of the system of equations. According to Khoei (2008), other limitations may exist, such as the existence of diagonal values that take the value zero, leading to difficulties in finding a solution. Nistor *et al.* (2009) coupled the X-FEM with the Lagrangian large sliding frictionless contact algorithm while Siavelis *et al.* (2013) applied the same technique to three-dimensional problems where fractures intersect and branch.

The Augmented Lagrangian Method eliminates the drawbacks of penalty and Lagrange multipliers techniques, and attempts to achieve a predetermined tolerance for the contact constraint through an iterative procedure. The main idea of this technique is to combine the penalty and Lagrange multipliers methods to inherit the advantages of both techniques, that is, decreasing the ill-conditioning of governing equations, and essentially satisfying the contact constraints with finite values of penalty parameters (Khoei, 2008). The values of the penalty parameter are calculated iteratively in an outer loop until a predetermined tolerance is achieved and then, the non-linear FEM problem is solved in an inner loop. Elguedj, Gravouil and Combescure (2007) present an augmented Lagrangian formulation in the XFEM framework that is able to deal with elasto-plastic fatigue crack growth. Hirmand, Vahab and Khoei (2015) implemented this method using a return mapping algorithm for the Coulomb friction rule, showing good accuracy of the proposed model in simulations of straight, curved and wave-shaped discontinuities.

The LARge Time INcrement (LATIN) Method shares similar features with the Augmented Lagrangian Method, i.e. runs two iterative procedures, one for the convergence in the penalty constraint, and other for the non-linear system of equations. The two iterative procedures are solved separately until convergence is achieved in both, as Figure 2.22 shows. Dolbow, Moës and Belytschko (2001) were the first to incorporate contact and friction in crack faces with the XFEM to simulate crack growth under opening/closing modes using the LATIN Method. Gravouil,

Pierres and Baietto (2011) scaled the same method to three dimensional models under cyclic fretting loading.

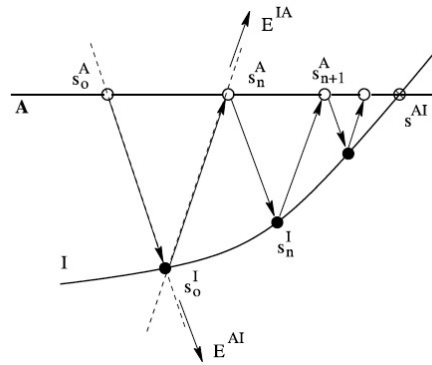


Figure 2.22 – The iterative procedure in the LATIN algorithm (Dolbow, Moës and Belytschko, 2001)

3

XFEM Formulation for Coupled Problems

This chapter focus on the theoretical formulations that give base to the implemented code in this thesis. As stated before, the eXtended Finite Element Method shares its base characteristics with the Finite Element Method. Consequently, the base concepts of the Finite Element Method (p. ex. the definition of topology or shape function) are not explained in this chapter and further reading about this may be done in works by Zienkiewicz, Taylor and Zhu (2013) or Potts and Zdravković (1999).

The physical differential equations that govern the behaviour of the implemented model are presented, as well as the developments and transformations made for them to be numerically computed. The physical equations are defined to couple both the hydro-mechanical behaviour in the porous region and in the fracture. Then the space is discretized by enrichment functions, which were established by Moes and Dolbow (1999) and Belytschko and Black (1999) and extended for intersections by Daux, Moes and Dolbow (2000), and time discretized by the Newmark technique. The set of resulting non-linear equations is linearized and solved using the Newton-Raphson method. The formulation follows the mathematical notation presented by Khoei *et al.* (2014).

Finally, the constitutive model used to simulate the behaviour of the natural fractures is presented. Although used together, the formulation for the contact and friction models is presented separately. The former is based on the penalty method while the latter uses Rueda *et al.* (2014) as reference.

3.1. Governing equations

Modelling of hydraulic fracture propagation in porous fractured media involves coupling of various physical phenomena. In the implementation presented in this work the following effects are considered: deformation of the continuous medium, deformation and friction in the fracture, pore fluid flow through the porous

medium surrounding the fracture, fluid flow within the fracture, fluid exchange between the fracture and the surrounding porous medium, and propagation of the fracture. Two different partial differential equations are used to correctly simulate those phenomena, equilibrium equation for the mechanical behaviour and continuity equation for the fluid flow.

Some simplifications or assumptions are made. It is assumed that the porous medium is saturated and both pore and fracture flow occur under laminar regime. In addition, both grains and pore fluid have a bulk modulus which is several orders of magnitude higher than the skeleton's bulk modulus, so they can be considered incompressible. Also, all inertial effects and body forces are neglected, as the in situ stress state is defined as an input. Though relevant in certain situations, these assumptions do not substantially affect the overall behaviour of the hydraulic fracture models.

The partial differential equations apply to the generalized fractured domain defined in Figure 3.1.

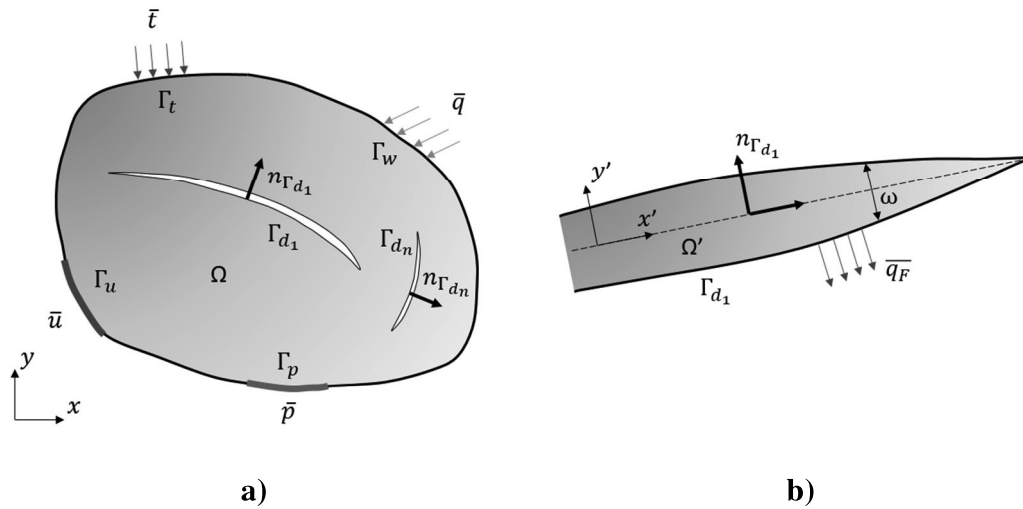


Figure 3.1 – Generalized fractured domain. a) Boundary conditions of a fractured body Ω with a geomechanical discontinuity Γ_c . b) Geometry of the fracture domain Ω' (adapted from Khoei et al. (2014))

Considering \mathbf{n}_Γ the outward unit normal vector to the general domain Ω , the boundary conditions (BC) of the domain are as follows:

- $\mathbf{u} = \bar{\mathbf{u}}$ on Γ_u (essential BC) and $\boldsymbol{\sigma} \cdot \mathbf{n}_\Gamma = \bar{\mathbf{t}}$ on Γ_t (natural BC), for the porous medium

- $\mathbf{p} = \bar{\mathbf{p}}$ on Γ_p (essential BC) and $\dot{\mathbf{w}} \cdot \mathbf{n}_r = \bar{q}$ on Γ_w (natural BC), for the fluid phase

Additional BC apply to the discontinuities having \mathbf{n}_{Γ_d} as the unit normal vector which points to the positive side Ω^+ and $[[\dot{\mathbf{w}}]]$ as the jump of fluid velocity in the discontinuity:

- $\boldsymbol{\sigma} \cdot \mathbf{n}_{\Gamma_d} = -\mathbf{p}_F \cdot \mathbf{n}_{\Gamma_d}$ and $[[\dot{\mathbf{w}}]] \cdot \mathbf{n}_{\Gamma_d} = \bar{q}_F$ on Γ_d (natural BC).

The linear momentum balance that characterizes the mechanical behaviour of the porous medium is given by

$$\nabla \cdot \boldsymbol{\sigma} = 0 \quad (3.1)$$

where $\boldsymbol{\sigma}$ is the stress tensor and ∇ the vector gradient operator.

The total stress tensor may be defined as $\boldsymbol{\sigma} = \boldsymbol{\sigma}' - p \cdot \mathbf{I}$, where $\boldsymbol{\sigma}'$ is the effective stress tensor, p the average pressure of pore fluid and \mathbf{I} the identity matrix. In this context, compressive stresses are negative.

The continuity equation governs the fluid phase. Although belonging to the same phase, different equations describe porous and fracture flow. This allows representing loss of pressure between fracture faces and surrounding porous medium, as the filter cake effect. Considering a saturated medium with incompressible fluid, the simplified continuity equation for the porous and the fracture flow follows

$$\nabla \cdot \dot{\mathbf{w}} + \nabla \cdot \dot{\mathbf{u}} = 0 \quad (3.2)$$

where $\dot{\mathbf{w}}$ is the fluid velocity, while $\dot{\mathbf{u}}$ is the solid-fluid mixture velocity, if the equation is applied on the porous or the fracture domain, or the fracture opening velocity, if on the fracture domain.

The constitutive mechanical equation for the porous medium is introduced as the strain- effective stress relationship in Eq. (3.3), where \mathbf{D} is a fourth order tangential stiffness matrix of the bulk material. Due to assumption of small strains and displacements the strain-displacement kinematic relation is given by Eq. (3.4), where ∇_s is the symmetric part of the gradient operator. The mechanical behaviour of the fracture is given by a traction-displacement relationship, such as the one in Eq. (3.5) where \mathbf{D}_F represents a second order tangential stiffness matrix, \mathbf{t}_F the fracture tractions and $[[u]]$ the fracture relative displacements.

$$d\boldsymbol{\sigma}' = \mathbf{D} \cdot d\boldsymbol{\varepsilon} \quad (3.3)$$

$$\boldsymbol{\varepsilon} = \nabla_s \mathbf{u} \quad (3.4)$$

$$d\mathbf{t}_F = \mathbf{D}_F \cdot d[\mathbf{u}] \quad (3.5)$$

$$\dot{\mathbf{w}} = -\mathbf{k} \cdot \nabla \mathbf{p} \quad (3.6)$$

One further assumption is laminar flow without gravitational effects both in the porous medium and in the fracture medium, following Darcy's Law, Eq. (3.6), where \mathbf{p} is the pressure and \mathbf{q} the flow rate. The variable \mathbf{k} depends on the domain of interest:

- In the porous medium, it represents the hydraulic conductivity matrix (\mathbf{k}_f), which is given by the constant second order matrix

$$\begin{bmatrix} k_x & 0 \\ 0 & k_y \end{bmatrix}$$

- In the fracture tangential direction, \mathbf{k} represents the fracture longitudinal transmissibility, which affects the longitudinal flow represented in Figure 3.2a. This is a scalar that is assumed to follow a cubic law, depending on the fracture aperture ω and fluid dynamic viscosity μ , given by Eq. (3.7).

$$k_{f_F} = \omega^2 / 12\mu \quad (3.7)$$

- In the fracture-porous region interface, it represents the conductivity of a very thin layer that causes loss of pressure in the flow transversal to the fracture (see Figure 3.2b). A scalar parameter c , named fracture face transversal conductivity, quantifies this effect. Although having different dimensions, this parameter is physically similar to the so-called leak-off coefficient. Considering p_F the fluid pressure in the discontinuity, p the pressure in the surrounding porous region and q_F as the flow rate between both, the adaptation of Darcy's equation gives

$$q_F = c(p - p_F) \quad (3.8)$$

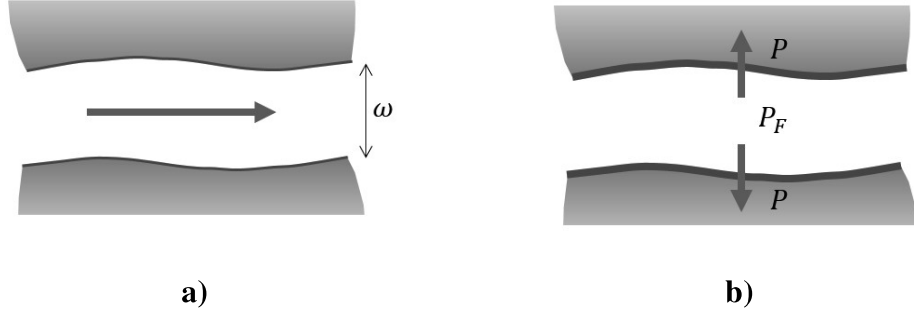


Figure 3.2 – Representation of fracture flow. a) Longitudinal flow. b) Transversal flow

3.2. Weak formulation

The weak form of the governing differential equations is obtained by integrating the product between each equation and admissible test functions. Then, in order to represent correctly the fractured domain, the Divergence Theorem for discontinuous functions is applied, as given in Eq. (3.9), in order to correctly represent the fractured domain.

$$\int_{\Omega} \text{div } \mathbf{F} \, d\Omega = \int_{\Gamma} \mathbf{F} \cdot \mathbf{n}_{\Gamma} \, d\Gamma - \int_{\Gamma_d} \llbracket \mathbf{F} \rrbracket \cdot \mathbf{n}_{\Gamma_d} \, d\Gamma \quad (3.9)$$

$$\int_{\Omega} \text{div } \mathbf{F} \, d\Omega = \int_{\Gamma} \mathbf{F} \cdot \mathbf{n}_{\Gamma} \, d\Gamma - \sum_i^{N_c} \int_{\Gamma_{d_i}} \llbracket \mathbf{F}_i \rrbracket \cdot \mathbf{n}_{\Gamma_{d_i}} \, d\Gamma \quad (3.10)$$

$\llbracket \mathbf{F} \rrbracket$ represents the jump of the function \mathbf{F} , being $\llbracket \mathbf{F} \rrbracket = \mathbf{F}^+ - \mathbf{F}^-$, i.e. \mathbf{F}^+ is the value of \mathbf{F} at the boundary \mathbf{n}_{Γ}^+ and \mathbf{F}^- is the value of \mathbf{F} at \mathbf{n}_{Γ}^- . If more than one discontinuity exists, the Divergence Theorem may be generalized to Eq. (3.10), where N_c is the number of discontinuities in the domain.

Defining $\mathbf{u}(\mathbf{x}, t)$, $p(\mathbf{x}, t)$ and $p_F(x, t)$ as trial functions and $\delta \mathbf{u}(\mathbf{x}, t)$, $\delta p(\mathbf{x}, t)$ and $\delta p_F(x, t)$ as test functions and integrating over the domain Ω , the weak form of equations (3.1) and (3.2) is respectively

$$\int_{\Omega} \delta \mathbf{u}(\nabla \cdot \boldsymbol{\sigma}) \, d\Omega = 0 \quad (3.11)$$

$$\int_{\Omega} \delta p(\nabla \cdot \dot{\mathbf{w}} + \nabla \cdot \dot{\mathbf{u}}) \, d\Omega = 0 \quad (3.12)$$

As for the fracture domain Ω' presented in Figure 3.1b, the weak form of equation (3.2) is

$$\int_{\Omega'} \delta p_F (\nabla \cdot \dot{\mathbf{w}} + \nabla \cdot \dot{\mathbf{u}}) d\Omega = 0 \quad (3.13)$$

Applying to Eqs. (3.11) to (3.13) the mechanical and hydraulic constitutive relationships, Eqs. (3.3) to (3.8), in the continuous region and in the fracture, gives

$$\begin{aligned} \int_{\Omega} \delta \boldsymbol{\varepsilon} \cdot \boldsymbol{\sigma}' d\Omega - \int_{\Omega} \delta \boldsymbol{\varepsilon} \cdot \mathbf{m} \cdot p d\Omega + \int_{\Gamma_d} \llbracket \delta \mathbf{u} \rrbracket (\mathbf{t}_F - p_F \cdot \mathbf{n}_{\Gamma_d}) d\Gamma \\ - \int_{\Gamma_t} \delta \mathbf{u} \cdot \bar{\mathbf{t}} d\Gamma = 0 \end{aligned} \quad (3.14)$$

$$\begin{aligned} \int_{\Omega} \nabla \delta p k_f \nabla p d\Omega + \int_{\Gamma_d} \delta p \llbracket \dot{\mathbf{w}} \rrbracket \mathbf{n}_{\Gamma_d} d\Gamma + \int_{\Omega} \delta p \cdot \nabla \dot{\mathbf{u}} d\Omega \\ + \int_{\Gamma_w} \delta p \cdot \bar{\mathbf{q}} d\Gamma = 0 \end{aligned} \quad (3.15)$$

$$\int_{\Omega'} \nabla \delta p_F k_{f_F} \nabla p_F d\Omega - \int_{\Gamma_d} \delta p_F \llbracket \dot{\mathbf{w}} \rrbracket \mathbf{n}_{\Gamma_d} d\Gamma + \int_{\Omega'} \delta p_F \nabla \dot{\mathbf{u}} d\Omega = 0 \quad (3.16)$$

For simplicity, Eqs. (3.14) to (3.16) reflect the presence of one discontinuity. However, this formulation may be generalized to any number of discontinuities, according to Eq. (3.10). At this point, the hydro-mechanical coupling is evident in each equation. In Eq. (3.14) the hydraulic coupling arises from the pore and fracture pressures, which are present in the second and third term, respectively. In Eq. (3.15) the fluid exchange through the fracture wall is in the second term, followed by the mechanical coupling in the third term. Finally, in Eq. (3.16) the fluid exchange with the porous medium is in the second term – repeating the exchange term of Eq. (3.15) – and the fracture deformation in the third term.

Considering the integrals over the discontinuity domain (Ω') presented in Eq. (3.16) and the fact that discontinuities have an aperture many orders of magnitude smaller than the other dimensions, a simplification is convenient. It consists in assuming the fluid pressures along the discontinuity cross section as constant, reducing the integration domain in one order – from Ω' to Γ . Thus, the first and third term of Eq. (3.16) are redefined as

$$\int_{\Omega'} \nabla \delta p_F k_{f_F} \nabla p_F d\Omega = \int_{\Gamma_d} \frac{\partial \delta p_F}{\partial x'} k_{f_F} 2h \frac{\partial p_F}{\partial x'} d\Gamma \quad (3.17)$$

$$\int_{\Omega'} \delta p_F \cdot \nabla \dot{\mathbf{u}} d\Omega = \int_{\Gamma_d} \delta p_F \cdot 2h \cdot \left\langle \frac{\partial \dot{u}_{x'}}{\partial x'} \right\rangle d\Gamma + \int_{\Gamma_d} \delta p_F \cdot [\![\dot{u}_{y'}]\!] d\Gamma \quad (3.18)$$

where x' and y' are the local coordinates of the discontinuity, as seen in Figure 3.1b, and h is the half-aperture of the fracture. The local x' and y' components of the velocity vector projected on the longitudinal and transversal directions are $\dot{u}_{x'}$ and $\dot{u}_{y'}$, respectively, which are assumed to vary linearly in the transversal direction. According to this hypothesis, the derivative of the velocity in x' direction may take an average value $\langle \varepsilon \rangle = (\varepsilon^+ + \varepsilon^-)/2$. Substituting the redefined terms in Eq. (3.16) and taking the flow rate jump, i.e. the flow through the fracture faces, as $[\![\dot{\mathbf{w}}]\!] = q_F$, gives the following equation

$$\begin{aligned} \int_{\Gamma_d} \frac{\partial \delta p_F}{\partial x'} k_{f_F} 2h \frac{\partial p_F}{\partial x'} d\Gamma - \int_{\Gamma_d} \delta p_F q_F \mathbf{n}_{\Gamma d} d\Gamma \\ + \int_{\Gamma_d} \delta p_F \cdot 2h \cdot \left\langle \frac{\partial \dot{u}_{x'}}{\partial x'} \right\rangle d\Gamma + \int_{\Gamma_d} \delta p_F \cdot [\![\dot{u}_{y'}]\!] d\Gamma = 0 \end{aligned} \quad (3.19)$$

3.3. Spatial discretization

3.3.1. XFEM discretization

The eXtended Finite Element Method (XFEM) to discretize Eqs (3.14), (3.15) and (3.19) consists in adopting special spatial discretization fields. In the standard FEM, the displacement and pressure fields, $\mathbf{u}(\mathbf{x}, t)$ and $\mathbf{p}(\mathbf{x}, t)$, respectively, within an element are given by the product between the vector of node variables in one element $u_i(t)$ and shape functions related to each node N_i , as Eq. (3.20) shows. \mathcal{N} is the set of all nodal points in the domain.

$$\mathbf{u}(\mathbf{x}, t) = \sum_{i \in \mathcal{N}} u_i(t) \cdot N_i \quad (3.20)$$

Independently of the number of nodes per element, the shape functions used in the standard FEM are smooth and continuous. As a consequence, the resulting fields are also continuous. Figure 3.3 shows an example of the values along the

element of a shape function for a node i , considering a 4-node element. Three perspectives are presented for easiness of understanding.

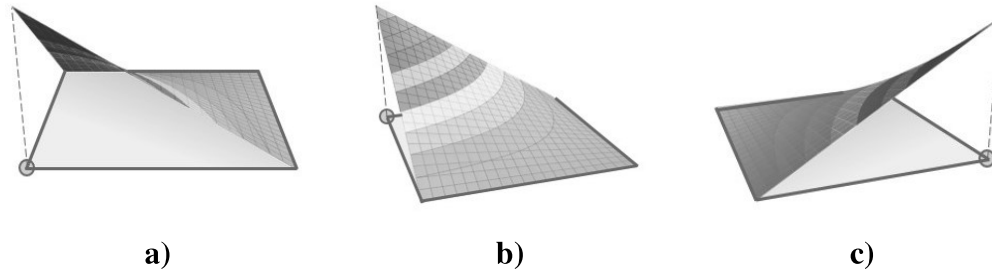


Figure 3.3 – Value of shape function in node i for a 4-node element. a) View 0°. b) View 70°. c) View 250°

The basic idea of the XFEM is to change shape functions to represent discontinuities in the displacement fields (or any other variable). For example, in order to represent a fracture explicitly within one element, for each standard degree of freedom the XFEM considers an additional degree of freedom (or “enriched degree of freedom”) which is multiplied by a discontinuous shape function, as seen in Eq. (3.21).

$$\mathbf{u}(\mathbf{x}, t) = \sum_{i \in \mathcal{N}} u_i(t) \cdot N_{u_i}^{std} + \sum_{j \in \mathcal{N}^{dis}} a_j(t) \cdot N_{u_j}^{enr} \quad (3.21)$$

This provides a discontinuous field that represents the jump in the displacement field given by the fracture faces. The additional degrees of freedom a_j are often called “enriched degrees of freedom” and the enriched shape function $N_{u_j}^{enr}$ is given by the product between the standard shape functions $N_{u_j}^{std}$ and an enrichment function ϑ , as seen in Eq. (3.22). The influence of these degrees of freedom is only considered in the \mathcal{N}^{dis} , which is the set of nodes whose support is bisected by the crack as seen in Figure 3.4.

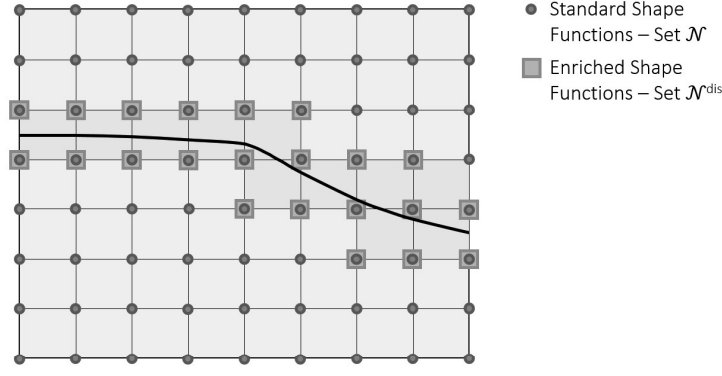


Figure 3.4 – Standard and Enriched degrees of freedom and their positions

It should be highlighted that the shape function N_u^{std} used to define the enriched shape function N_u^{enr} does not have to be the standard shape function. However, in this work, the standard shape functions are also used to compute the enriched shape functions.

$$N_u^{enr} = N_u^{std} \cdot \vartheta \quad (3.22)$$

According to Fries and Belytschko (2010), the approximation presented in Eq. (3.21) can reproduce any enrichment function exactly in Ω as long as the Partition of Unity is valid, i.e.

$$\sum_{j \in \mathcal{N}^{dis}} N_{u_j}^{enr} = 1 \quad (3.23)$$

3.3.2. Enrichment functions

As the XFEM is generalized for any kind of enrichment function ϑ , proper functions must be defined considering the type of problem of interest. In this study, only linear quadrilateral elements are used, i.e. 4 node elements, so it must be considered that the chosen enrichment functions are multiplied by linear shape functions.

For the simulation of hydraulic or natural fractures these functions must meet the following requirements: 1) show a discontinuity in the fracture position; 2) have a discontinuous derivative in the fracture position; and 3) be linear on each side of the fracture. A signed level set function guarantees these conditions.

$$\varphi(x) = \min \|x - x^*\| \cdot \text{sign} \left((x - x^*) \cdot \mathbf{n}_{\Gamma_d} \right) \quad (3.24)$$

The level set function for a point x is the closest distance to the point x^* located on the discontinuity. The signed level set function H is

$$H(\varphi(x)) = \begin{cases} +1, & \varphi(x) \geq 0 \\ -1, & \varphi(x) < 0 \end{cases} \quad (3.25)$$

As for the pore pressure fields, two different types of patterns are expected to occur in the studied problems. For the sake of simplicity, these will be called hydraulic fracture type and natural fracture type. Fluid injection in hydraulic fractures usually induces longitudinal and transversal flow. This leads to high pressures inside the fracture, which dissipate in the surrounding porous medium (Figure 3.5a). Furthermore, the possible occurrence of a filter cake may lead to loss of pressure on the fracture faces. As seen in Figure 3.5b, this loss of pressure may be different on both faces of the fracture. The hydraulic or mechanical conditions may also differ between fracture faces, resulting in $P_A \neq P_B$ (Figure 3.5c).

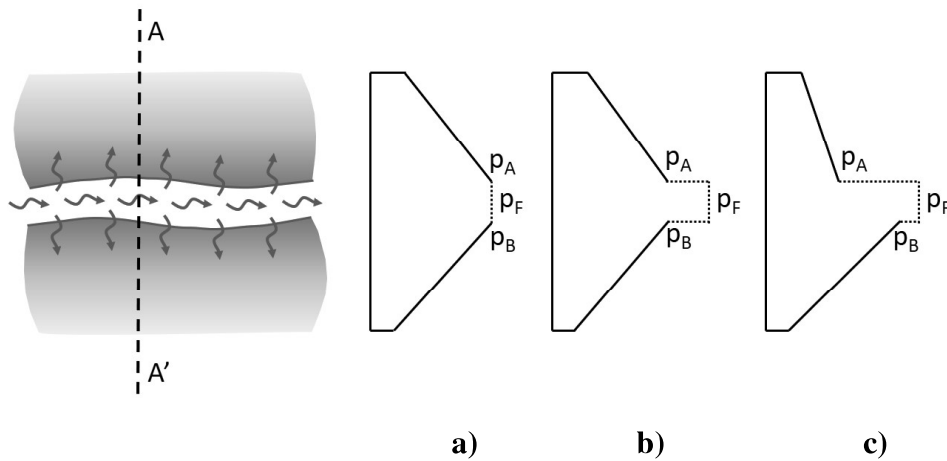


Figure 3.5 – Pore pressure patterns (section A-A') near a hydraulic fracture. a) Filter cake not considered. b) Filter cake with loss of pressure. c) Filter cake with different top and bottom leak-off conditions

In natural fractures, a different pattern is expected. In the cases of dominant transversal flow, loss of pressure related to the fracture may be significant or not, as seen in Figure 3.6. Regarding the focus of this research on studying the intersection between hydraulic and natural fractures, high pressures inside a natural fracture may occur, causing a change of behaviour from the patterns represented in Figure 3.6 to the ones presented in Figure 3.5.

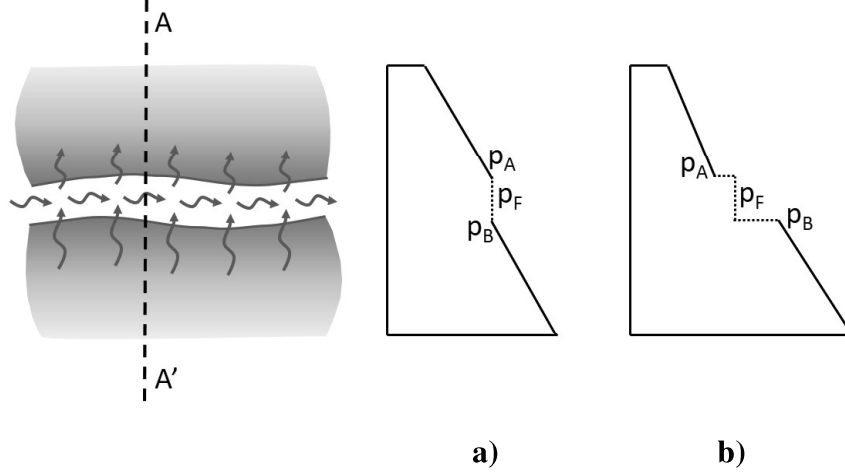


Figure 3.6 – Pore pressure patterns (section A-A') near a natural fracture. a) Without loss of pressure through the fracture. b) With loss of pressure in the fracture

Based on these considerations, the pore pressure field of a fractured element must: 1) show a discontinuity in the fracture position; 2) have a derivative which is discontinuous at the fracture face; and 3) be linear at each side of the fracture. These are the same conditions as those for the displacement fields. Consequently, the same enrichment function (signed level set function H) is adequate to represent the pore pressure fields in a fractured domain.

For hydro-mechanical coupling in the element domain, it may be stated that the sets \mathcal{N} and \mathcal{N}^{dis} are the same for both mechanical and hydraulic discretization, (3.26) and (3.27), respectively.

$$\mathbf{u}(\mathbf{x}, t) = \sum_{i \in \mathcal{N}} u_i(t) \cdot N_{u_i}^{std} + \sum_{j \in \mathcal{N}^{dis}} a_j(t) \cdot N_{u_j}^{std} \cdot H(x) \quad (3.26)$$

$$\mathbf{p}(\mathbf{x}, t) = \sum_{i \in \mathcal{N}} p_i(t) \cdot N_{p_i}^{std} + \sum_{j \in \mathcal{N}^{dis}} p_{a_j}(t) \cdot N_{p_j}^{std} \cdot H(x) \quad (3.27)$$

As stated by Belytschko *et al.* (2001), it is beneficial to replace the enrichment function in Eqs. (3.26) and (3.27) by $(H(x) - H_j)$. The enrichment function then vanishes in all elements except those that contain the discontinuity. Another advantage is that the enrichment variable vanishes in the nodal points, which means that the interpretation of the results on those nodes only depends on the standard part of the solution. This variation, often called shifted formulation, is applied in all

enrichments used in this work. However, for the sake of notation simplicity, the shifted formulation is represented by H in further developments.

It should be highlighted that, since only a sign function is used to enrich the degrees of freedom, there should not be a concern about blending elements, i.e. the non-fractured elements that have coincident nodes with enriched elements. As stated by Fries (2008), the sign enrichment is a special case that does not lead to problems in blending elements. The reason is that the sign enrichment is a constant function in the blending elements and as long as the partition of unity functions are of the same or lower order than the shape functions, the unwanted terms in the blending elements can be compensated.

From Eq. (3.10) it is noticeable that the coupled hydro-mechanical problem may be expanded to several fractures in the domain. Eq. (3.28) presents the displacement discretization of a domain with N_c fractures.

$$\mathbf{u}(\mathbf{x}, t) = \sum_{i \in \mathcal{N}} u_i(t) \cdot N_{u_i}^{std} + \sum_{k=1}^{N_c} \sum_{j \in \mathcal{N}^{dis}} a_{j,k}(t) \cdot N_{u_j}^{std} \cdot H_k(x) \quad (3.28)$$

Figure 3.7 shows the values of the shape function for a node j multiplied by the enrichment shifted function $(H(x) - H_j)$, considering a 4-node element.

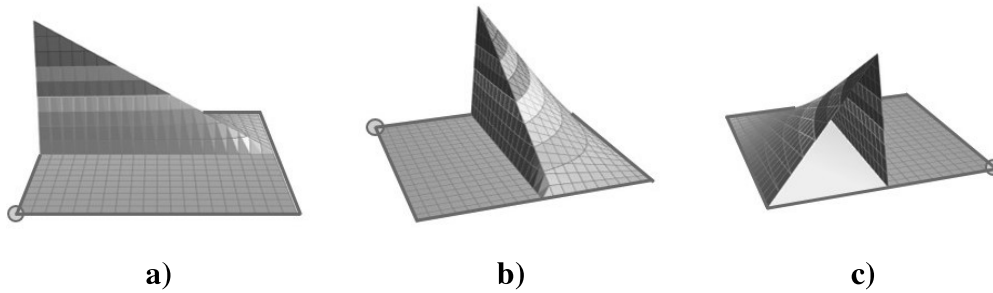


Figure 3.7 – Value of shape function in node j multiplied by the enrichment shifted function $(H(x) - H_j)$ for 4-node element. a) View 0°. b) View 70°. c) View 250°

3.3.3. Intersections

If fractures intersect each other, then the discretization needs to be adapted so it represents the intersections correctly. A junction enrichment function, J , represents an intersection between two fractures (Daux, Moes and Dolbow, 2000).

This function depends on the enrichment functions of each fracture, H_I and H_{II} , as Eq. (3.29) and Figure 3.8 present.

$$J(x) = \begin{cases} 0, & H_I(x) \geq 0 \\ H_{II}(x), & H_I(x) < 0 \end{cases} \quad (3.29)$$

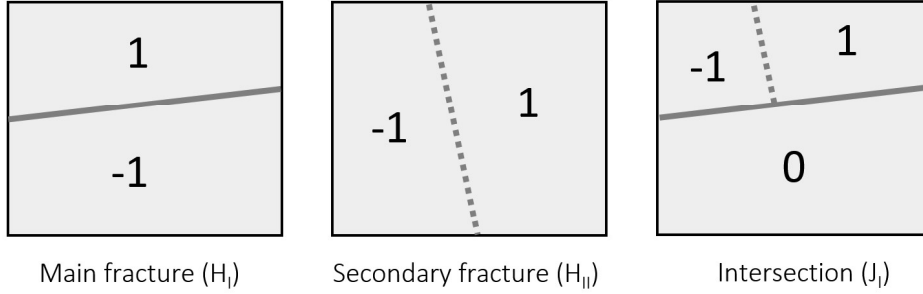


Figure 3.8 – Enrichment function J (adapted from (Daux, Moes and Dolbow, 2000))

Figure 3.9 shows the values along the element of a shape function for a node j multiplied by the enrichment shifted function $(J(x) - J_j)$, considering a 4-node element.

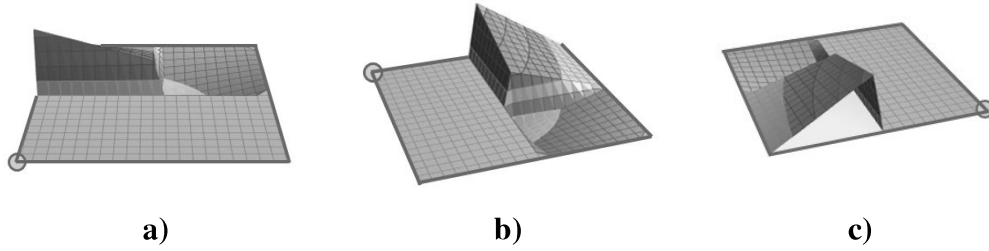


Figure 3.9 – Value of shape function in node j multiplied by the enrichment shifted function $(J(x) - J_j)$ for a 4-node element. a) View 0°. b) View 70°. c) View 250°

The application of the new enrichment function, requires a new set of degrees of freedom \mathcal{N}^{int} . Figure 3.10 pictures the different enhanced degrees of freedom and shape functions for an intersection situation.

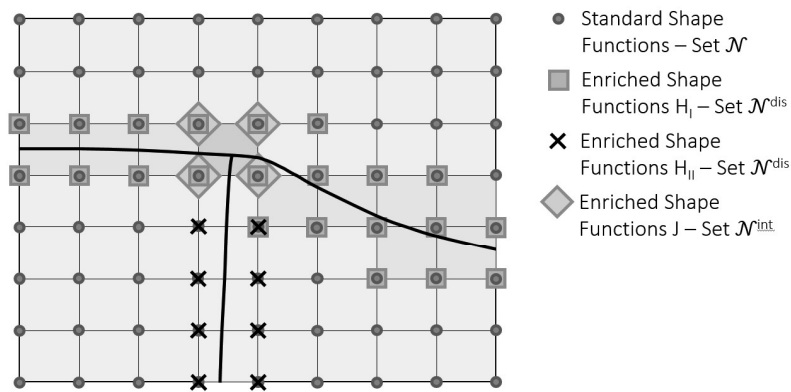


Figure 3.10 –Intersection enriched degrees of freedom and their positions

The generalization of the junction enrichment functions for a number of fracture intersections is straightforward. Yet, a particular case requires special attention. When one fracture crosses another, this must be treated as two different intersections. In this way, one main and two secondary fractures are defined. Thus, different junction enrichments J_I and J_{II} describe the intersection between the main fracture and each secondary fracture. Figure 3.11 shows this pattern and the enrichment functions.

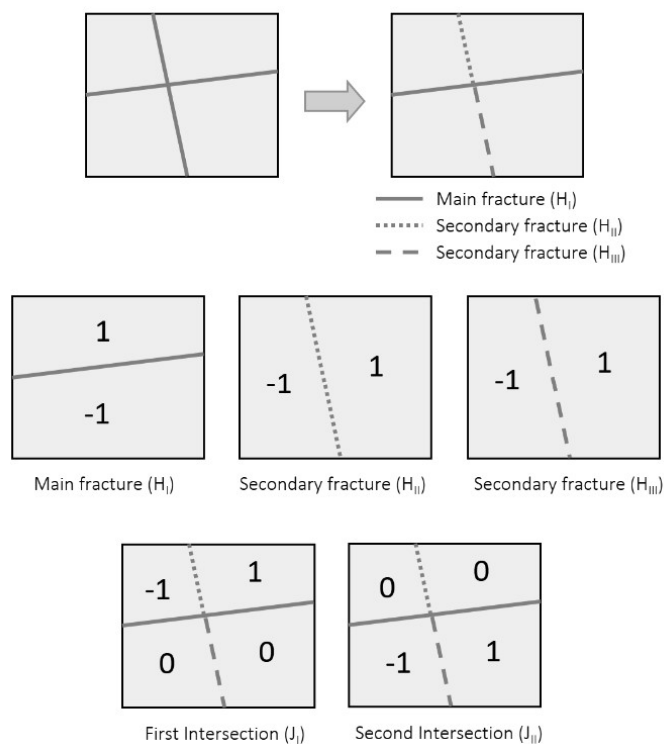


Figure 3.11 –Secondary fracture enrichment when crossing occurs

Each fracture intersection requires a new enriched degree of freedom b related to a specific enrichment function J . Eq. (3.30) provides the displacement field generalized for N_x intersections and N_c fractures.

$$\begin{aligned} \mathbf{u}(\mathbf{x}, t) = & \sum_{i \in \mathcal{N}} u_i(t) \cdot N_{u_i}^{std} + \sum_{k=1}^{N_c} \sum_{j \in \mathcal{N}^{dis}} a_{j,k}(t) \cdot N_{u_j}^{std} \cdot H_k(x) \\ & + \sum_{k=1}^{N_x} \sum_{j \in \mathcal{N}^{int}} b_{j,k}(t) \cdot N_{u_j}^{std} \cdot J_k(x) \end{aligned} \quad (3.30)$$

All considerations regarding enrichment functions and discretizations for displacements are considered applicable to the pore pressure discretization at intersections, once the pore pressure enrichment functions are the same. Consequently, the discretization of a pore pressure field with intersecting discontinuities follows

$$\begin{aligned} \mathbf{p}(\mathbf{x}, t) = & \sum_{i \in \mathcal{N}} p_i(t) \cdot N_{p_i}^{std} + \sum_{k=1}^{N_c} \sum_{j \in \mathcal{N}^{dis}} p_{a_{j,k}}(t) \cdot N_{p_j}^{std} \cdot H_k(x) \\ & + \sum_{k=1}^{N_x} \sum_{j \in \mathcal{N}^{int}} p_{b_{j,k}}(t) \cdot N_{p_j}^{std} \cdot J_k(x) \end{aligned} \quad (3.31)$$

3.3.4. Fracture discretization

Unlike the displacements and pore pressures, which are integrated in the domain Ω , the fracture fluid pressures, given by p_F , are integrated and discretized within the fracture level Γ . This allows the consideration of a jump between the fracture pressure and the surrounding pore pressures, as observed in Figure 3.5c. The discretization of the fracture pressure using Eq. (3.32), new degrees of freedom are placed at every intersection between the fracture and the element sides. Additional degrees of freedom are introduced at intersections between fractures, as Figure 3.12 presents.

$$p_F(x, t) = \sum_{i \in \mathcal{N}^d} p_{F_i}(t) \cdot N_{p_{F_i}}^{std} \quad (3.32)$$

According to Zienkiewicz, Taylor and Zhu (2013), the solution is implicit and unconditionally stable for $\beta = \gamma = \theta = 1$, then

$$\dot{\bar{U}}_{n+1} = \frac{(\bar{U}_{n+1} - \bar{U}_n)}{\Delta t} \quad (3.37)$$

Attributing the time index and substituting Eq. (3.37) in Eq. (3.34), the following equations are obtained

$$\Psi_{\bar{U}_{n+1}} = \mathbf{K}\bar{U}_{n+1} - \mathbf{Q}\bar{\mathbb{P}}_{n+1} + \mathbf{f}_{\bar{U}_{n+1}}^{\text{int}} - \mathbf{f}_{\bar{U}_{n+1}}^{\text{ext}} = 0 \quad (3.38)$$

$$\begin{aligned} \Psi_{\bar{\mathbb{P}}_{n+1}} &= \frac{1}{\Delta t} \mathbf{Q}^T \bar{U}_{n+1} + (\mathbf{H} + \mathbf{L1})\bar{\mathbb{P}}_{n+1} - \mathbf{L2}\bar{\mathbb{P}}_{F_{n+1}} - \mathbf{q}_{\bar{\mathbb{P}}_{n+1}}^{\text{ext}} \\ &\quad - \frac{1}{\Delta t} \mathbf{Q}^T \bar{U}_n = 0 \end{aligned} \quad (3.39)$$

$$\Psi_{\bar{\mathbb{P}}_{F_{n+1}}} = -\mathbf{L2}^T \bar{\mathbb{P}}_{n+1} + (\mathbf{H}_F + \mathbf{L3})\bar{\mathbb{P}}_{F_{n+1}} - \mathbf{q}_{\bar{\mathbb{P}}_{F_{n+1}}}^{\text{int}} = 0 \quad (3.40)$$

3.5. Newton-Raphson algorithm

The set of Eqs. (3.38), (3.39) and (3.40) may be non-linear if at least one of three conditions occur: material non-linearity in the porous region – Eq. (3.3), material non-linearity in the fracture region – Eq. (3.5), or fracture longitudinal transmissibility depending on fracture aperture – Eq. (3.7). In this case, the equations need to be linearized in order to be solved. The Newton-Raphson iterative algorithm solves the system of discrete non-linear equations. By expanding Eqs. (3.38), (3.39) and (3.40) with the first-order truncated Taylor series, the linear approximation of the coupled system is obtained

$$\begin{aligned} \begin{Bmatrix} \Psi_{\bar{U}_{n+1}}^{i+1} \\ \Psi_{\bar{\mathbb{P}}_{n+1}}^{i+1} \\ \Psi_{\bar{\mathbb{P}}_{F_{n+1}}}^{i+1} \end{Bmatrix} &= \begin{Bmatrix} \Psi_{\bar{U}_{n+1}}^i \\ \Psi_{\bar{\mathbb{P}}_{n+1}}^i \\ \Psi_{\bar{\mathbb{P}}_{F_{n+1}}}^i \end{Bmatrix} + \begin{bmatrix} \frac{\partial \Psi_{\bar{U}}}{\partial \bar{U}} & \frac{\partial \Psi_{\bar{U}}}{\partial \bar{\mathbb{P}}} & \frac{\partial \Psi_{\bar{U}}}{\partial \bar{\mathbb{P}}_F} \\ \frac{\partial \Psi_{\bar{\mathbb{P}}}}{\partial \bar{U}} & \frac{\partial \Psi_{\bar{\mathbb{P}}}}{\partial \bar{\mathbb{P}}} & \frac{\partial \Psi_{\bar{\mathbb{P}}}}{\partial \bar{\mathbb{P}}_F} \\ \frac{\partial \Psi_{\bar{\mathbb{P}}_F}}{\partial \bar{U}} & \frac{\partial \Psi_{\bar{\mathbb{P}}_F}}{\partial \bar{\mathbb{P}}} & \frac{\partial \Psi_{\bar{\mathbb{P}}_F}}{\partial \bar{\mathbb{P}}_F} \end{bmatrix}_{n+1}^i \begin{Bmatrix} d\bar{U}_n^i \\ d\bar{\mathbb{P}}_n^i \\ d\bar{\mathbb{P}}_{F_n}^i \end{Bmatrix} \\ &= 0 \end{aligned} \quad (3.41)$$

The solution for a certain step $n+1$ follows by solving Eq. (3.41) iteratively until reaching convergence, i.e. the vector of residuals $\{d\bar{\mathbf{U}}_n^i \quad d\bar{\mathbf{P}}_n^i \quad d\bar{\mathbf{P}}_{F_n}^i\}^T$ at iteration i is smaller than a pre-defined tolerance. The Jacobian term J is a non-symmetric matrix given by

$$J = \begin{bmatrix} \frac{\partial \Psi_{\mathbf{U}}}{\partial \bar{\mathbf{U}}} & \frac{\partial \Psi_{\mathbf{U}}}{\partial \bar{\mathbf{P}}} & \frac{\partial \Psi_{\mathbf{U}}}{\partial \bar{\mathbf{P}}_F} \\ \frac{\partial \Psi_{\mathbf{P}}}{\partial \bar{\mathbf{U}}} & \frac{\partial \Psi_{\mathbf{P}}}{\partial \bar{\mathbf{P}}} & \frac{\partial \Psi_{\mathbf{P}}}{\partial \bar{\mathbf{P}}_F} \\ \frac{\partial \Psi_{\bar{\mathbf{P}}_F}}{\partial \bar{\mathbf{U}}} & \frac{\partial \Psi_{\bar{\mathbf{P}}_F}}{\partial \bar{\mathbf{P}}} & \frac{\partial \Psi_{\bar{\mathbf{P}}_F}}{\partial \bar{\mathbf{P}}_F} \end{bmatrix} \quad (3.42)$$

$$= \begin{bmatrix} \mathbf{K} + \frac{\partial \mathbf{f}_{\mathbf{U}}^{\text{int}}}{\partial \bar{\mathbf{U}}} & -\mathbf{Q} + \frac{\partial \mathbf{f}_{\mathbf{U}}^{\text{int}}}{\partial \bar{\mathbf{P}}} & \frac{\partial \mathbf{f}_{\mathbf{U}}^{\text{int}}}{\partial \bar{\mathbf{P}}_F} \\ \frac{1}{\Delta t} \mathbf{Q}^T & (\mathbf{H} + \mathbf{L1}) & -\mathbf{L2} \\ -\frac{\partial \mathbf{q}_{\bar{\mathbf{P}}_F}^{\text{int}}}{\partial \bar{\mathbf{U}}} & -\mathbf{L2}^T - \frac{\partial \mathbf{q}_{\bar{\mathbf{P}}_F}^{\text{int}}}{\partial \bar{\mathbf{P}}} & (\mathbf{H}_F + \mathbf{L3}) - \frac{\partial \mathbf{q}_{\bar{\mathbf{P}}_F}^{\text{int}}}{\partial \bar{\mathbf{P}}_F} \end{bmatrix}$$

In order to optimize computations, the Jacobian may be transformed into a symmetric matrix (Khoëi *et al.*, 2014). Both the definition of the terms and the changes on the matrix are presented in Annex B. As a result, the implemented Jacobian matrix is

$$J = \begin{bmatrix} \mathbf{K} + \mathbf{T} & -\mathbf{Q} & -\mathbf{Q}_F \\ -\mathbf{Q}^T & -\Delta t (\mathbf{H} + \mathbf{L1}) & \Delta t \cdot \mathbf{L2} \\ -\mathbf{Q}_F^T & \Delta t \cdot \mathbf{L2}^T & -\Delta t \cdot (\mathbf{H}_F + \mathbf{L3}) \end{bmatrix} \quad (3.43)$$

Scaling of the Jacobian in Eq. (3.43) is possible for as many enriched degrees of freedom of displacement (β and γ), pore-pressure (δ and ζ) as present in the model (see Annex B for example). Therefore, the integrals that compose the Jacobian are

$$\mathbf{K}_{\beta\gamma} = \int_{\Omega} (\mathbf{B}_{\mathbf{u}}^{\beta})^T \mathbf{D} \mathbf{B}_{\mathbf{u}}^{\gamma} d\Omega \quad (3.44)$$

$$\mathbf{T}_{\beta\gamma} = \int_{\Gamma_d} \llbracket \mathbf{N}_{\mathbf{u}}^{\beta} \rrbracket^T \mathbf{D}_F \llbracket \mathbf{N}_{\mathbf{u}}^{\gamma} \rrbracket d\Gamma \quad (3.45)$$

$$\mathbf{Q}_{\beta\zeta} = \int_{\Omega} (\mathbf{B}_{\mathbf{u}}^{\beta})^T \mathbf{m} \mathbf{N}_{\mathbf{p}}^{\zeta} d\Omega \quad (3.46)$$

$$\mathbf{Q}_{F\beta\mathbf{P}_F} = \int_{\Omega} \llbracket \mathbf{N}_{\mathbf{u}}^{\beta} \rrbracket^T \mathbf{n}_{\Gamma d} \mathbf{N}_{\mathbf{P}_F}^{\text{std}} d\Omega \quad (3.47)$$

$$\mathbf{H}_{\delta\zeta} = \int_{\Omega} (\mathbf{B}_p^\delta)^T k_F \mathbf{B}_p^\zeta d\Omega \quad (3.48)$$

$$\mathbf{L1}_{\delta\zeta} = \int_{\Gamma_d} (\mathbf{N}_p^\delta)^T c \mathbf{N}_p^\zeta d\Gamma \quad (3.49)$$

$$\mathbf{L2}_{\delta p_F} = \int_{\Gamma_d} (\mathbf{N}_p^\delta)^T c \mathbf{N}_{p_F}^{\text{std}} d\Gamma \quad (3.50)$$

$$\mathbf{L3} = \int_{\Gamma_d} (\mathbf{N}_{p_F}^{\text{std}})^T c \mathbf{N}_{p_F}^{\text{std}} d\Gamma \quad (3.51)$$

$$\mathbf{H}_F = \int_{\Gamma_d} (\mathbf{B}_{p_F}^{\text{std}})^T \mathbf{t}_{\Gamma_d} (2h) k_{Fd} \mathbf{B}_{p_F}^{\text{std}} \mathbf{t}_{\Gamma_d} d\Gamma \quad (3.52)$$

with $\mathbf{m} = \{1 \ 1 \ 0\}^T$. Moreover, the following integrals are used to compute Eqs. (3.38), (3.39) and (3.40).

$$\mathbf{f}_\beta^{\text{ext}} = \int_{\Gamma_t} (\mathbf{N}_u^\beta)^T \bar{t} d\Gamma \quad (3.53)$$

$$\mathbf{q}_\delta^{\text{ext}} = \int_{\Gamma_w} (\mathbf{N}_p^\delta)^T \bar{q}_w d\Gamma \quad (3.54)$$

$$\mathbf{f}_\beta^{\text{int}} = \int_{\Gamma_d} [\![\mathbf{N}_u^\beta]\!]^T \mathbf{D}_F \bar{\beta} d\Gamma - \int_{\Gamma_d} [\![\mathbf{N}_u^\beta]\!]^T (p_F \mathbf{n}_{\Gamma_d}) d\Gamma \quad (3.55)$$

$$\mathbf{q}_{p_F}^{\text{int}} = \int_{\Gamma_d} (\mathbf{N}_{p_F}^{\text{std}})^T \mathbf{t}_{\Gamma_d} (2h) \langle \nabla \dot{u} \rangle \mathbf{t}_{\Gamma_d} d\Gamma + \int_{\Gamma_d} (\mathbf{N}_{p_F}^{\text{std}})^T [\![\dot{u}]\!] \mathbf{n}_{\Gamma_d} d\Gamma \quad (3.56)$$

3.6. Fracture constitutive behaviour

3.6.1. Contact penalty method

When studying interaction between fractures, it is expected that the relative displacements between fracture faces vary considerably. For example, while a hydraulic fracture approaches a natural fracture, compression and friction between the natural fracture faces may occur. However, right after the intersection between hydraulic and natural fracture, the fluid starts filling and pressurizing the natural fracture faces, resulting in a separation of its faces. Therefore, the difference of behaviour that occurs between compression and separation must be correctly modelled.

A formulation based on the contact penalty method limits fracture closure in this work. This method assumes the following conditions, known as the standard Kuhn-Tucker conditions (Khoei, 2008).

$$g_N \geq 0 \quad (3.57)$$

$$t_N \leq 0 \quad (3.58)$$

$$g_N \cdot t_N = 0 \quad (3.59)$$

Eq. (3.57) indicates that the normal fracture opening $g_N = \llbracket u \rrbracket n_{\Gamma_d}$ cannot be negative, i.e. no superposition of faces occurs. Eq. (3.58) governs the normal tractions on the interface, which must always be compressive. Finally, Eq. (3.59) designates that the normal tractions on the interface vanish when there is a gap, i.e. the fracture is open.

The contact constraints are guaranteed through the integral of the fracture material constitutive matrix \mathbf{T} in Eq. (3.45), where the stiffness matrix \mathbf{D}_F is defined by the tangential and normal stiffness, k_t and k_n , respectively.

$$\mathbf{D}_F = \begin{bmatrix} k_t & 0 \\ 0 & k_n \end{bmatrix} \quad (3.60)$$

In the case of a compressive traction on the fracture faces, the value of the normal stiffness k_n takes the value of a penalty factor. The accuracy of satisfying contact constraints highly depends on the penalty factor, which should take an order of magnitude higher than the deformability of the surrounding medium. The larger the value of the penalty parameter, the more accurate contact constraints are. However, very large values for the penalty parameter result in an ill conditioned formulation (Khoei, 2008).

Another evident limitation of this method exists when intersections are modelled. Figure 3.13a shows an eventual fracture intersection and the integration points of each fracture that are closer to the intersection. The colour scheme indicates that each integration point only avoids fracture superposition in its corresponding fracture, i.e. only fracture faces with the same colour check the contact against each other. When a state of deformation similar to the presented in Figure 3.13b is obtained, the contact model is applied between faces of each fracture (yellow faces and green faces do not overlap) but it is not applied in the intersection (yellow and green faces overlap with red and blue faces, respectively). Therefore, a superposition, represented by an orange region in Figure 3.13b, exists in the model.

Although being an important effect in certain cases, in this research it is considered that this limitation does not have a strong influence in hydraulic fracture models, where the fractures tend to open as intersections are created (due to fluid pressure) and contact is less likely to occur.

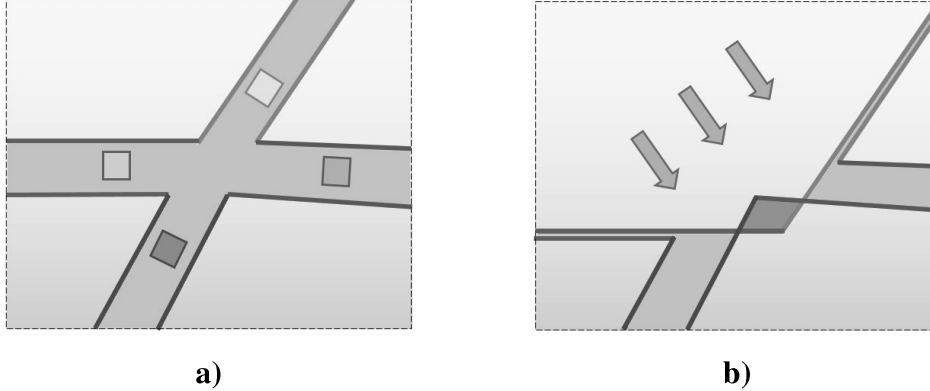


Figure 3.13 – Zoom of an intersection and fractures integration points.
a) Situation with all fractures opened. b) Situation of contact between fractures

3.6.2. Mohr-Coulomb model

Simulation of frictional behaviour of natural fractures adopts a Mohr-Coulomb model for discontinuities. The formulation of this model is based on the research by Rueda *et al.* (2014). The Mohr-Coulomb model is an elastoplastic constitutive model with a failure surface represented by a function f , seen in Figure 3.14 and given by Eq. (3.61).

$$f = \tau + \sigma'_n \times \tan \varphi' - c' \quad (3.61)$$

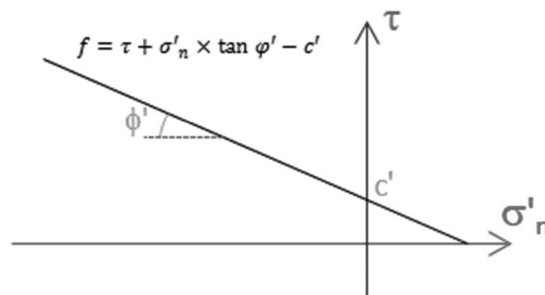


Figure 3.14 – Mohr Coulomb failure surface

where τ is the shear stress, σ'_n the normal stress, φ' the effective friction angle and c' the effective cohesion of the fracture filling.

Additionally, a tensile cut-off failure surface f_n is defined to limit tension stresses, as Eq. (3.62) and Figure 3.15 show.

$$f_n = \sigma'_n - R_t \quad (3.62)$$

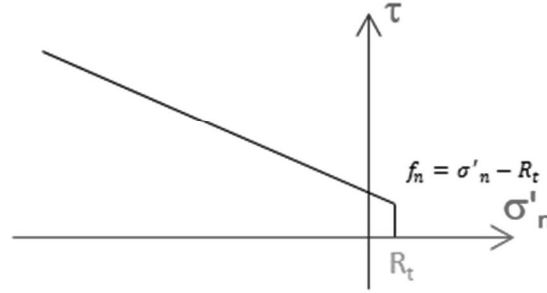


Figure 3.15 – Tensile cut-off failure surface

The constitutive model must define both an elastoplastic stiffness matrix and the stress state, considering the actual deformation state. As the final stress state is not known a-priori, an implicit procedure is used. In this work both functions (3.61) and (3.62) are verified to check if plastic deformations occur. If f or f_n are positive, it means the stress state σ_{trial} , is not admissible, so it should be corrected and the plastic deformations computed. Two correction paths are formulated, vertical and perpendicular to the failure surface, as seen in Figure 3.16. The first may be called a non-associated formulation without occurrence of dilatation, while the second is an associated formulation.

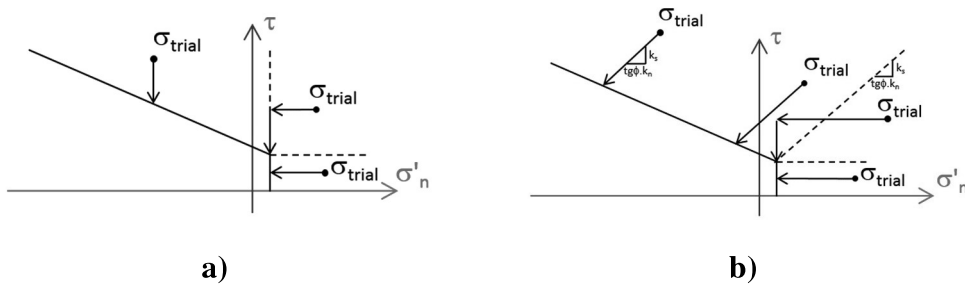


Figure 3.16 – Return paths for Mohr Coulomb model. a) vertical return. b) perpendicular return

The final change in stress state and the elastoplastic stiffness are given by Eq. (3.63) and Eq. (3.64), respectively.

$$\{\Delta\sigma\} = [D^e]\{\Delta\varepsilon\} - [D^e]\{\Delta\varepsilon^p\} = [D^e]\{\Delta\varepsilon\} - [D^e]\Lambda \left\{ \frac{\partial g}{\partial \sigma} \right\} \quad (3.63)$$

$$[D^{ep}] = [D^e] - \frac{[D^e] \left\{ \frac{\partial g}{\partial \sigma} \right\} \left\{ \frac{\partial f}{\partial \sigma} \right\}^T [D^e]}{\left\{ \frac{\partial f}{\partial \sigma} \right\}^T [D^e] \left\{ \frac{\partial g}{\partial \sigma} \right\}} \quad (3.64)$$

where $[D^e]$ is the elastic stiffness matrix, given in Eq. (3.60) and

- $\left\{ \frac{\partial f}{\partial \sigma} \right\}$ is the derivative of the failure surface
 - Mohr Coulomb surface: $\left\{ \frac{\partial f}{\partial \sigma} \right\} = \left\{ \begin{matrix} 1 \\ \tan \varphi' \end{matrix} \right\}$
 - Tensile cut-off surface: $\left\{ \frac{\partial f_n}{\partial \sigma} \right\} = \left\{ \begin{matrix} 0 \\ 1 \end{matrix} \right\}$
- $\left\{ \frac{\partial g}{\partial \sigma} \right\}$ is the derivative of the plastic potential function
 - Mohr Coulomb surface:
 - Vertical return: $\left\{ \frac{\partial g}{\partial \sigma} \right\} = \left\{ \begin{matrix} 1 \\ 0 \end{matrix} \right\}$
 - Perpendicular return: $\left\{ \frac{\partial g}{\partial \sigma} \right\} = \left\{ \begin{matrix} 1 \\ \tan \varphi' \end{matrix} \right\}$
 - Tensile cut-off surface: $\left\{ \frac{\partial g_n}{\partial \sigma} \right\} = \left\{ \begin{matrix} 0 \\ 1 \end{matrix} \right\}$
- Λ is a parameter that guarantees that $f(\sigma_{trial}) = 0$
 - Mohr Coulomb surface:
 - Vertical return: $\Lambda = \frac{f(\sigma^{trial})}{k_s}$
 - Perpendicular return: $\Lambda = \frac{f(\sigma^{trial})}{k_s + k_n \tan^2 \varphi'}$
 - Tensile cut-off surface: $\Lambda = \frac{f_n(\sigma^{trial})}{k_n}$

4

Implementation

The core of this research is the delivery of an implementation that is capable of simulating the propagation of hydraulic fractures and their intersection with existing fractures. Different codes in different languages were implemented and put together in a suite named XFEMHF. In this chapter all the implementation steps are presented explained. A more detailed description is made of the subroutines that are plugged in a finite element solver, which is the software Abaqus, by Simulia (2014).

First, the Abaqus software is presented, with focus to the user subroutines tool. Then, after an overview of every step of the XFEMHF code, each of the subroutines are explained in detail. An explanation on the type of elements and their integration procedures is also given and, finally, the limitations of the implementation are discussed.

4.1.

Abaqus Software

4.1.1.

General Description

Abaqus is a widely used commercial software, both in industry and academia, mainly known for its adaptability to very different kinds of numerical problems. In its essence, it is a solver for linear system of equations which allows the incorporation of non-linear problems with different physics in various types of finite elements.

Within a wide variety of modules and add-ons, the Abaqus finite element suite includes a graphical interface for input, monitoring of simulations and output interpretation (Abaqus/CAE) and three modules: Abaqus/Standard, a general-purpose finite element program, Abaqus/Explicit, an explicit dynamics finite element program and Abaqus/CFD, a general-purpose computational fluid dynamics program (Simulia, 2014). For the sake of simplicity, from this point the

word Abaqus is meant to represent the module used in this work, which is Abaqus/Standard v6.14.

Abaqus offers an extensive diversity of element types and material models, applicable to different physical analyses: mechanical, pore hydraulic, thermal, electrical, electromagnetic and acoustic. Some of the available elements also allow coupled simulations between two or more of the previously mentioned physics.

Although it offers a wide variety of functionalities, also allows users to integrate their own subroutines in the calculation, which expand even more the software capabilities. More than 50 available user subroutines have many different functions, such as definition of complex constitutive models (p. ex. CREEP, HARDINI, UDMGINI, UMAT), definition of complex boundary conditions (p. ex. DFLOW, DLOAD, DISP), definition of constraints (p. ex. MPC, UMESHMOTION), definition of elements (p. ex. UEL and UELMAT) and management with external applications (UEXTERNALDB).

Abaqus solves non-linear problems by breaking the simulation into a number of time increments and finds the approximate equilibrium configuration at the end of each time increment. Using the Newton method, it often takes Abaqus several iterations to determine an acceptable solution to each time increment (Simulia, 2014). The calculations may be subdivided in:

- Steps: define an analysis procedure or loading. Different loads, boundary conditions, analysis procedures, and output requests can be used in each step,
- Increments: are part of a step. In nonlinear analyses each step is broken into increments so that the nonlinear solution path can be followed. The size of each increment may be fixed by the user or automatically chosen by Abaqus,
- Iterations: are an attempt at finding an equilibrium solution in an increment. If the model is not in equilibrium at the end of the iteration, Abaqus tries another iteration.

4.1.2. XFEM in Abaqus

Abaqus presents different techniques or elements to simulate discontinuities in a FEM model. Within the XFEM, which is called in the Abaqus Documentation as an “enriched feature”, the software differentiates between stationary and propagating cracks. Considering the focus of this research, in this chapter only the coupled hydro-mechanical element with XFEM for propagating cracks is detailed.

Abaqus implements the XFEM using the Phantom Node technique (Song, Areias and Belytschko, 2006), which was based on a previous work by Hansbo and Hansbo (2004). This technique considers the duplication of the mesh elements, being the duplicated nodes called “Phantom Nodes”, represented in Figure 4.1 by hollow circles. Moreover, additional nodes, known as “Edge-Phantom Nodes” (red triangles in Figure 4.1), allow the representation of the fluid pressure inside the fracture. Prior to damage initiation only one copy of the element is active. Upon damage initiation the displacement and pore pressure degrees of freedom associated with the corner phantom nodes are activated and both copies of the element are allowed to deform independently, pore pressures are allowed to diffuse independently, and the created interface behaviour is enforced with a traction-separation cohesive law. The pore fluid pressure at the top and bottom faces of the fracture are interpolated from the pore pressure degrees of freedom at the corner real nodes and phantom nodes. The difference with the fracturing fluid pressure (interpolated at the edge-phantom node) is the driving force that controls the leakage of fracturing fluid into the porous medium (Zielonka *et al.*, 2014).

The fracture geometry is mathematically described by the Level-Set Method, which assumes that two signed distance functions per node are generally required to describe a crack geometry (Simulia, 2014).

The propagation criterion may be based on stress or strain state, which interpolated to the crack tip or computed in the element ahead of the crack tip. Its direction is set to have perpendicular direction to the minimum principal stress in the tip region.

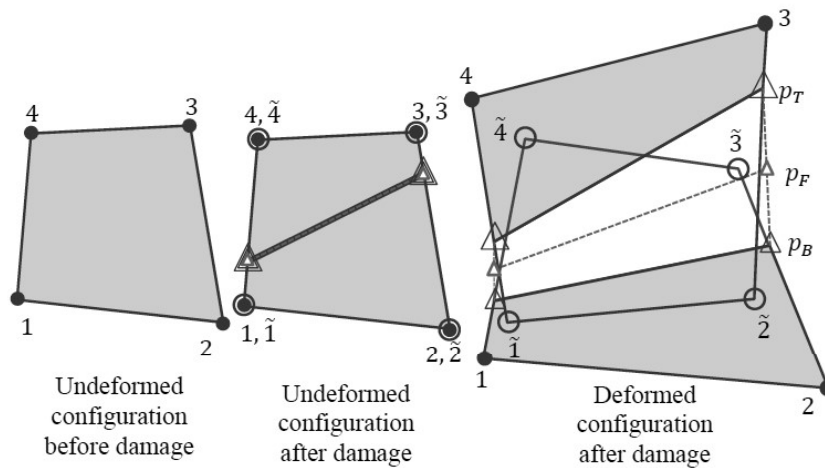


Figure 4.1 – Implementation of the XFEM with “corner” and “edge” phantom nodes (Zielonka *et al.*, 2014)

Areias and Belytschko (2006) showed that the kinematic decomposition in the Phantom Node method is equivalent to the one in the extended finite element method (XFEM) by Moes and Dolbow (1999) and Belytschko and Black (1999), having the advantage of being of easier implementation in a standard FEM code. On the other hand, it turns the implementation of partially cracked elements cumbersome.

The Abaqus XFEM elements have had a very positive effect of facilitating the use of this technique both in industry and academia (see Chapter 2). However, these cannot be used in the scope of this research, once Abaqus refers that XFEM elements cannot be intersected by more than one fracture (Simulia, 2014). Therefore, the built-in Abaqus XFEM elements are not part of this research, being substituted by the use of user elements coded in subroutines.

4.1.3. Abaqus User Subroutines

To achieve this thesis's proposed goals, two Abaqus user subroutines were used. The two user subroutines that manage and organize the workflow composed by most of the code written for this research are presented next. Figure 4.2 shows the flow of an Abaqus calculation and when each of the subroutines are called.

UEXTERNALDB

Though very simple, this is an extremely helpful subroutine when the user needs external procedures to be run during the simulation. This user subroutine is

called once at the beginning of the analysis, at the beginning of each increment, at the end of each increment, and at the end of the analysis (in addition, the user subroutine is also called once at the beginning of a restart analysis). In addition to the number of the step, number of the increment and the time interval information, the variable LOP given to the user defines in which phase of the calculation (step, increment, etc.) the subroutine is being called. This way, it is possible to manage the calls to:

- Read the input files at the beginning of the calculation,
- Other processes or subroutines at the beginning/end of each increment/step
- Prepare output files at the end of each step or the calculation.

UEL

The User ELeMent subroutine gives the user the freedom to define any type of element topology and which governing equations are considered in that element. The user defines in the input the number of nodes of the element and their position. Furthermore, the input must also define the degrees of freedom, up to 30, that are attributed to each node.

Each time element calculations are required, i.e. for every element in every iteration, the UEL subroutine is called. Then, the code must perform all the calculations that are appropriate for the topology and the physics of the element. The subroutine must deliver the jacobian matrix of the Newton-Raphson method (AMATRX), the right-hand-side vector of the overall system of equations (RHS) and an array containing the values of the eventual solution-dependent state variables associated with the element (SVARS).

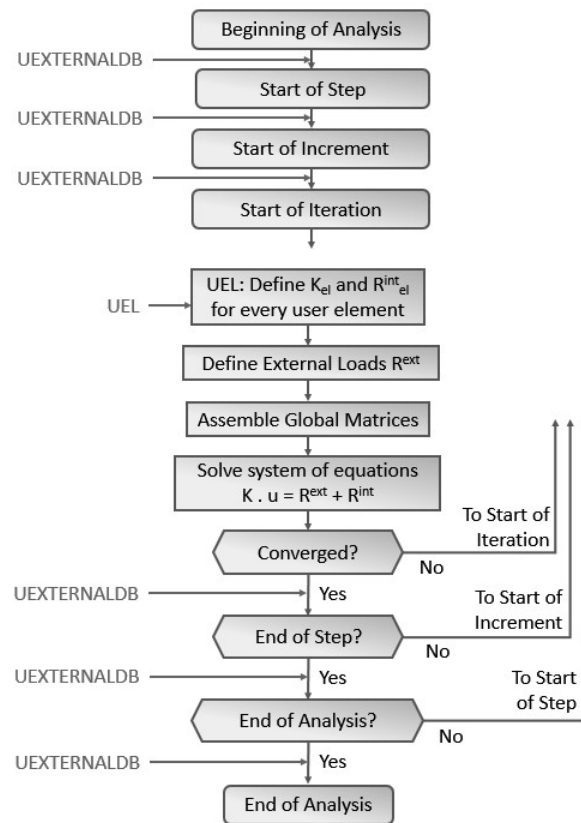


Figure 4.2 – Calls of user subroutines within the flow in Abaqus

4.2. XFEMHF code

4.2.1. Overview

As usual in research focused in code implementation, different software or codes were used to achieve the proposed goals.

A known limitation of the Abaqus graphical interface (Abaqus/CAE) is that it does not support the definition and visualization of user elements. Although not being the main focus of the research, the input and output tools are also essential. In a first step, during implementation, as they make the code validation easier. In a second step, because they guarantee that other users run simulations without need of advanced knowledge about the background process, allowing further contributions to the research topic.

The whole process of preparing, running and analysing a simulation may be described in three main steps, as seen in Figure 4.3.

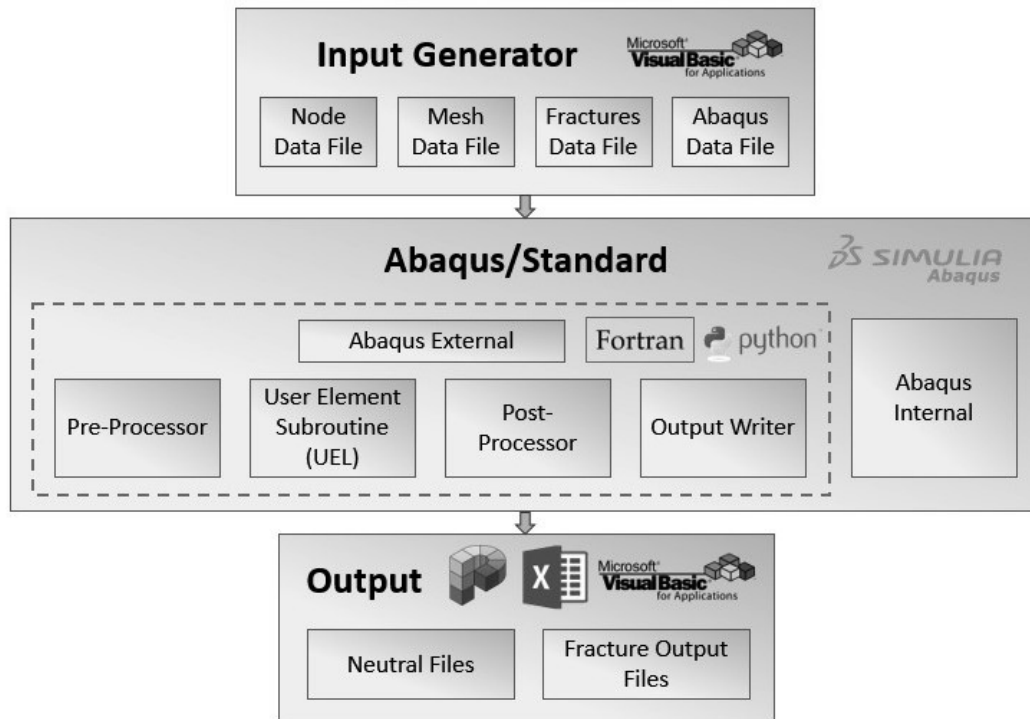


Figure 4.3 – Main steps of a simulation

Input generator

Four input files must be defined for every simulation: node data, mesh (topological) data, fracture data and Abaqus regular input data. These files are automatically generated by a code developed in VBA – Visual Basic for Applications.

Abaqus internal and external subroutines

The core code of this research is written in Fortran and compiled by Abaqus/Standard; therefore, this Chapter focus specifically in this step. The XFEM formulation is implemented in the external Abaqus User Subroutines, while several processes that are common with the standard FEM, such as the global stiffness matrix assembling or the convergence checker, are left to be done by the Abaqus internal subroutines. In specific cases, which will be referred in Chapter 4.2.2.2, a Python Script is used to interpret and adapt results during the simulation.

Output

The results may be visualized in the software Pos3D (Carvalho, Martha and Filho, 1997) which reads a Neutral File type generated during the simulation. For some specific variables along the fractures, a code developed in VBA interprets the fracture results and properly shows them in MS Excel graphs.

4.2.2. Abaqus algorithm

4.2.2.1. General algorithm

As mentioned before, the core of the implementation of this research is the Abaqus + User subroutines algorithm, i.e. the intermediate step of Figure 4.3. A more detailed flow of this algorithm is shown in Figure 4.4, where the boxes with dashed outlines represent the parts of the simulation where the code implemented in this research is called.

Starting by doing some Abaqus internal checks, the simulation then runs a user subroutine that reads all the input files generated in the first step of Figure 4.3 and allocates the auxiliary matrices and vectors in memory. Next, a geometry pre-processor is run. Based on the mesh and initial fracture information provided in the input files, this processor attributes all the values related with enrichment functions to the nodes and integration points of the model. Further information about the geometry pre-processor is present in Chapter 4.2.3. Then, the loops over steps, increments and iterations start. At the beginning of a new increment, the simulator checks if propagation occurred at the end of the previous increment – evidently, this does not happen at the first increment of the first step of the simulation. If propagation occurred, then new enriched degrees of freedom are active and the pre-processor is run, in order to update all the enrichment related data in the newly-propagating segments.

The loop over the iterations starts with a loop over all mesh elements. For each element the UEL subroutine computes the Jacobian matrix, the right-hand-side and the state variables are computed. This procedure is explained in more detail in Chapter 4.2.4. After assembling all the external forces defined in the input, the internal functions of Abaqus use the element matrices to assemble the global matrices and solve the linear system of equations. If convergence is not attained, another iteration is run.

When the solution converges, the increment finishes and a fracture geometry post-processor is called. This procedure checks if propagation criteria are met anywhere in the model. In case propagation occurs, the direction and length of the new fracture segments are also computed. A more detailed explanation of this procedure is delivered in Chapter 4.2.5. When the loop over the increments restarts,

the coordinates of the new fracture segments are used by the pre-processor to place them in the mesh and compute their enrichment data, which will be used in the next increment.

Finally, when the last increment of the last step converges, the simulations finishes by writing all Abaqus output files and also the user output files that are interpreted in the third step of Figure 4.3.

4.2.2.2. The specific case of in-situ stress state

In most geotechnical events involving hydraulic and natural fractures the overburden cannot be neglected. Furthermore, it is widely known that the in-situ stress state extremely affects the way fractures behave and propagate. Consequently, this effect must also be considered in the developed simulator.

The in-situ stress state occurs due to various phenomena that happened during the geological history of the layer, such as overburden, tectonic movements and metamorphism. The modelling of all these effects to attain a correct in-situ stress state is extremely difficult. For that reason, that modelling is usually disregarded when only short periods of time (in a geological time scale) are to be simulated, being substituted by the input definition of an initial stress state. Therefore, the consideration of in-situ stresses in Abaqus is not straightforward, given that an initial stress field must be simulated as an equilibrium state which is the result of the gravitational fields and the model's boundary conditions. Due to the use of a User Element Subroutine (UEL), Abaqus cannot interpret the in-situ stresses from the input file and consequently a specific algorithm has to be defined.

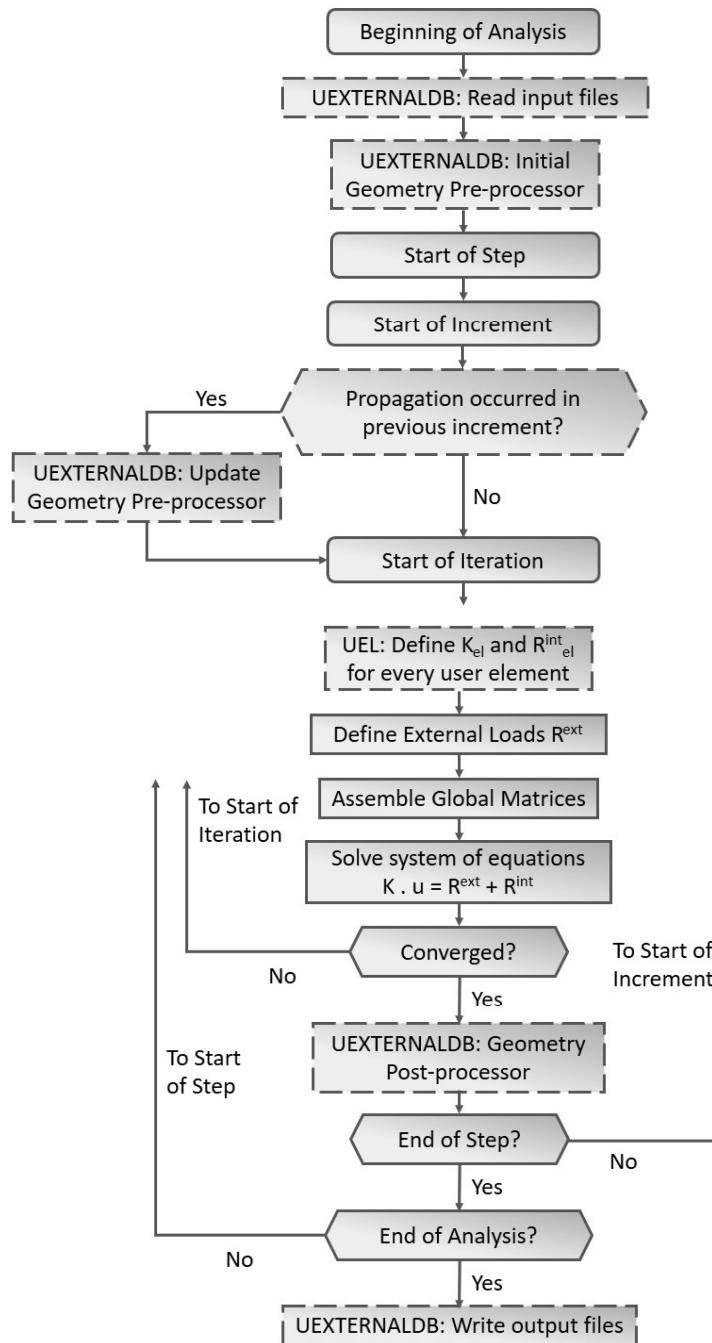


Figure 4.4 – Flow of a XFEMHF simulation – dashed outlines represent coded subroutines and continuous represent Abaqus internal routines

The implemented code contemplates the following steps, in order to consider in-situ stresses in the model (see Figure 4.5):

- On a first Abaqus analysis, all degrees of freedom of the mesh are considered to be fixed (i.e. boundary conditions set to zero). The in-situ stresses are applied to the whole model as internal stresses and

one calculation step is run. The obtained reactions in every degree of freedom are output to a specific file and the simulation finishes;

- A Python script compiled by Abaqus is then run. This script translates the reactions in the previous mentioned output file to a new format, which is readable by Abaqus;
- A second Abaqus analysis is run. In the first step of this simulation, all the reactions obtained in the first simulation are applied to all degrees of freedom. Together with the internal stresses applied previously, this will guarantee that the simulation starts in equilibrium with zero displacement and the defined in-situ stress. Then, all the steps are defined as in a regular simulation, with all the loads and boundary conditions that the user requests.

Due to Abaqus limitations, this simulation must be run in two separated analyses. If this process was run in one single analysis, the Abaqus preparation subroutines would search for the files with the reactions generated by the Python script at the beginning of the analysis. As these files are generated after the geostatic step of the simulation, the preparation subroutines would deliver an error and Abaqus would abort before starting computations.

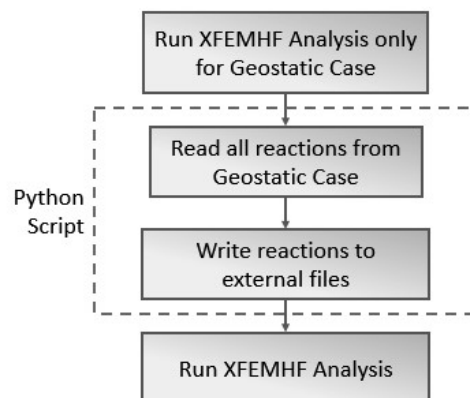


Figure 4.5 – General flow of a XFEMHF simulation with initial stress state

4.2.3. Fracture geometry pre-processor

The fracture geometry pre-processor runs at the beginning of the simulation and then updates data at the beginning of each increment that follows a propagation

event, as seen in Figure 4.4. It should be noted that fractures do not change geometry during the iterations of an increment, so there is no need to run this procedure inside the increment loop.

The goal of this procedure is to define the enrichment data for the mesh, so the element matrices are built accordingly. The following information is delivered by the pre-processor:

- Which nodes and elements in the mesh are enriched, and which fracture is associated with that enrichment
- Enrichment function values at every enriched node
- Local coordinates and weight of integration points in enriched elements
- Enrichment function values at every integration point of the enriched elements
- Position of all fracture segments
- Local coordinates and weight of all fracture integration points
- Value of the jump function at every fracture integration point
- Fracture segments direction and length

At the first run, which can be called the "general definition stage", the pre-processor has the flow presented in Figure 4.6. After the reading of all the input data, each set of enrichment functions (H_i , H_{ii} , H_{iii} , etc.) is attributed to the initial fractures. Then, all the nodes and elements that are affected by fractures have their enrichment degrees of freedom activated. It must be noted that, because specific tip enrichments are not being used, the representation of the tip is achieved by deactivating the enrichment in the nodes that belong to the element border that is touched by the tip.

In sequence, all the elements that are cut by fractures are divided into sub-domains, allowing definition of the position of the integration points, as explained in Chapter 4.2.7.2. Next, the enrichment functions in every enriched node and integration points of enriched elements are computed. Although different types of enrichment functions are allowed in this implementation, only the signed level set function (H) is used in the simulations, as stated in Chapter 3.3.2.

Following, the fracture pressure degrees of freedom are attributed to the nodes, using the methodology described in Chapter 4.2.6. Then, the fracture

integration points are placed and their weights attributed. Finally, the geometry of the fractures segments is stored, after computing their lengths and directions.

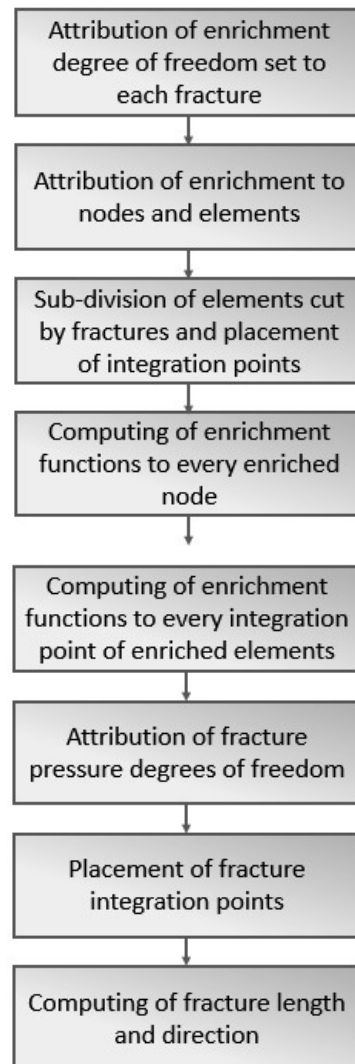


Figure 4.6 – General flow of the general definition stage of the pre-processor

The update stage run the same procedure for the enrichment data in the newly fractured elements and nodes, while the data in elements and nodes that had no change is kept the same.

A special procedure is considered in the geometry pre-processor in specific cases, when the continuous region is impermeable. As leak-off does not occur and no injection or fixed pressure points exist inside the fracture, there is no border or point for fluid to leave or enter it. Therefore, because the fluid is incompressible, the fracture cannot have any volumetric deformation to comply with the continuity equation. This way, all the displacements between the natural fracture faces may be

highly compromised before intersection with hydraulic fractures occur. A way to overcome this problem is to define a criterion of fracture pressure activation, which allows the fracture pressure degrees of freedom to be deactivated at the beginning of the simulation and then be activated. Three types of criterion are implemented:

- The fracture pressure in a segment is activated as soon as that segment is in contact with another segment which has its pressure activated;
- The fracture pressure in a segment is activated as soon as a limit value of a pre-defined grandness – fracture aperture, fracture normal stress, fracture shear stress, fracture relative stress;
- A mixture of the previous two criteria, i.e., the pressure in a segment is activated when that segment is in contact with another segment with activated pressure and if a certain limit value is reached.

4.2.4. UEL algorithm

This is an essential step for any FEM simulation, as it is where the physical behaviour of the governing equations is represented through the construction of the elemental matrices that compose the global system of equations. These matrices are obtained by computing the integrals presented in Eqs. (3.38) to (3.40) and Eq. (3.43). Auxiliary procedures are also used to compute the non-linear terms, such as the elastoplastic stiffness matrix for material constitutive behaviour or the fracture longitudinal transmissibility.

A general flow of the coded UEL subroutine is presented in Figure 4.7. As stated previously, this procedure is run for every user element in every iteration of the simulation. Therefore, the first step of the routine is to select, both from the input files or the pre-processor, only the data relevant to that particular element. Then, two domains are integrated separately: the continuous region and the fracture.

First, the procedure loops over all the integration points in the continuous area. For each, it builds the shape functions and their derivatives (N and B , respectively), for both standard and enriched degrees of freedom, and also for both displacements and pore-pressures. Then, the code computes the stresses and the material stiffness matrix, which is elastic in the continuous region (see Figure 4.8). These matrices are then used to compute the contribution of the integration point for each of the area integrals, K , Q and H present in Eq. (3.43).

Second, the procedure loops over all the integration points in the fractures. Evidently, this part of the procedure is not run if there are not fractures in the element. For each fracture integration point, the routine builds the shape functions, their derivatives and the jump functions (N , B and $[[N]]$, respectively), considering the contribution of the fracture pressure degrees of freedom. After, the code computes stresses and the material stiffness matrix, which may be elastoplastic in the fracture region (see Figure 4.8). The fracture longitudinal transmissibility is then computed, by applying the cubic law is used. It should be noted that the cubic law uses the fracture aperture to compute the transmissibility. Considering that, even when in contact, fractures present a larger transmissibility due to its roughness, a hydraulic aperture is used. At the beginning of a simulation, the hydraulic aperture is different from the mechanical aperture, taking a value defined by the user in the input files. All the previously mentioned matrices are then used to compute the contribution of the integration point for each of the fracture integrals, T , L , Q_{ap_f} and $H_{p_f p_f}$ present in Eq. (3.43).

Finally, all the computed integrals are inserted in the jacobian and the right-hand-side matrices and all the rows and columns related with deactivated degrees of freedom are zeroed.

It should be noted that every time the procedure is run, it stores and updates significant state variables related with every integration point, namely the stress tensor and plastic deformations.

Figure 4.8 presents the general steps taken to compute the stresses and the material stiffness matrix in every integration point (from continuous or fracture region), based on the material constitutive behaviour defined by the user.

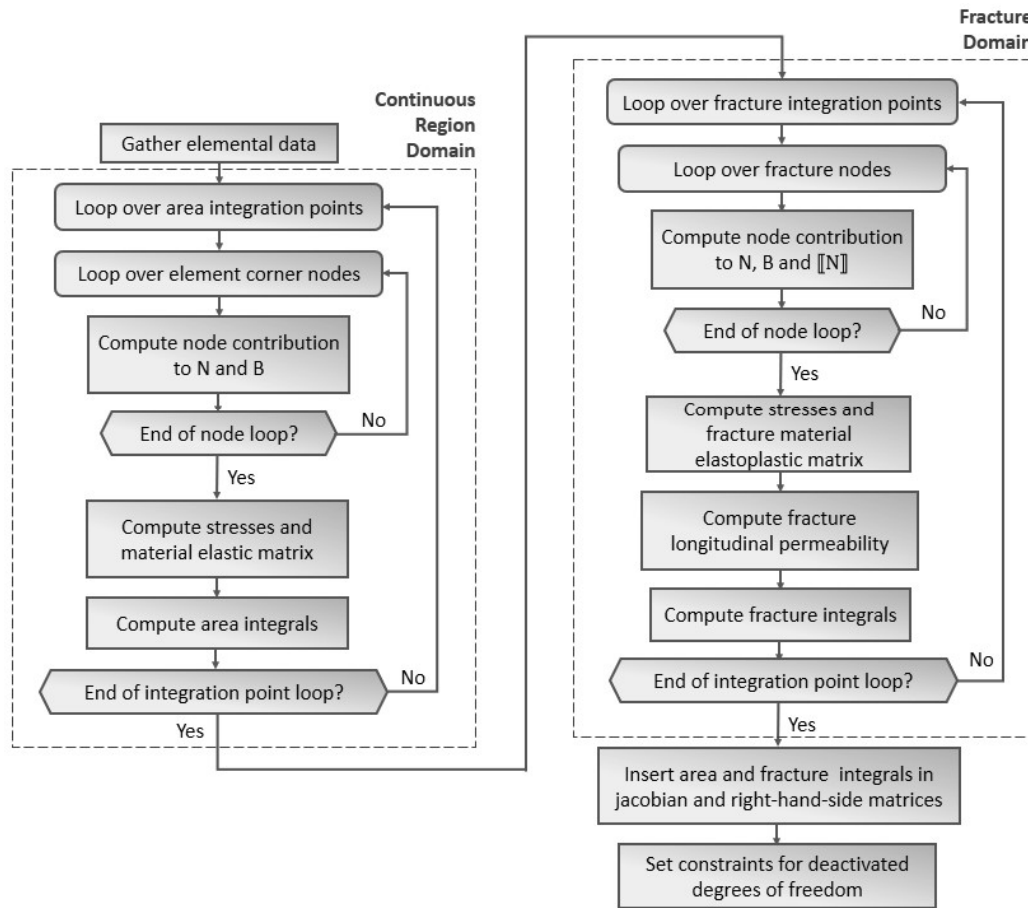


Figure 4.7 – General flow of the UEL subroutine

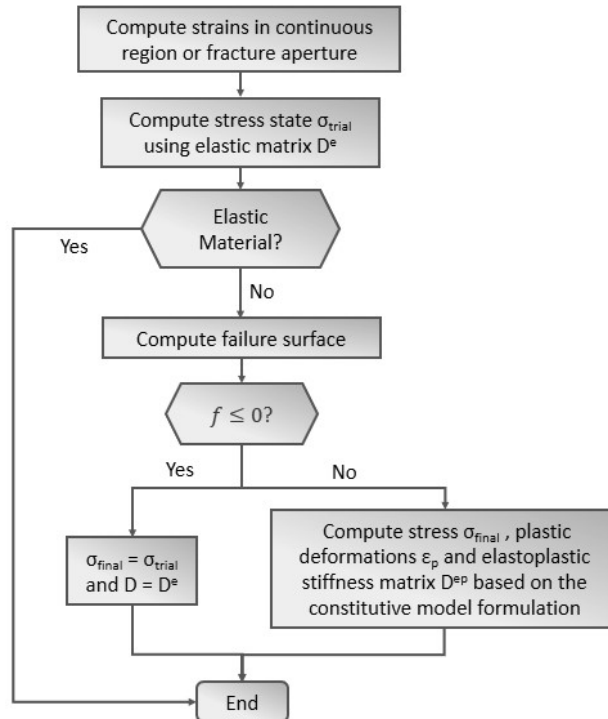


Figure 4.8 – General flow of the material constitutive subroutine

4.2.5. Fracture geometry post-processor

At the end of each increment, the algorithm checks the occurrence of fracture propagation. The verification is made using a user-defined propagation criterion. If a fracture propagates, then both the direction and length of propagation are computed. As seen in Figure 4.9, the post processor starts by defining in which regions of the model the propagation should be checked. Then, the propagation criterion is verified in each region. For every region where propagation occurs, the direction of the propagating segment is defined based on the direction criterion. Finally, the length of the propagating segment is computed. With the computed direction and length, the new coordinates for the propagating segments are obtained.

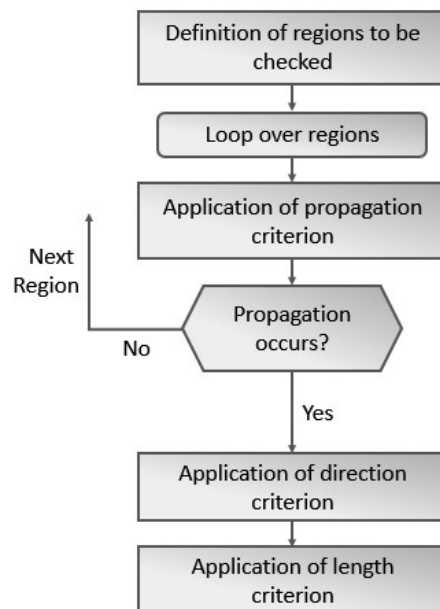


Figure 4.9 – General flow of the fracture geometry post-processor

The adopted propagation criterion is based on the average minimum principal stress at the integration points of a region that is perpendicular to the fracture tip, as seen in Figure 4.10. The region may have different shapes. However, in this implementation, the region may be square or rectangular, depending on the user's choice. If it is square, its side is equal to the dimension of the average. If it is rectangular, then its dimensions are equal to the mesh average element.

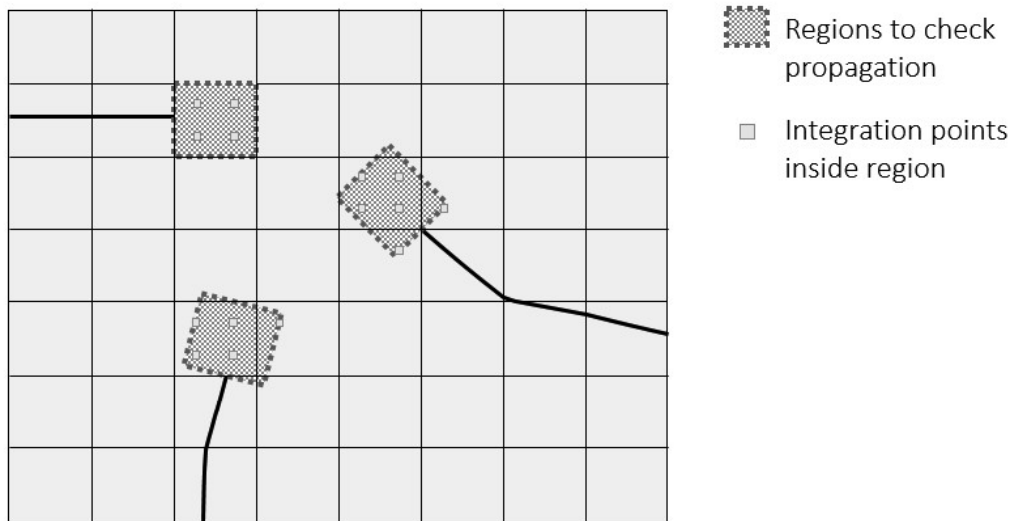


Figure 4.10 – Examples of regions where propagation is checked

A specific treatment is made when a fracture tip is close to another fracture. Considering that stress fields are usually different at each side of a fracture, it would not be correct to pick the stresses in the opposite side of the fracture tip. This way, the region is redefined considering only the part that is of interest to the fracture tip, as seen in Figure 4.11.

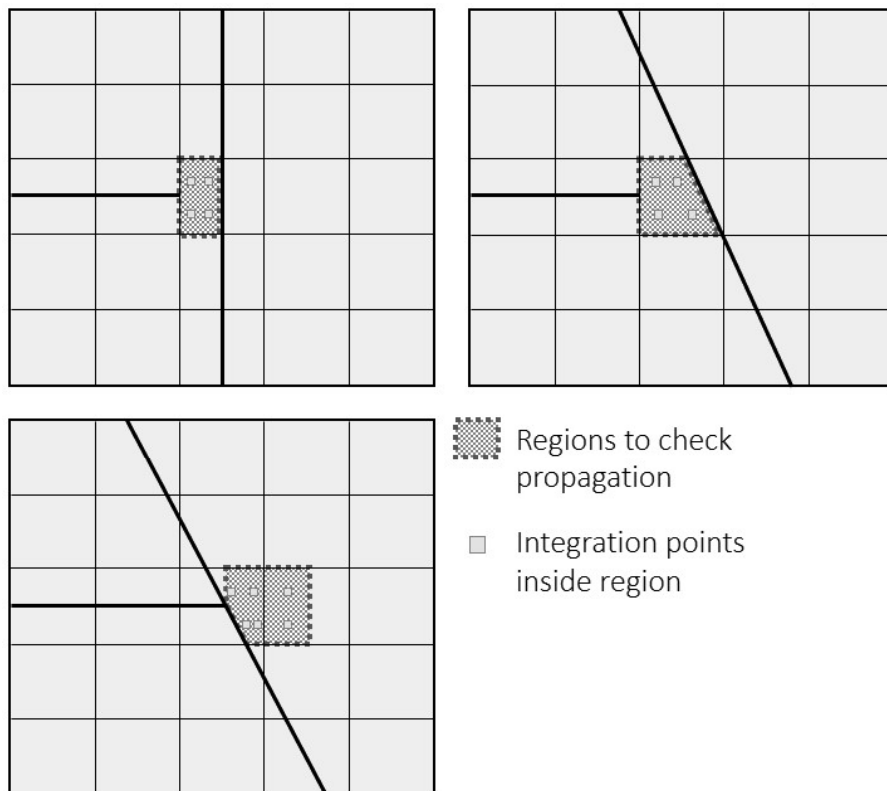


Figure 4.11 – Examples of regions close to other fractures

Once the borders of the region are defined, the following criterion is applied

$$\overline{\sigma_3} > \sigma_t \quad (4.1)$$

Where $\overline{\sigma_3}$ is the average of the minimum principal stresses in the region's integration points and σ_t is the tensile strength of the rock. The direction criterion used is also based on the average of the principal stresses. Propagation occurs perpendicularly to the average of the minimum principal stress in the computed region.

Finally, the length of a propagating segment is such that propagation always extends up to the next element border. Consequently, only one element is allowed to propagate per increment. This is a similar approach as the one used in the Abaqus built-in XFEM elements. Despite the fact that this approach may lead to a decrease of the crack tip speed, as mentioned by Song, Areias and Belytschko (2006), this problem can be overcome by using sufficiently refined meshes.

4.2.6. Element topology

As mentioned previously, the Abaqus user element subroutine allows the implementation of any kind of finite element in the code. In this work, only one element was coded. However, its implementation is flexible enough to model different situations: standard porous finite element with hydro mechanical coupling, enriched porous finite element with coupling between the hydro mechanical porous region and the fracture fluid pressure, enriched porous finite element with multiple fractures and intersections with coupling between the hydro mechanical porous region and the fracture fluid pressure.

This flexibility is achieved by allocating degrees of freedom to all the mentioned situations, activating and deactivating them during the simulation depending on the modelling needs. For example, if there is need to simulate an impermeable element with one fracture, all the pore pressure degrees of freedom and intersection degrees of freedom should be deactivated. Once Abaqus does not allow run time deactivation, this is achieved by zeroing every coefficient related to those degrees of freedom.

The basis of the user element is a Q4 plane strain linear segment, with the corner nodes storing the standard displacement and pore pressure degrees of

freedom. Additionally, the same corner nodes also store the displacement and pore pressure enriched degrees of freedom.

These degrees of freedom would be enough to model a multi fractured porous medium if there was no need to consider the fracture fluid pressure. However, considering the importance of working with the fracture fluid pressure as a variable (as explained in Chapter 3.1), additional degrees of freedom are added to consider it.

By principle, it would be correct to place the fracture pressure degrees of freedom coincident with the fracture segments extremities. However, as seen in Figure 4.12, that is not possible with Abaqus. As known, XFEM is a technique that allows simulation of fracture propagation without prior knowledge of the fracture path, i.e. each new fracture segment is positioned as the simulation runs. Consequently, at the beginning of the simulation it is not possible to know which elements will be intersected by fractures or to state where the fracture pressure degrees of freedom will be. As Abaqus does not allow the placement of new nodes in elements while the simulation runs, it is impossible to guarantee that the fracture pressure degrees of freedom will be positioned coincident with the fracture segments.

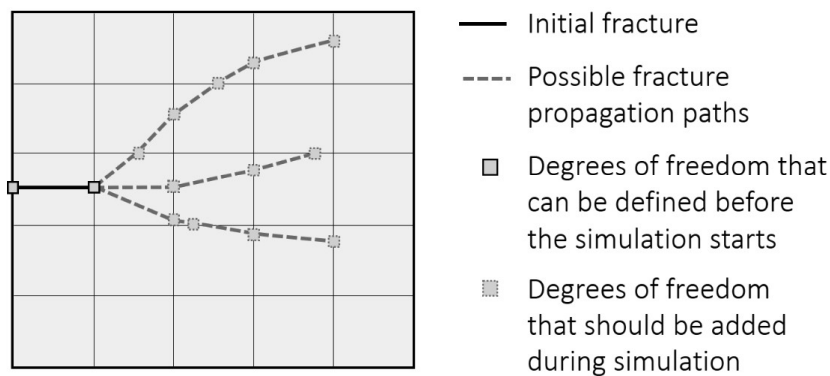


Figure 4.12 – Possible positions of fracture pressure degrees of freedom in possible fracture propagation segments

To overcome this situation, the following workaround is implemented (see Figure 4.13):

- 9 nodes are considered in every element since the beginning of the simulation – the already existing 4 corner nodes + 4 element border middle nodes + 1 node at the element centroid

- Every time a fracture propagates into a new element, an algorithm in the pre-processor defines which nodes should store the new fracture variables
- If other fractures propagate into the same element (creating an intersection), the algorithm stores the new fracture variables in other nodes that are still available

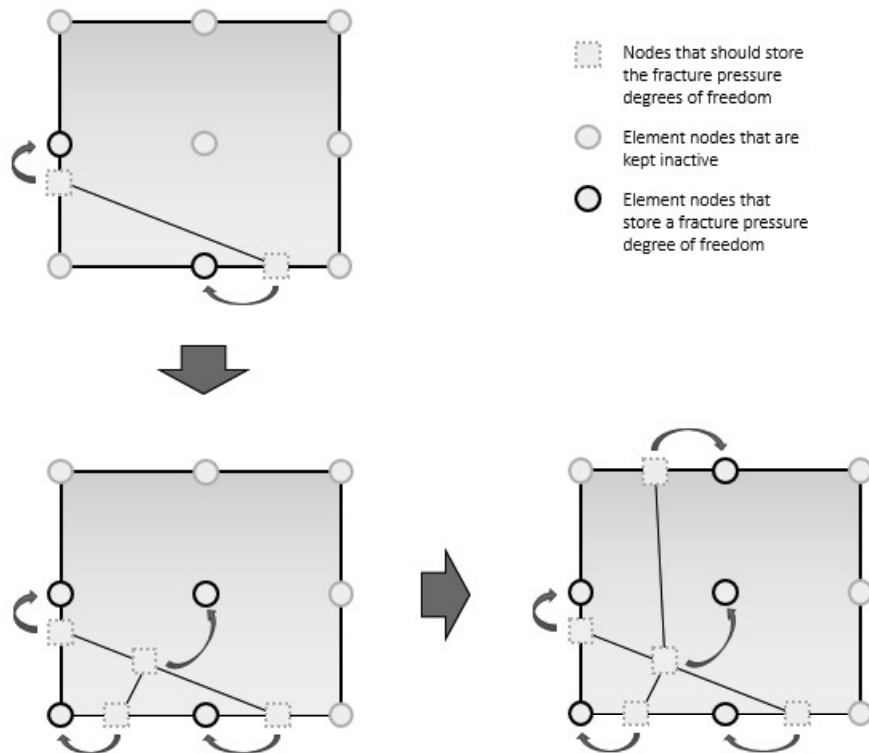


Figure 4.13 – Storage of fracture pressure degrees of freedom

4.2.7. Numerical integration

4.2.7.1. Introduction

As stated previously, the Finite Element Method demands the problem sub-domains (i.e. elements) to integrate smooth and continuous functions. In such cases as the discretization with interface elements, the integration on both sides of the fracture is made in separate continuous elements and the fracture domain integration is made directly in the interface elements that represent that fracture. In XFEM, the fracture domain is within the continuous region, leading to the need of

performing two types of integrations in the same element. In 2D the fracture domain (Γ) requires line integration and the element domain (Ω) requires area integration.

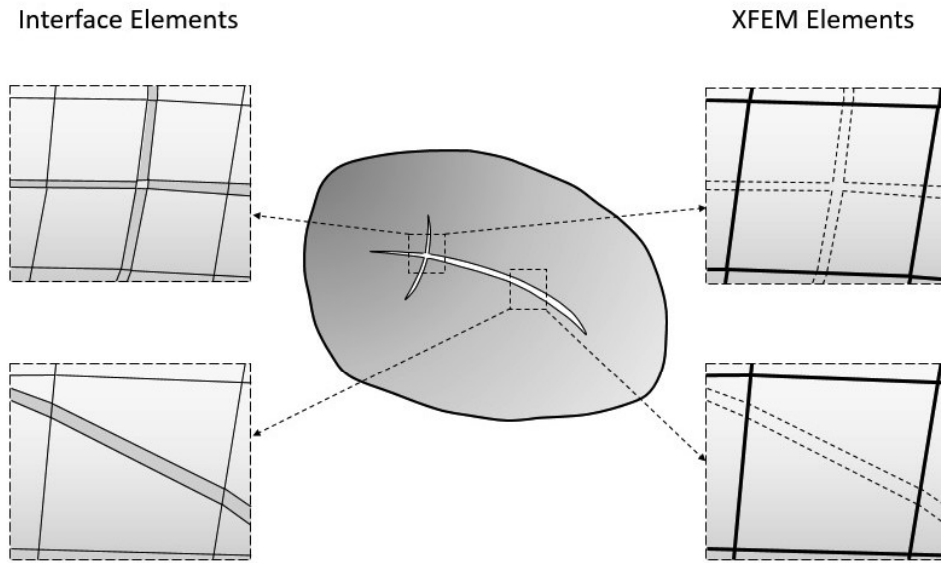


Figure 4.14 – Difference of element definition between Interface elements and XFEM elements. On the left, black continuous lines represent element borders, grey hatches represent continuous elements and green hatches represent interface elements. On the right, black continuous lines represent element borders, grey hatches represent continuous elements and dashed lines represent the fracture inside the element domain

4.2.7.2. Continuous Region

In this work, the integration over continuous regions, i.e. Ω in 2D elements, is performed by using the Gauss Method. In elements where all the enriched degrees of freedom are deactivated, i.e. non-fractured elements, the integration may be performed following the conventional techniques, such as presented in Potts and Zdravković (1999).

For enriched elements, the explicit consideration of fractures inside the element domain requires the implementation of non-standard techniques for element integration. The integrand in the element domain is no longer continuous with continuous derivative (C^1 class) due to the presence of the enrichment functions (see Figure 3.7 or Figure 3.9). However, functions that develop on both sides of the fracture are C^1 class and therefore the standard Gauss integration technique applies. Thus, sub-regions within the element where continuity applies

may be integrated separately and the results be summed. Eq. (4.2) shows a Gauss integration procedure applied to the element sub-regions $nsubreg$. $iIPsub$ is the number of integration points in the sub-region, W the Gaussian weight and f the function to be integrated.

$$\iint_{-1}^1 f(x,y) dx dy = \sum_{j=1}^{nSubReg} \sum_{i=1}^{iIPsub} W_{i,j} \cdot f(x_{i,j}, y_{i,j}) \quad (4.2)$$

The subdivision process starts by cutting the element in sub-regions delimited by the fracture. Then the following rules apply:

- If the sub-region has four sides, Gauss integration for quadrilateral elements apply, as in the sub-regions defined in Figure 4.15a) and b);
- If the sub-region has three sides, Gauss integration for triangular elements apply, as seen in the lower left sub-region in Figure 4.15c);
- If the sub-region has five sides or more, further subdivision defines triangles with vertices coinciding with the original sub-region vertices and its centroid. In these triangles, Gauss integration for triangular elements applies, as seen in the upper right sub-regions in Figure 4.15c);

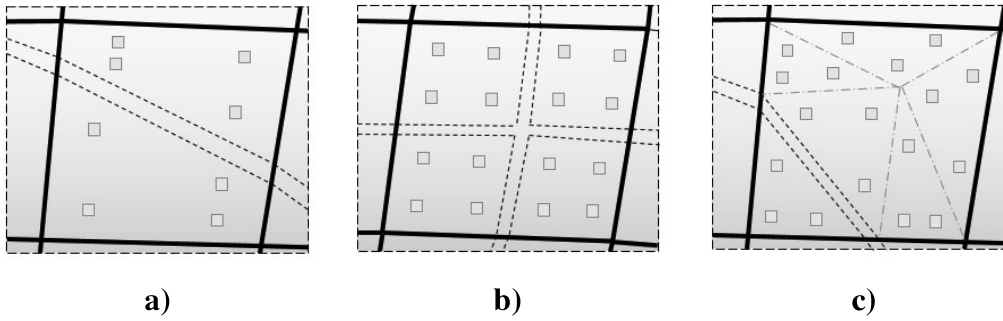


Figure 4.15 – Examples of integration points position in sub-regions

For both non-fractured elements and sub-regions, the Gauss integration order is defined by the user, varying on a range from 1 to 7.

4.2.7.3. Discontinuous Region

The integrals over fracture regions, i.e. Γ_d , are computed along fictitious line elements that coincide with the fracture position. Although these elements do not exist in the mesh topology, their implementation is critical to represent the fracture hydraulic and constitutive behaviour. The integration performed over these

elements also uses the Gauss integration rule. It is worth pointing out that a fracture intersected by another fracture may show a different behaviour on each side of the intersection. Therefore, the placement of Gauss points must consider not only the fracture position but also its intersections. Figure 4.16 shows some examples of the positioning of integration points along the discontinuity. In this research, only a second order integration scheme is used.

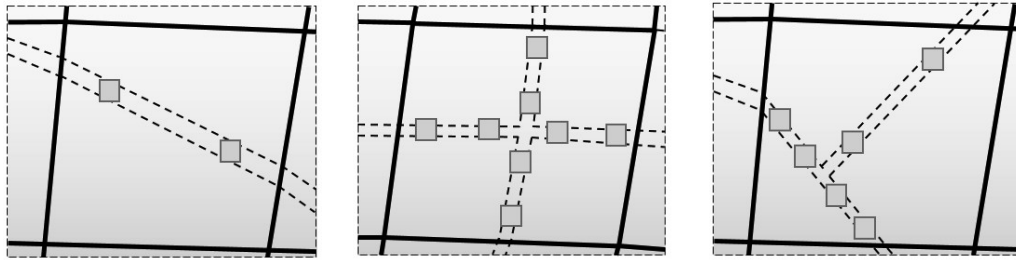


Figure 4.16 – Examples of integration points position in fractures

4.2.8. Limitations of the implementation

Abaqus is a powerful and very versatile tool, both for the built in and external user implementations. Nevertheless, the use of a commercial software where only a part of the code algorithm is reachable by the user brings naturally some limitations.

An already mentioned limitation of Abaqus is the impossibility to use the graphical interface both for input and output when using user elements. This issue which was overcome by the additional codes and software referred in Chapter 4.2.1.

The main limitation of the implementation is the way Abaqus deals with degrees of freedom of user elements. The degrees of freedom that are access by a user element must be defined in the input before the simulation starts. As stated before, the principle of XFEM develops around the concept of activation of new degrees of freedom in the run. To guarantee that all possible degrees of freedom will be available during the simulation, they need to be previously declared in the input. This means that many elements that are never fractured during a simulation have stored within them the deactivated degrees of freedom. This has obviously a negative effect in the calculation time and memory consumption.

Other related limitation is the number of degrees of freedom that Abaqus allows for user elements, which is limited to 30 per node. This is overcome by

attributing the same enrichment degree of freedom to different fractures, which is not problematic as long as different fractures do not share the same enriched nodes. However, when modelling intersection between fractures there are nodes that have enriched degrees of freedom from different fractures, so these fractures must have different enrichment degrees of freedom. This to say that with a limited number of degrees of freedom per node the number of fractures in the model is not limited, but the number of intersections inside one element is.

The degrees of freedom of user elements may be attributed to any physical grandness, as the differential equations are defined in the code. However, every time Abaqus runs a step, a keyword related with the type of calculation must be defined. For example, static problems, where only displacement (position 1 to 3) and rotation degrees of freedom (position 4 to 6) are active, or consolidation, where both displacement (position 1 to 3) and pore pressure (position 8) degrees of freedom are active. Although the implemented code has only intent of computing displacements and fluid pressures, the need of extra degrees of freedom for the enrichments demands a type of calculation that allows the maximum number of degrees of freedom possible. This is achieved by choosing a coupled displacement-temperature calculation. This way, the degrees of freedom 1 to 6 (displacement and rotation) and 7 and 11-30 (temperature) are available.

Finally, it must be highlighted that the computational geometry functions used in the fracture geometry pre and post-processor allow only the use of regular meshes.

5

Validation tests

The implementation described previously is validated in this chapter. This is achieved by comparing the results of the XFEMHF code with analytical or other software solutions. First, the results of a single propagating planar fracture are compared with the analytical solution of the near-K vertex of the KGD model.

Next, a group of simulations focus in flow through fractured media. A problem with unidimensional flow in a fractured element is compared with the analytical solution. Plus, bi-dimensional flow both in permanent and transient regimes is tested in three examples and compared with models with interface elements. In all models of this section a variation of hydraulic parameters is applied, in order to validate different percolation behaviours.

Finally, the validation of the contact model with friction is achieved, first by using a one-element mesh with a single fracture followed by a multi-fractured problem. The single element models are used for three different situations where fracture position or load conditions change. First, an element with a horizontal fracture is subjected to a vertical cyclic displacement applied at its top. Second, an element with a horizontal fracture is subjected to a horizontal monotonic displacement at its top for three different vertical confining stresses. Third, an element with an inclined fracture is subjected to a vertical cyclic displacement applied at its top. In the multi-fractured model an unconfined compression test is simulated and the stress trajectories of the fractures are plotted against the implemented Mohr-Coulomb failure surface.

5.1.

KGD analytical solution

General description of the simulation

As stated in Chapter 2, there are analytical formulations for propagating fractures in a homogeneous medium. The KGD solution assumes a fracture which is infinite in one of its dimensions, so this means it can be modelled using a two-

dimensional plane strain model. In this simulation, a numerical model is compared with the KGD K-vertex analytical storage-toughness solution, as presented by Bungier, Detournay and Garagash (2005).

Model geometry and mesh

The model's dimensions are 45 m x 30 m and the mesh is regular with 75 elements in each direction, as seen in Figure 5.1. An initial fracture of 1,2 m is placed at half-height on the left side of the model.

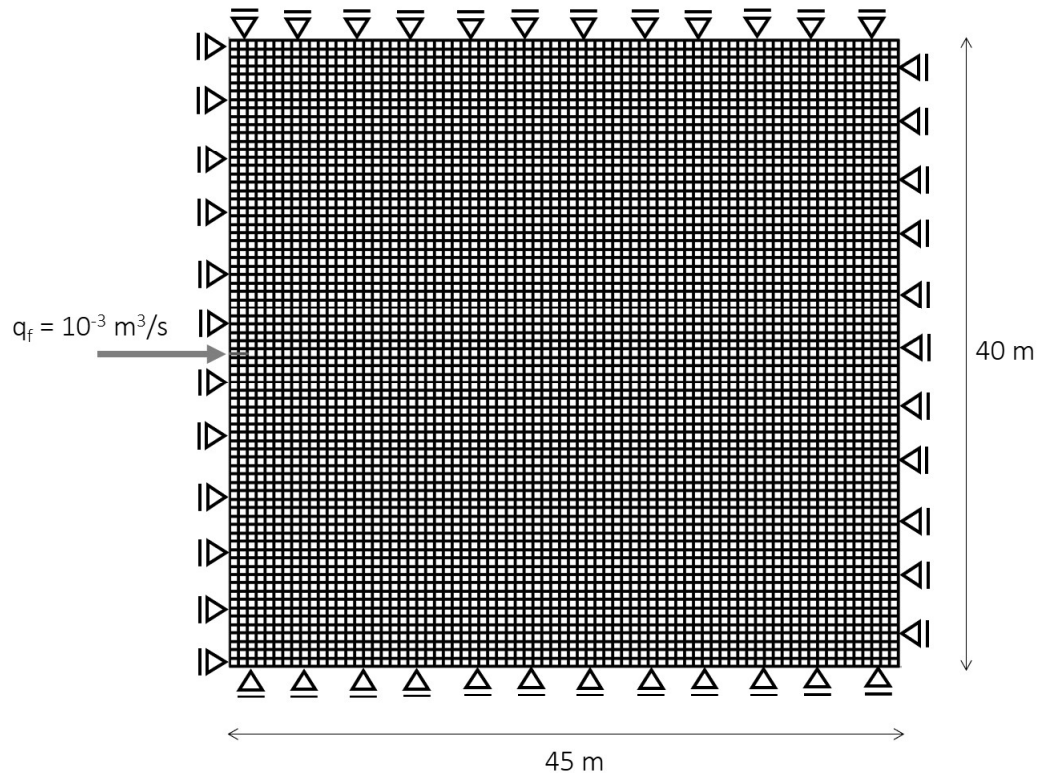


Figure 5.1 – Geometry of the mesh and boundary conditions

Material properties

The material properties are presented in Table 5.1 and Table 5.2. Considering that the KGD K-vertex storage-toughness solution is valid for almost impermeable materials, it is assumed that the rock is impermeable. The parameters are adopted based in the work by Zielonka *et al.* (2014).

Table 5.1 – Hydraulic properties

	Parameter	All Models
Fractures	Initial hydraulic aperture (m)	2×10^{-3}
	Fluid Viscosity (kPa.s)	10^{-7}

Table 5.2 – Mechanical properties

	Parameter	
Continuous Region	E (kPa)	17×10^7
	ν	0,2
	σ_t (kPa) - Numerical	1250
	K_{IC} (kPa.m ^{1/2}) - Analytical	1460

Boundary and loading conditions

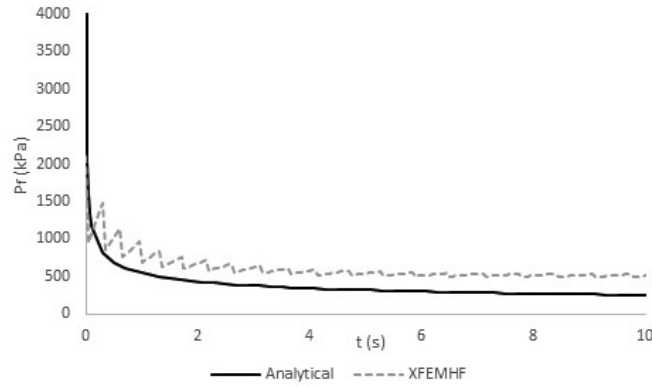
Along the borders of the model the displacements are fixed in the perpendicular direction, as seen in Figure 5.1. The simulations are set to run one single step of 10 s with time increments of size between 0,5 s and 2 s. The fluid injection in the fracture is given by a constant volumetric flux of 1×10^{-3} m³/s at the hydraulic fracture mouth. No in-situ stress state was defined for this analysis.

Results

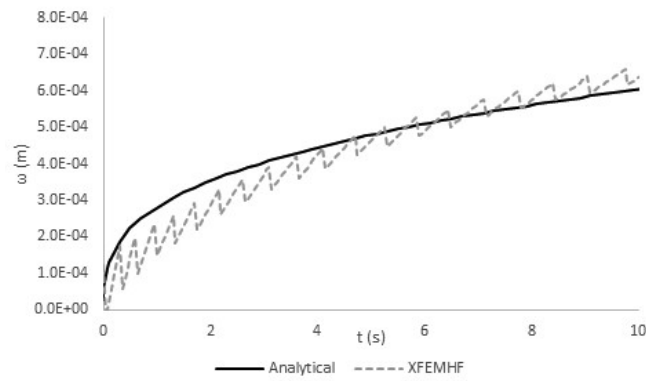
Figure 5.2 presents the variation of injection pressure, fracture aperture and fracture length over time, for both analytical and numerical solution. It is noticeable that, although some slight differences exist, the results and the tendencies of the numerical model are in good agreement with the analytical solution.

The differences in results may be explained mostly due to three factors. First, it is known how mesh refinement influence the results. As stated by Zielonka et al. (2014), the relative error between solutions decrease monotonically as the mesh is refined. Second, the fact that the model has finite dimensions, in opposition to the infinite medium of the analytical solution, thus leading to possible influence of the boundary conditions at the borders of the model. Third, the theoretical formulations are different. As the KGD solution relies on the stress intensity factor for fracture

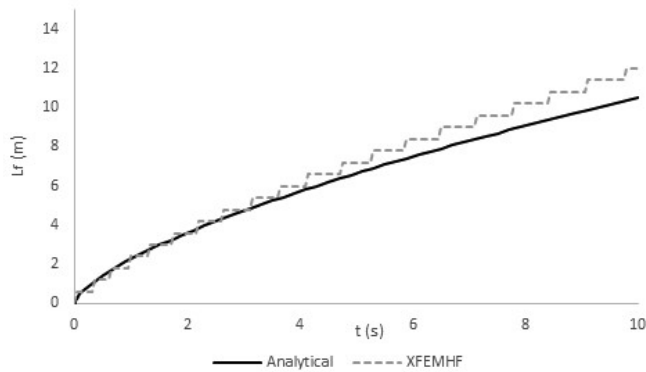
propagation, the numerical model bases its propagation criterion on the average stress state in a region in the front of the crack tip. As there is no analytical relation between critical stress intensity factor and tensile strength, the solutions may be similar but exact match would only be possible by doing back-analysis to find the correspondent tensile stress.



a)



b)



c)

Figure 5.2 – Plots for KGD analytical and numerical solution.
a) Injection pressure vs time. b) Fracture maximum aperture vs time.
c) Fracture length vs time.

5.2. Flow in a fractured medium

5.2.1. Unidimensional percolation

General description of the simulation

A unidimensional flow simulation of two distinct situations – percolation through (Situation 1) and percolation from (Situation 2) a fracture – may be compared with an analytical solution. Figure 5.3 shows a schematic model for flow through materials with different permeabilities. On the left side of Figure 5.3 a gradient of pore pressure is imposed in the bottom and top of the model ($P_{r,b}$ and $P_{r,t}$), leading to a one-way flow. On the right side of Figure 5.3 a pressure is imposed inside the fracture (P_f) and a gradient is created by imposing a lower pressure on the bottom and top of the model ($P_{r,b}$ and $P_{r,t}$). It is assumed that the filter cake is a layer of infinitesimal length with conductivity equivalent to the fracture face transversal conductivity being $c = k/L$.

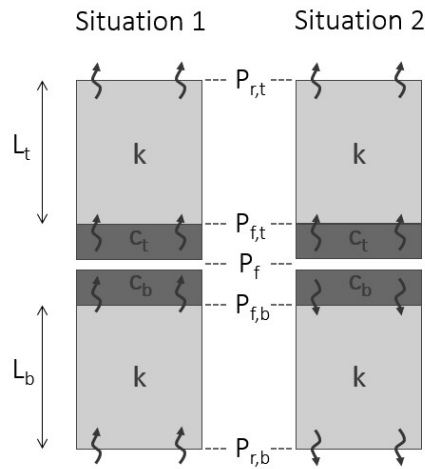


Figure 5.3 – Two situations of unidimensional fluid percolation in a model with different layers. On the left side, percolation from the bottom to the top of the model. On the right side, percolation from the fracture to the porous medium

Considering that the different layers are placed in series, the equivalent resistance (or conductivity) may be computed as

$$k_{eq} = \frac{\sum L}{\sum \frac{L}{k}} \quad (5.1)$$

Therefore, following Darcy's law the volumetric flux in the model is given by

Situation 1	Situation 2
$k_{eq} = \frac{\sum L}{\sum \frac{L}{k}} = \frac{L_b + L_t}{\frac{L_b}{k} + \frac{1}{c_b} + \frac{1}{c_t} + \frac{L_t}{k}}$	$k_{eq} = \frac{\sum L}{\sum \frac{L}{k}} = \frac{L_b}{\frac{L_b}{k} + \frac{1}{c_b}}$
$q = -k \frac{\Delta p}{L} = -k_{eq} \frac{p_{r,t} - p_{r,b}}{L_b + L_t}$	$q = -k \frac{\Delta p}{L} = -k_{eq} \frac{p_{r,t} - p_f}{L_t}$

The pressures may then be computed for both situations as

$$q = -k \frac{p_{r,t} - p_{f,t}}{L_t} \Leftrightarrow p_{f,t} = p_{r,t} - q \frac{L_t}{k}$$

$$q = -k \frac{p_{f,b} - p_{r,b}}{L_b} \Leftrightarrow p_{f,b} = p_{r,b} - q \frac{L_b}{k}$$

$$q = -c_b(p_f - p_{f,b}) \Leftrightarrow p_f = p_{f,b} - \frac{q}{c_b} \text{ (only for situation 1)}$$

Model geometry and mesh

Given that a unidimensional situation is being modelled, the single element model presented in Figure 5.4 was defined.

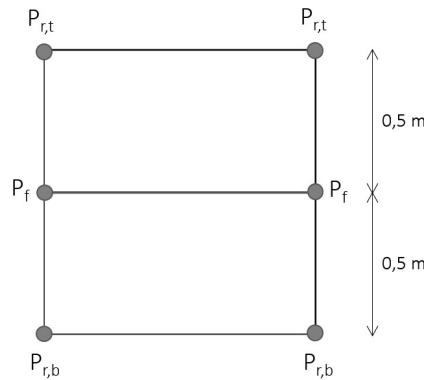


Figure 5.4 – Geometry and boundary conditions of the mesh

Material properties

Six different simulations were defined by changing material properties or boundary conditions. The hydraulic properties both for the porous region and the fractures are presented in Table 5.5.

Table 5.3 – Hydraulic properties

	Parameters	Situation 1			Situation 2		
		Case 1	Case 2	Case 3	Case 4	Case 5	Case 6
Porous Region Hydraulic Conductivity	$k = k_x = k_y$ (m/s)	10^{-8}					
Fracture face transversal conductivity.	c_{top} (m/s.kPa ⁻¹)	1	10^{-8}	10^{-13}	1	10^{-8}	10^{-10}
	c_{bottom} (m/s.kPa ⁻¹)						10^{-8}

Boundary and loading conditions

The flow regime is guaranteed by imposing constant pressures in the bottom and the top of the model (and also in the fracture, in Situation 2), following the values presented in Table 5.4. Considering that a permanent regime occurs, the time interval and the number of steps are indifferent.

Table 5.4 – Model boundary conditions

	Situation 1			Situation 2		
	Case 1	Case 2	Case 3	Case 4	Case 5	Case 6
$P_{r,b}$ (kPa)	1000			0		
$P_{r,t}$ (kPa)	0			0		
P_f (kPa)	-			1000		

Results

The pressure profiles along a vertical section of the model are presented in Figure 5.5. It is evident that the numerical simulation results match exactly the analytical solutions. When the fluid flows from the bottom to the top of the model (situation 1) it is noticeable how the decrease of the fracture face transversal conductivity c increases the jump of pressure between the fracture faces. When the

injection is made from the fracture (situation 2) the XFEM element is capable of simulating both the loss of pressure in the fracture faces (filter cake) and through the porous medium. Results of Calculation 6 show how different fracture face transversal conductivity in the top and bottom faces of the fracture influence the pressure profile in both halves of the model.

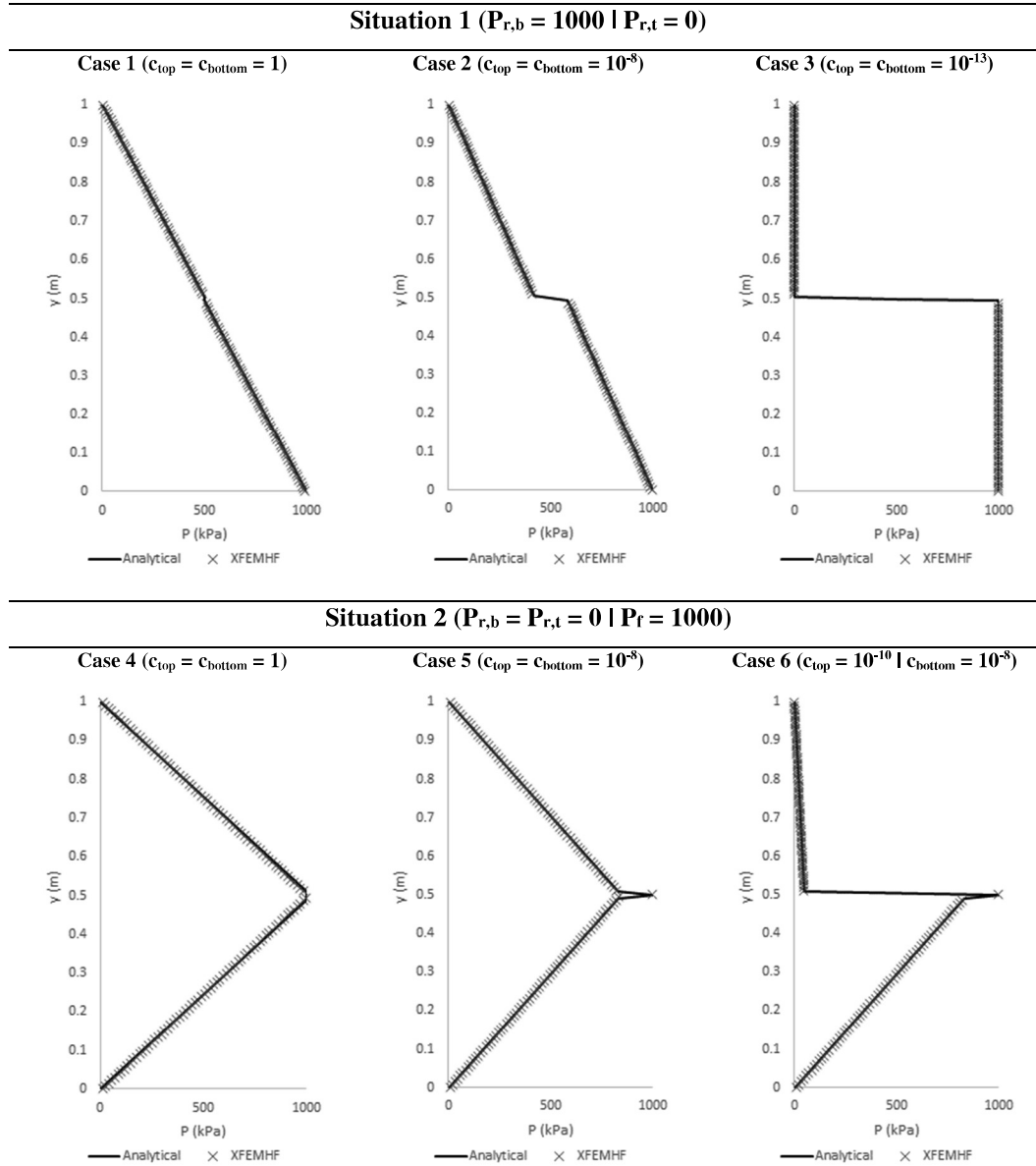


Figure 5.5 – Pressure profiles of the model and analytical solution for each calculation

5.2.2. Injection in fracture intersection

General description of the simulation

This model contemplates two intersecting fractures with a flow injection in the intersection. The pressure gradient between the injection point and the porous medium is created by imposing a null pressure in the corner nodes of the model. In this model, only hydraulic variables are considered: pore-pressures and fracture pressures. As there are no deformations in the model, a permanent regime is obtained.

Two calculations are performed with variation of the fracture faces transversal conductivity. The results are compared with an Abaqus model with interface elements.

Model geometry and mesh

The model is symmetric, both in horizontal and vertical direction. Its dimensions are 10 m x 10 m and the mesh is regular with 15 elements in each direction, as seen in Figure 5.6.

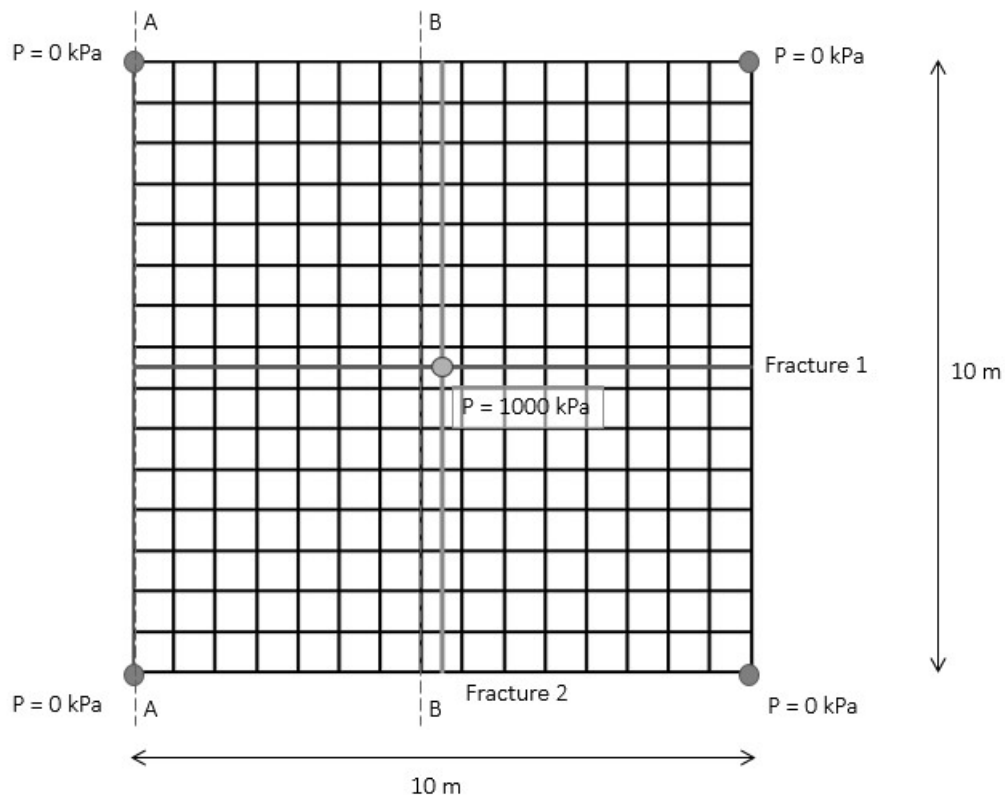


Figure 5.6 – Geometry of the mesh and boundary conditions

Material properties

The hydraulic properties both for the porous region and the fractures are presented in Table 5.5. An isotropic hydraulic conductivity and equal fracture face transversal conductivity for every fracture are used.

Table 5.5 – Hydraulic properties

	Parameter	Case 1	Case 2
Porous Region	Hydraulic conductivity: $k = k_x = k_y$ (m/s)	10^{-8}	
Fracture	Fracture face transversal conductivity: $c = c_{\text{top}} = c_{\text{bottom}}$ (m/s.kPa ⁻¹)	10^{-12}	10^{-9}
	Hydraulic aperture (m)	2×10^{-3}	2×10^{-3}
	Fluid Viscosity (kPa.s)	10^{-6}	

Boundary and loading conditions

The flow regime is guaranteed by imposing a constant pressure in the fracture intersection of 1000 kPa and a pressure of 0 kPa in the corners of the node, as indicated in Figure 5.6. Considering that a permanent regime occurs, the time interval and the number of steps are indifferent.

Results

Figure 5.7 shows the pore-pressure fields for the two calculations run, as well as the results obtained using Abaqus with interface elements. Figure 5.8 presents the values of the pore-pressures along the sections A-A and B-B (defined in Figure 5.6). It is easily noticeable that the comparison of the two simulation tools shows a very good agreement. Slightly differences are due to the way the different output tools plot their results.

As the porous medium and the fracture longitudinal transmissibility are the same in both calculations, the change in the fracture face transversal conductivity strongly affects the pore-pressure fields. For lower values of the coefficient (Case 1: $c = 10^{-12}$) a drop of pressure from 1000 kPa to around 30 kPa occurs between the fracture and the porous medium in both sections. On the other hand, a much smaller drop of pressure is verified in Case 2, since the increase of the coefficient obviously reduces the gradient.

Overall, it is shown that the implemented code is able to simulate the effect of the hydraulic behaviour in intersection of fractures and the leak-off to the porous region.

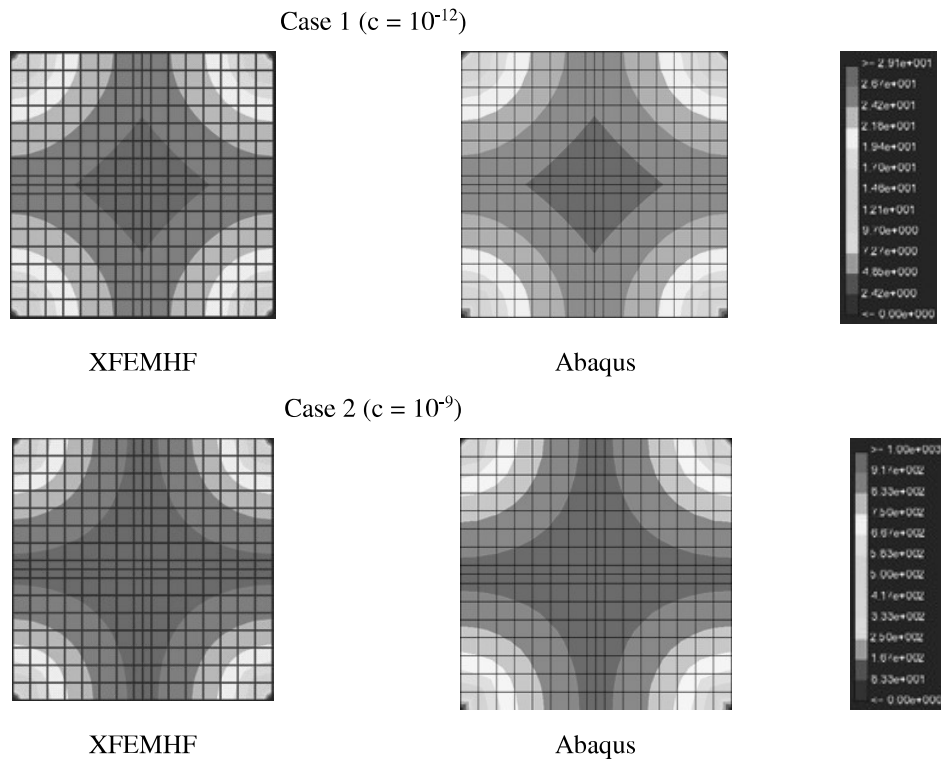


Figure 5.7 – Pore-pressure fields

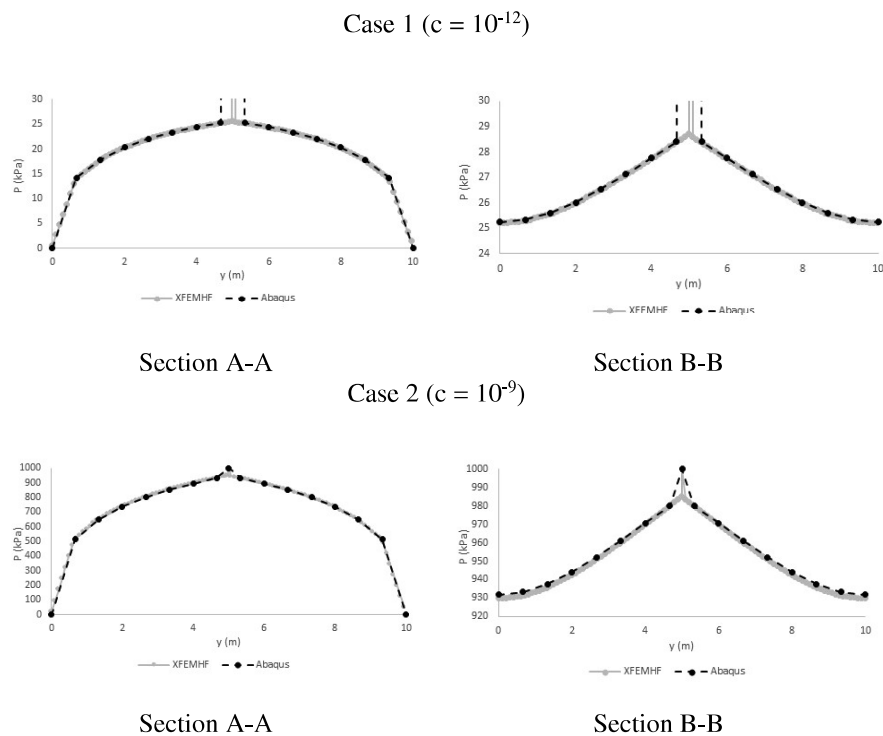


Figure 5.8 – Pore-pressures in sections A-A and B-B

5.2.3. Percolation through a fractured medium

General description of the simulation

In this model, four randomly orientated fractures intersect each other. A pressure gradient is created. Only the hydraulic variables are considered: pore-pressures and fracture pressures, obtaining a permanent regime. Four calculations are performed with variation of the fracture face transversal conductivity and the fracture hydraulic aperture. The results are compared with a model where the fractures are represented by interface elements.

Model geometry and mesh

The model dimensions are 30 m x 15 m and the mesh is regular with 30 and 15 elements in the horizontal and vertical directions, respectively, as seen in Figure 5.9. The fractures have different orientations and lengths that were defined randomly.

Figure 5.10 shows the mesh with interface elements represented in red. A total of 1382 elements are used, where 73 are 4-node two-dimensional cohesive elements (COH2D4P) and 1309 are 4-node bilinear displacement and pore pressure elements (CPE4P).

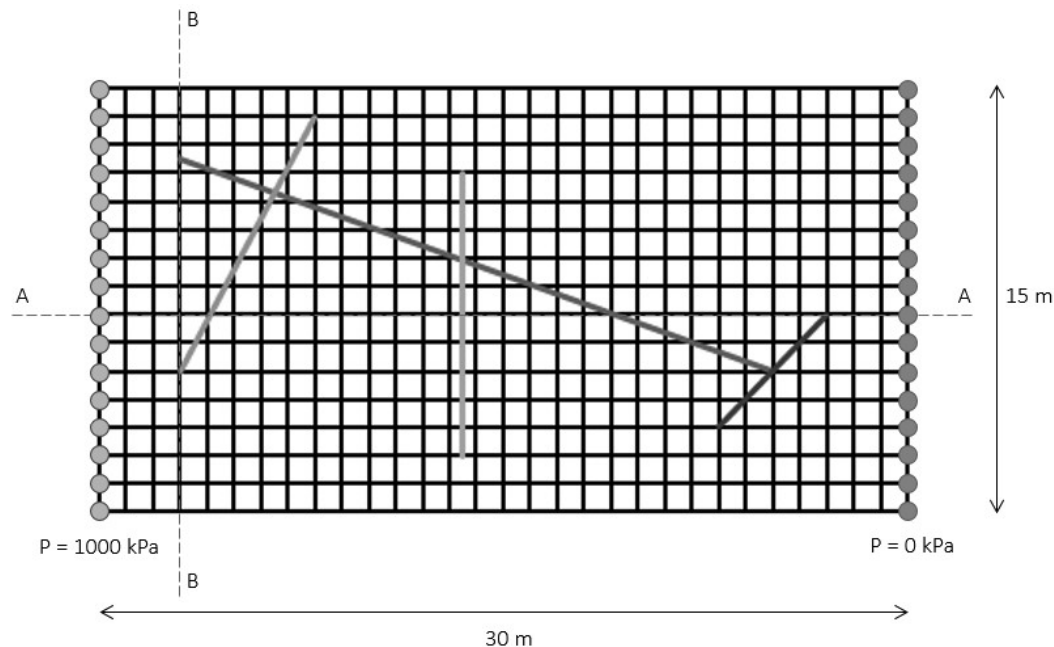


Figure 5.9 – Geometry of the mesh and boundary conditions

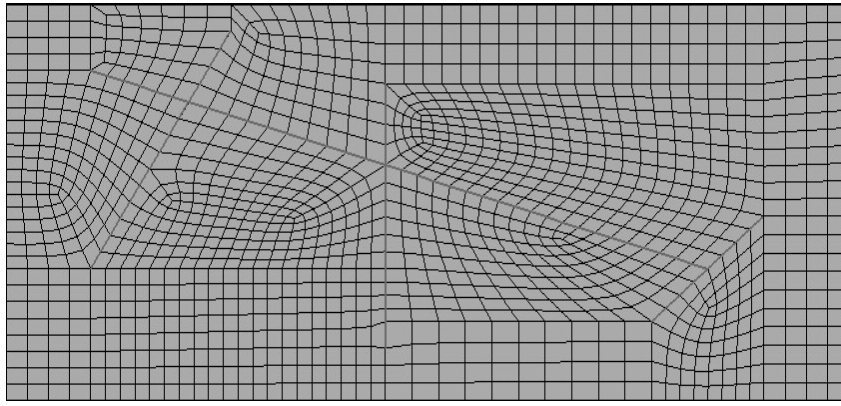


Figure 5.10 – Geometry of the mesh of Abaqus with interface elements model

Material properties

The hydraulic properties both for the porous region and the fractures are presented in Table 5.6. The porous media is isotropic and the fracture face transversal conductivity and hydraulic apertures are the same for every fracture in each of the calculations.

Table 5.6 – Hydraulic properties

	Parameter	Case 1	Case 2	Case 3	Case 4
Porous Region	Hydraulic conductivity: $k = k_x = k_y$ (m/s)	10^{-8}			
Fracture	Fracture face transversal conductivity: $c = c_{top} = c_{bottom}$ (m/s.kPa ⁻¹)	10^{-7}	10^{-7}	10^{-12}	10^{-12}
	Hydraulic aperture (m)	2×10^{-3}	2×10^{-6}	2×10^{-3}	2×10^{-6}
	Fluid Viscosity (kPa.s)	10^{-6}			

Boundary and loading conditions

The flow regime is guaranteed by imposing a constant pressure of 1000 kPa at the left border and a null pressure at the right border, as indicated in Figure 5.9. Considering that a permanent regime occurs, the time interval and the number of steps are indifferent.

Results

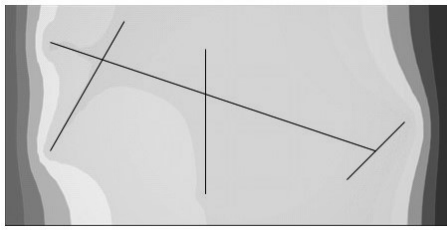
Figure 5.11 shows the pore-pressure fields for the four simulations, as well as the results obtained using Abaqus with interface elements. Figure 5.12 presents the values of the pore-pressures along sections A-A and B-B defined in Figure 5.9. It is easily noticeable from both figures that the XFEMHF simulations show very good agreement with the interface element solution.

A sensitivity analysis of two parameters – fracture longitudinal transmissibility and fracture face transversal conductivity – shows the strong influence that these have on the pressure fields.

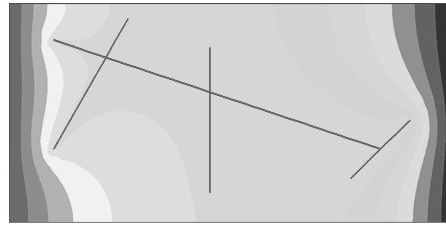
The calculation with higher values of fracture transversal and longitudinal transmissibility (Case 1: $c = 10^{-7}$ || $w_{init} = 2 \times 10^{-3}$) shows that when both permeabilities are high, fluid easily flows to the fractures, showing an effect of “drainage canals”. The fluid from the porous region tends to flow to the fracture, reducing the fluxes in the middle part of the model. Then, it leaves the right sided fracture to reach the model border, as seen in Figure 5.13. This effect also proves that the fracture intersections are capable of transmitting the fluid flow between different fractures.

In Case 2 ($c = 10^{-7}$ || $w_{init} = 2 \times 10^{-6}$), the longitudinal transmissibility is reduced by means of the fracture aperture. Keeping a higher transversal conductivity, the flow easily enters or leaves the fractures. However, the drainage effect related with the longitudinal flow no longer occurs. This way, the flow crosses the fractures but does not enter in this preferential path, keeping the same direction in the porous region.

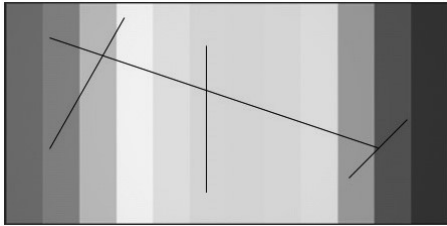
Case 3 ($c = 10^{-12}$ || $w_{init} = 2 \times 10^{-3}$) and Case 4 ($c = 10^{-12}$ || $w_{init} = 2 \times 10^{-3}$) show that the reduction of the fracture face transversal conductivity decreases the transversal conductivity to a point that the flow is no longer capable of entering the fractures. Therefore, the fractures represent a barrier and the fluid has to deviate to continue to flow through the porous region, as seen in Figure 5.13. Despite the difference in the longitudinal transmissibility between Case 3 and Case 4, there is no significant difference in the results, as the flow does not flow along the fractures.

Case 1 ($c = 10^{-7} \parallel w_{init} = 2 \times 10^{-3}$)

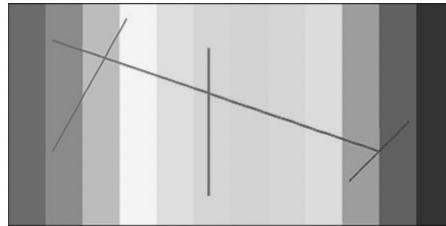
XFEMHF



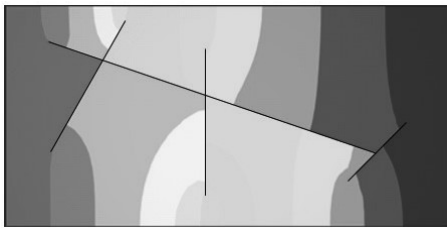
Abaqus

Case 2 ($c = 10^{-7} \parallel w_{init} = 2 \times 10^{-6}$)

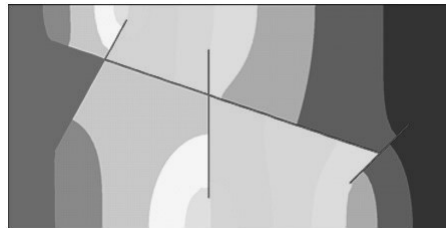
XFEMHF



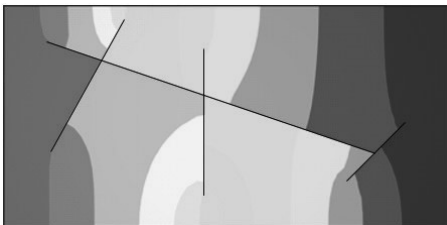
Abaqus

Case 3 ($c = 10^{-12} \parallel w_{init} = 2 \times 10^{-3}$)

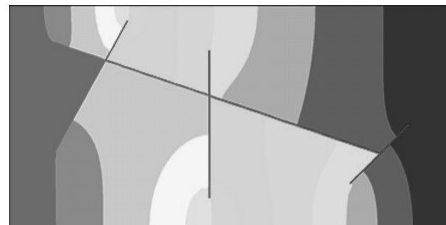
XFEMHF



Abaqus

Case 4 ($c = 10^{-12} \parallel w_{init} = 2 \times 10^{-6}$)

XFEMHF

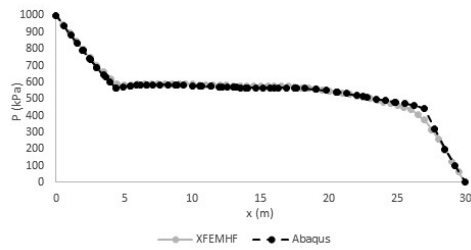


Abaqus

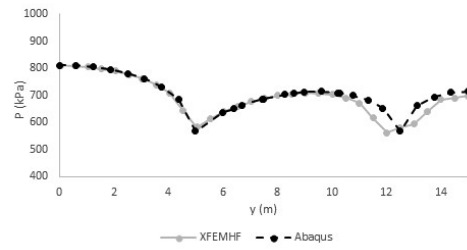


Figure 5.11 – Pore-pressure fields

Case 1 ($c = 10^{-7} \parallel w_{init} = 2 \times 10^{-3}$)

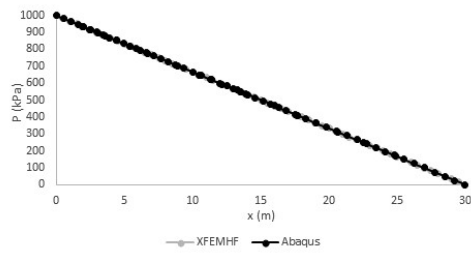


Section A-A

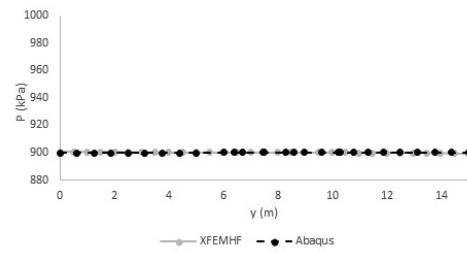


Section B-B

Case 2 ($c = 10^{-7} \parallel w_{init} = 2 \times 10^{-6}$)

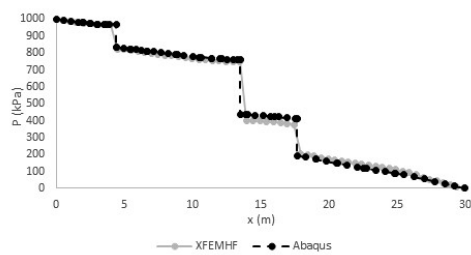


Section A-A

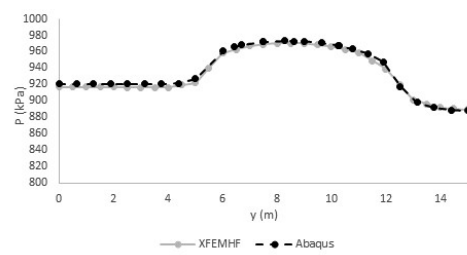


Section B-B

Case 3 ($c = 10^{-12} \parallel w_{init} = 2 \times 10^{-3}$)

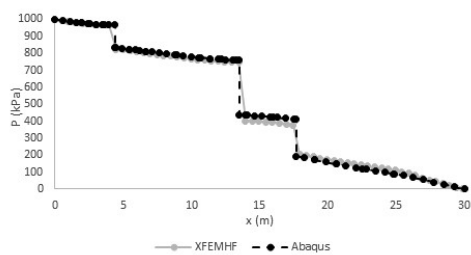


Section A-A

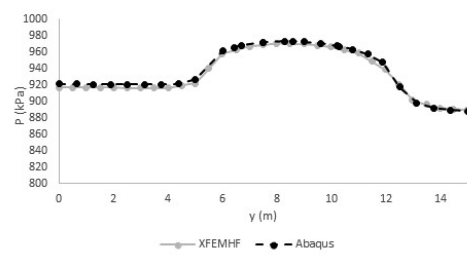


Section B-B

Case 4 ($c = 10^{-12} \parallel w_{init} = 2 \times 10^{-6}$)



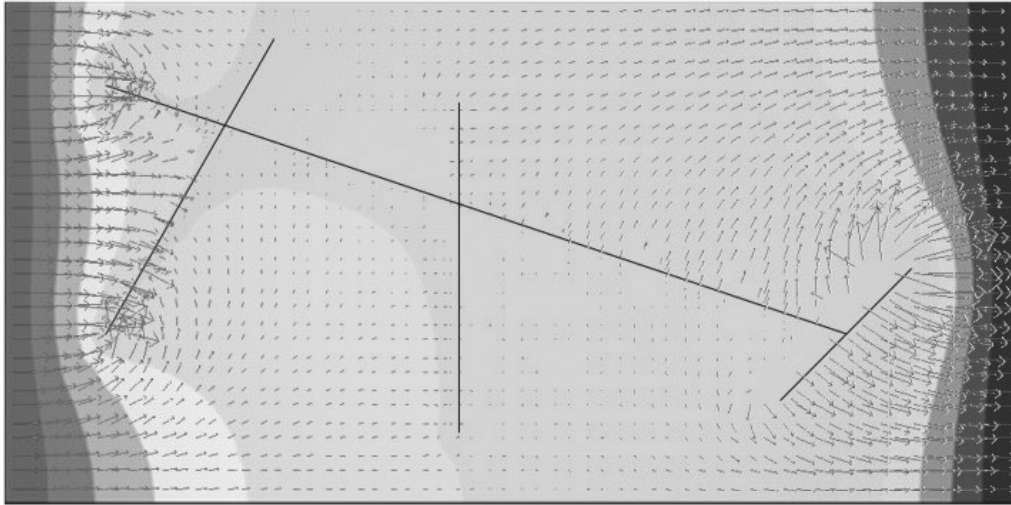
Section A-A



Section B-B

Figure 5.12 – Pore-pressures in sections A-A and B-B

Case 1 ($c = 10^{-7} \parallel w_{init} = 2 \times 10^{-3}$)



Case 4 ($c = 10^{-12} \parallel w_{init} = 2 \times 10^{-6}$)

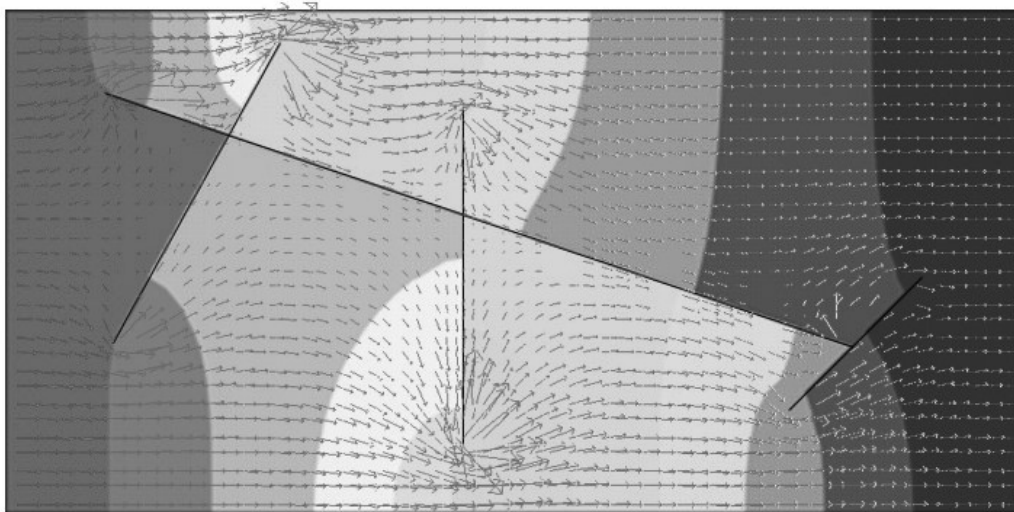


Figure 5.13 – Flow vectors along the model

5.2.4. Consolidation in a fractured medium

General description of the simulation

In this model, a distributed uniform load is applied at the top of the model while the pressure is imposed to be zero in the same border. All the physics are considered and coupled: displacements, pore-pressures and fracture pressures, obtaining a transient regime. The displacement boundary conditions are set to the model to represent a unidimensional consolidation problem. However, four randomly orientated and intersected fractures exist in the model. Four calculations are performed with variation of the fracture face transversal conductivity and the

fracture hydraulic aperture. The results are compared with a model with interface elements generated and run in the software GeMA (Mendes, Gattass and Roehl, 2016).

Model geometry and mesh

This model has the same geometry as the one presented in Chapter 5.2.3. The model's dimensions are 30 m x 15 m and the mesh is regular with 30 and 15 elements in the horizontal and vertical directions, respectively, as seen in Figure 5.14. The fractures have different orientations and lengths that were defined randomly.

Figure 5.15 shows the mesh used in the GeMA simulation, with the interface elements represented in red. The mesh was generated by the software Sigma2D (Miranda and Martha, 2017) and total of 1382 elements are used, where 73 are 4-node two-dimensional cohesive elements and 1309 are 4-node bilinear displacement and pore pressure elements.

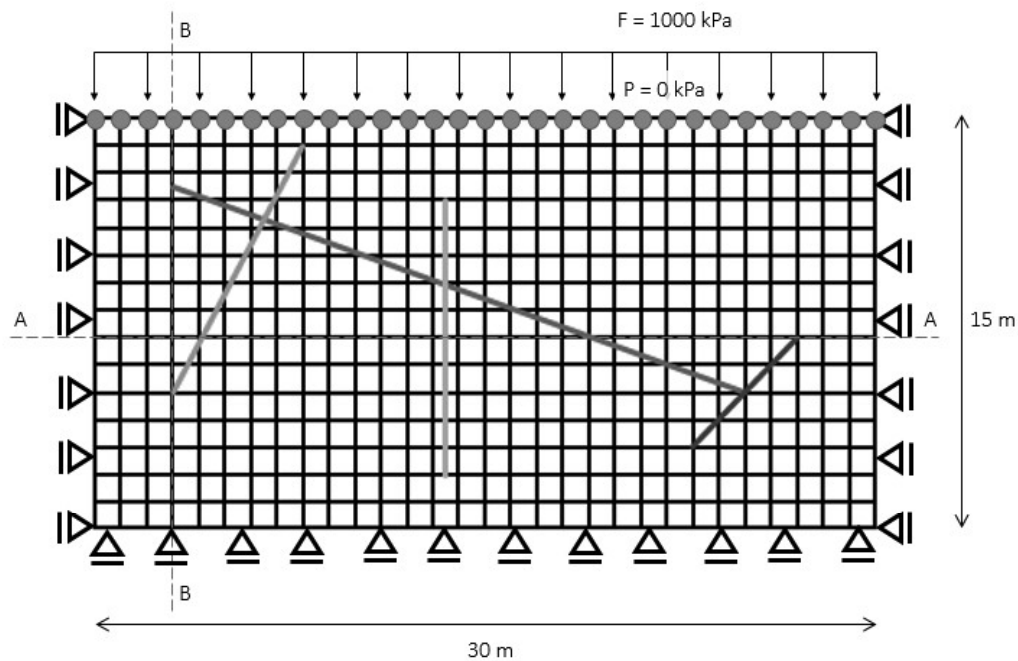


Figure 5.14 – Geometry of the mesh and boundary conditions

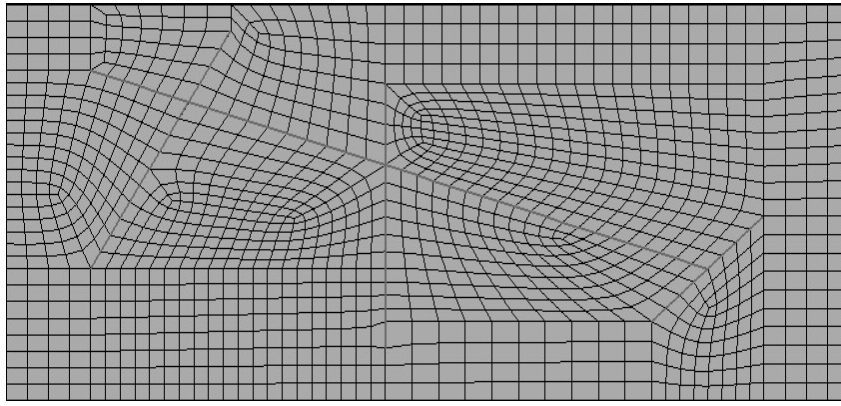


Figure 5.15 – Geometry of the mesh of GeMA with interface elements model

Material properties

The hydraulic properties both for the porous region and the fractures are presented in Table 5.6. An isotropic hydraulic conductivity is used in the porous medium. The fracture face transversal conductivity and initial hydraulic apertures are the same for every fracture in each of the calculations and the variation between analyses is similar to the one presented in Chapter 5.2.3. As this model contemplates deformations, the hydraulic aperture changes during the simulation.

Table 5.7 – Hydraulic properties

	Parameter	Case 1	Case 2	Case 3	Case 4
Porous Region	Hydraulic conductivity: $k = k_x = k_y$ (m/s)	10^{-8}			
Fracture	Fracture face transversal conductivity: $c = c_{top} = c_{bottom}$ (m/s.kPa ⁻¹)	10^{-7}	10^{-7}	10^{-14}	10^{-14}
	Initial hydraulic aperture (m)	2×10^{-3}	2×10^{-6}	2×10^{-3}	2×10^{-6}
	Fluid Viscosity (kPa.s)	10^{-6}			

The mechanical properties of the porous region are defined in Table 5.8. The fractures have a traction free behaviour. However, if subjected to compression, the contact between faces is modelled.

Table 5.8 – Mechanical properties

	Parameter	Case 1	Case 2	Case 3	Case 4
Porous Region	E (kPa)	40×10^3			
	ν	0,3			

Boundary and loading conditions

To simulate an effect similar to a unidimensional consolidation problem the bottom border of the model is fixed in the vertical direction, while the right and left borders are restrained to horizontal displacements. The displacement of the model is guaranteed by a uniform distributed load of 1000 kPa in the top border. As for hydraulic boundary conditions, the top border is fixed to a pressure of 0 kPa.

The previous mentioned boundary conditions are applied in a first step with a time interval of 10^{-7} s. This very small time interval may be considered as an instantaneous application of the load, guaranteeing that consolidation practically does not occur during the step.

The loads and boundary conditions are then kept constant for 50 varying time intervals, while consolidation occurs.

Results

Figure 5.16 shows the pore-pressure fields for the four simulations at the same time ($t = 95 \times 10^5$ s), as well as the results obtained using GeMA with interface elements. Figure 5.17 presents the values of the pore-pressures along the sections A-A and B-B (defined in Figure 5.14). It is easily noticeable from both figures that the XFEMHF simulations show a very good agreement with the GeMA built-in with interface elements.

Similarly to Chapter 5.2.3, a very simple sensitivity analysis of two parameters – fracture longitudinal transmissibility and fracture face transversal conductivity – shows the strong influence that these have in the pressure fields and model behaviour.

The calculation with higher values of fracture transversal and longitudinal transmissibility (Case 1: $c = 10^{-7}$ || $w_{init} = 2 \times 10^{-3}$) shows that when both permeabilities are high, then fluid easily flows to the fractures, which have an effect of “drainage canals”. The fluid from the porous region tends to flow to the fracture, reducing the pore pressures drastically in the vicinity of the fractures. Figure 5.18

shows how the fractures work as drains, collecting fluid from the more pressurized regions to as near as closer to the top border. This effect also proves that the fracture intersections are capable of transmitting the fluid flow between different fractures. This way, it should be expected that with influence of the “drains”, the consolidation occurs faster than in a standard unidimensional consolidation, as seen in Figure 5.19

In Case 2 ($c = 10^{-7}$ || $w_{init} = 2 \times 10^{-6}$), the longitudinal transmissibility is reduced by means of the fracture aperture. Keeping a higher transversal conductivity, the flow easily enters or leaves the fractures. However, the drainage effect related with the longitudinal flow no longer occurs, due to the reduction of longitudinal transmissibility. This way, the flow crosses the fractures but does not enter in this preferential path, keeping the same direction in the porous region. The lack of influence of the fractures is visible in Figure 5.19, as the curve for this calculation overlaps the standard unidimensional consolidation solution.

In Case 3 ($c = 10^{-14}$ || $w_{init} = 2 \times 10^{-3}$) and Case 4 ($c = 10^{-14}$ || $w_{init} = 2 \times 10^{-3}$) it is shown that the reduction of the fracture face transversal conductivity decreases the transversal conductivity to a point that the flow is no longer capable of entering the fractures. Therefore, the fractures represent a barrier and the fluid has to deviate to continue to flow along the porous region. As seen in Figure 5.18, the flow is almost inexistent under the group of fractures. Despite the difference in the longitudinal transmissibility between Case 3 and Case 4, there is no significant difference in the results, as the flow does not flow along the fractures. The influence that the reduction of fracture transversal flow has in the model is visible in Figure 5.19, as the time vs deformation curve shows that in Case 3 and 4 the sample takes more time to consolidate.

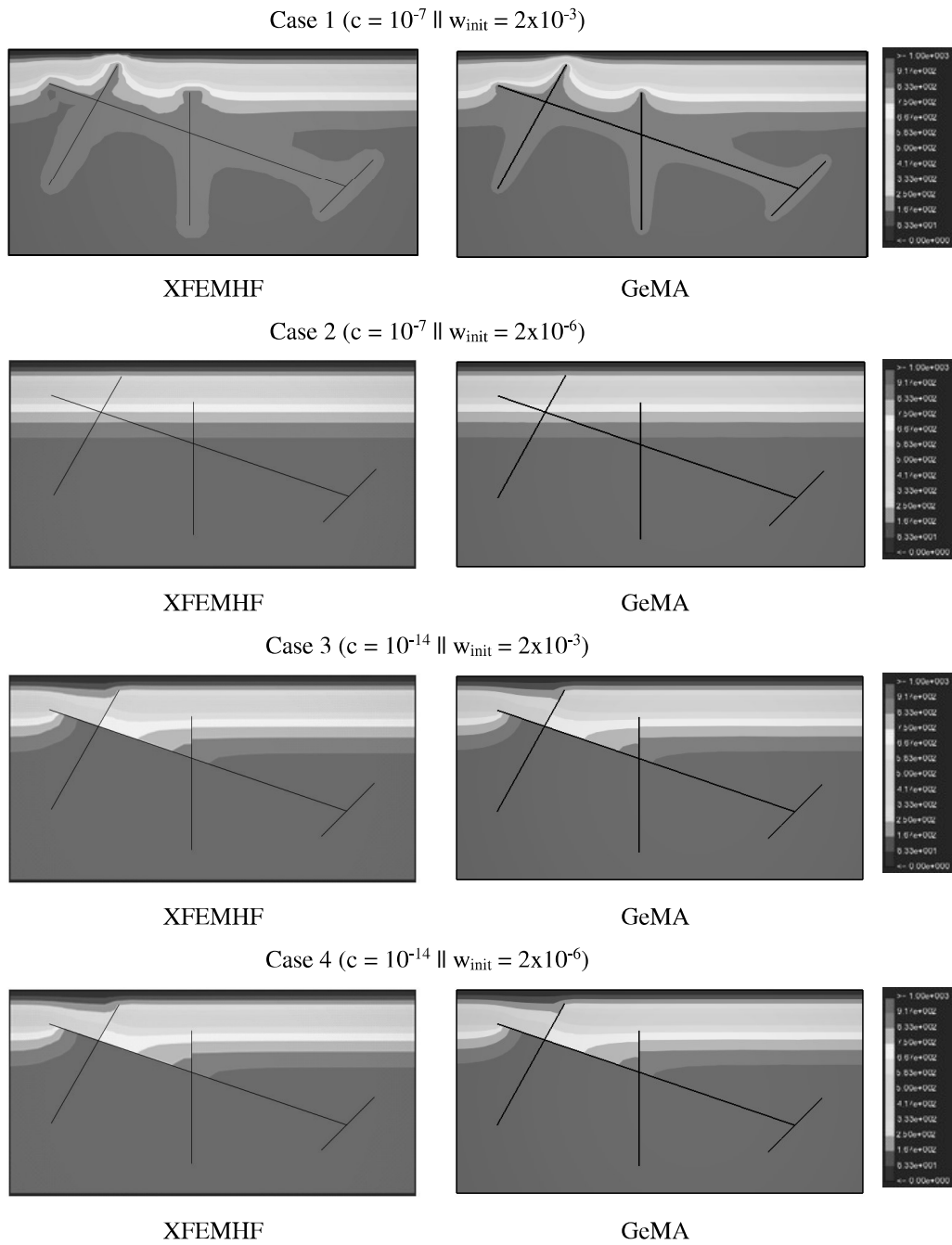
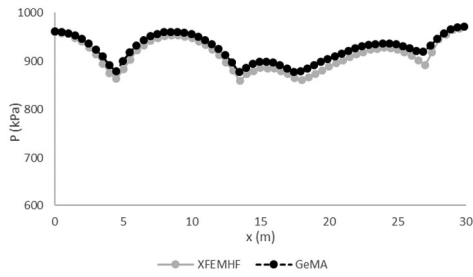
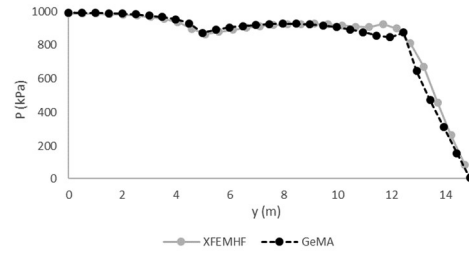


Figure 5.16 – Pore-pressure fields at time 95×10^5 s

Case 1 ($c = 10^{-7} \parallel w_{init} = 2 \times 10^{-3}$)

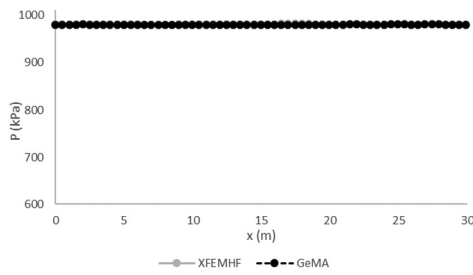


Section A-A

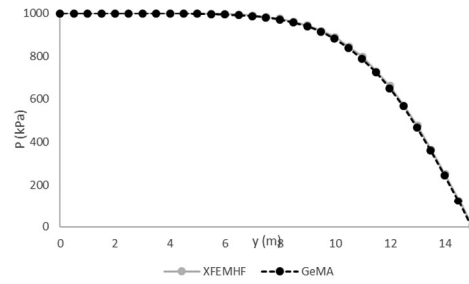


Section B-B

Case 2 ($c = 10^{-7} \parallel w_{init} = 2 \times 10^{-6}$)

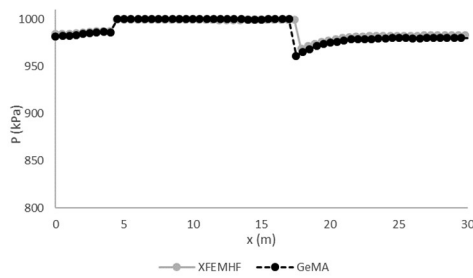


Section A-A

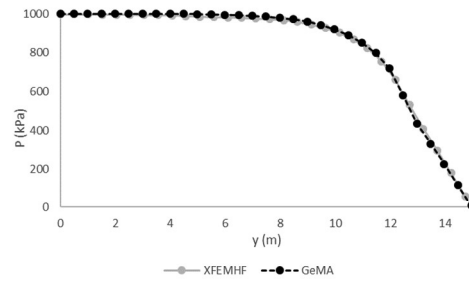


Section B-B

Case 3 ($c = 10^{-14} \parallel w_{init} = 2 \times 10^{-3}$)

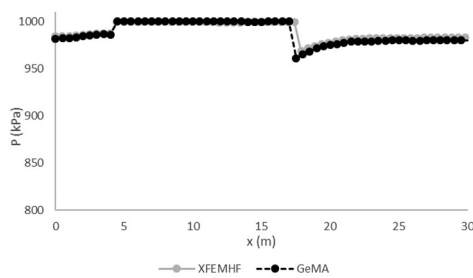


Section A-A

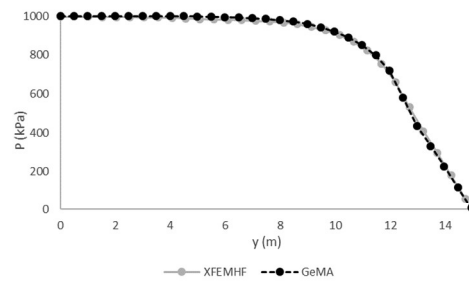


Section B-B

Case 4 ($c = 10^{-14} \parallel w_{init} = 2 \times 10^{-6}$)

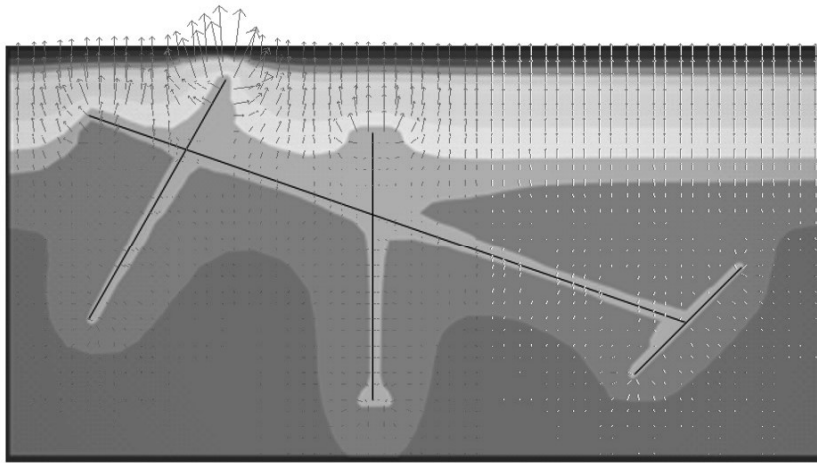
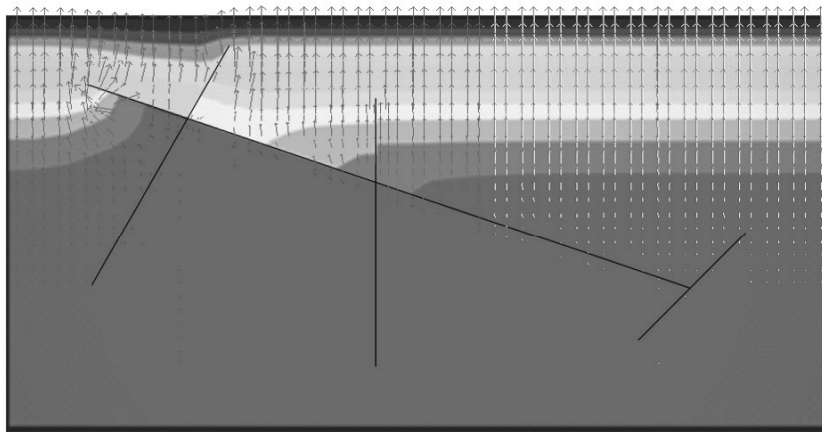
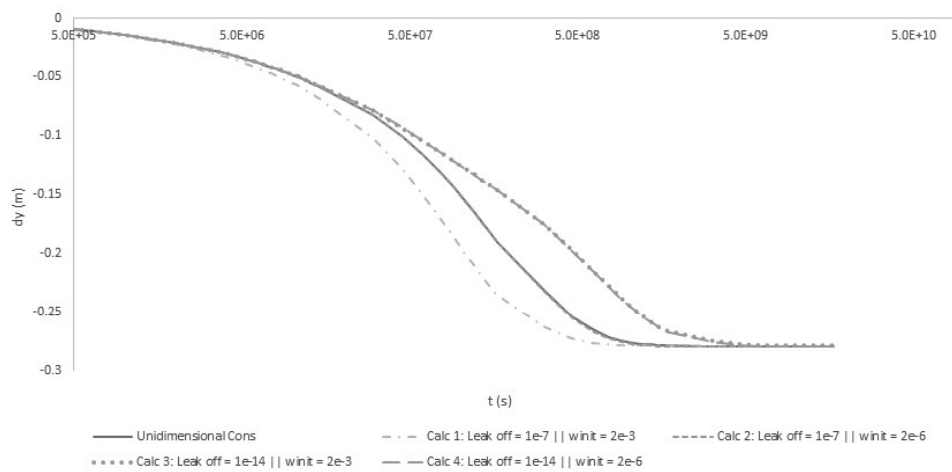


Section A-A



Section B-B

Figure 5.17 – Pore-pressures in sections A-A and B-B at time 95×10^5 s

Case 1 ($c = 10^{-7} \parallel w_{init} = 2 \times 10^{-3}$)Case 4 ($c = 10^{-14} \parallel w_{init} = 2 \times 10^{-6}$)**Figure 5.18 – Flow vectors along the model at time 95×10^5 s****Figure 5.19 – Vertical displacement in the top border's mid-point for all four analyses with XFEMHF**

5.3. Contact and friction

5.3.1. Single element with horizontal fracture

5.3.1.1. Vertical cyclic load

General description of the simulation

The objective of this simulation is to show in a simplistic manner how the implemented contact model works. A cyclic prescribed displacement is applied in the top of a single element with one horizontal fracture and the fracture behaviour depends on its relative position. If the fracture faces touch each other, contact exists. If not, fracture faces move independently. In this simulation only mechanical degrees of freedom are used.

Model geometry and mesh

The model has a single square element with dimensions 1,0 m x 1,0 m, as seen in Figure 5.20. The fracture is horizontal at half-height of the element.

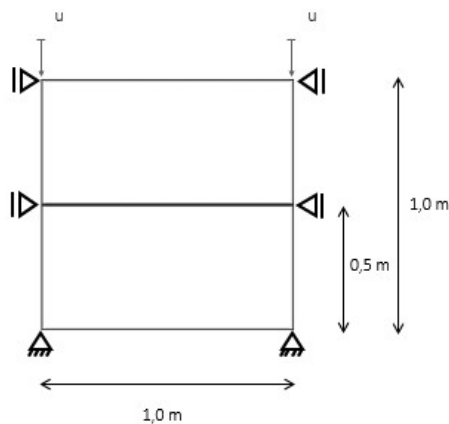


Figure 5.20 – Geometry of the mesh and boundary conditions

Material properties

The mechanical properties of the solid region are defined in Table 5.9. The fractures have a traction free behaviour. However, if subjected to compression, the contact between faces is modelled using a penalty parameter of 10^{11} kPa.

Table 5.9 – Mechanical properties

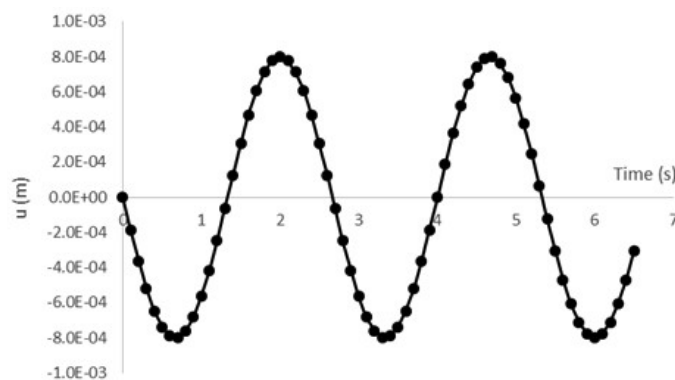
	Parameter	Value
Solid Region	E (kPa)	10^6
	ν	0,3

Initial conditions

To assess the effect of initial stresses in the contact behaviour, two distinct calculations are made, one without initial stresses and other with an initial vertical stress of 500 kPa.

Boundary and loading conditions

The boundary conditions are set in order that only vertical displacements occur in the model, as seen in Figure 5.20. A prescribed vertical displacement at the top of the model, u , is applied in 65 increments of a fixed length of 1 second each and follows the sinusoidal function presented in Figure 5.21. It must be reminded that, although the notion of time is used, the calculation in each increment is static.

**Figure 5.21 – Prescribed vertical displacement at the top of the model****Results**

The results show that the contact model simulates the effect of contact between faces correctly. Figure 5.22 shows a set of frames taken from the deformed mesh at the end of 8 increments, with the undeformed mesh being represented by grey dashed lines. In both models it is visible that when contact exists in the fracture faces, the compression in the continuous region is transmitted and the whole model

deforms monolithically (see $t = 0,3$ s and $t = 2,9$ s). It is also noticeable that when the fracture faces are not in contact, the upper half of the model translates vertically without affecting the lower half (see $t = 1,6$ s, $t = 2,0$ s and $t = 2,6$ s). The main difference between the simulations with and without in-situ stress is visible in increment $t = 1,4$ s. In the case without in-situ stress, a positive displacement at the top of the model results in an opening of the fracture. On the other hand, when in-situ stresses exist, the before fracture opening the model expands to relieve the initial stresses. This way, as seen in $t = 1,4$ s the two element halves are still in contact and therefore the fracture opening will be smaller.

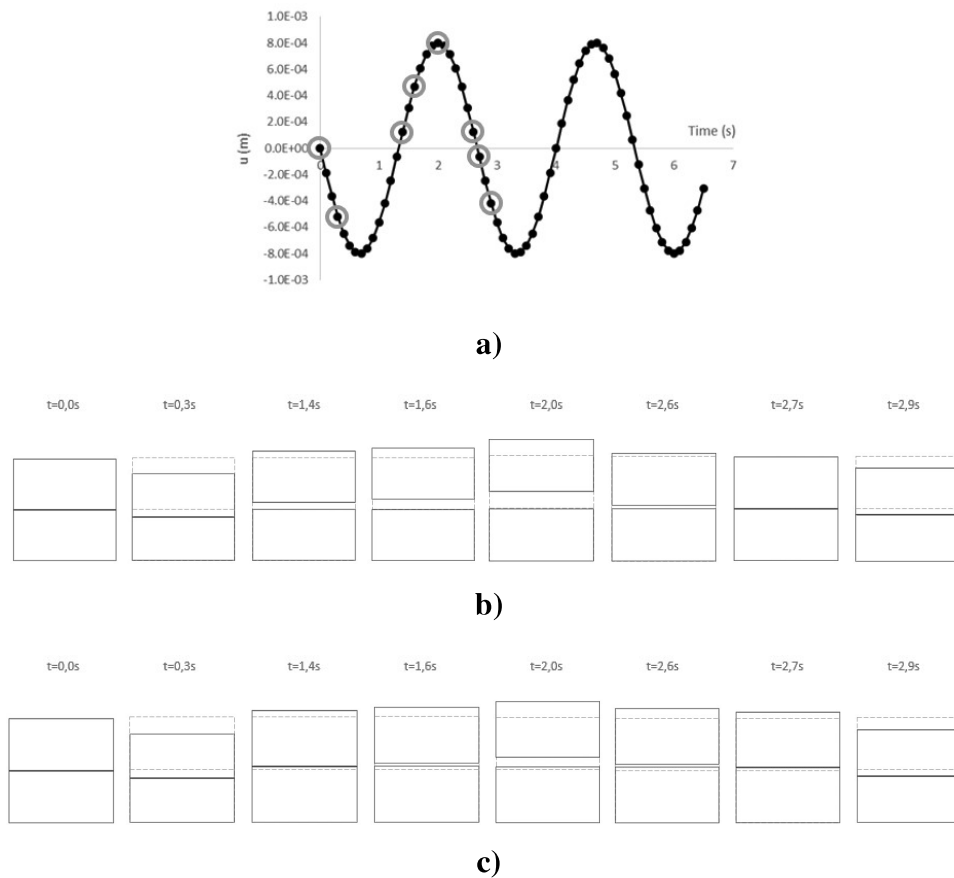
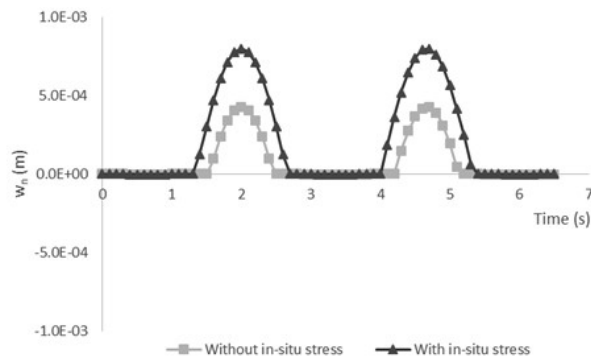


Figure 5.22 – Deformed mesh at the end of 8 increments. a) Time increments represented. b) Model without in-situ stress. c) Model with in-situ stress of 500 kPa

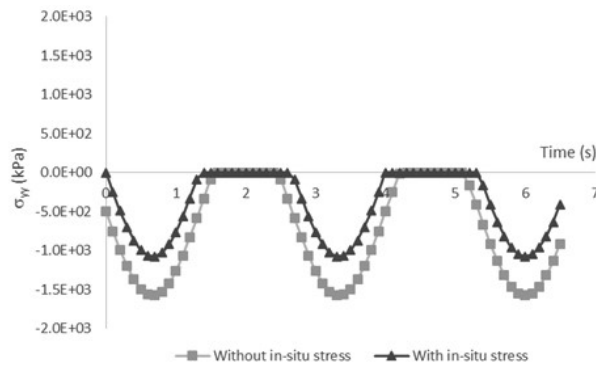
Figure 5.23 gives further insight about the contact behaviour. As expected, while in compression, the fracture opening assumes a very small negative value, which can be considered zero, i.e. the fracture faces are in contact. When the fracture faces move apart, there is no stress transmission between the two halves of

the model. Consequently, the vertical stress in the continuous region is reduced to zero.

As stated previously, the expansion due to the stress relief in the model with initial stresses results in a smaller fracture opening (see Figure 5.23a). Therefore, the contact and the compressive stresses in the model occur in longer periods, as seen in Figure 5.23b.



a)



b)

Figure 5.23 – Fracture opening (a) and vertical stress in the continuous region (b)

Finally, it is visible in Figure 5.24 that the initial normal stress in the fracture is correctly computed, as a value of 500 kPa is obtained in the first increment of Figure 5.24b. It may also be stated that the penalty method correctly represents the effect of compression when in contact and a stress-free situation when the fracture opens.

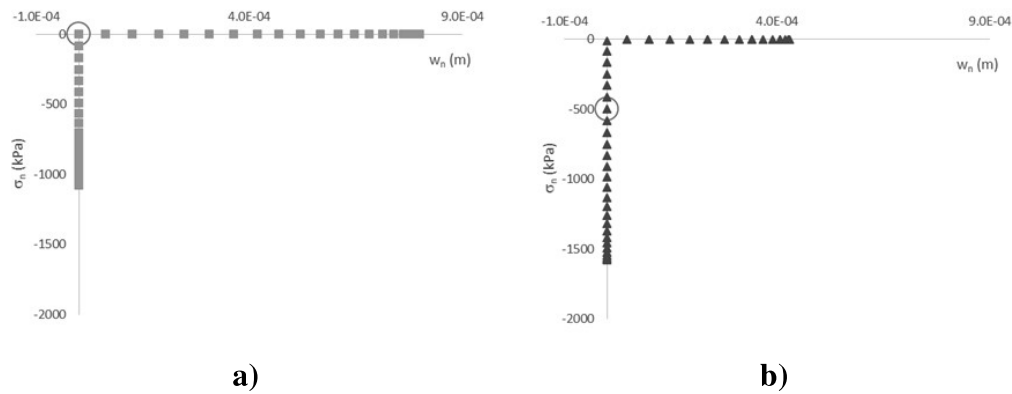


Figure 5.24 – Fracture opening vs Normal stress in the fracture for every increment (grey circle points the first increment). a) Simulation without in-situ stress. b) Simulation with in-situ stress

5.3.1.2. Horizontal load

General description of the simulation

This model shows how the implemented contact and friction models work. A horizontal prescribed displacement is applied in the upper half of a single element with one horizontal fracture. The boundary conditions are defined in a way that only shear stress occur, and different initial stress conditions are defined to confirm the effect that confinement has in shear strength.

Model geometry and mesh

The model has a single square element with dimensions 1,0 m x 1,0 m, as seen in Figure 5.25. The fracture is horizontal at half-height of the element.

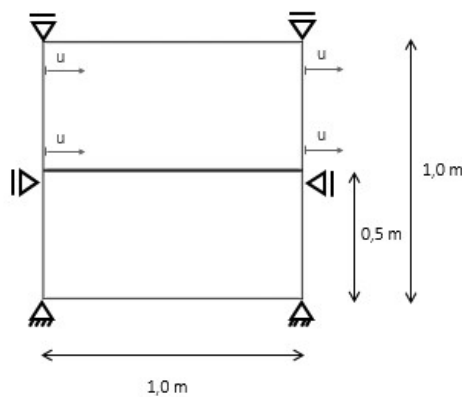


Figure 5.25 – Geometry of the mesh and boundary conditions

Material properties

The mechanical properties of the solid region and the fracture are defined in Table 5.10. The fracture has a friction behaviour given by the Mohr Coulomb model. A non-associated law is used, i.e. no dilatation occurs due to shear deformations.

Table 5.10 – Mechanical properties

	Parameter	Value
Solid Region	E (kPa)	10^6
	ν	0,3
Fracture	K_n (kPa)	0^{**}
	K_s (kPa)	10^7
	ϕ' (°)	35
	c' (kPa)	0

**value in traction. In compression, a penalty factor is applied

Initial conditions

To assess the effect of the confinement stresses in the friction behaviour, six distinct initial stresses are defined, as seen in Table 5.11.

Boundary and loading conditions

The defined boundary conditions (see Figure 5.25) fix the lower half of the model in every direction, while the upper half is only able to translate horizontally. After a first step for definition of initial stress, a horizontal displacement is prescribed and subdivided in 20 increments. In the first three tests a positive displacement is applied, while in the other three tests a negative value is used, as seen in Table 5.11.

Table 5.11 – Prescribed horizontal displacement and initial vertical stress

	Initial vertical stress (kPa)	Prescribed horizontal displacement (m)
Test 1	-1346,1	5×10^{-4}
Test 2	-2692,3	5×10^{-4}
Test 3	-4038,4	5×10^{-4}
Test 4	-673,1	-5×10^{-4}
Test 5	-2019,2	-5×10^{-4}
Test 6	-3365,3	-5×10^{-4}

Results

In the deformed mesh presented in Figure 5.26 it is visible that only translation between both parts of the model occurs. Figure 5.27 shows the resulting shear stress in the fracture. As expected, the fracture behaves elastically initially and when failure occurs it deforms at constant shear stress. It is also visible that the value for which the failure is reached changes for each confinement stress.

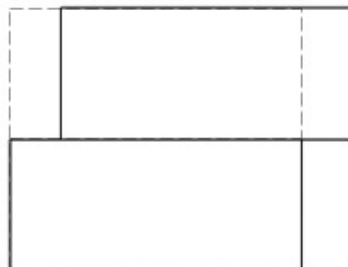


Figure 5.26 – Deformed mesh

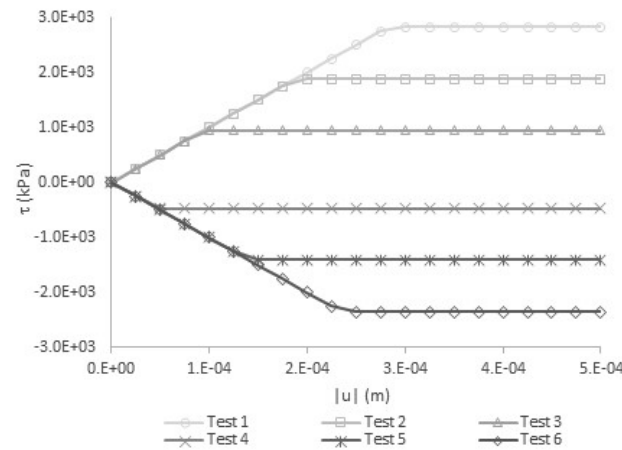


Figure 5.27 – Horizontal displacement versus shear stress in the fracture

In Figure 5.28, the normal and shear stresses in the fracture are plotted, so is the Mohr-Coulomb failure surface (in dashed lines). As only the shear stress varies during the simulations, the stress paths are vertical. It is evident that failure occurs at different shear values, depending on the normal stress, as stated by the Mohr-Coulomb constitutive law.

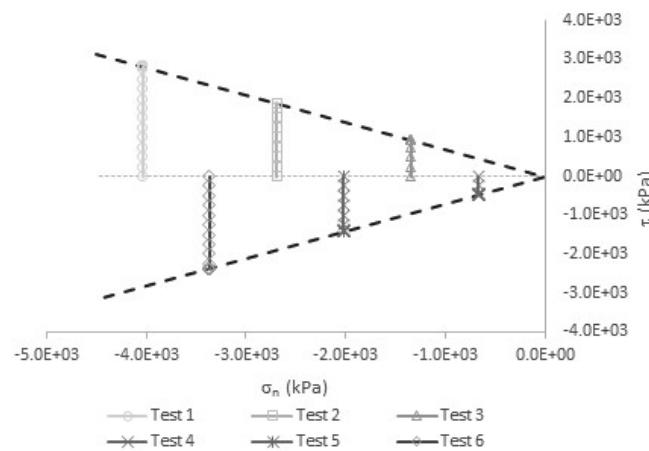


Figure 5.28 – Normal stress versus shear stress in the fracture

5.3.2. Single element with inclined fracture

General description of the simulation

As stated by several authors (Jiao and Qiao, 2008; Das, 2013; Esterhuizen, 2014), the results of a uniaxial compression test of a sample with a single fracture are strongly dependent on the fracture inclination. In order to simulate that effect, a model with a single element and one inclined fracture is subjected to uniaxial

compression so the uniaxial strength is obtained for different fracture inclinations and compared with the analytical solution.

The analytical strength of a single fractured sample subjected to uniaxial stress may be obtained by the Mohr-Coulomb equation, as presented by Das (2013). The equation is given by

$$\sigma_1 = \frac{2 \cdot c}{(1 - \tan \varphi \cdot \cot \beta) \sin 2\beta} \quad (5.2)$$

where c is the fracture cohesion, φ the friction angle and β the fracture angle with the horizontal. This solution is only valid for values of the inclination angle between φ and 90° , where it takes values of infinite. Therefore, it is assumed that the intact rock strength is 20 MPa so the fracture influences the results in a range between 36° and 84° . Moreover, the lowest strength is achieved for a fracture angle of $\pi/4 + \varphi/2$.

Model geometry and mesh

The model has a single rectangular element with dimensions 0,1 m x 0,01 m, as seen in Figure 5.29. A high height-width ratio is used in order to be sure that for all the tested inclinations the fracture crosses the element in the vertical boundaries. This way, different influence of the boundary conditions for different inclinations is avoided. Although it is widely known that such ratios are not recommended, it is considered that in this simple model it does not affect the results.

The fracture left extremity position is constant, while the right extremity changes with the fracture inclination. Seven different inclinations are tested: 37° , 40° , 50° , 60° , 70° , 80° and 83° .

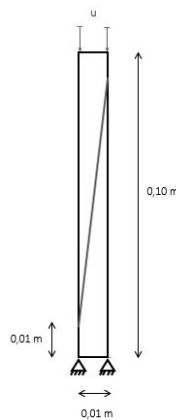


Figure 5.29 – Mesh and boundary conditions

Material properties

The mechanical properties of the solid region and the fracture are defined in Table 5.12. The fracture has a friction-cohesive behaviour given by the Mohr Coulomb model. A non-associated law is used, i.e. no dilatation occurs due to shear deformations.

Table 5.12 – Mechanical properties

	Parameter	Value
Solid Region	E (kPa)	5×10^6
	ν	0,25
Fracture	K_n (kPa)	0 ^{**}
	K_s (kPa)	10^8
	ϕ (°)	30
	c (kPa)	2000

^{**}value in traction. In compression, a penalty factor is applied

Boundary and loading conditions

As seen in Figure 5.29, the model is fixed in its bottom and a prescribed displacement is applied at its top until failure occurs.

Results

Figure 5.30 shows that the obtained results match with the analytical solution. As expected, the fracture inclination affects the uniaxial strength in a range between 36° and 84° . As the inclination increases from 36° , the strength reduces reaching its bottom value at 60° , such as predicted by the Mohr-Coulomb model ($\pi/4 + \phi/2 = 60^\circ$). Figure 5.31 presents the fracture stress paths (normal and shear stresses) for the different inclinations. It is noticeable that failure occurs when the Mohr-Coulomb surface is reached and that the values of normal and shear stress at failure increase with a decrease of fracture inclination. This happens because lower inclinations imply higher normal stresses and consequently higher shear strength.

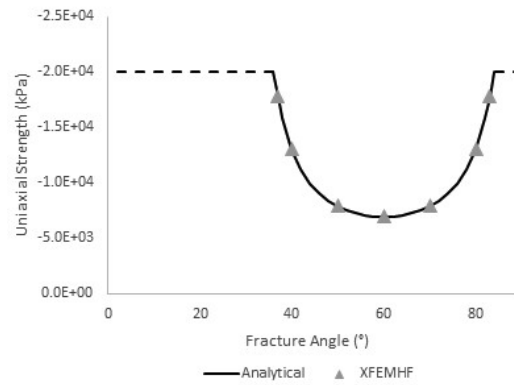


Figure 5.30 – Uniaxial strength variation with fracture inclination
(assumed rock intact strength is plotted in dashed lines)

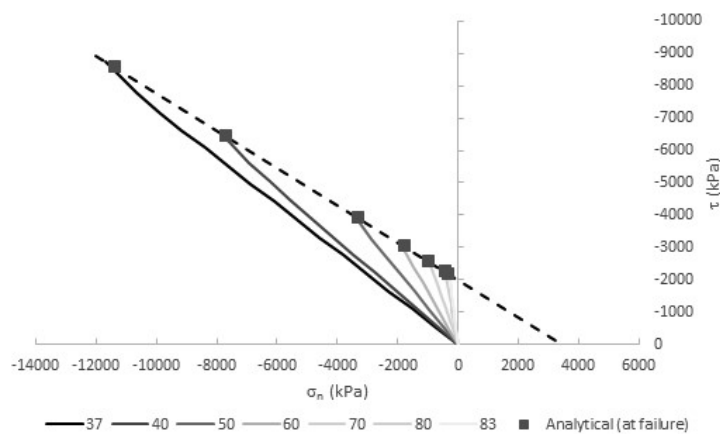


Figure 5.31 – Fracture stress paths for different fracture inclinations

5.3.3. Multi-fractured medium

General description of the simulation

In this simulation, a sample with three intersecting fractures is subjected to a uniaxial compression at its top until failure is reached. As there is no analytical solution for this problem, the objective of this simulation is to assure that no fracture point crosses the failure surface defined by the Mohr-Coulomb model.

Model geometry and mesh

The model's dimensions are 15 m x 20 m and the mesh is regular with 15 and 20 elements in the horizontal and vertical directions, respectively, as seen in Figure

5.32. Three fractures are positioned in the sample in a way that two intersections occur.

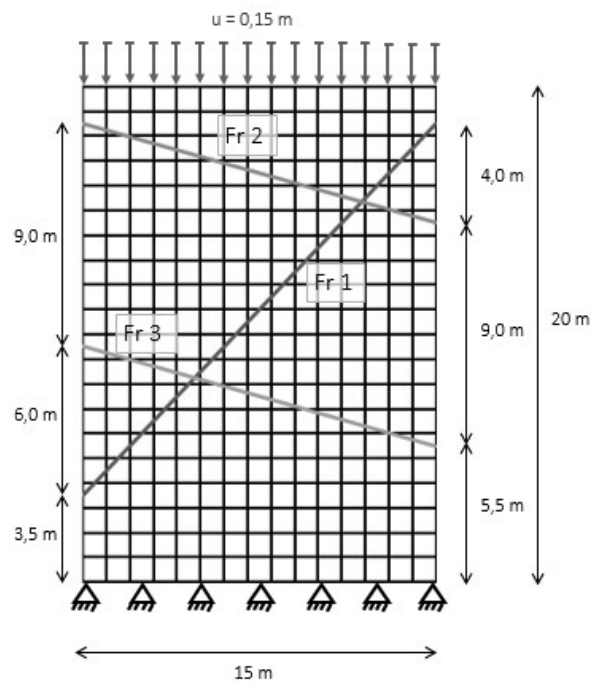


Figure 5.32 – Mesh and boundary conditions

Material properties

The mechanical properties of the solid region and the fractures are defined in Table 5.13. The fractures have a friction-cohesive behaviour given by the Mohr Coulomb model. A non-associated law is used, i.e. no dilatation occurs due to shear deformations.

Table 5.13 – Mechanical properties

	Parameter	Value
Solid Region	E (kPa)	10^6
	ν	0,3
Fractures	K_n (kPa)	0**
	K_s (kPa)	10^5
	ϕ (°)	25
	c (kPa)	0

**value in traction. In compression, a penalty factor is applied

Boundary and loading conditions

As seen in Figure 5.32, the model is fixed in its bottom and a prescribed displacement of 0,15 m separated in 40 increments is applied at its top. Each increment size is defined by Abaqus automatic time incrementation algorithm, which reduces the increment size when convergence is harder to achieve and increases the increment size when few iterations are needed to converge.

Results

The simulation returned the expected behaviour of the model when subjected to the uniaxial load. In the deformed meshes at the end of two increments present in Figure 5.33 it is visible that relative movement between fracture faces occurred in every fracture.

Along the model there is no noticeable superposition of faces, except in the intersections (highlighted by grey dashed circumferences). This is an expected limitation of the model, as explained in Chapter 3.6.1.

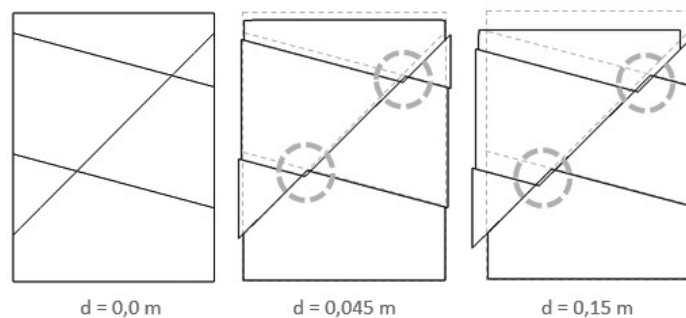


Figure 5.33 – Deformed mesh in different increments

Figure 5.34 shows the curve displacement-reaction at the top of the model. Although the Mohr-Coulomb model has an elastic-perfectly plastic constitutive behaviour, the whole model reacts with a stronger non-linearity due to the geometric position of the fractures.

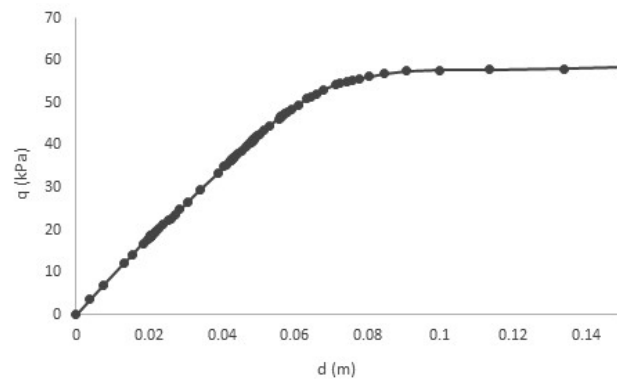


Figure 5.34 – Prescribed displacement vs reaction at the top of the model

Figure 5.35 presents the stress state in every fracture integration point of the model for each of the 3 fractures separately (see Figure 5.32 for each fracture number). Right after the first increment (Figure 5.35a), it is noticeable that even subjected to normal stress, all fractures are still in the elastic region. At an intermediate increment (Figure 5.35b), the shear stresses acting in the fractures increases. Shear stresses in fractures 1 and 2 take positive signs while fracture 3 has mostly negative values, as expected, due to each fracture inclination. It is also visible in Figure 5.35b that fracture 3 already has part of it in a failure situation. Finally, in the last increment of the simulation Figure 5.35c all the points in fracture 3 are in failure. Given that fracture 3 crosses the model from one side to the other, this corresponds to a generalized failure, as visible in Figure 5.34.

From the obtained results, it is noticeable that after reaching failure, deformation occurs at constant stress, so it may be concluded that all the fractures are modelling correctly the implemented contact-friction behaviour.

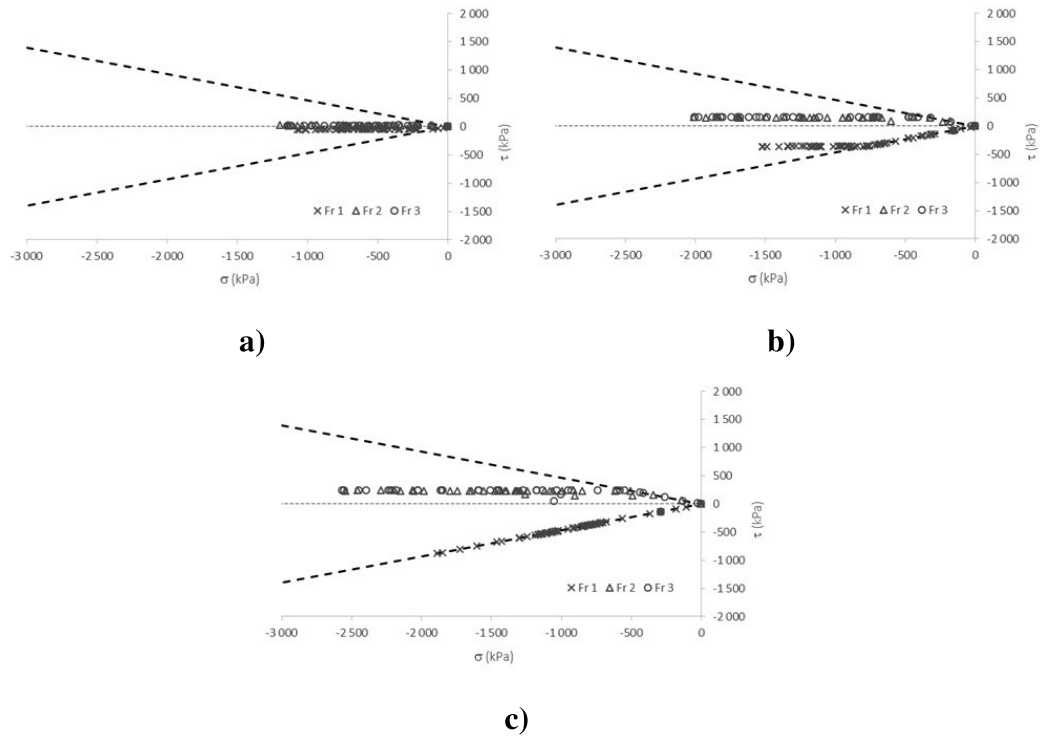


Figure 5.35 – Fracture stress state (normal and shear stresses) for every fracture integration points of the model. a) $d = 0,002$ m. b) $d = 0,045$ m. c) $d = 0,15$ m.

6 Applications

A group of tests was defined in order to prove the applicability of the developed tool. This chapter presents the characteristics of the models, as well as the results, comparisons and discussion regarding the advantages and limitations of the implemented code.

In the first part of the Chapter, modelling of laboratory situations is carried out to study the intersections between hydraulic and natural fractures. Four research works mentioned in the literature review (Chapter 2.2.2) are used as basis for the simulation and the published laboratory results are compared with the numerical modelling.

In the second part, a more complex situation is modelled, by considering multiple and intersecting natural fractures in a synthetic model. A sensitivity analysis is also performed in order to understand the effect that two parameters have in the model behaviour.

Finally, a different application is tested. The percolation under a dam foundation is modelled and a comparison with existing results in the literature is made. Additionally, an analysis of the influence that fracture location and aperture may have in the hydraulic behaviour of the foundation is carried out.

6.1. Comparison with laboratory tests

6.1.1. Blanton tests

General description of the simulation

As stated in the Literature Review (Chapter 2.2.2), Blanton (1982) performed a group of laboratory tests, demonstrating the applicability of some analytical formulations to predict what happens when a hydraulic fracture intersects a natural fracture. The research work includes 11 laboratory tests in hydrostone where the natural fracture orientation and the confining stresses vary, with the results shown

in Figure 2.8. In this research, four different natural fracture angles of approach and six different differential stresses are combined, in order to represent the 11 laboratorial tests.

As there is no allusion to conductivity parameters in the reference paper, the hydrostone is considered to be impermeable, i.e., only displacements and fracture pressures are computed.

A qualitative analysis of the results is made, by checking the type of interaction that occurs between fractures and comparing it with the laboratory tests.

Model geometry and mesh

The same geometry is used for all simulations, with a 0,0305 m x 0,0305 m square model divided in a 51x51 element grid. Figure 6.1 shows the mesh used in the analyses with two different orientations for the natural fracture, 60° and 90°. The small circular perforation of the laboratory specimens is represented by a small initial fracture.

Material properties

The material properties are presented in Table 6.1 and Table 6.2. As the samples were created in laboratory, the roughness is expected to be very low, so a value of the initial hydraulic aperture of 1×10^{-6} is adequate. The fracture parameters were not provided by Blanton (1982), so a friction coefficient of 36,9° and cohesionless behaviour are assumed to be suitable. The tangential stiffness before plastification, i.e., for very small relative displacements and high compression stresses, takes the value 1×10^{10} kPa. A non-associated law is used, i.e. no dilatation occurs due to shear deformations.

Initial conditions

The laboratory tests were made applying different combination of confinement pressures so these are also taken into account in the numerical models, by means of a geostatic step. The applied in-situ stresses are presented in Table 6.3. Considering that in every numerical model the propagation is horizontal, the maximum and minimum stresses are applied in the horizontal and vertical directions, respectively.

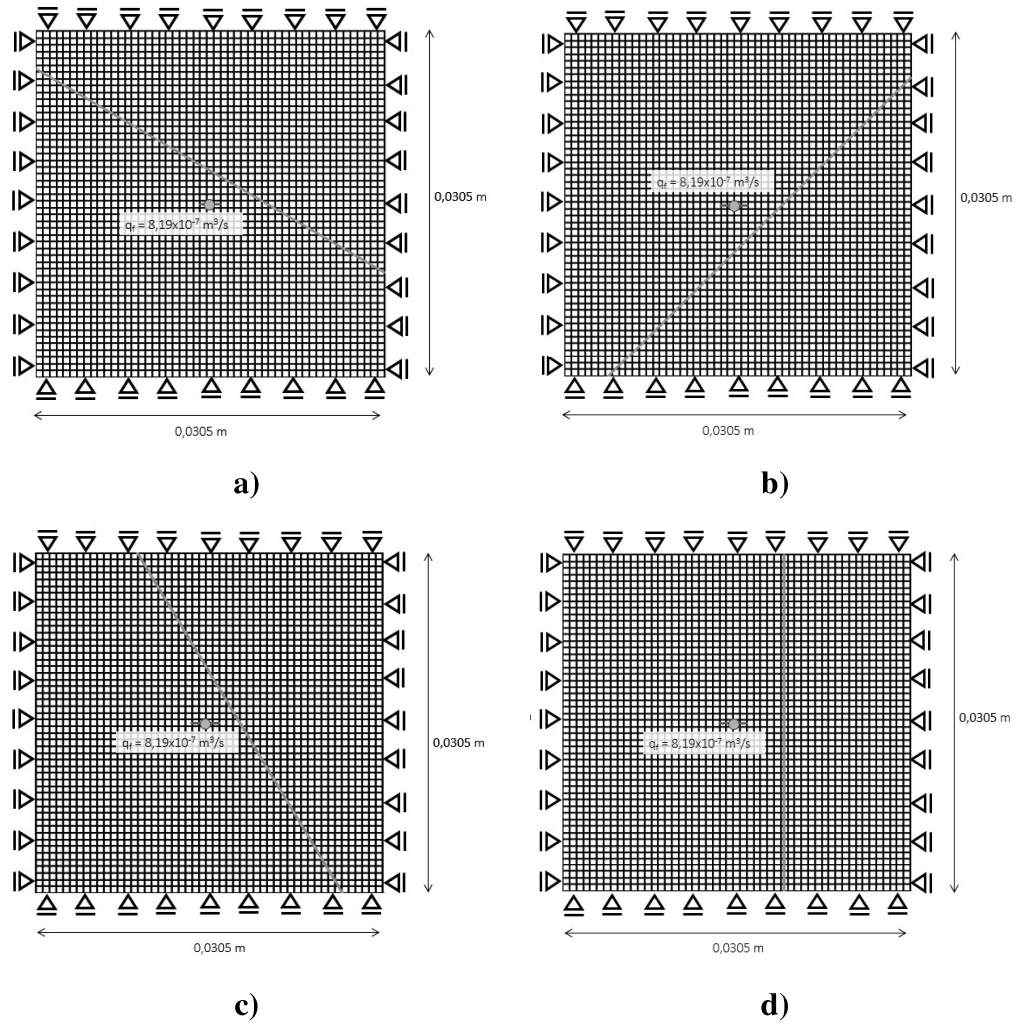


Figure 6.1 – Models used to simulate the different fracture orientations.

a) 30°. b) 45°. c) 60°. d) 90°

Table 6.1 – Hydraulic properties

	Parameter	All Models
Fractures	Initial hydraulic aperture (m)	$1 \times 10^{-6} *$
	Fluid Viscosity (kPa.s)	10^{-6}

*assumed value

Table 6.2 – Mechanical properties

	Parameter	All Models
Porous Region	E (kPa)	1×10^7
	ν	0,22
	σ_t (kPa)	3100*
Natural Fracture	K_n (kPa)	0**
	K_s (kPa)	$1 \times 10^{10*}$
	ϕ' (°)	36,9*
	c' (kPa)	0*

*assumed values

**value in traction. In compression, a penalty factor is applied

Table 6.3 – In-situ Stresses

Model	σ_{\max} (kPa)	σ_{\min} (kPa)
4	12×10^3	10×10^3
7	19×10^3	10×10^3
8	20×10^3	5×10^3
9	20×10^3	5×10^3
11	20×10^3	5×10^3
12	18×10^3	5×10^3
13	16×10^3	5×10^3
14	16×10^3	5×10^3
20	14×10^3	5×10^3
21	14×10^3	5×10^3
22	10×10^3	5×10^3

Boundary and loading conditions

The contact with the flatjacks is simulated by displacement fixities and the fluid injection in fracture is defined by a prescribed constant volumetric flux of $8,19 \times 10^{-7} \text{ m}^3/\text{s}$ inside the initial hydraulic fracture.

Once the surrounding material is impermeable, the third pressure activation criterion (see Chapter 4.2.3) is used in the natural fracture. This means that when the simulation starts, the natural fracture has its fracture pressure degrees of

freedom deactivated, so its deformations occur without the influence of the vacuum created by the fracture fluid. Then, when the hydraulic fracture intersects the natural fracture, the segments of the natural fracture with an aperture larger than 2×10^{-7} m have the fracture pressure degrees of freedom activated.

Results

Overall, it may be stated that the numerical procedure provided very good agreement with the laboratory tests. Figure 6.2 presents the intersection behaviour observed in each of the 11 models plotted against the laboratory tests. All models except number 8 predicted the intersection behaviour correctly. As expected, the models with lower angles of approach and differential stresses predict opening, while the model with a perpendicular intersection shows crossing. In all the other simulations with intermediate values of angles and differential stresses, the predicted behaviour is arrest.

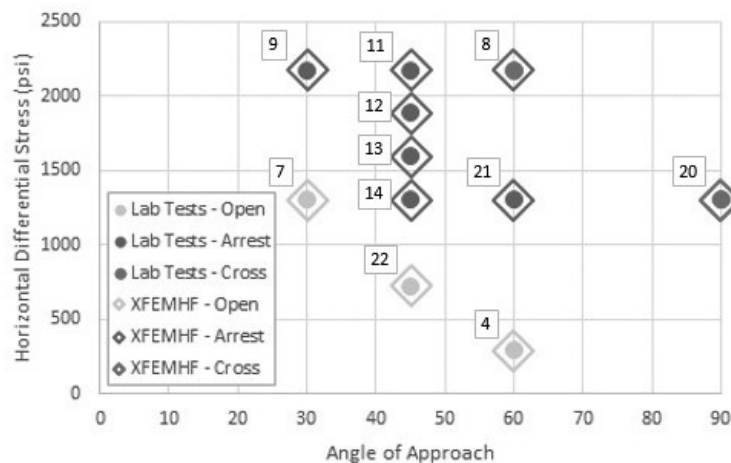


Figure 6.2 – Comparison of the numerical simulations with the laboratory tests numbered according to Blanton (1982)

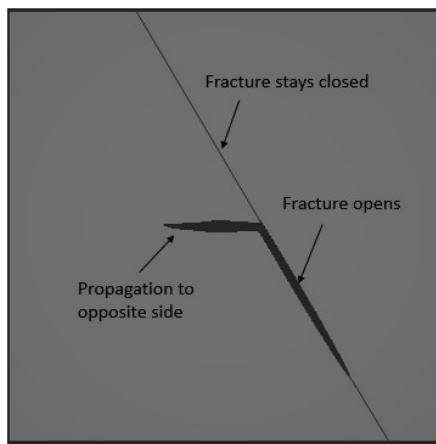
Figure 6.3 shows the deformed models and compares them with pictures of the available laboratory tests. According to the test photos, the author used the same sample to perform two tests, by rotating the applied confining stresses between tests. Thus, the same sample provided two results for different differential stresses and angles. For the sake of clearness, in some occasions the pictures are rotated in order to match the directions used in the numerical models. Lines are also drawn to highlight the hydraulic fracture paths in each laboratory test.

From a more attentive analysis of Figure 6.3 it is noticeable that when opening occurs (models 4, 7 and 22), only half of the pre-existing fracture opens. This is mainly due to the compression that the hydraulic fracture induces in the closer half of the pre-existing fracture. Contrarily, on the other half of the pre-existing fracture tension occurs, leading to its opening. Despite the superposition with the other direction's test, it may be assumed by the picture taken that this occurred in the tests. It should also be noted that when opening events occur the propagation length on the opposite side of the pre-existing fracture tends to be smaller. This is easily understood considering that the fluid is stored in the pre-existing fracture, reducing the pressure inside the hydraulic fracture.

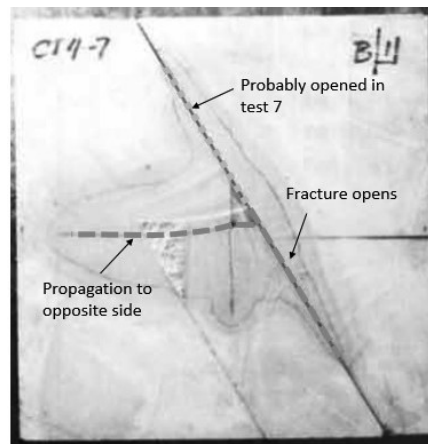
When arrest events occur (models 8, 9, 11, 12, 13, 14 and 21) slight opening may be spotted in the pre-existing fracture. However, the hydraulic fracture is not capable of opening or crossing the pre-existing fracture, propagating instead to the opposite direction. This was also observed by the author, who stated that the opposite fracture wing grew to a greater length and no fluid flow occurred along the pre-existing fracture (Blanton, 1982).

In model 20 crossing takes place and it is visible how the pre-existing fracture almost does not influence the hydraulic fracture behaviour. This is mainly due to the high differential stresses, which result in a high compressive stress in the pre-existing fracture faces. Associated with the high angle of approach of 90° , the entrance of fluid in the pre-existing fracture is highly constrained.

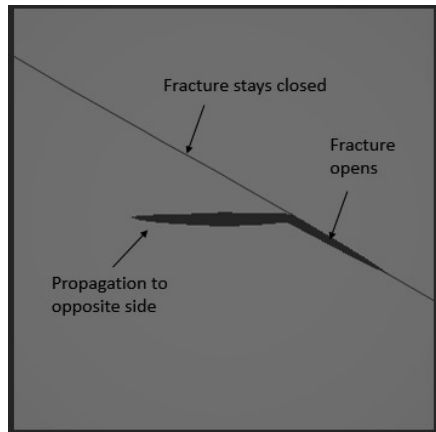
Only one numerical simulation – number 8 – predicted a different intersection type. The main reason for this difference may be related with other parameters that also influence the intersection behaviour. Other researchers have shown that also fracture friction (Hanson, Shaffer and Anderson, 1981), fracture length (Lamont and Jessen, 1963) or viscosity of the injection fluid (Cheng, Jin, Y. Chen, *et al.*, 2014) also influence fracture interaction. Obviously, many other limitations of the model may have led to this result, such as the negligence of dynamic or pore-pressure effects, or even a less realistic computing of the stress at the crack tip due to the use of the signed enrichment function.

Model 4 ($\beta = 60^\circ \parallel \Delta\sigma = 2 \times 10^3$ kPa) – Opening

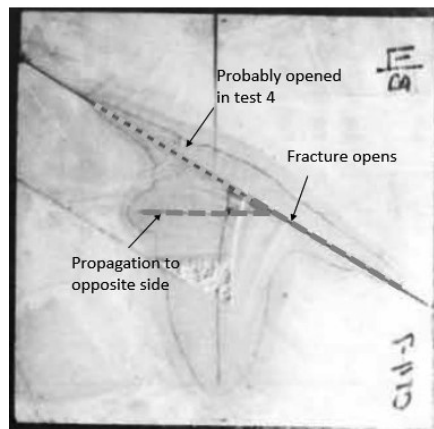
XFEMHF



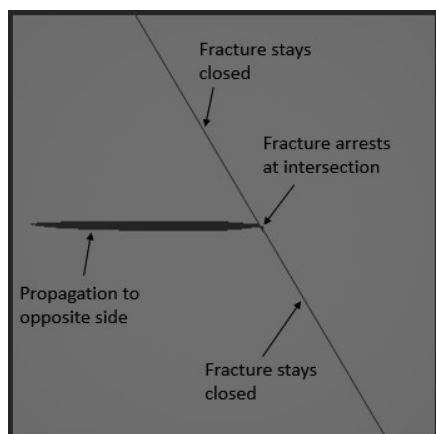
Laboratory Tests

Model 7 ($\beta = 30^\circ \parallel \Delta\sigma = 9 \times 10^3$ kPa) – Opening

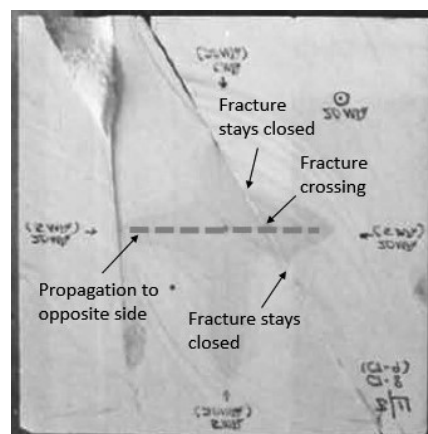
XFEMHF



Laboratory Tests

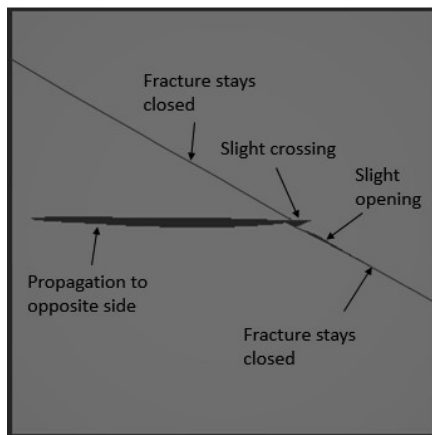
Model 8 ($\beta = 60^\circ \parallel \Delta\sigma = 15 \times 10^3$ kPa) – Arrest (Numerical) or Crossing (Lab)

XFEMHF

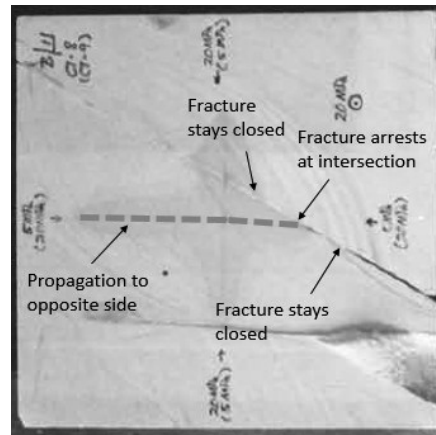


Laboratory Tests

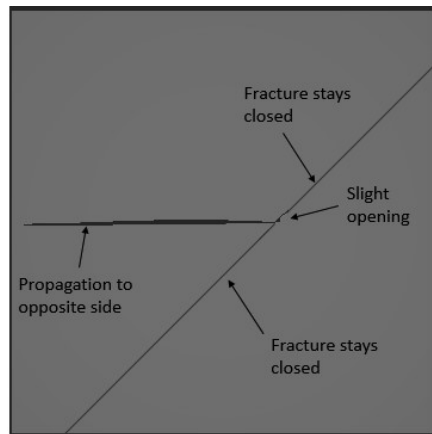
Figure 6.3 – Comparison of deformed models with the laboratory tests (when available)

Model 9 ($\beta = 30^\circ \parallel \Delta\sigma = 15 \times 10^3 \text{ kPa}$) – Arrest

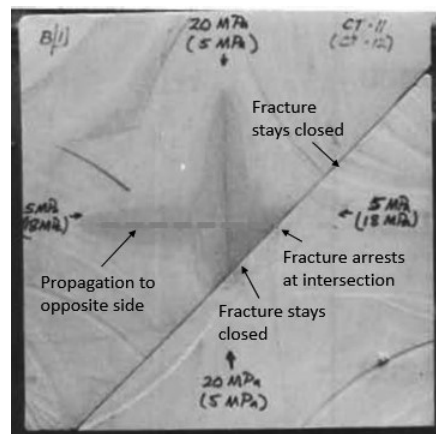
XFEMHF



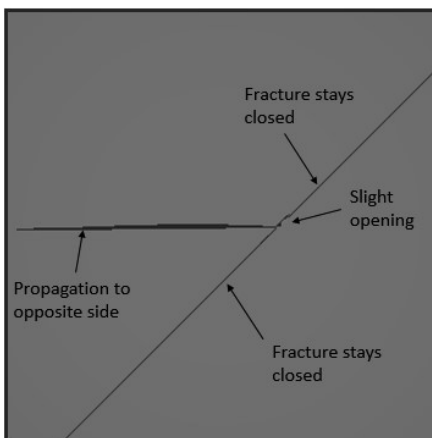
Laboratory Tests

Model 11 ($\beta = 45^\circ \parallel \Delta\sigma = 15 \times 10^3 \text{ kPa}$) – Arrest

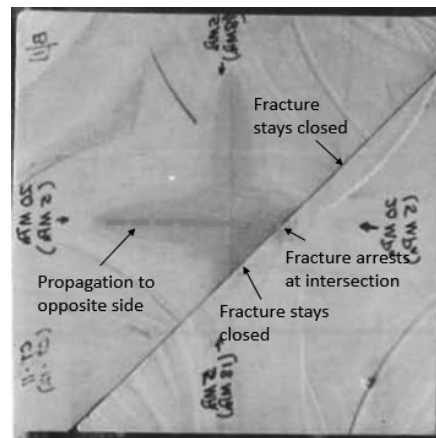
XFEMHF



Laboratory Tests

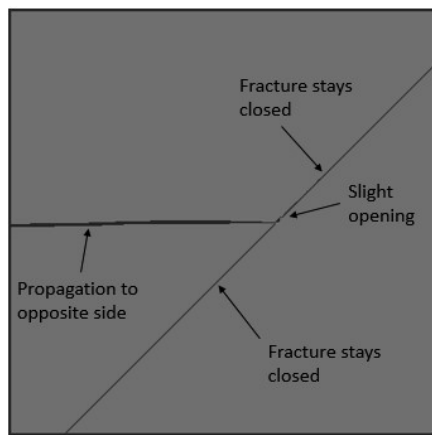
Model 12 ($\beta = 45^\circ \parallel \Delta\sigma = 13 \times 10^3 \text{ kPa}$) – Arrest

XFEMHF



Laboratory Tests

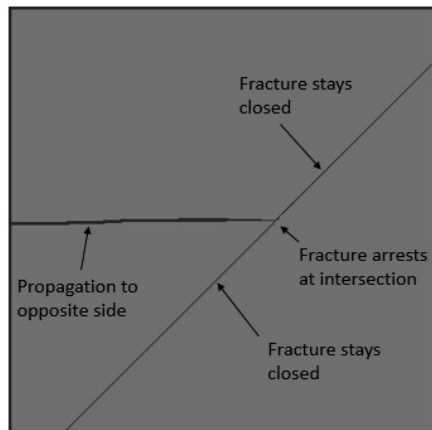
Figure 6.3 (cont.) – Comparison of deformed models with the laboratory tests (when available)

Model 13 ($\beta = 45^\circ \parallel \Delta\sigma = 11 \times 10^3 \text{ kPa}$) – Arrest

(Not Available)

XFEMHF

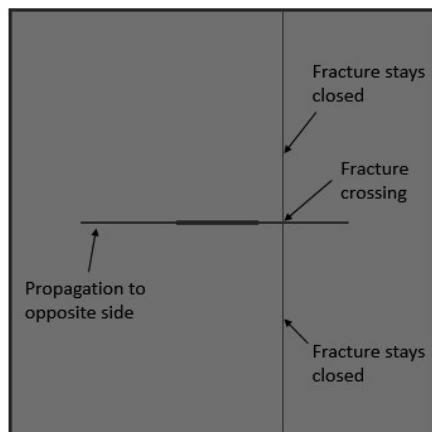
Laboratory Tests

Model 14 ($\beta = 45^\circ \parallel \Delta\sigma = 9 \times 10^3 \text{ kPa}$) – Arrest

(Not Available)

XFEMHF

Laboratory Tests

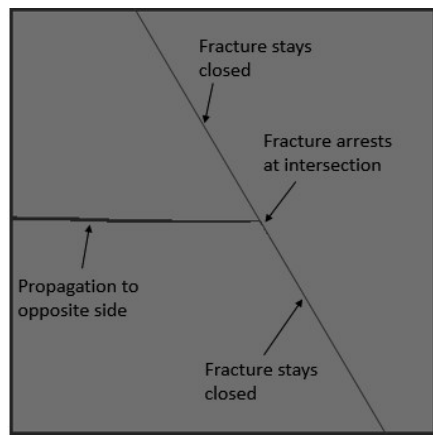
Model 20 ($\beta = 90^\circ \parallel \Delta\sigma = 9 \times 10^3 \text{ kPa}$) – Crossing

(Not Available)

XFEMHF

Laboratory Tests

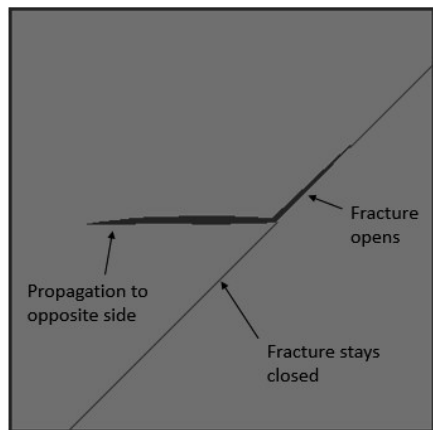
Figure 6.3 (cont.) – Comparison of deformed models with the laboratory tests (when available)

Model 21 ($\beta = 60^\circ \parallel \Delta\sigma = 9 \times 10^3 \text{ kPa}$) – Arrest

(Not Available)

XFEMHF

Laboratory Tests

Model 22 ($\beta = 45^\circ \parallel \Delta\sigma = 5 \times 10^3 \text{ kPa}$) – Opening

(Not Available)

XFEMHF

Laboratory Tests

Figure 6.3 (cont.) – Comparison of deformed models with the laboratory tests (when available)

The output of fracture variables allows a better knowledge of the behaviour of the existing fracture around the intersection. By plotting the relative shear (shear stress divided by the shear strength) along the pre-existing fracture for model 22, as seen in Figure 6.4, it is clear that the closer to the intersection, the higher is the relative shear acting in the faces. In the first presented time increment ($t = 0,06 \text{ s}$), the high compression under the hydraulic fracture increases the shear strength, therefore decreasing the relative shear. As intersection occurs ($t = 0,07 \text{ s}$), the flow enters the pre-existing fracture and a reduction of the horizontal fracture aperture happens. This brings a rapid reduction of the effect of the hydraulic fracture in the pre-existing fracture, i.e., a decrease of the compression in the region under the hydraulic fracture that leads to an increase of the relative shear and a reduction of

the tensile forces in the region above the hydraulic fracture that leads to a decrease of the relative shear. As the fluid enters the pre-existing fracture ($t = 0,09$ s and $t = 0,11$ s), the fracture faces lose contact and the shear strength is lost (relative shear of 100%). Then, the fluid has more and more impact in separating and pressurizing the fracture faces, continuing the opening event.

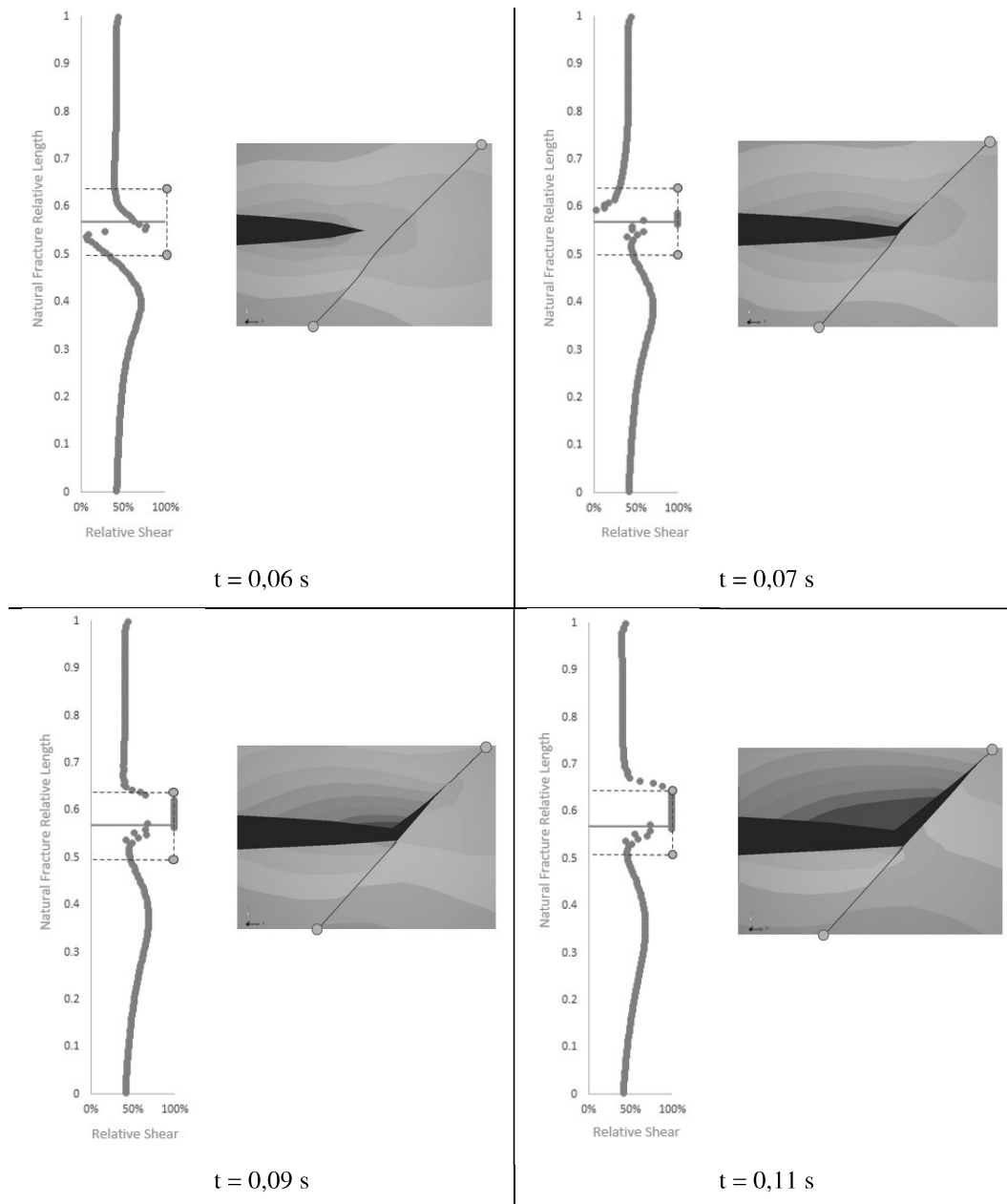


Figure 6.4 – Relative shear stresses in the pre-existing fracture for model 22. Red dashed lines denote the extremities of the fracture represented in the near figure. Orange line represents the level of the intersection.

A similar analysis, yet with different results, may be done to model 20 (see Figure 6.5). Naturally, the region closer to the intersection is subjected to higher

relative shears. Until the hydraulic fracture reaches the pre-existing fracture, the relative shears are very low, as seen in the increment previous to the intersection ($t = 0,07$ s). As the compression in the fracture faces is high, the strength increases and the transmission of shear stresses between the fracture faces generate tensile stresses on the opposite side. Consequently, the tensile strength is reached on the across the pre-existing fracture and the hydraulic fracture continues to propagate.

When the intersection occurs ($t = 0,08$ s), there is a sudden increase of the relative shears, but only the closest points to the intersection reach the shear strength and failure. The rest of the fracture keeps a compressive state, which does not allow the penetration of fluid in the pre-existing fracture. Then, as the hydraulic fracture moves away from the intersection ($t = 0,09$ s and $t = 0,12$ s), the displacements due to hydraulic fracture tend to be similar in both sides of the pre-existing fracture, reducing the shear stresses.

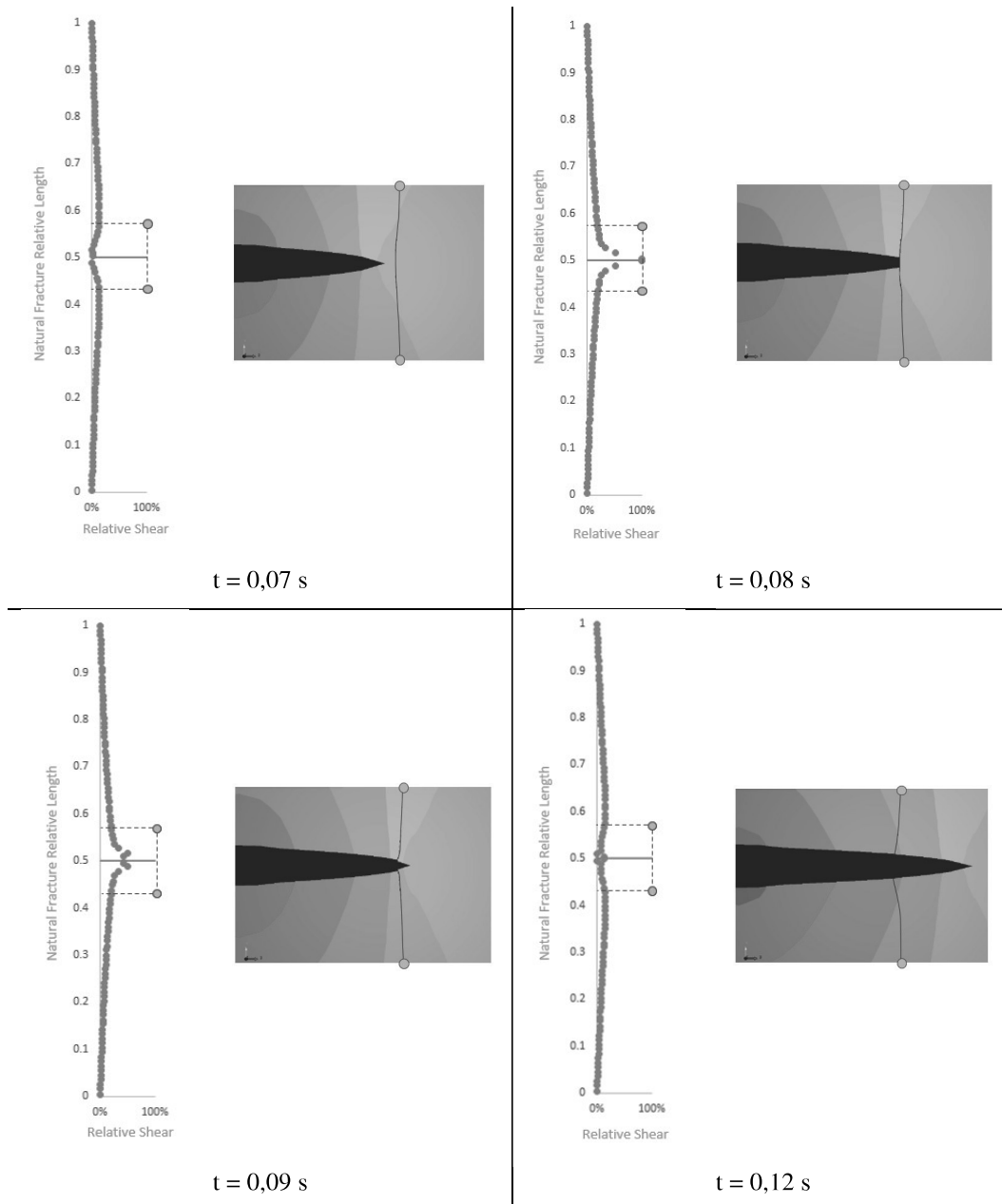


Figure 6.5 – Relative shear stresses in the pre-existing fracture for model 20. Red dashed lines denote the extremities of the fracture represented in the near figure. Orange line represents the level of the intersection.

6.1.2. Khoei tests

General description of the simulation

Khoi *et al.* (2015) performed hydraulic fracturing laboratory tests in two naturally fractured nearly impermeable carbonate rock samples. Moreover, the authors compared the laboratory tests with numerical simulations using the XFEM

technique. In this section, the simulation of the two laboratory tests is performed and compared with both the laboratory and numerical results of Khoei *et al.* (2015).

As referred by Khoei *et al.* (2015), the rock is considered to be impermeable, i.e., only displacements and fracture pressures are computed. A qualitative analysis of the results is made, by checking the type of interaction that occurs between fractures and comparing it with the laboratory tests.

Model geometry and mesh

Two models are defined to match the laboratory specimens' dimensions. Figure 6.6 shows a schematic representation of the models and Figure 6.7 the meshes used in the analyses. Table 6.4 indicates the dimensions of the models and the coordinates of the initial notch and the natural fracture.

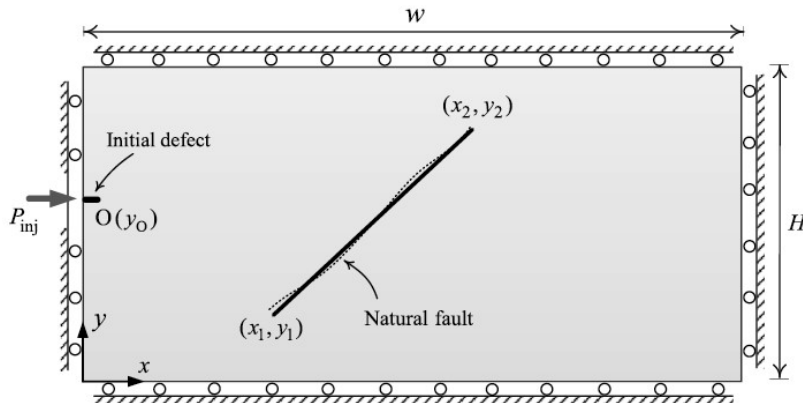
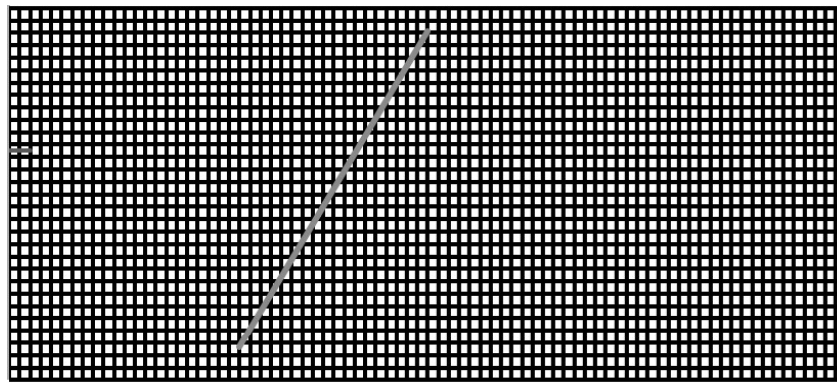
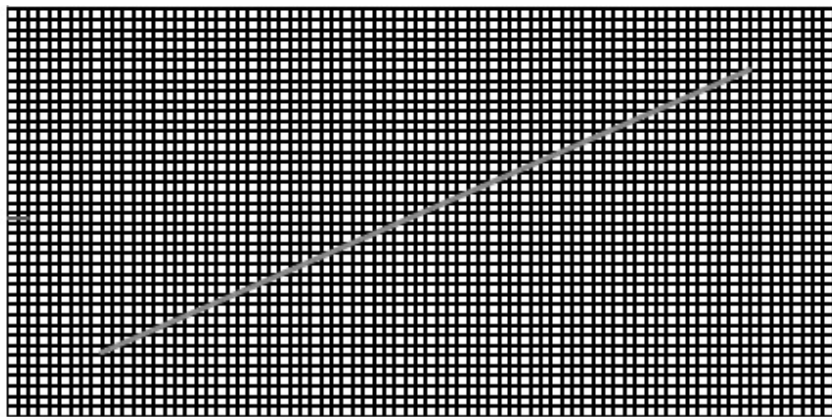


Figure 6.6 – Schematic view of the geometry and boundary conditions of hydraulic fracturing experimental tests



a)



b)

Figure 6.7 – Meshes used in the simulations. a) Specimen 1. b) Specimen 2

Table 6.4 – Geometry and material properties of the two hydraulic fracturing experiments

	Width (mm)	Height (mm)	(x₁,y₁) (mm)	(x₂,y₂) (mm)	y₀ (mm)
Specimen 1	111	45	(30,5;4)	(55,4;42,16)	27,9
Specimen 2	110	54	(12,13;8,82)	(98,12;46,07)	26,9

Material properties

The material properties are presented in Table 6.8 and Table 6.6. Some parameters were not provided in the reference paper, so values based in accumulated experience with rocks were assumed. It must be noted that the tensile strength values provided in the reference are considered to be much higher than acceptable values for rocks. Therefore, a value for the tensile strength was also assumed in these simulations.

Table 6.5 – Hydraulic properties

	Parameter	All Models
Fractures	Initial hydraulic aperture (m)	5×10^{-5} *
	Fluid Viscosity (kPa.s)	10^{-6} *

*assumed value

Table 6.6 – Mechanical properties

	Parameter	Specimen 1	Specimen 2
Porous Region	E (kPa)	$36,5 \times 10^6$	$32,5 \times 10^6$
	ν	0,25	0,25
	σ_t (kPa)	6000*	6000*
Natural Fracture	K_n (kPa)	0**	0**
	K_s (kPa)	1×10^9 *	1×10^9 *
	ϕ' (°)	36,7	36,7
	c' (kPa)	0	0

*assumed values

**value in traction. In compression, a penalty factor is applied

Boundary and loading conditions

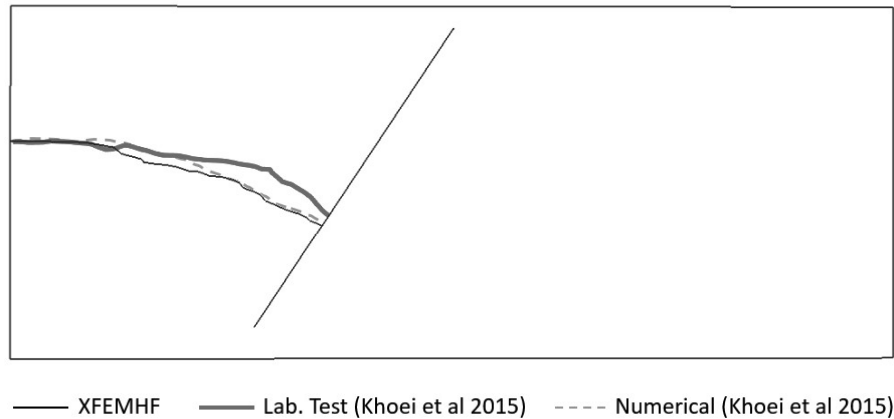
The contact test apparatus is simulated by displacement fixities and the fluid injection in fracture is defined by a prescribed constant pressure of 39300 kPa inside the initial hydraulic fracture.

Once the surrounding material is impermeable and the confinement level is low, i.e. there are no initial stresses applied in the model, the first pressure activation criterion (see Chapter 4.2.3) is used in the natural fracture. This means that when the simulation starts, the natural fracture has its fracture pressure degrees of freedom deactivated, so its deformations occur without the influence of the vacuum created by the fracture fluid. Then, when the hydraulic fracture intersects the natural fracture, all the segments of the natural fracture have their fracture pressure degrees of freedom activated.

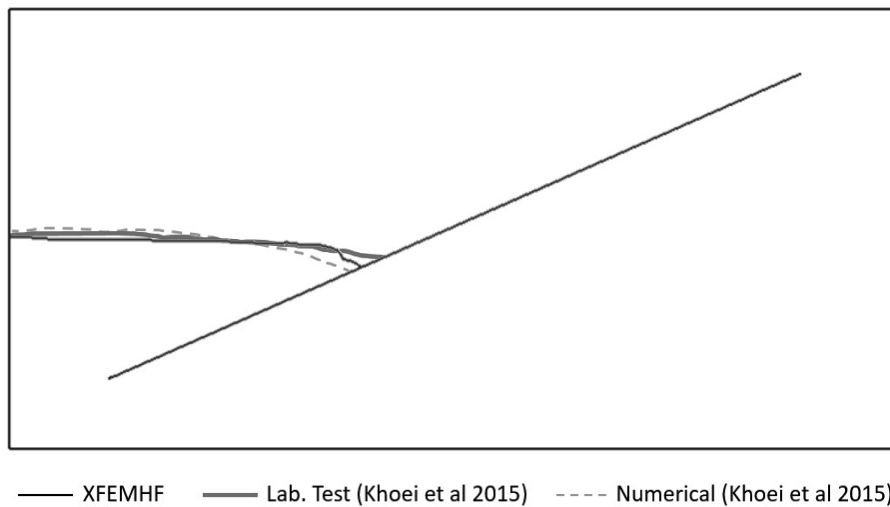
Results

Figure 6.8 shows the crack trajectories obtained in the laboratory tests and numerical simulations with XFEMHF and by Khoei *et al.* (2015). The numerical

simulation trajectories obtained for both specimens are in very good agreement with the laboratory trajectories. Effects that are not taken into account in the numerical simulations, such as the heterogeneity of the material, may explain the slight differences in the comparison with the laboratory tests. It is easily noticeable how the presence of the natural fracture affects the hydraulic fracture trajectory, which has tendency to curve so the junction between fractures occurs closer to perpendicular.



a)



b)

Figure 6.8 – Comparison of crack trajectory between the numerical solution with XFEMHF, laboratory test and numerical solution by Khoei *et al.* (2015). a) Specimen 1. b) Specimen 2

Figure 6.9 presents the displacement fields in both numerical analyses, XFEMHF and the one presented by Khoei *et al.* (2015). As stated before, Khoei *et al.* (2015) used the XFEM and a very similar formulation to perform the

simulations. However, it must be noted that slight differences that exist between the formulations and the implementations applied in each research work may explain the differences in the numerical results. It is known that the tip enrichments are different, and so are the criteria involved with propagation. Therefore, the comparison between numerical tools is carried out more in a qualitative perspective than quantitative. From that viewpoint, it is noticeable how the displacement fields show similar tendencies.

The same qualitative analysis may be performed by comparing the aperture and normal stress profiles along the natural fracture in three different phases of the analysis, defined by the length of the hydraulic fracture L_f . Figure 6.10 and Figure 6.11 compare the results between research works. Despite slight differences in the values, the shape and the development in time show a very good agreement between simulations. In both specimen simulation is noticeable that as the hydraulic fracture approaches the natural fracture, the latter tends to open at its mid-length, where the hydraulic fracture is closer. Moreover, the contact stress in the region farer to the contact increases, due to the displacements that occur in the hydraulic fracture.

Comparing the two specimens, the different natural fracture inclinations show that, the more vertical is the natural fracture (specimen 1), the more symmetric is the normal stress increase in its extremities. On the other hand, a lower angle of approach (specimen 2) show that the compressive stresses in the lower part of the natural fracture are much higher, while the variations in the upper part are almost none.

Finally, Figure 6.12 presents the plots for two different time increments of the maximum principal stress at the right side of the natural fracture, i.e. at the opposite side of the hydraulic fracture. It is visible that the results obtained with XFEMHF are much smoother than the ones obtained by Khoei *et al.* (2015). However, the same tendency is patent, showing that an increase of the maximum principal stress occurs closer to the junction and at the natural fracture tips as the hydraulic fracture approaches. This shows how the presence of a hydraulic fracture increases the chances of propagation from the natural fracture, both from its tips or the junction.

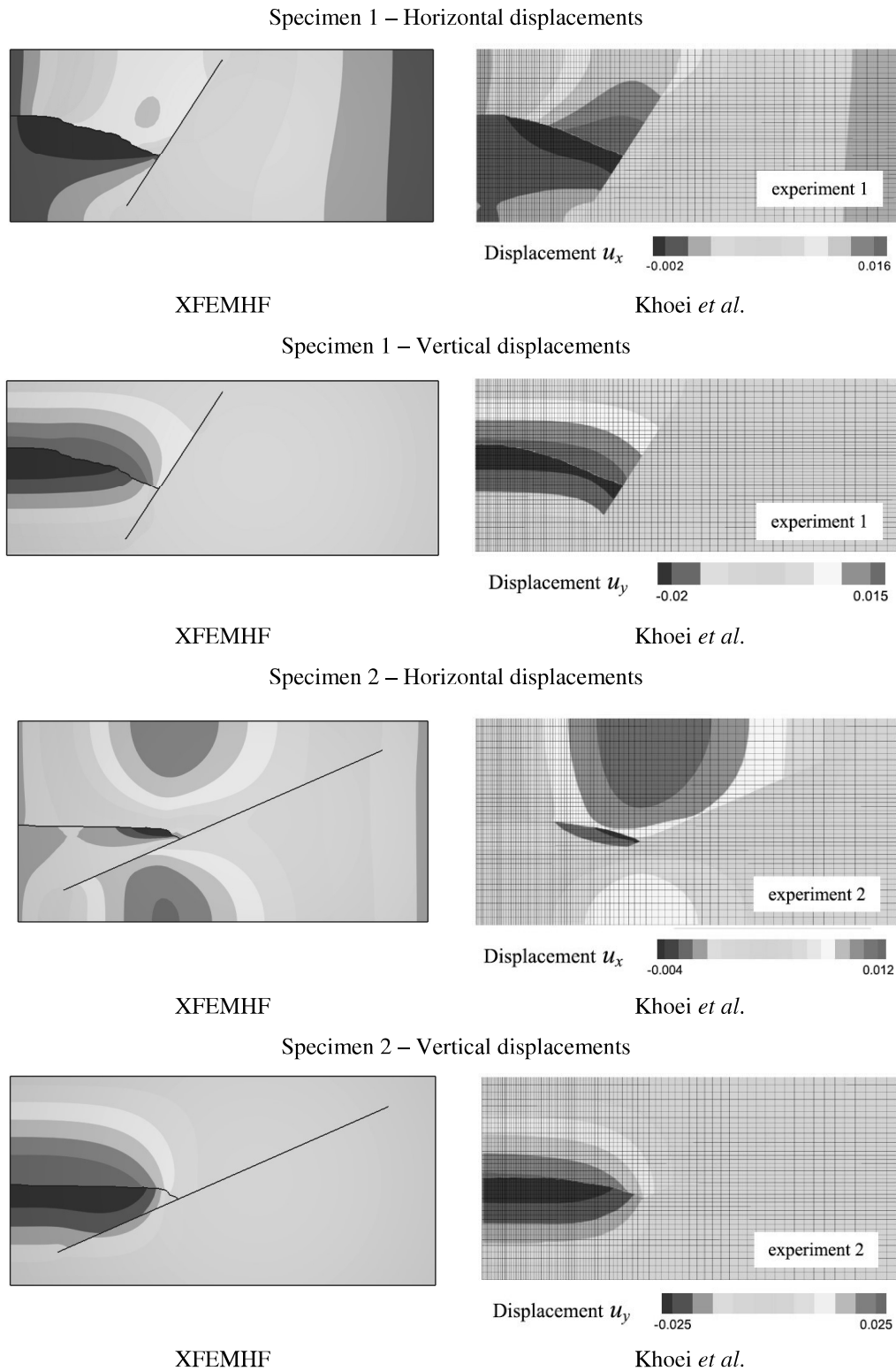
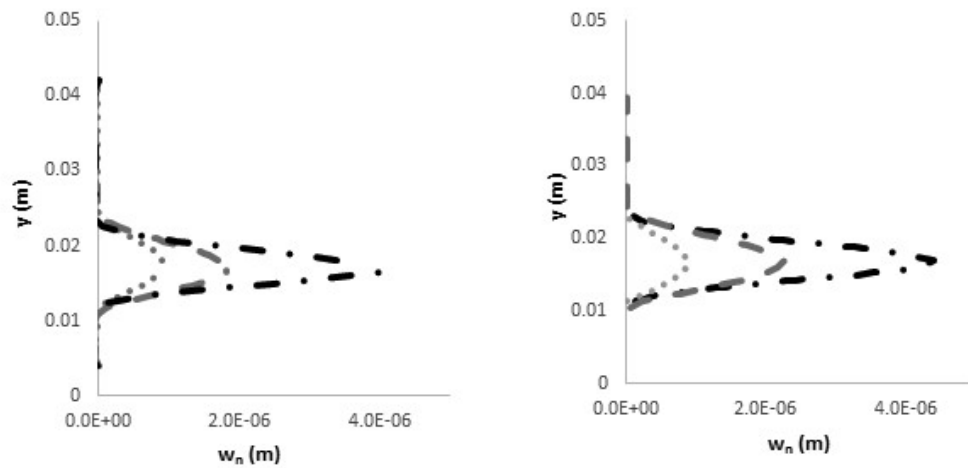


Figure 6.9 – Comparison of displacement fields when junction occurs between numerical solutions (the same colour scale is used in both simulations)

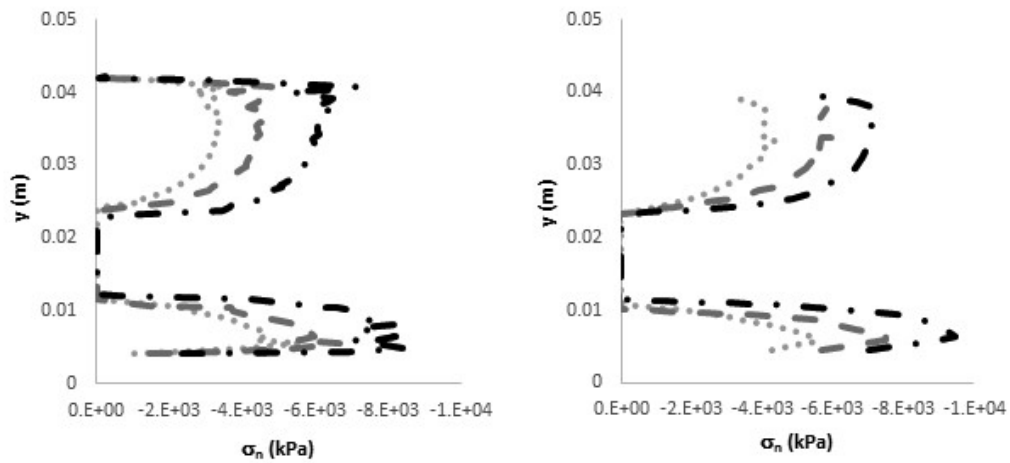
Specimen 1 – Natural fracture aperture



XFEMHF

Khoei *et al.*

Specimen 1 – Natural fracture normal stress



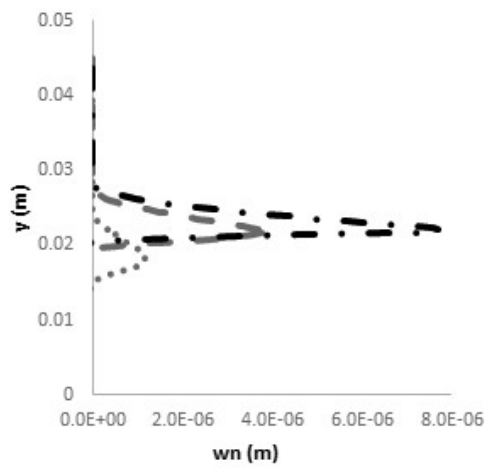
XFEMHF

Khoei *et al.*

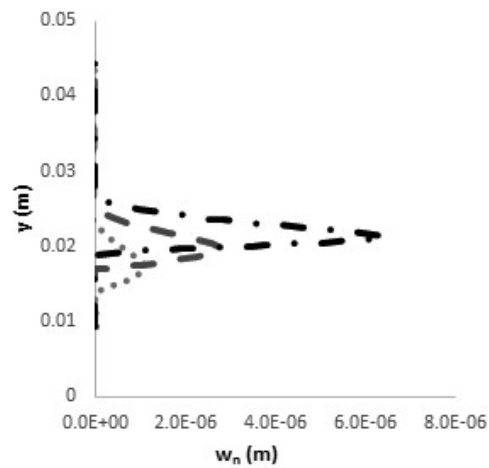
..... $L_f = 26,10$ mm - - - - $L_f = 30,96$ mm - . - . - $L_f = 36,15$ mm

Figure 6.10 – Comparison of fracture aperture and normal stress along the natural fracture between numerical solutions for specimen 1

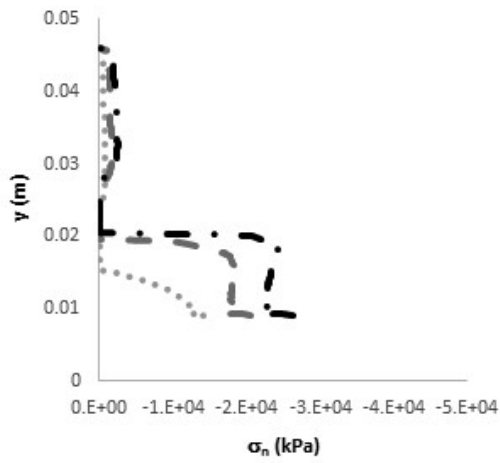
Specimen 2 – Natural fracture aperture



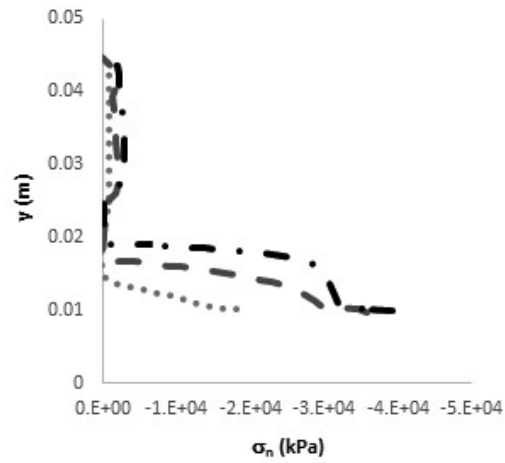
XFEMHF

Khoei *et al.*

Specimen 2 – Natural fracture normal stress



XFEMHF

Khoei *et al.*

..... $L_f = 18,59$ mm - - - - $L_f = 30,68$ mm - · - · - $L_f = 38,90$ mm

Figure 6.11 – Comparison of fracture aperture and normal stress along the natural fracture between numerical solutions for specimen 2

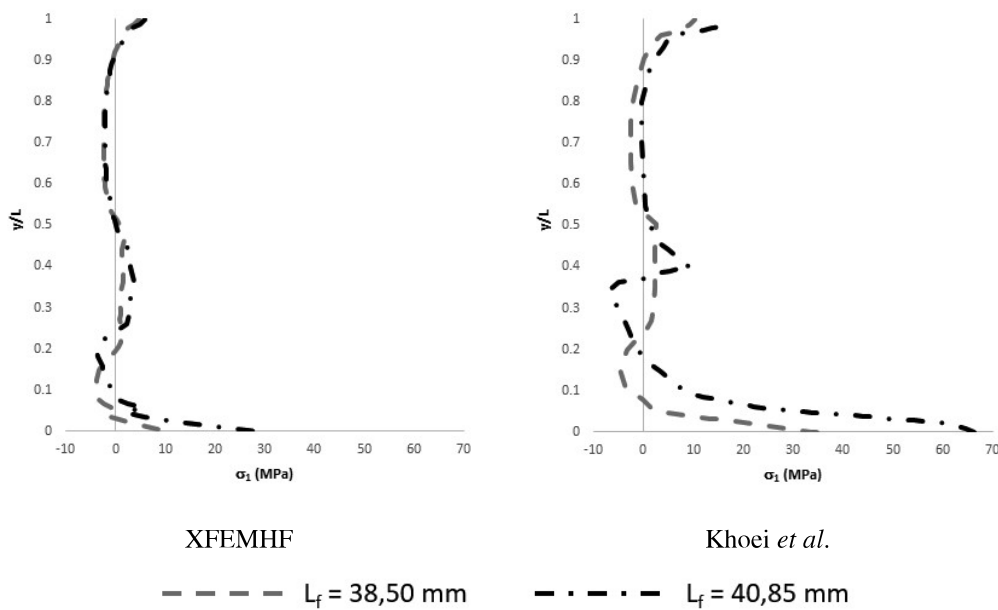
Specimen 1 – Maximum principal stress σ_1 at the right side of the natural fracture

Figure 6.12 – Comparison between numerical solutions for specimen 1 of maximum principal stress σ_1 at the right side of the natural fault

6.2.

Propagation of hydraulic fracture in multi-fractured medium

General description of the simulation

The simulations presented in Chapter 6.1 show how to use the developed research in understanding the behaviour of the intersection between one hydraulic fracture and one natural fracture. However, the implementation is generalized for any number of fractures and fracture intersections. Therefore, it is relevant to go further and apply the XFEMHF code in simulations where more fractures and intersections occur.

To the knowledge of the author, no clear information on laboratory tests or numerical simulations of hydraulic fractures propagating in a multi-fractured porous medium exists. Therefore, this work proposes a synthetic model of propagation in a multi-fractured medium.

The model's geometry is defined and a sensibility analysis is performed by changing two parameters, setting a combination of thirty different simulations to be run. The changed parameters are the differential in-situ stress and the in-situ fracture aperture. The sensibility of the created fracture network to each of the varying parameters is analysed in the results.

Additionally, a qualitative comparison is made with the conclusions presented by Zhou and Xue (2011). In their research work, Zhou and Xue (2011) performed hydraulic fracturing laboratory tests in cement blocks that were previously subjected to heat and cooling, in order to form natural fractures inside the blocks. By performing the injections at different differential stresses, the authors found that these influence the fracture network patterns, as Figure 6.13 shows. Three types of geometries were observed in the laboratory tests. The first is a vertical dominating fracture with multiple branches, which was created at high difference stresses, with the dominating fracture still propagating close to the preferred direction, i.e. the direction of maximum stress. The second is a radial net-fracture geometry around the wellbore, which occurs for low stress difference. The third is a partly vertical fracture with random branches for intermediate values of stress difference. Figure 6.14 shows a plot of the results for each test against the differential in-situ stresses. The results show that the higher the differential in-situ stresses, the less the natural fractures affect the hydraulic fracture path.

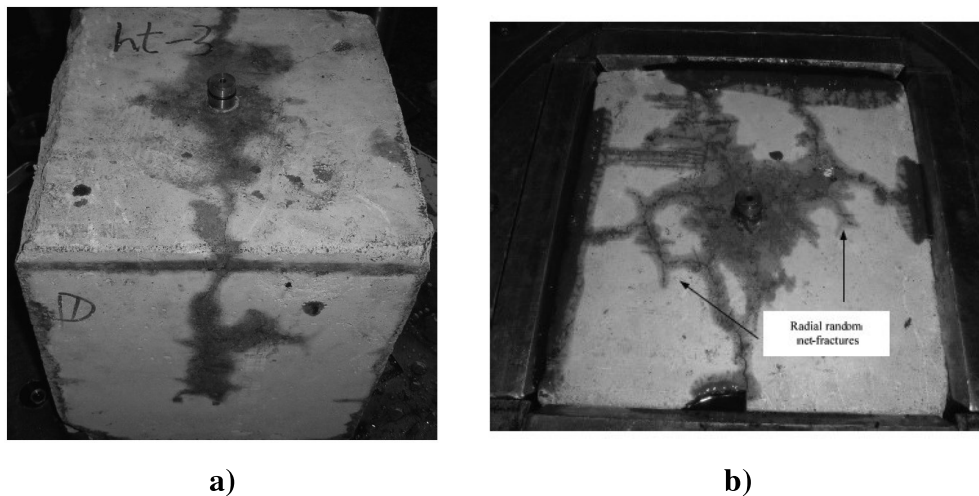


Figure 6.13 – Fracture patterns obtained in different tests. a) Dominating fracture with multiple branches at large difference of horizontal stress. b) Radial random net-fractures at low difference of horizontal stress (Zhou and Xue, 2011)

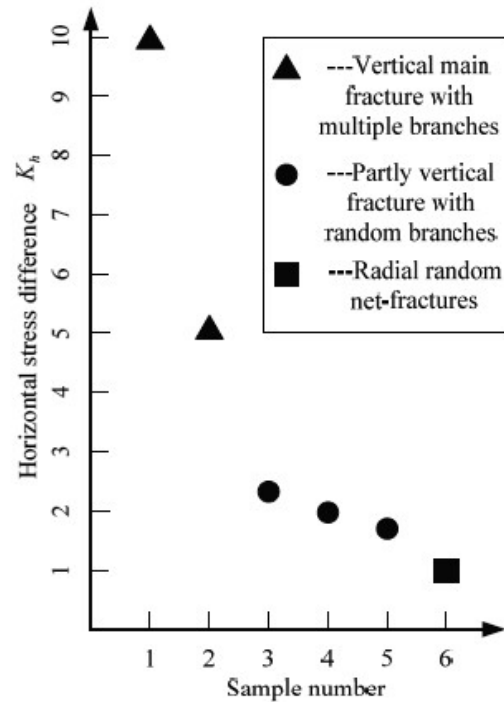


Figure 6.14 – The relation between fracture geometry and in-situ stress contrast (Zhou and Xue, 2011)

Model geometry and mesh

All simulations use a 2,0 m x 1,5 m rectangular model divided in a 75x51 regular element grid. Figure 6.15 shows one initial hydraulic fracture and 9 natural fractures that are placed in a way that two sets of natural fractures are represented with inclinations of 81° (sub-vertical) and -14° (sub-horizontal). The natural fractures are positioned so 5 intersections occur.

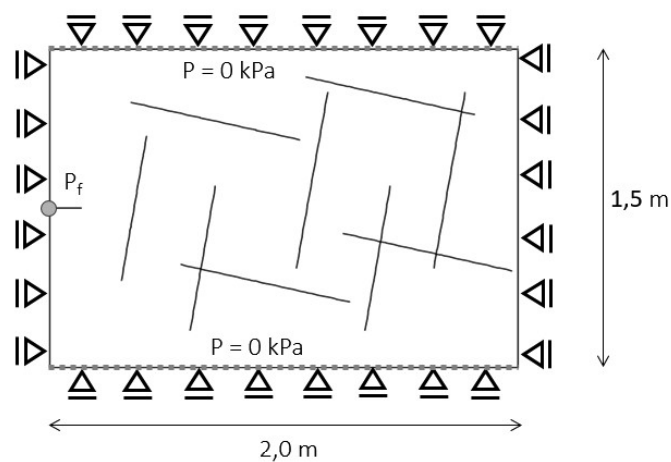


Figure 6.15 –Geometry of the model and boundary conditions.

Material properties

Table 6.7 and Table 6.8 present the fixed parameters chosen for the materials. Although assumed, it is judged that the parameters are within a range of representing correctly a typical fractured rock medium. As for the fracture mechanical behaviour, a non-associated law is used, i.e. no dilatation occurs due to shear deformations.

Table 6.7 – Hydraulic properties

	Parameter	All Cases
Porous Region	Hydraulic conductivity: $k = k_x = k_y$ (m/s)	10^{-11}
Fractures	Fracture face transversal conductivity: $c = c_{top} = c_{bottom}$ (m/s.kPa ⁻¹)	10^{-3}
	Fluid Viscosity (kPa.s)	10^{-6}

Table 6.8 – Mechanical properties

	Parameter	All Cases
Porous Region	E (kPa)	1×10^7
	ν	0,22
	σ_t (kPa)	1100
Natural Fractures	K_n (kPa)	0 ^{**}
	K_s (kPa)	10^8
	ϕ' (°)	36,9
	c' (kPa)	0

^{**}value in traction. In compression, a penalty factor is applied

Variable properties

The sensibility analysis is performed by varying the in-situ hydraulic fracture aperture and the in-situ stresses. The in-situ hydraulic fracture aperture varies

within three values: 1×10^{-6} , 5×10^{-5} , 5×10^{-4} m. The maximum and minimum value of in-situ hydraulic fracture aperture, 5×10^{-4} and 1×10^{-6} m, respectively, are thought to be representative of limit values for fracture aperture. Those orders of magnitude agree with the range of values studied by Witherspoon *et al.* (1980), who validated the cubic law for use in fracture flow of rock samples subjected to in-situ stresses up to 20 MPa with apertures between $2,5 \times 10^{-4}$ and 4×10^{-6} m.

A geostatic step is used to apply ten different combinations of initial stresses with the values presented in Table 6.9. The maximum and minimum stresses are applied in the horizontal and vertical directions, respectively. The maximum in-situ stress is kept with a constant value of 5×10^3 kPa while the minimum in-situ stress varies between 5×10^3 and $0,312 \times 10^3$ kPa. A dimensionless parameter K_h is used to indicate the relation between maximum and minimum in-situ stresses.

Table 6.9 – In-situ Stresses

σ_{\max} (kPa)	σ_{\min} (kPa)	$K_h = \frac{\sigma_{\max} - \sigma_{\min}}{\sigma_{\min}}$
5×10^3	5×10^3	0
5×10^3	$4,545 \times 10^3$	0,1
5×10^3	$2,5 \times 10^3$	1
5×10^3	$2,0 \times 10^3$	1,5
5×10^3	$1,428 \times 10^3$	2,5
5×10^3	$1,0 \times 10^3$	4
5×10^3	$0,769 \times 10^3$	5,5
5×10^3	$0,625 \times 10^3$	7
5×10^3	$0,454 \times 10^3$	10
5×10^3	$0,312 \times 10^3$	15

Boundary and loading conditions

Along the whole model border the displacements are fixed perpendicularly to it, as seen in Figure 6.15. To allow the flow of fluid outside the model, the pressure at the top and bottom borders is fixed.

The simulations are set to run one single step of 100 s with increment time limited to a maximum of 2 s. Fluid injection in the hydraulic fracture is given by an imposed fracture pressure that follows the ramp function $P_f = 2000.t.$, as presented in Figure 6.16.

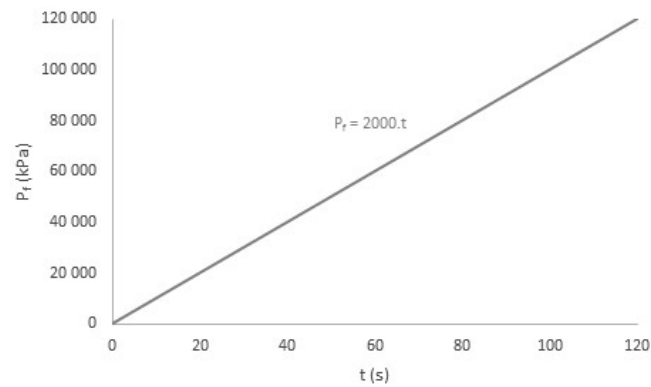


Figure 6.16 – Fluid Pressure applied at the hydraulic fracture mouth

Results

The results show that the implemented code is capable of simulating the propagation of a hydraulic fracture in a multi-fractured medium. It may be stated that the created fracture networks are highly dependent on the parameters that varied. Figure 6.17 shows the deformed geometry and the pore pressure fields for three calculations with very different in-situ stress relations. It is evident that as the stress parameter K_h increases, the events of fracture opening are less likening to occur and the hydraulic fracture tends to cross the natural fractures. For a low value of K_h , opening occurs in the natural fractures and their tips propagate until reaching other natural fractures.

The pore-pressure fields indicate that the pattern of pore-pressures is strongly affected by the leak-off in the fractures. For higher values of K_h , higher pore-pressures concentrate close to the hydraulic fracture. On the other hand, for lower values of K_h , the higher-pressure regions are much more dependent on the natural fractures position and depend on their communication.

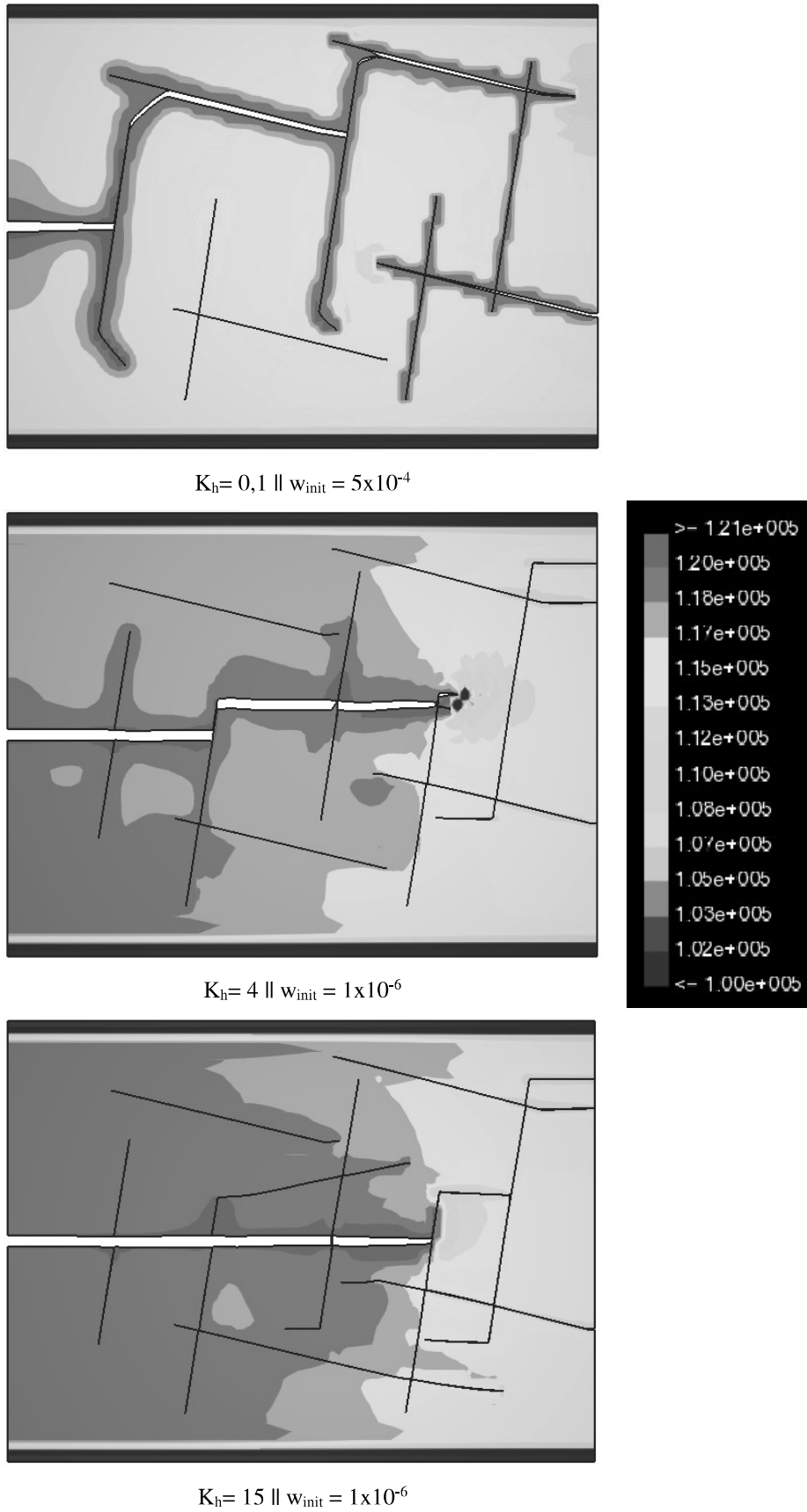


Figure 6.17 – Deformed models and pore-pressure fields at $t = 100$ s

In order to analyse the effect that the parameter variation has on the final fracture network pattern, Figure 6.18 shows the fracture networks for every computed simulation and highlights the propagated segments in blue. Different intersection types showed in previous examples are observed, namely crossing and opening. It is noticeable from all the deformed models that the natural fracture tips also propagate when their fluid pressure increases. It is also easily visible how higher differential stresses result in networks with more propagation segments. This is explained by the fact that, with a constant maximum in-situ stress in between simulations, a higher value of K_h is the result of a lower minimum in-situ stress, which consequently increases the possibility of propagation events.

For every simulation with very low differential stress parameters K_h at or near an isotropic state ($K_h = 0$ or $K_h = 0,1$), only opening events occur. As the parameter K_h increases, crossing becomes more and more predominant and the fracture network becomes more complex, increasing communication between natural fractures.

Comparisons of results for equal in-situ stress states show that for a very low in-situ hydraulic aperture (1×10^{-6} m) crossing events tend to happen more often. This may be explained by the difficulty of the fluid to enter natural fractures. For high and intermediate fracture apertures, 5×10^{-4} m and 5×10^{-5} m, respectively, the results are slightly similar.

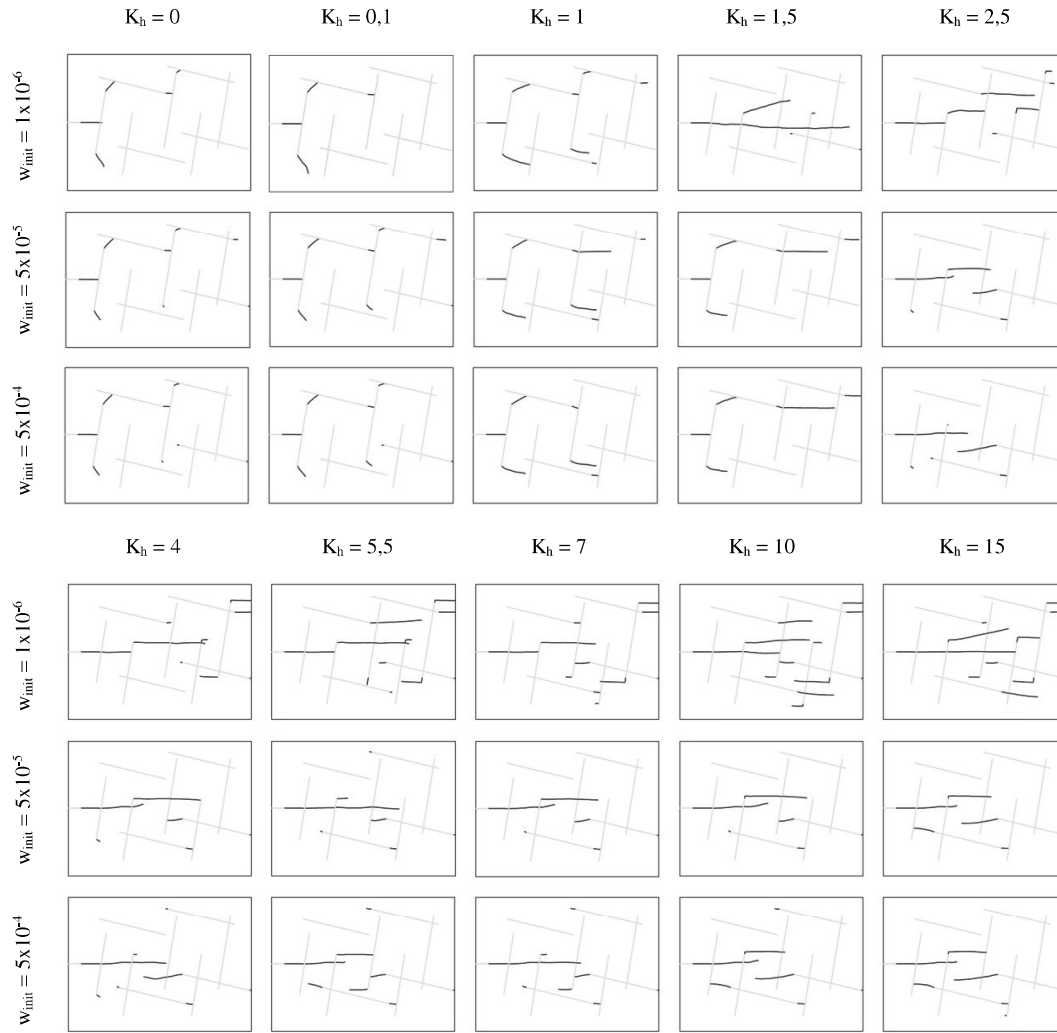


Figure 6.18 – Final fracture network ($t = 100$ s). Initial fractures in light grey and propagated segments in blue

Figure 6.19 complements the analysis of the results by showing the relative fracture aperture, i.e. the fracture aperture divided by the maximum fracture aperture in each simulation, at the end of the treatment. In this figure, it is visible that sub-horizontal fractures experience much larger apertures than the sub-vertical ones. This is expected, as the minimum in-situ stress acts in the vertical direction.

For values of K_h lower than 1, the fracture apertures tend to increase uniformly in the fracture network, indicating that the network grows in a more random manner, depending on the natural fracture position and not so much on the simulation parameters.

As the differential stress increases, the natural fractures aperture are much higher on the sub-horizontal fractures and the fracture network tends to develop

towards the preferred direction, i.e. the maximum in-situ-stress. For lower values of in-situ fracture aperture, this effect is even more evident.

The effect of stress shadowing between fractures is also noticeable in Figure 6.19. When the fracture network develops in parallel fractures (e.g. the simulation with $K_h = 7$ and $w_{init} = 5 \times 10^{-5}$), both fractures show a decrease in their aperture due to the compression effect between each other.



Figure 6.19 – Relative fracture opening in the final fracture network ($t = 100$ s).

Finally, a qualitative evaluation of the fracture pattern based in Figure 6.19 is plotted in Figure 6.20. Although being a very subjective analysis, three types of fracture network patterns are differentiated: random growth of fractures that is dependent on the initial fracture network, a partial horizontal hydraulic fracture

with multiple branches and a main horizontal hydraulic fracture with branches. It is concluded that high values of differential in-situ stress result in propagation of the hydraulic fracture in the preferred direction, while the in-situ fracture aperture may influence the flow of injection fluid into the natural fractures. For lower values of differential in-situ stress, the final fracture network tends to be similar to the initial one.

Even considering that it is not the object of this chapter to simulate a real laboratory test, the resulting plot of Figure 6.20 may be compared with the plot presented by Zhou and Xue (2011) (see Figure 6.14). Though many aspects of the simulation, such as rock parameters, boundary conditions and model geometry, are not the same, a similar behaviour may be interpreted from both numerical and laboratory results.

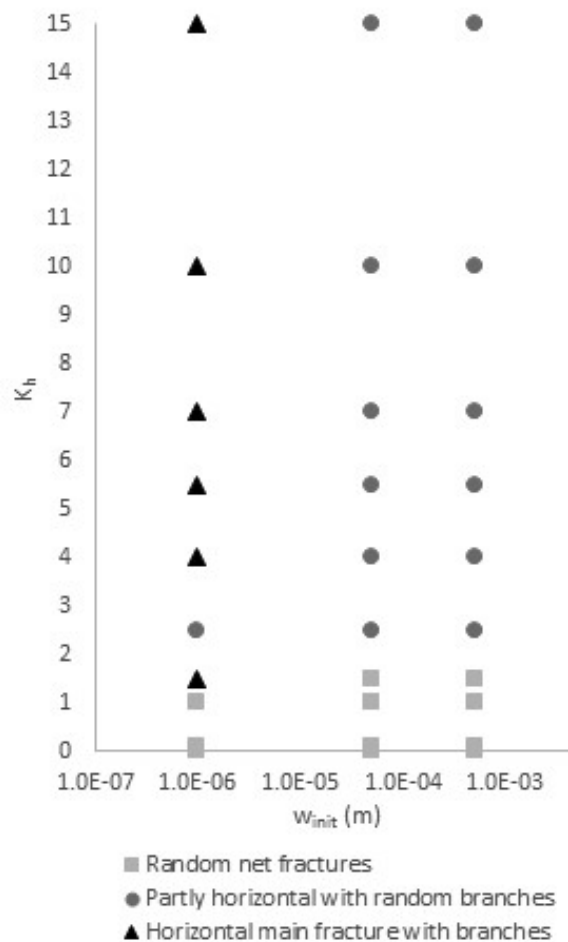


Figure 6.20 – Description of the final fracture network pattern ($t = 100$ s).

6.3. Percolation through a dam foundation

General description of the simulation

The main objective of this simulation is to demonstrate that the implemented code can be applied to simulate engineering problems other than intersection between hydraulic and natural fractures. The explicit consideration of fractures and their longitudinal and transversal flow is essential in many problems in rock foundations or reservoir geomechanics. In this simulation, the percolation through a fractured dam foundation is analysed in two sets of calculations.

In the first set, a foundation with one family of fractures equally spaced is subjected to a variation of the parameters that influence fractures longitudinal and transversal permeabilities. The models are based in the work by Segura and Carol (2004), as seen in Figure 6.21, and results are compared to the ones presented by the authors. The authors used and compared three types of interface elements – one, two and three nodes in the transversal direction. In this chapter, the current implementation is compared with the solutions of the models where the element with three nodes in the transversal direction was used.

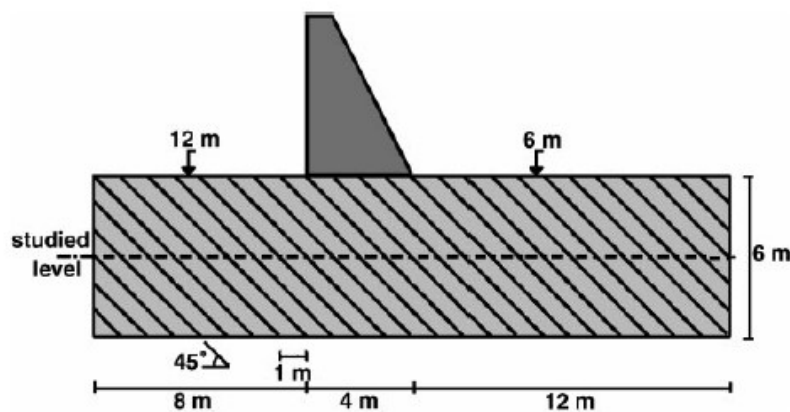


Figure 6.21 – Schematic model used by (Segura and Carol, 2004)

In the second set of calculations, a second family of fractures is introduced and its influence is analysed. All the performed calculations consider only the variables of the hydraulic part, i.e. the pore-pressures and the fracture fluid pressures.

Model geometry and mesh

Four different geometries – Dam0, Dam1, Dam2, Dam3 – were defined to perform the analyses and are presented in Figure 6.22. The first geometry (Dam0) is for the benchmark analysis of a homogeneous medium without fractures. Dam1, which is used in the first set of calculations, has 29 fractures equally spaced $\sqrt{2}$ m with inclination angle of 45° . For the second set of calculations, the geometries Dam2 and Dam3 are used. In the geometry Dam2 one fracture with inclination of 10° is introduced and in model Dam3 this fracture is replicated with a spacing of 1,5 m.

Both Dam0 and Dam1 have a 15 x 60 quadrilateral element regular mesh, while Dam2 and Dam3 have more refined meshes with 30 x 120 elements. Although a pre-study revealed that the coarser mesh provides results with sufficient quality, the existence of more fractures demands the use of a finer mesh to avoid the repetition of the same degree of freedom for different fractures in the same element (explained in Chapter 4.2.8).

Material properties

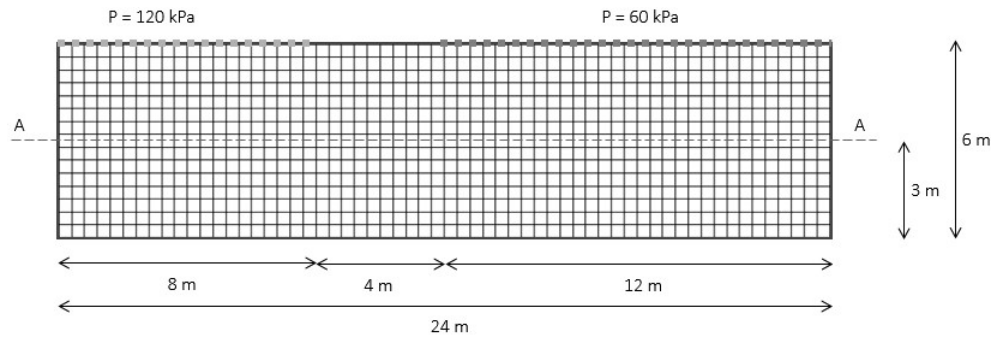
The parameters chosen for both the porous region and the fractures are presented from Table 6.10 to Table 6.12. Given the relation between hydraulic head h and hydraulic pressure p

$$p = h \times \gamma_w \quad (6.1)$$

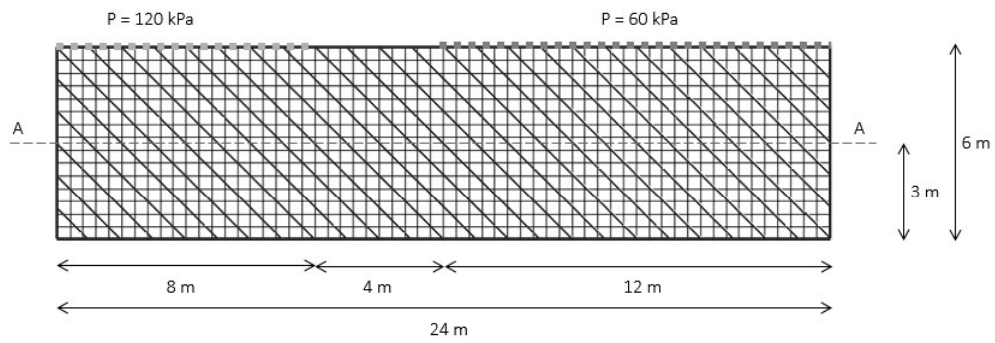
where γ_w is the water's volumetric weight, the flow rate and the transversal permeability in Segura and Carol (2004) may be presented as

$$q = k_t \Delta h = \frac{k_t}{\gamma_w} \Delta p \quad (6.2)$$

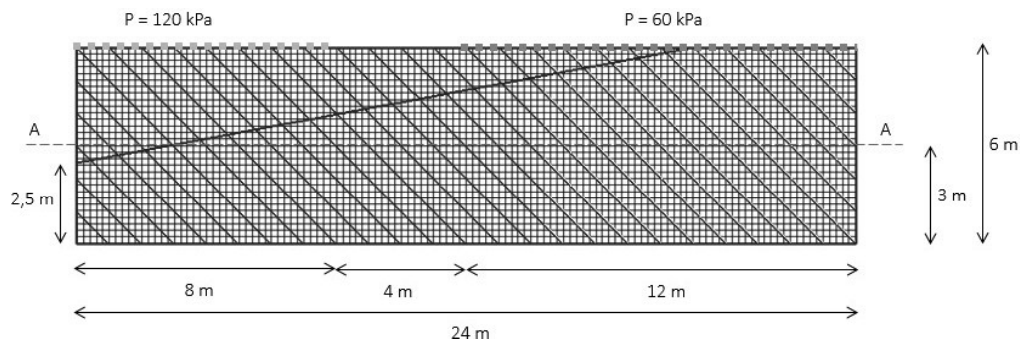
where the conductivity term k_t/γ_w (units $[1/T]/[F/L^3]$) may be defined to be equal to the fracture face transversal conductivity as implemented in this research (units $[L/T]/[F/L^2]$).



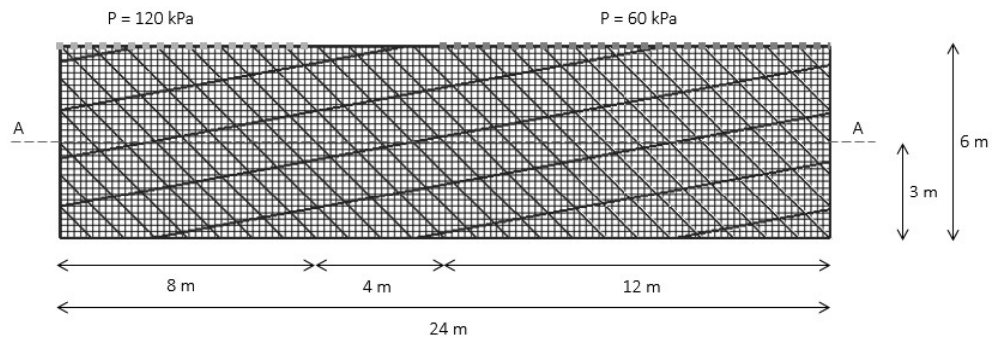
a)



b)



c)



d)

Figure 6.22 – Geometry and boundary conditions for the models:

a) Dam0. b) Dam1. c) Dam2. d) Dam3

Table 6.10 – Hydraulic properties

	Parameter	Dam0	Dam1	Dam2	Dam3
Porous Region	Hydraulic conductivity: k = k _x = k _y (m/s)	10 ⁻⁷			
Fractures	Hydraulic aperture: w _{init} (m)	-	See Table 6.11	See Table 6.12	
	Fracture face transversal conductivity: c = c _{top} = c _{bottom} (m/s.kPa ⁻¹)	-		10 ⁻⁵	
	Fluid Viscosity (kPa.s)	10 ⁻⁶			

In the first set of calculations, the fracture hydraulic parameters – fracture hydraulic aperture and fracture face transversal conductivity – vary according to the analyses performed by Segura and Carol (2004). Table 6.11 presents the values used in every calculation.

In the second set of calculations, a second family of fractures is introduced. The fracture properties vary so the influence of the second set of fractures may be understood. To reduce the complexity of the analysis, only the hydraulic aperture varies, while the fracture face transversal conductivity is kept constant with a value of 10^{-5} m/s.kPa⁻¹. This value was chosen sufficiently high so that the transversal conductivity would not affect the results. The values of the hydraulic aperture for each calculation is presented in Table 6.12.

Table 6.11 – Hydraulic properties of fractures in the first set of calculations

Model	w_{init} (m)	c (m/s.kPa ⁻¹)
Dam1a	1×10^{-4}	10^{-5}
Dam1b	1×10^{-4}	10^{-8}
Dam1c	1×10^{-4}	10^{-9}
Dam1d	5×10^{-5}	10^{-5}
Dam1e	5×10^{-5}	10^{-8}
Dam1f	5×10^{-5}	10^{-9}
Dam1g	1×10^{-5}	10^{-5}
Dam1h	1×10^{-5}	10^{-8}
Dam1i	1×10^{-5}	10^{-9}

Table 6.12 – Hydraulic properties of fractures in the second set of calculations

Model	Fracture family	w_{init} (m)
Dam2a	45°	1×10^{-4}
	10°	1×10^{-4}
Dam2b	45°	1×10^{-4}
	10°	1×10^{-3}
Dam3a	45°	1×10^{-4}
	10°	1×10^{-4}
Dam3b	45°	1×10^{-4}
	10°	1×10^{-3}
Dam3c	45°	1×10^{-3}
	10°	1×10^{-4}

Boundary and loading conditions

As seen in Figure 6.22, the boundary conditions were set equally to every calculation. The effect of the water levels of 12 m and 6 m is introduced as imposed

pressures in the boundaries of 120 kPa and 60 kPa, respectively. All calculations are performed in a single increment, assuming that a permanent regime exists.

Results – Set 1 of Calculations – Comparison with Segura and Carol (2004)

The pore-pressure shadings for all the models with geometry Dam1 (1 set of fractures) are presented in Figure 6.23, together with the values of fracture face transversal conductivity and hydraulic aperture used in each calculation. It may be easily observed that the pore-pressure field changes considerable between each calculation.

For the calculations with the lowest fracture face transversal conductivity (leftmost column – $1 \times 10^{-9} \text{ m/s.kPa}^{-1}$), the fractures work as barriers to the fluid flow, retaining values of similar pressure in each space between fractures. With the increase in the transversal conductivity (middle and rightmost columns – 1×10^{-8} and $1 \times 10^{-5} \text{ m/s.kPa}^{-1}$), the percolation occurs with less loss of energy and this “barrier effect” vanishes.

As for the longitudinal transmissibility, which is directly related with the fracture aperture, it is noticeable that a lower conductivity (upper row – $1 \times 10^{-5} \text{ m}$) results in a more distributed pressure field. Higher apertures (middle and lower rows – 5×10^{-5} and $1 \times 10^{-4} \text{ m}$) facilitate the use of the fractures as canals for the fluid percolation. This leads to a concentration of pressure gradients in the middle of the model, which is the region where the fluid needs to leave the fractures and cross the less permeable porous medium.

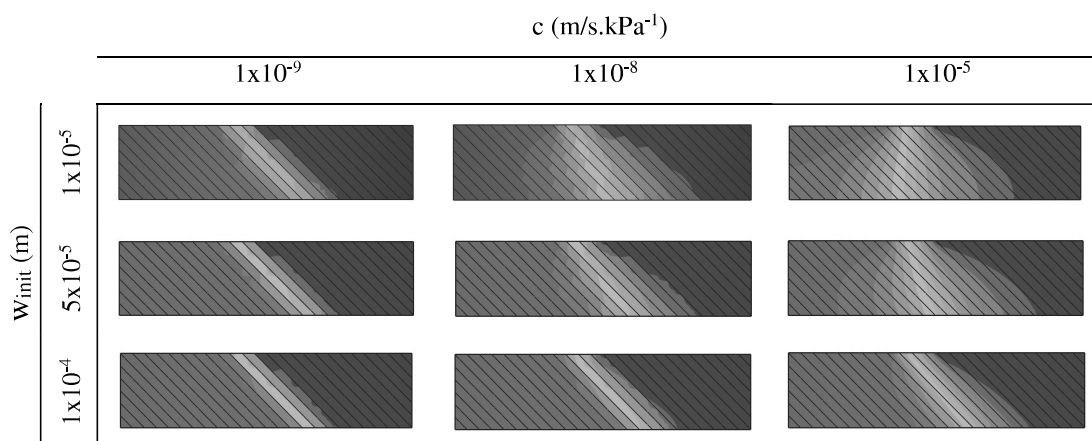


Figure 6.23 – Resulting pore pressures in models Dam1a to Dam1i (colour scale: red is 120 kPa, blue is 60 kPa)

From the analysis of Figure 6.24, it may be observed how the volume of fluid that enters (or leaves) the model decreases with the decrease of both longitudinal and transversal conductivity, as expected. In the cases with high values of fracture face transversal conductivity, the results almost match the ones presented by Segura and Carol (2004). As the fracture transversal flow decreases, the relative error between methods increases. The same assumptions may be made from observation of Figure 6.25. The pore-pressures along section A-A match for the models with high fracture face transversal conductivity, while a slight error is observable in the cases with lower values.

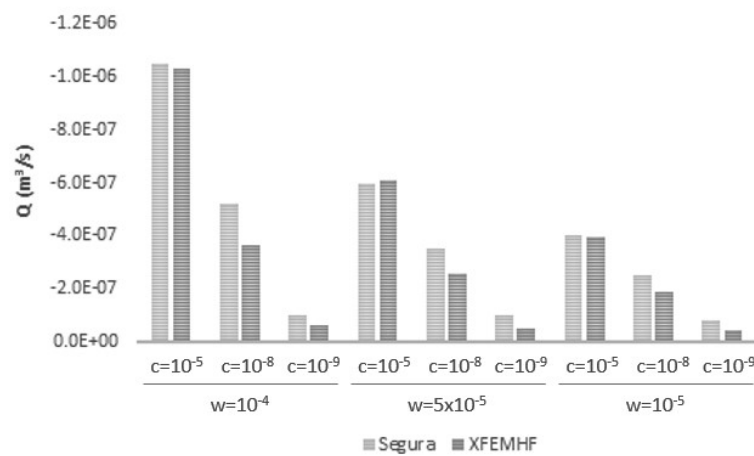
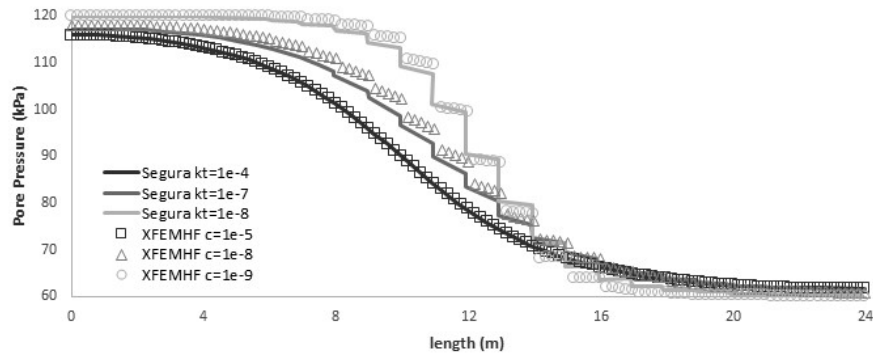
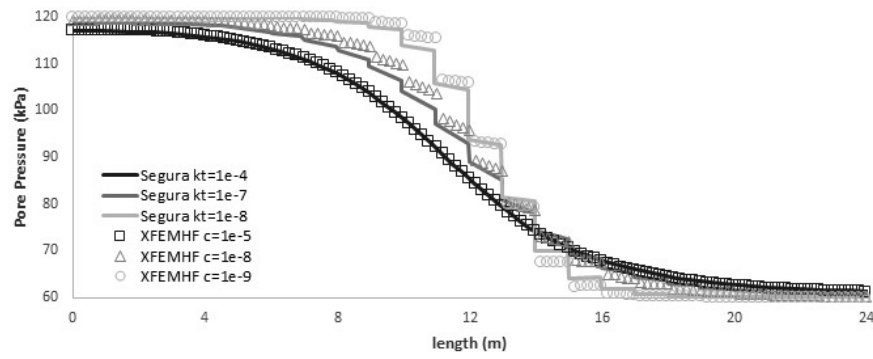


Figure 6.24 – Volumetric flow rate in models Dam1a to Dam1i

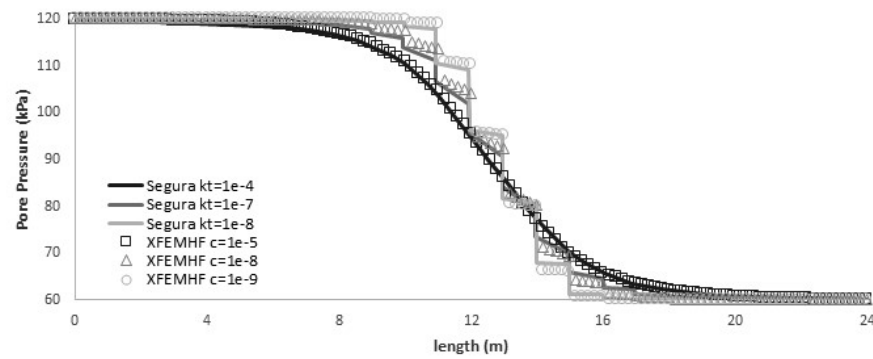
Although the comparison is made between different types of elements, it may be stated that the results show good agreement. It must be highlighted that the results from Segura and Carol (2004) were taken from printed plots, which may explain some of the differences. Other reasons may be the type mesh used by the authors and the way boundary conditions are applied, which were not detailed in the paper.



a)



b)



c)

Figure 6.25 – Pore Pressure values in section A-A. a) Models Dam1a, Dam1b and Dam1c – $w_{init}=10^{-4}$ m. b) Models Dam1d, Dam1e and Dam1f – $w_{init}=5 \times 10^{-5}$ m. c) Models Dam1g, Dam1h and Dam1i – $w_{init}=10^{-5}$ m.

Results – Set 2 of Calculations

In the second set of calculations, more fractures are introduced and higher fracture longitudinal permeabilities are used, so their effect is quantified. The values of the volumetric flow rates are presented in Figure 6.26 for comparison between models and the model Dam0 (without fractures) is used as benchmark. As seen in

Figure 6.27, the pore pressures field in model Dam0 shows a wide gradient of pore pressures along the model, with volumetric fluxes of the same order of magnitude of model Dam1a. As a new fracture is introduced with the same longitudinal transmissibility (model Dam2a), the volumetric fluxes increase as expected, as well as the pore-pressure gradients are more concentrated. However, with the increase of the longitudinal transmissibility of that single fracture (model Dam2b) a change of magnitude order of the volumetric flux is observed. It is also noticeable from Figure 6.28 that the gradient in the porous mediums reduces drastically, as almost all the pressure dissipates when the 10° fracture is reached. As expected, the increase of longitudinal transmissibility of this fracture creates a “canal” for the fluid to flow directly to the outer boundary.

The models Dam3a, Dam3b and Dam3c show that the hydraulic aperture and fracture position have much more influence in the flow than the number of fractures itself. As seen in Figure 6.29 together with Figure 6.26, the existing of a second set of fractures with the same longitudinal transmissibility increases the volumetric fluxes in a low level (model dam3a). However, an increase in the longitudinal transmissibility, as in models Dam3b and Dam3c, considerably increases the volumetric fluxes and changes the pore pressure gradients. The differences between models Dam3b and Dam3c show that the geometrical position of each set of fractures strongly influences the results, i.e. the increasing of longitudinal transmissibility is much more effective in fractures that are in a position that create paths for the fluid to flow easily. This is also supported if the fluxes and pore pressure fields of models Dam2b and Dam3b are compared. Despite the increasing in the volumetric fluxes, the presence of more fractures does not change the pore pressure fields considerably, as the single fracture of model Dam2b is the only fracture in model Dam3b that reaches directly the outer boundary of the model.

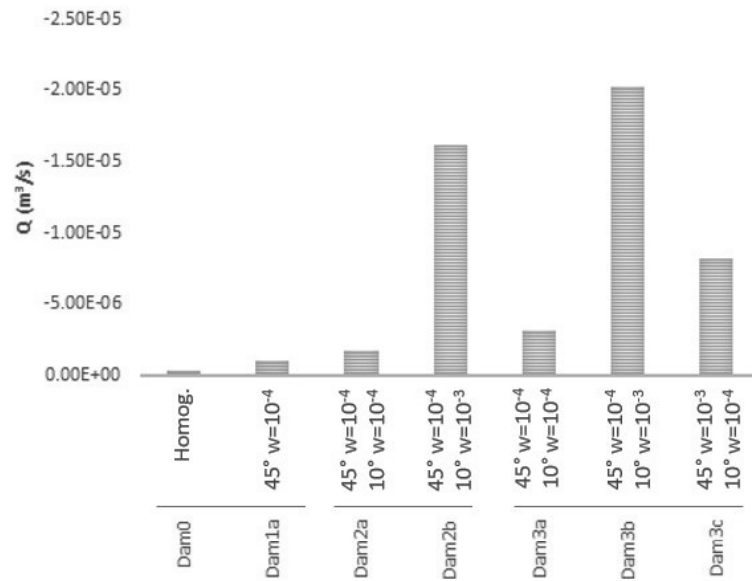


Figure 6.26 – Volumetric flow rate in models Dam0, Dam1a, Dam2a, Dam2b, Dam3a, Dam3b and Dam 3c

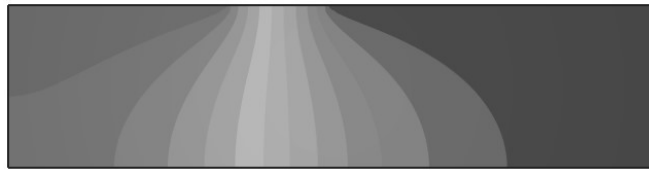
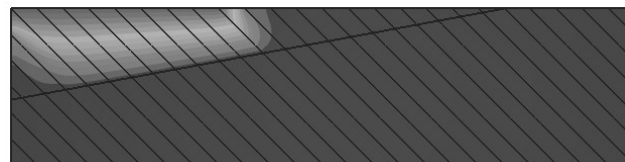


Figure 6.27 – Pore Pressure values for model Dam0 (colour scale: red is 120 kPa, blue is 60 kPa)

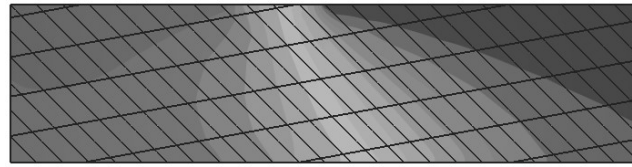


Dam2a ($45^\circ w_{\text{init}} = 1 \times 10^{-4}$, $10^\circ w_{\text{init}} = 1 \times 10^{-4}$)

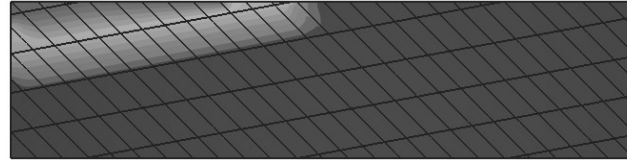


Dam2b ($45^\circ w_{\text{init}} = 1 \times 10^{-4}$, $10^\circ w_{\text{init}} = 1 \times 10^{-3}$)

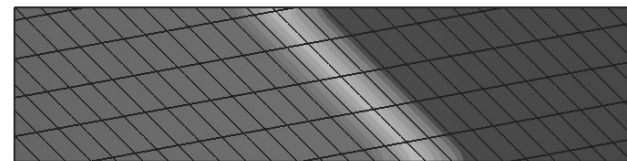
Figure 6.28 – Pore Pressure values for models Dam2a and Dam 2b (colour scale: red is 120 kPa, blue is 60 kPa)



Dam3a ($45^\circ w_{init} = 1 \times 10^{-4}$, $10^\circ w_{init} = 1 \times 10^{-4}$)



Dam3b ($45^\circ w_{init} = 1 \times 10^{-4}$, $10^\circ w_{init} = 1 \times 10^{-3}$)



Dam3c ($45^\circ w_{init} = 1 \times 10^{-3}$, $10^\circ w_{init} = 1 \times 10^{-4}$)

Figure 6.29 – Pore Pressure values for models Dam3a, Dam3b and Dam3c (colour scale: red is 120 kPa, blue is 60 kPa)

7 Conclusions

This thesis presents a new finite element based on the eXtended Finite Element Method, which is able to represent complex phenomena of fracture intersection and crossing with frictional behaviour. In addition, the formulation takes into account fully coupled behaviour with exchange of fluid between the fracture and the surrounding medium. The use of a fracture face transversal conductivity allows the eventual loss of pressure given by a filter cake when leak-off occurs.

The main objective of this thesis was achieved, as the implemented code provides very good predictions of the coupled fluid-rock fracture behaviour and is capable of correctly simulating the interaction between hydraulic and natural fractures. Overall, it may be stated that the implemented element can bring a valuable contribution to a deeper understanding of the phenomena involving propagation of hydraulic fractures in naturally fractured rocks. This knowledge is fundamental to the correct modelling of hydraulic fracturing in unconventional reservoirs.

During the development of each different step of the thesis, i.e. literature review, formulation, implementation and application, many interesting considerations were registered and can be compiled in the following items.

Literature Review

- The XFEM is a recent technique (~20 years) that is being applied by many researchers that work with fracture mechanics. The growing interest in this technique to simulate hydraulic fracturing is even more recent and noticeable by the increasing number of research works published in the past few years.
- A few research works have focused on using XFEM to simulate intersection between hydraulic and natural fractures and none was found that could show all the capabilities proposed in this work.

- Only a reduced number of laboratory tests to simulate the interaction between hydraulic and natural fracture were found. The results are usually interpreted qualitatively, i.e. by describing the behaviour of fracture interaction in different patterns, mainly crossing, arresting and opening.
- Very simple analytical solutions to predict the behaviour of fracture interaction exist. Those have shown to be accurate when compared with laboratory tests of interaction between one hydraulic and one natural fracture.

Formulation and Implementation

- The presented element formulation may be generalized for any number of discontinuities and intersections within the problem domain.
- The XFEM discretization only requires the presence of enriched degrees of freedom in the nodes surrounding the discontinuities, leading to a very reduced influence in the global jacobian matrix size.
- Independently of the fracture position, the degrees of freedom that store the enrichment for the displacements and the pore pressure are coincident with the original mesh. On the other hand, to take into account the variable of the fluid pressure within the fracture, extra degrees of freedom must be considered
- The implementation of the proposed XFEM element is complemented with two algorithms. The first defines the geometric attributes of the discontinuities, such as the values of the enrichment functions in the mesh nodes, position of the pressure fracture degrees of freedom, fracture intersections and position of the integration points in the integration sub-domains. The second algorithm computes if propagation occurs based in user defined criterion and which direction and length the propagating segment takes.
- Abaqus is a powerful tool that allows the use of several user subroutines to be integrated with the solver. The proposed element is completely implemented by using two user subroutines: UEL and UEXTERNALDB.
- Despite the high level of usability provided by Abaqus user subroutines, some difficulties arise from the fact that only part of the process is accessible, i.e. the Abaqus software architecture is fixed and cannot be adapted. The main limitations are the limited number of degrees of freedom per node and the need to activate all the degrees of freedom beforehand.

Application

- Comparisons of permanent regime models with interface elements (Chapter 5.2) shows very good agreement in the problems of flow in fractured medium.
- The numerical procedure proves to be very efficient in predicting the results obtained in laboratory tests (Chapter 6.1).
- The example in Chapter 6.2 shows the capability of the proposed XFEM element to simulate different fracture paths in complex fractured rocks. Not only the hydraulic fracture but also the natural fractures tips were able to propagate in any direction.
- In this thesis the effect of some parameters on interaction between propagating and natural fractures was also investigated. In agreement with the literature, the computed examples indicate that differential in-situ stresses and angles of approach play an essential role.
- However, other parameters may completely change the fracture network affected by the treatment, such as the initial hydraulic aperture, which is directly related with fracture roughness.
- The fracture face transversal conductivity coefficient c represents a transversal conductivity of the fracture for cases of percolation through fractured media. It is visible that a very low fracture face transversal conductivity makes the fracture play as a barrier to the fluid flow, while high values facilitate the percolation into the fracture.
- As any other method based in the FEM, the accuracy of results depends on mesh quality. However, by using the XFEM technique the mesh geometry takes a less important role, as seen in all the examples of this thesis, where regular meshes are used.
- It is evident that fractures may take unpredictable paths in fractured rocks. Therefore, XFEM is a very effective tool on modelling fracture propagation in fractured mediums, as there is no need to previously conform the mesh to the fracture path.

Further research and implementation work

- As stated widely in the literature, the tip behaviour has extreme influence on the way a fracture propagates. Therefore, it is recommended that specific tip

enrichment is implemented. Tip behaviour prediction may also be improved if more realistic constitutive models are used, such as a cohesive one.

- The propagation criterion has a strong influence on the path that the fracture follows. Further studies should be addressed with the objective of clarifying which criteria suit better to each kind of problem.
- Considering that it was shown that fracture transversal and longitudinal transmissibility strongly influence the behaviour of the hydraulic and natural fractures, further numerical and laboratory research should focus on defining different longitudinal transmissibility laws that consider effects such as fracture roughness.
- Modelling the presence of proppant within the injection fluid may bring further knowledge about screen out in the intersections between hydraulic and natural fractures.
- Fractures are surfaces that develop in a three-dimensional space. Although some simplification assumptions may be taken to obtain good results in plane strain models, realistic predictions of field problems can only be achieved with 3D models. It must be taken into account that the level of complexity strongly increases when implementing geometric pre and post-processors in 3D.

References

ADACHI, J. *ET AL.* **Computer simulation of hydraulic fractures**, International Journal of Rock Mechanics and Mining Sciences, 44(5), pp. 739–757. 2007.

ADACHI, J. I. AND DETOURNAY, E. **Plane strain propagation of a hydraulic fracture in a permeable rock**, Engineering Fracture Mechanics. Pergamon. , 75(16), pp. 4666–4694. 2008.

AGARWAL, K. AND SHARMA, M. M. **Modeling Fracture Propagation in Unconsolidated Sands**, 45th US Rock Mechanics/Geomechanics Symposium 2011.

AREIAS, P. M. A. AND BELYTSCHKO, T. **A comment on the article ‘A finite element method for simulation of strong and weak discontinuities in solid mechanics’ by A. Hansbo and P. Hansbo [Comput. Methods Appl. Mech. Engrg. 193 (2004) 3523-3540]**, Computer Methods in Applied Mechanics and Engineering, 195(9–12), pp. 1275–1276. 2006.

BAZANT, Z. P. AND PLANES, J. **Fracture and size effect in concrete and other quasibrittle materials**. CRC Press. 1998.

BELYTSCHKO, T. *ET AL.* **Arbitrary discontinuities in finite elements**, International Journal for Numerical Methods in Engineering, 50(4), pp. 993–1013. 2001.

BELYTSCHKO, T. AND BLACK, T. **Elastic crack growth in finite elements with minimal remeshing**, International Journal for Numerical Methods in Engineering, 45(5), pp. 601–620. 1999.

BENDEZU, M. A. L. *ET AL.* **Finite element modeling of the hydraulic fracture problem in impermeable media using a cohesive zone model**, in Proceedings of the XXXIV Iberian Latin-American Congress on Computational Methods in Engineering 2013.

BENZLEY, S. E. **Representation of singularities with isoparametric finite elements**, International Journal for Numerical Methods in Engineering. John Wiley & Sons, Ltd. , 8(3), pp. 537–545. 1974.

BLANTON, T. **An Experimental Study of Interaction Between Hydraulically Induced and Pre-Existing Fractures**, Proceedings of SPE Unconventional Gas Recovery Symposium, pp. 559–571. 1982.

DE BORST, R., REMMERS, J. J. C. AND NEEDLEMAN, A. **Mesh-independent discrete numerical representations of cohesive-zone models**, Engineering Fracture Mechanics, pp. 160–177. 2006.

DE BORST, R., RÉTHORÉ, J. AND ABELLAN, M.-A. **A Numerical Approach for Arbitrary Cracks in a Fluid-Saturated Medium**, Archive of Applied Mechanics. Springer-Verlag. , 75(10–12), pp. 595–606. 2006.

BUDYN, É. *ET AL.* **A method for multiple crack growth in brittle materials without remeshing**, International Journal for Numerical Methods in Engineering. John Wiley & Sons, Ltd. , 61(10), pp. 1741–1770. 2004.

BUNGER, A. P., DETOURNAY, E. AND GARAGASH, D. I. **Toughness-dominated hydraulic fracture with leak-off**, International Journal of Fracture. Kluwer Academic Publishers. , 134(2), pp. 175–190. 2005.

BUSETTI, S., MISH, K. AND RECHES, Z. **Damage and plastic deformation of reservoir rocks: Part 1. damage fracturing**, AAPG Bulletin, 96(9), pp. 1687–1709. 2012.

CARRIER, B. AND GRANET, S. **Numerical modeling of hydraulic fracture problem in permeable medium using cohesive zone model**, Engineering Fracture Mechanics, 79, pp. 312–328. 2012.

CARTER, B. J. *ET AL.* **Simulating fully 3D hydraulic fracturing**, in Modelling in geomechanics, pp. 526–556. 2000.

CARTER, B. J., INGRAFFEA, A. R. AND ENGELDER, T. **Modeling Ithaca's natural hydraulic fractures** 2000.

CARVALHO, M. T. M. DE, MARTHA, L. F. AND FILHO, W. C. **Pos3D** 1997.

CHEN, Y. Z. AND LIN, X. Y. **Numerical solution for the T-stress in branch crack problem with infinitesimal branch length**, Engineering Fracture Mechanics, 77(13), pp. 2593–2600. 2010.

CHEN, Z. *ET AL.* **Cohesive zone finite element-based modeling of hydraulic fractures**, Acta Mechanica Solida Sinica, 22(5), pp. 443–452. 2009.

CHEN, Z. **An ABAQUS Implementation of the XFEM for Hydraulic Fracture Problems**, International Conference for Effective and Sustainable Hydraulic Fracturing, pp. 725–739. 2013.

CHENG, W., JIN, Y., CHEN, M., *ET AL.* **A criterion for identifying hydraulic fractures crossing natural fractures in 3D space**, Petroleum Exploration and Development. Research Institute of Petroleum Exploration & Development, PetroChina. , 41(3), pp. 371–376. 2014.

CHENG, W., JIN, Y., CHEN, Y., *ET AL.* **Experimental Investigation about Influence of Natural Fracture on Hydraulic Fracture Propagation under Different Fracturing Parameters**, in 8th Asian Rock Mechanics Symposium, pp. 1712–1718. 2014.

CLIFTON, R. J. AND ABOU-SAYED, A. S. **A Variational Approach To The Prediction Of The Three-Dimensional Geometry Of Hydraulic Fractures**, in SPE/DOE Low Permeability Gas Reservoirs Symposium. Society of Petroleum Engineers. 1981.

COHEN, C. E., WENG, X. AND KRESSE, O. **Influence of fracturing fluid and reservoir temperature on production for complex hydraulic fracture network in shale gas reservoir**, Society of Petroleum Engineers - Asia Pacific Unconventional Resources Conference and Exhibition 2013: Delivering Abundant Energy for a Sustainable Future, 2(2012), pp. 922–941. 2013.

COMI, C. AND MARIANI, S. **Extended finite element simulation of quasi-brittle fracture in functionally graded materials**, Computer Methods in Applied Mechanics and Engineering, 196(41–44), pp. 4013–4026. 2007.

COX, J. V. **An extended finite element method with analytical enrichment for cohesive crack modeling**, International Journal for Numerical Methods in Engineering, 78(1), pp. 48–83. 2009.

CROUCH, S. L. AND STARFIELD, A. M. **Boundary Element Methods in Solid Mechanics. With Applications in Rock Mechanics**. Allen & Unwin. 1983.

DAHI-TALEGHANI, A. AND OLSON, J. E. **Numerical Modeling of Multistranded-Hydraulic-Fracture Propagation: Accounting for the Interaction Between Induced and Natural Fractures**, SPE Journal, 16(3), pp. 575–581. 2011.

DAMJANAC, B. *ET AL.* **Three-Dimensional Numerical Model of Hydraulic Fracturing in Fractured Rock Masses**, in Effective and Sustainable Hydraulic Fracturing. InTech. 2013.

DANESHY, A. A. **Hydraulic Fracture Propagation in the Presence of Planes of Weakness**, SPE European Spring Meeting. Society of Petroleum

Engineers. , pp. 1–5. 1974.

DAS, K. C. **Enriched finite element method and Applications in reinforced jointed rock mass**. Indian Institute of Technology Kharagpur 2013.

DAS, K. C., SANDHA, S. S. AND NARANG, A. **XFEM Formulation of Geomechanics Problems with Multiple Intersecting Discontinuities**, in 10th Biennial International Conference & Exposition 2013.

DAUX, C., MOES, N. AND DOLBOW, J. **Arbitrary branched and intersecting cracks with the extended finite element method**, International Journal for Numerical Methods in Engineering, 48(12), pp. 1741–1760. 2000.

DESROCHES, J. *ET AL.* **On the modelling of near tip processes in hydraulic fractures**, International Journal of Rock Mechanics and Mining Sciences and, 30(7), pp. 1127–1134. 1993.

DETOURNAY, E. **Propagation Regimes of Fluid-Driven Fractures in Impermeable Rocks**, International Journal of Geomechanics, 4(1), pp. 35–45. 2004.

DETOURNAY, E. AND GARAGASH, D. I. **The near-tip region of a fluid-driven fracture propagating in a permeable elastic solid**, Journal of Fluid Mechanics. Cambridge University Press. , 494, pp. 1–32. 2003.

DOLBOW, J., MOES, N. AND BELYTSCHKO, T. **An extended finite element method for modeling crack growth with frictional contact**, Computer Methods in Applied Mechanics and Engineering, 190(51–52), pp. 6825–6846. 2001.

DONG, C. Y. AND DE PATER, C. J. **Numerical implementation of displacement discontinuity method and its application in hydraulic fracturing**, Computer Methods in Applied Mechanics and Engineering, 191(8–10), pp. 745–760. 2001.

DUARTE, C. A., RENO, L. G. AND SIMONE, A. **A high-order generalized FEM for through-the-thickness branched cracks**, International Journal for Numerical Methods in Engineering. John Wiley & Sons, Ltd. , 72(3), pp. 325–351. 2007.

DYSKINA, A. V. AND CABALLERO, A. **Orthogonal crack approaching an interface**, Engineering Fracture Mechanics. Pergamon. , 76(16), pp. 2476–2485. 2009.

ELGUEDJ, T., GRAVOUIL, A. AND COMBESCURE, A. **A mixed augmented Lagrangian-extended finite element method for modelling elastic-plastic fatigue crack growth with unilateral contact**, International Journal for Numerical

Methods in Engineering. John Wiley & Sons, Ltd. , 71(13), pp. 1569–1597. 2007.

ESTERHUIZEN, G. S. **Extending empirical evidence through numerical modelling in rock engineering design**, Journal of the Southern African Institute of Mining and Metallurgy, 114(10), pp. 755–764. 2014.

FJAER, E. **Petroleum related rock mechanics**. Elsevier. 2008.

FRIES, T.-P. AND BAYDOUN, M. **Crack propagation with the extended finite element method and a hybrid explicit-implicit crack description**, International Journal for Numerical Methods in Engineering. John Wiley & Sons, Ltd. , 89(12), pp. 1527–1558. 2012.

FRIES, T.-P. AND BELYTSCHKO, T. **The extended/generalized finite element method: An overview of the method and its applications**, International Journal for Numerical Methods in Engineering. John Wiley & Sons, Ltd. , 84(3), p. n/a-n/a. 2010.

FRIES, T. P. **A corrected XFEM approximation without problems in blending elements**, International Journal for Numerical Methods in Engineering. John Wiley & Sons, Ltd. , 75(5), pp. 503–532. 2008.

GEERTSMA, J. AND DE KLERK, F. **A Rapid Method of Predicting Width and Extent of Hydraulically Induced Fractures**, Journal of Petroleum Technology. Society of Petroleum Engineers. , 21(12), pp. 1571–1581. 1969.

GINER, E. *ET AL.* **An Abaqus implementation of the extended finite element method**, Engineering Fracture Mechanics. Elsevier Ltd. , 76(3), pp. 347–368. 2009.

GRACIE, R. AND CRAIG. JAMES R. **Modelling well leakage in multilayer aquifer systems using the extended finite element method**, Finite Elements in Analysis and Design. Elsevier. , 46(6), pp. 504–513. 2010.

GRAVOUIL, A., PIERRES, E. AND BAIETTO, M. C. **Stabilized global-local X-FEM for 3D non-planar frictional crack using relevant meshes**, International Journal for Numerical Methods in Engineering. John Wiley & Sons, Ltd. , 88(13), pp. 1449–1475. 2011.

GRAZINA, J. C. D. **Modelação dinâmica com acoplamento viscoso de maciços elastoplásticos. Aplicação a estruturas de suporte flexíveis submetidas a acções sísmicas**. Universidade de Coimbra 2009.

GU, H. *ET AL.* **Hydraulic Fracture Crossing Natural Fracture at Nonorthogonal Angles: A Criterion and Its Validation**, SPE Production & Operations, 27(1), pp. 20–26. 2012.

HAMIDI, F. AND MORTAZAVI, A. **A new three dimensional approach to numerically model hydraulic fracturing process**, Journal of Petroleum Science and Engineering, 124, pp. 451–467. 2014.

HANSBO, A. AND HANSBO, P. **A finite element method for the simulation of strong and weak discontinuities in solid mechanics**, Computer Methods in Applied Mechanics and Engineering, 193(33–35), pp. 3523–3540. 2004.

HANSON, M. E., SHAFFER, R. J. AND ANDERSON, G. D. **Effects of Various Parameters on Hydraulic Fracturing Geometry**, Society of Petroleum Engineers Journal, 21(4), pp. 435–443. 1981.

HIRMAND, M., VAHAB, M. AND KHOEI, A. R. **An augmented Lagrangian contact formulation for frictional discontinuities with the extended finite element method**, Finite Elements in Analysis and Design. Elsevier. , 107, pp. 28–43. 2015.

HU, Y. *ET AL.* **Simulation of hydraulic fracturing in rock mass using a smeared crack model**, Computers & Structures, 137, pp. 72–77. 2014.

HUANG, H. *ET AL.* **On the use of enriched finite element method to model subsurface features in porous media flow problems**, Computational Geosciences. Springer Netherlands. , 15(4), pp. 721–736. 2011.

JI, H., CHOPP, D. AND DOLBOW, J. E. **A hybrid extended finite element/level set method for modeling phase transformations**, International Journal for Numerical Methods in Engineering. John Wiley & Sons, Ltd. , 54(8), pp. 1209–1233. 2002.

JIAO, J. AND QIAO, C. **Elasto-plastic analysis of jointed rock masses using the numerical manifold method**, in Boundaries of Rock Mechanics. Taylor & Francis. , pp. 83–88. 2008.

KARFAKIS, M. G. AND AKRAM, M. **Effects of chemical solutions on rock fracturing**, International Journal of Rock Mechanics and Mining Sciences and. Pergamon. , 30(7), pp. 1253–1259. 1993.

KESHAVERZI, R. AND JAHANBAKHSI, R. **Investigation of Hydraulic and Natural Fracture Interaction: Numerical Modeling or Artificial Intelligence?**, Effective and Sustainable Hydraulic Fracturing. InTech. , pp. 1039–1058. 2013.

KESHAVERZI, R., MOHAMMADI, S. AND BAYESTEH, H. **Hydraulic Fracture Propagation in Unconventional Reservoirs : The Role of Natural fractures**, 46th US Rock Mechanics Geomechanics Symposium, pp. 1–8, NaN-129. 2012.

KHOEI, A. R. **Extended Finite Element Method Theory and Applications** 2008.

KHOEI, A. R. *ET AL.* **A mesh-independent finite element formulation for modeling crack growth in saturated porous media based on an enriched-FEM technique**, International Journal of Fracture, 188(1), pp. 79–108. 2014.

KHOEI, A. R. *ET AL.* **An enriched FEM technique for modeling hydraulically driven cohesive fracture propagation in impermeable media with frictional natural faults: Numerical and experimental investigations**, International Journal for Numerical Methods in Engineering, 104(6), pp. 439–468. 2015.

KHOEI, A. R. AND NIKBAKHT, M. **Contact friction modeling with the extended finite element method (X-FEM)**, Journal of Materials Processing Technology, 177(1–3), pp. 58–62. 2006.

KHOEI, A. R. AND TAHERI MOUSAVI, S. M. **Modeling of large deformation - Large sliding contact via the penalty X-FEM technique**, Computational Materials Science. Elsevier. , 48(3), pp. 471–480. 2010.

KHOEI, A. R., VAHAB, M. AND HIRMAND, M. **Modeling the interaction between fluid-driven fracture and natural fault using an enriched-FEM technique**, International Journal of Fracture, 197(1), pp. 1–24. 2016.

KHRISTIANOVIC, S. A. AND ZHELTOV, Y. P. **Formation of Vertical Fractures by Means of Highly Viscous Liquid**, Proceeding of the 4th World Petroleum Congress. World Petroleum Congress. , 5, pp. 579–586. 1955.

KRESSE, O. *ET AL.* **Numerical Modeling of Hydraulic Fracturing In Naturally Fractured Formations**, Hydraulic Fracturing Quarterly. American Rock Mechanics Association. , 1(1), pp. 61–68. 2014.

LAMB, A. R., GORMAN, G. J. AND ELSWORTH, D. **A fracture mapping and extended finite element scheme for coupled deformation and fluid flow in fractured porous media**, International Journal for Numerical and Analytical Methods in Geomechanics, 37(17), pp. 2916–2936. 2013.

LAMONT, N. AND JESSEN, F. W. **The Effects of Existing Fractures in Rocks on the Extension of Hydraulic Fractures**, Journal of Petroleum Technology, 15(2), pp. 203–209. 1963.

LECAMPION, B. **An extended finite element method for hydraulic fracture problems**, Communications in Numerical Methods in Engineering. John Wiley &

Sons, Ltd. , 25(2), pp. 121–133. 2009.

LEE, S.-H. *ET AL.* **Combined extended and superimposed finite element method for cracks**, International Journal for Numerical Methods in Engineering. John Wiley & Sons, Ltd. , 59(8), pp. 1119–1136. 2004.

LENOACH, B. **The crack tip solution for hydraulic fracturing in a permeable solid**, Journal of the Mechanics and Physics of Solids. Pergamon. , 43(7), pp. 1025–1043. 1995.

LI, L. C. *ET AL.* **Numerical simulation of 3D hydraulic fracturing based on an improved flow-stress-damage model and a parallel FEM technique**, Rock Mechanics and Rock Engineering, 45(5), pp. 801–818. 2012.

LI, Q. *ET AL.* **A review on hydraulic fracturing of unconventional reservoir**, Petroleum. Elsevier Ltd. , 1(1), pp. 8–15. 2015.

LIU, F. AND BORJA, R. I. **A contact algorithm for frictional crack propagation with the extended finite element method**, International Journal for Numerical Methods in Engineering. John Wiley & Sons, Ltd. , 76(10), pp. 1489–1512. 2008.

MARIANI, S. AND PEREGO, U. **Extended finite element method for quasi-brittle fracture**, International Journal for Numerical Methods in Engineering, 58(1), pp. 103–126. 2003.

MELENK, J. M. AND BABUŠKA, I. **The partition of unity finite element method: basic theory and applications**, Research report / Seminar für Angewandte Mathematik. Eidgenössische Technische Hochschule, Seminar für Angewandte Mathematik. , 1996(1)1996.

MENDES, C. A. T., GATTASS, M. AND ROEHL, D. **The GeMA framework – An innovative framework for the development of multiphysics and multiscale simulations**, in VII European Congress on Computational Methods in Applied Sciences and Engineering, pp. 5–10. 2016.

MERGHEIM, J., KUHLE, E. AND STEINMANN, P. **A finite element method for the computational modelling of cohesive cracks**, International Journal for Numerical Methods in Engineering, 63(2), pp. 276–289. 2005.

MEYER, B. R. **Three-Dimensional Hydraulic Fracturing Simulation on Personal Computers: Theory and Comparison Studies**, in SPE Eastern Regional Meeting. Society of Petroleum Engineers. 1989.

MIRANDA, A. C. DE O. AND MARTHA, L. F. **Hierarchical template-based**

quadrilateral mesh generation, Engineering with Computers. Springer London. , 33(4), pp. 701–715. 2017.

MOËS, N. AND BELYTSCHKO, T. **Extended finite element method for cohesive crack growth**, Engineering Fracture Mechanics, 69(7), pp. 813–833. 2002.

MOES, N. AND DOLBOW, J. **A finite element method for crack growth without remeshing**, Int. J. Numer., 150(February), pp. 131–150. 1999.

MOHAMMADNEJAD, T. AND ANDRADE, J. E. **Numerical modeling of hydraulic fracture propagation, closure and reopening using XFEM with application to in-situ stress estimation**, International Journal for Numerical and Analytical Methods in Geomechanics, 40(15), pp. 2033–2060. 2016.

MOHAMMADNEJAD, T. AND KHOEI, A. R. **Hydro-mechanical modeling of cohesive crack propagation in multiphase porous media using the extended finite element method**, International Journal for Numerical and Analytical Methods in Geomechanics, 37(10), pp. 1247–1279. 2013.

MOUGAARD, J. F., POULSEN, P. N. AND NIELSEN, L. O. **An enhanced cohesive crack element for XFEM using a double enriched displacement field**, 6th International Conference on Fracture Mechanics of Concrete and Concrete Structures, pp. 139–146. 2007.

MURPHY, H. D. AND FEHLER, M. C. **Hydraulic Fracturing of Jointed Formations**, in International Meeting on Petroleum Engineering. Society of Petroleum Engineers. 1986.

NAGEL, N. *ET AL.* **Simulating Hydraulic Fracturing in Real Fractured Rocks-Overcoming the Limits of Pseudo3D Models**, SPE Hydraulic Fracturing Technology Conference, 24-26 January, The Woodlands, Texas, (2010)2011.

NISTOR, I. *ET AL.* **An X-FEM approach for large sliding contact along discontinuities**, International Journal for Numerical Methods in Engineering. John Wiley & Sons, Ltd. , 78(12), pp. 1407–1435. 2009.

NORDGREN, R. P. **Propagation of a Vertical Hydraulic Fracture**, Society of Petroleum Engineers Journal. Society of Petroleum Engineers. , 12(4), pp. 306–314. 1972.

PAPANASTASIOU, P. **The effective fracture toughness in hydraulic fracturing**, International Journal of Fracture, 96(2), pp. 127–147. 1999.

PERKINS, T. K. AND KERN, L. R. **Widths of Hydraulic Fractures**, Journal of

Petroleum Technology. Society of Petroleum Engineers. , 13(9), pp. 937–949. 1961.

POTTS, D. M. AND ZDRAVKOVIĆ, L. **Finite element analysis in geotechnical engineering : theory**. Telford. 1999.

RAHIM, Z. *ET AL.* **Improved Gas Recovery - 2 (Conclusion): Productivity increase using hydraulic fracturing—expectation vs. reality**. 2012.

REMIJ, E. W. *ET AL.* **The enhanced local pressure model for the accurate analysis of fluid pressure driven fracture in porous materials**, Computer Methods in Applied Mechanics and Engineering. Elsevier B.V. , 286, pp. 293–312. 2015.

RENSHAW, C. E. AND POLLARD, D. D. **An experimentally verified criterion for propagation across unbounded frictional interface in brittle, linear elastic materials**, Int. J. Rock Mech. Min. Sci. & Geomech., 32(3), pp. 237–249. 1995.

RÉTHORÉ, J., BORST, R. DE AND ABELLAN, M.-A. **A two-scale approach for fluid flow in fractured porous media**, International Journal for Numerical Methods in Engineering. John Wiley & Sons, Ltd. , 71(7), pp. 780–800. 2006.

RÉTHORÉ, J., DE BORST, R. AND ABELLAN, M.-A. **A discrete model for the dynamic propagation of shear bands in a fluid-saturated medium**, International Journal for Numerical and Analytical Methods in Geomechanics. John Wiley & Sons, Ltd. , 31(2), pp. 347–370. 2007.

RUEDA, J. C. *ET AL.* **Numerical models for detection of fault reactivation in oil and gas fields**, American Rock Mechanics Association, (ARMA 14-7354) 2014.

SALIMZADEH, S. AND KHALILI, N. **A three-phase XFEM model for hydraulic fracturing with cohesive crack propagation**, Computers and Geotechnics. Elsevier Ltd. , 69, pp. 82–92. 2015.

SEGURA, J. M. AND CAROL, I. **On zero-thickness interface elements for diffusion problems**, International Journal for Numerical and Analytical Methods in Geomechanics, 28(9), pp. 947–962. 2004.

SETHIAN, J. A. **A fast marching level set method for monotonically advancing fronts.**, Proceedings of the National Academy of Sciences of the United States of America. National Academy of Sciences. , 93(4), pp. 1591–5. 1996.

SETTARI, A. **Quantitative Analysis of Factors Influencing Vertical and Lateral Fracture Growth**, SPE Production Engineering. Society of Petroleum Engineers. , 3(3), pp. 310–322. 1988.

SHENG, M. *ET AL.* **Enriched finite elements for branching cracks in deformable porous media**, Engineering Analysis with Boundary Elements. Elsevier. , 50, pp. 435–446. 2015.

SHIMIZU, H., MURATA, S. AND ISHIDA, T. **The distinct element analysis for hydraulic fracturing in hard rock considering fluid viscosity and particle size distribution**, International Journal of Rock Mechanics and Mining Sciences, 48(5), pp. 712–727. 2011.

SHOJAEI, A., DAHI TALEGHANI, A. AND LI, G. **A continuum damage failure model for hydraulic fracturing of porous rocks**, International Journal of Plasticity. Elsevier Ltd. , 59, pp. 199–212. 2014.

SIANELIS, M. *ET AL.* **Large sliding contact along branched discontinuities with X-FEM**, Computational Mechanics, 52(1), pp. 201–219. 2013.

SILVA, P. A. B. V. DA **Uma Implementação do Método Estendido dos Elementos Finitos para Análise de Propagação de Fraturas Bidimensionais**, p. 105. 2015.

SILVESTRE, J. R. *ET AL.* **Modelling of coupled fluid-mechanical problems in fractured geological media using enriched finite elements**, International Journal for Numerical and Analytical Methods in Geomechanics, 39(10), pp. 1104–1140. 2015.

SIMULIA **Abaqus v6.14**, Abaqus Documentation. Providence, RI, USA 2014.

SNEDDON, I. N. **The Distribution of Stress in the Neighbourhood of a Crack in an Elastic Solid**, Proceedings of the Royal Society A: Mathematical, Physical and Engineering Sciences. The Royal Society. , 187(1009), pp. 229–260. 1946.

SOBHANIARAGH, B., MANSUR, W. J. AND PETERS, F. C. **Three-dimensional investigation of multiple stage hydraulic fracturing in unconventional reservoirs**, Journal of Petroleum Science and Engineering. Elsevier. , 146, pp. 1063–1078. 2016.

SONG, J. H., AREIAS, P. M. A. AND BELYTSCHKO, T. **A method for dynamic crack and shear band propagation with phantom nodes**, International Journal for Numerical Methods in Engineering, 67(6), pp. 868–893. 2006.

SOUSA, J. ., CARTER, B. J. AND INGRAFFEA, A. R. **Numerical simulation of 3D hydraulic fracture using Newtonian and power-law fluids**, International Journal of Rock Mechanics and Mining Sciences & Geomechanics Abstracts.

Pergamon. , 30(7), pp. 1265–1271. 1993.

STAZI, F. L. *ET AL.* **An extended finite element method with higher-order elements for curved cracks**, Computational Mechanics. Springer-Verlag. , 31(1–2), pp. 38–48. 2003.

SUKUMAR, N. *ET AL.* **Extended finite element method for three-dimensional crack modelling**, International Journal for Numerical Methods in Engineering, 48(11), pp. 1549–1570. 2000.

SUKUMAR, N. *ET AL.* **Three-dimensional non-planar crack growth by a coupled extended finite element and fast marching method**, International Journal for Numerical Methods in Engineering. John Wiley & Sons, Ltd. , 76(5), pp. 727–748. 2008.

VALKÓ, P. AND ECONOMIDES, M. J. **Hydraulic fracture mechanics**. Wiley. 1995.

VENTURA, G., BUDYN, E. AND BELYTSCHKO, T. **Vector level sets for description of propagating cracks in finite elements**, International Journal for Numerical Methods in Engineering. John Wiley & Sons, Ltd. , 58(10), pp. 1571–1592. 2003.

WANG, H. Y. **Numerical investigation of fracture spacing and sequencing effects on multiple hydraulic fracture interference and coalescence in brittle and ductile reservoir rocks**, Engineering Fracture Mechanics. Pergamon. , 157, pp. 107–124. 2016.

WANG, T. *ET AL.* **Simulation of hydraulic fracturing using particle flow method and application in a coal mine**, International Journal of Coal Geology. Elsevier. , 121, pp. 1–13. 2014.

WARPINSKI, N. *ET AL.* **Hydraulic fracture model comparison study: Complete results** 1993.

WARPINSKI, N. R. AND SMITH, M. B. **Recent Advances in Hydraulic fracturing**, in Recent Advances in Hydraulic fracturing. Richardson. , pp. 57–80. 1989.

WARPINSKI, N. R. AND TEUFEL, L. W. **Influence of Geologic Discontinuities on Hydraulic Fracture Propagation**, Journal of Petroleum Technology, 39(2), pp. 209–220. 1987.

WELLS, G. N. AND SLUYS, L. J. **A new method for modelling cohesive cracks using finite elements**, International Journal for Numerical Methods in

Engineering, 50(12), pp. 2667–2682. 2001.

WITHERSPOON, P. A. *ET AL.* **Validity of Cubic Law for fluid flow in a deformable rock fracture**, Water Resources Research, 16(6), pp. 1016–1024. 1980.

XU, B. AND WONG, R. C. K. **A 3d finite element model for history matching hydraulic fracturing in unconsolidated sands formation**, Journal of Canadian Petroleum Technology, 49(4), pp. 58–66. 2010.

YAO, Y. *ET AL.* **Cohesive Fracture Mechanics Based Analysis to Model Ductile Rock Fracture**, 44th US Rock Mechanics Symposium, (2)2010.

YOUN, D.-J. **Hydro-mechanical coupled simulation of hydraulic fracturing using the extended finite element method (XFEM)**, PhD Thesis. Colorado School of Mines. Arthur Lakes Library. Colorado School of Mines. Arthur Lakes Library. 2016.

ZHANG, G. M. *ET AL.* **Three-dimensional finite element simulation and parametric study for horizontal well hydraulic fracture**, Journal of Petroleum Science and Engineering, 72(3–4), pp. 310–317. 2010.

ZHANG, X. AND JEFFREY, R. G. **The role of friction and secondary flaws on deflection and re-initiation of hydraulic fractures at orthogonal pre-existing fractures**, Geophysical Journal International, 166(3), pp. 1454–1465. 2006.

ZHANG, Z. AND GHASSEMI, A. **Simulation of hydraulic fracture propagation near a natural fracture using virtual multidimensional internal bonds**, International Journal for Numerical and Analytical Methods in Geomechanics. John Wiley & Sons, Ltd. , 35(4), pp. 480–495. 2011.

ZHOU, J. *ET AL.* **Analysis of fracture propagation behavior and fracture geometry using a tri-axial fracturing system in naturally fractured reservoirs**, International Journal of Rock Mechanics and Mining Sciences. Pergamon. , 45(7), pp. 1143–1152. 2008.

ZHOU, J. AND XUE, C. **Experimental Investigation of Fracture Interaction between Natural Fractures and Hydraulic Fracture in Naturally Fractured Reservoirs**, Proceedings of SPE EUROPEC/EAGE Annual Conference and Exhibition, (May 2011), pp. 1–12. 2011.

ZHOU, L. AND HOU, M. Z. **A new numerical 3D-model for simulation of hydraulic fracturing in consideration of hydro-mechanical coupling effects**, International Journal of Rock Mechanics and Mining Sciences. Elsevier. , 60, pp.

370–380. 2013.

ZI, G. *ET AL.* **A method for growing multiple cracks without remeshing and its application to fatigue crack growth**, Modelling and Simulation in Materials Science and Engineering. IOP Publishing. , 12(5), pp. 901–915. 2004.

ZI, G. AND BELYTSCHKO, T. **New crack-tip elements for XFEM and applications to cohesive cracks**, International Journal for Numerical Methods in Engineering, 57(15), pp. 2221–2240. 2003.

ZIELONKA, M. G. *ET AL.* **Development and Validation of Fully-Coupled Hydraulic Fracturing Simulation Capabilities**, SIMULIA Community Conference, SCC2014, pp. 1–31. 2014.

ZIENKIEWICZ, O. C., TAYLOR, R. L. (ROBERT L. AND ZHU, J. Z. **Finite element method : its basis and fundamentals**. Butterworth-Heinemann. 2013.

Annex A

Resulting space discretization

The weak formulation of the differential equations gives the following equalities (repeated from equations presented in Chapter 3 of the main document):

$$\begin{aligned} \int_{\Omega} \delta \varepsilon. \sigma' d\Omega - \int_{\Omega} \delta \varepsilon. m. p d\Omega + \int_{\Gamma_d} \llbracket \delta u \rrbracket (t_F - p_F. n_{\Gamma_d}) d\Gamma \\ - \int_{\Gamma_t} \delta u. \bar{t} d\Gamma = 0 \end{aligned} \quad (\text{A.1})$$

$$\begin{aligned} \int_{\Omega} \nabla \delta p k_f \nabla p d\Omega + \int_{\Gamma_d} \delta p \llbracket \dot{w} \rrbracket n_{\Gamma_d} d\Gamma + \int_{\Omega} \delta p. \nabla \dot{u} d\Omega \\ + \int_{\Gamma_w} \delta p. \bar{q} d\Gamma = 0 \end{aligned} \quad (\text{A.2})$$

$$\begin{aligned} \int_{\Gamma_d} \frac{\partial \delta p_F}{\partial x'} k_{f_F} 2h. \frac{\partial p_F}{\partial x'} d\Gamma - \int_{\Gamma_d} \delta p_F q_F n_{\Gamma_d} d\Gamma + \\ \int_{\Gamma_d} \delta p_F 2h. \langle \frac{\partial \dot{u}_{x'}}{\partial x'} \rangle d\Gamma + \int_{\Gamma_d} \delta p_F. \llbracket \dot{u}_{y'} \rrbracket d\Gamma = 0 \end{aligned} \quad (\text{A.3})$$

It may be admitted that the test functions δu , δp and δp_F follow the same discretization rules as the variables u , p and p_F . It is also considered that the vector of the nodal variables for each element node is given by \bar{u} . Although generalized for any number of enriched degrees of freedom, for the sake of clearness the discretization is developed for one enriched displacement variable a and one enriched pressure variable p_a . Eq. (A.4) to Eq. (A.16) present the discretization of the variables and their derivatives.

$$u = N_u^{std} \bar{u} + N_u^{enr} \bar{a} \quad (\text{A.4})$$

$$\delta u = N_u^{std} \delta \bar{u} + N_u^{enr} \delta \bar{a} \quad (\text{A.5})$$

$$\llbracket u \rrbracket = \llbracket N_u^{std} \rrbracket \bar{u} + \llbracket N_u^{enr} \rrbracket \bar{a} = \llbracket N_u^{enr} \rrbracket \bar{a} \quad (\text{A.6})$$

$$\varepsilon = B_u^{std} \bar{u} + B_u^{enr} \bar{a} \quad (\text{A.7})$$

$$\delta \varepsilon = B_u^{std} \delta \bar{u} + B_u^{enr} \delta \bar{a} \quad (\text{A.8})$$

$$\nabla \dot{u} = B_u^{std} \dot{\bar{u}} + B_u^{enr} \dot{\bar{a}} \quad (\text{A.9})$$

$$p = N_p^{std} \bar{p} + N_p^{enr} \bar{p}_a \quad (\text{A.10})$$

$$\delta p = N_p^{std} \delta \bar{p} + N_p^{enr} \delta \bar{p}_a \quad (\text{A.11})$$

$$\nabla p = B_p^{std} \bar{p} + B_p^{enr} \bar{p}_a \quad (\text{A.12})$$

$$\delta \nabla p = B_p^{std} \delta \bar{p} + B_p^{enr} \delta \bar{p}_a \quad (\text{A.13})$$

$$p_F = N_{p_F}^{std} \bar{p}_F \quad (\text{A.14})$$

$$\delta p_F = N_{p_F}^{std} \delta \bar{p}_F \quad (\text{A.15})$$

$$\nabla p_F = B_{p_F}^{std} \bar{p}_F \quad (\text{A.16})$$

Replacing the variables in Eq. (3.14), the following equation is obtained

$$\begin{aligned} & \int_{\Omega} \delta \varepsilon . D . \varepsilon d\Omega - \int_{\Omega} \delta \varepsilon . m . p d\Omega + \int_{\Gamma_d} \llbracket \delta u \rrbracket (t_F - p_F . n_{\Gamma_d}) d\Gamma \\ & - \int_{\Gamma_t} \delta u . \bar{t} d\Gamma \\ & = \int_{\Omega} (B_u^{std})^T \delta \bar{u} D B_u^{std} \bar{u} d\Omega \\ & + \int_{\Omega} (B_u^{std})^T \delta \bar{u} D B_u^{enr} \bar{a} d\Omega \\ & + \int_{\Omega} (B_u^{enr})^T \delta \bar{a} D B_u^{std} \bar{u} d\Omega \\ & + \int_{\Omega} (B_u^{enr})^T \delta \bar{a} D B_u^{enr} \bar{a} d\Omega \\ & - \int_{\Omega} m (B_u^{std})^T \delta \bar{u} N_p^{std} \bar{p} d\Omega \\ & - \int_{\Omega} m (B_u^{std})^T \delta \bar{u} N_p^{enr} \bar{p}_a d\Omega \\ & - \int_{\Omega} m (B_u^{enr})^T \delta \bar{a} N_p^{std} \bar{p} d\Omega \\ & - \int_{\Omega} m (B_u^{enr})^T \delta \bar{a} N_p^{enr} \bar{p}_a d\Omega \\ & + \int_{\Gamma_d} \llbracket N_u^{enr} \rrbracket^T \delta \bar{a} D_F \llbracket N_u^{enr} \rrbracket \bar{a} d\Gamma \\ & + \int_{\Gamma_d} \llbracket N_u^{enr} \rrbracket^T \delta \bar{a} (-p_F n_{\Gamma_d}) d\Gamma \\ & - \int_{\Gamma_t} (N_u^{std})^T \delta \bar{u} \bar{t} d\Gamma - \int_{\Gamma_t} (N_u^{enr})^T \delta \bar{a} \bar{t} d\Gamma \\ & = 0 \end{aligned} \quad (\text{A.17})$$

Assembling the test functions, it gives

$$\begin{aligned}
\delta \bar{u} \left\{ \int_{\Omega} (B_u^{std})^T D B_u^{std} \bar{u} d\Omega + \int_{\Omega} (B_u^{std})^T D B_u^{enr} \bar{a} d\Omega \right. \\
- \int_{\Omega} m (B_u^{std})^T N_p^{std} \bar{p} d\Omega \\
- \int_{\Omega} m (B_u^{std})^T N_p^{enr} \bar{c} d\Omega - \int_{\Gamma_t} (N_u^{std})^T \bar{t} d\Gamma \Big\} \\
+ \delta \bar{a} \left\{ \int_{\Omega} (B_u^{enr})^T D B_u^{std} \bar{u} d\Omega \right. \\
+ \int_{\Omega} (B_u^{enr})^T D B_u^{enr} \bar{a} d\Omega \\
- \int_{\Omega} m (B_u^{enr})^T N_p^{std} \bar{p} d\Omega \\
- \int_{\Omega} m (B_u^{enr})^T N_p^{enr} \bar{p}_a d\Omega \\
+ \int_{\Gamma_d} \llbracket N_u^{enr} \rrbracket^T D_F \llbracket N_u^{enr} \rrbracket \bar{a} d\Gamma \\
- \int_{\Gamma_d} \llbracket N_u^{enr} \rrbracket^T (p_F n_{\Gamma_d}) d\Gamma - \int_{\Gamma_t} (N_u^{enr})^T \bar{t} d\Gamma \Big\} \\
= 0
\end{aligned} \tag{A.18}$$

Considering that this condition is valid for any test function, the term within the brackets must equal zero. Arranging the terms into a matrix form, the following relation is obtained

$$\begin{bmatrix} K_{uu} & K_{ua} \\ K_{au} & K_{aa} \end{bmatrix} \begin{Bmatrix} \bar{u} \\ \bar{a} \end{Bmatrix} - \begin{bmatrix} Q_{up} & Q_{uc} \\ Q_{ap} & Q_{ac} \end{bmatrix} \begin{Bmatrix} \bar{p} \\ \bar{p}_a \end{Bmatrix} = \begin{Bmatrix} f_u^{ext} \\ f_a^{ext} \end{Bmatrix} - \begin{Bmatrix} f_u^{int} \\ f_a^{int} \end{Bmatrix} \tag{A.19}$$

where

$$K_{uu} = \int_{\Omega} (B_u^{std})^T D B_u^{std} d\Omega \tag{A.20}$$

$$K_{ua} = \int_{\Omega} (B_u^{std})^T D B_u^{enr} d\Omega \tag{A.21}$$

$$K_{au} = \int_{\Omega} (B_u^{enr})^T D B_u^{std} d\Omega \tag{A.22}$$

$$K_{aa} = \int_{\Omega} (B_u^{enr})^T D B_u^{enr} d\Omega \tag{A.23}$$

$$Q_{up} = \int_{\Omega} (B_u^{std})^T m N_p^{std} d\Omega \tag{A.24}$$

$$Q_{uc} = \int_{\Omega} (B_u^{std})^T m N_p^{enr} d\Omega \quad (\text{A.25})$$

$$Q_{ap} = \int_{\Omega} (B_u^{enr})^T m N_p^{std} d\Omega \quad (\text{A.26})$$

$$Q_{ac} = \int_{\Omega} (B_u^{enr})^T m N_p^{enr} d\Omega \quad (\text{A.27})$$

$$f_u^{ext} = - \int_{\Gamma_t} (N_u^{std})^T \bar{t} d\Gamma \quad (\text{A.28})$$

$$f_a^{ext} = \int_{\Gamma_t} (N_u^{enr})^T \bar{t} d\Gamma \quad (\text{A.29})$$

$$f_u^{int} = 0 \quad (\text{A.30})$$

$$f_a^{int} = \int_{\Gamma_d} \llbracket N_u^{enr} \rrbracket^T D_F \bar{a} d\Gamma - \int_{\Gamma_d} \llbracket N_u^{enr} \rrbracket^T (p_F n_{\Gamma_d}) d\Gamma \quad (\text{A.31})$$

$$m = \{1 \quad 1 \quad 0\}^T \quad (\text{A.32})$$

Generalizing the equations and terms, it gives

$$[K]\{\bar{\mathbb{U}}\} - [Q]\{\bar{\mathbb{P}}\} + f_{\mathbb{U}}^{int} - f_{\mathbb{U}}^{ext} = 0 \quad (\text{A.33})$$

$$K_{\beta\gamma} = \int_{\Omega} (B_u^{\beta})^T D B_u^{\gamma} d\Omega \quad (\text{A.34})$$

$$Q_{\beta\zeta} = \int_{\Omega} (B_u^{\beta})^T m N_p^{\zeta} d\Omega \quad (\text{A.35})$$

$$f_{\beta}^{int} = \int_{\Gamma_d} \llbracket N_u^{\beta} \rrbracket^T D_F \bar{\beta} d\Gamma - \int_{\Gamma_d} \llbracket N_u^{\beta} \rrbracket^T (p_F n_{\Gamma_d}) d\Gamma \quad (\text{A.36})$$

$$f_{\beta}^{ext} = \int_{\Gamma_t} (N_u^{\beta})^T \bar{t} d\Gamma \quad (\text{A.37})$$

For the continuity in the porous region, the replacement of Eqs. (A.4) to (A.16) in Eq. (A.2) gives

$$\begin{aligned}
& \int_{\Omega} \nabla \delta p k_f \nabla p \, d\Omega + \int_{\Gamma_d} \delta p \cdot c(p - p_F) n_{\Gamma_d} \, d\Gamma + \int_{\Omega} \delta p \cdot \nabla \dot{u} \, d\Omega \\
& + \int_{\Gamma_w} \delta p \cdot \bar{q} \, d\Gamma \\
& = \int_{\Omega} (B_p^{std})^T \delta \bar{p} k_f B_p^{std} \bar{p} \, d\Omega \\
& + \int_{\Omega} (B_p^{std})^T \delta \bar{p} k_f B_p^{enr} \bar{p}_a \, d\Omega \\
& + \int_{\Omega} (B_p^{enr})^T \delta \bar{p}_a k_f B_p^{std} \bar{p} \, d\Omega \\
& + \int_{\Omega} (B_p^{enr})^T \delta \bar{p}_a k_f B_p^{enr} \bar{p}_a \, d\Omega \\
& + \int_{\Gamma_d} (N_p^{std})^T \delta \bar{p} c N_p^{std} \bar{p} \, d\Gamma \\
& + \int_{\Gamma_d} (N_p^{std})^T \delta \bar{p} c N_p^{enr} \bar{p}_a \, d\Gamma \\
& + \int_{\Gamma_d} (N_p^{enr})^T \delta \bar{p}_a c N_p^{std} \bar{p} \, d\Gamma \\
& + \int_{\Gamma_d} (N_p^{enr})^T \delta \bar{p}_a c N_p^{enr} \bar{p}_a \, d\Gamma \\
& - \int_{\Gamma_d} (N_p^{std})^T \delta \bar{p} c N_{p_F}^{std} \bar{p}_F \, d\Gamma \\
& - \int_{\Gamma_d} (N_p^{enr})^T \delta \bar{p}_a c N_{p_F}^{std} \bar{p}_F \, d\Gamma \\
& + \int_{\Omega} (N_p^{std})^T \delta \bar{p} m B_u^{std} \dot{\bar{u}} \, d\Omega \\
& + \int_{\Omega} (N_p^{std})^T \delta \bar{p} m B_u^{enr} \dot{\bar{a}} \, d\Omega \\
& + \int_{\Omega} (N_p^{enr})^T \delta \bar{p}_a m B_u^{std} \dot{\bar{u}} \, d\Omega \\
& + \int_{\Omega} (N_p^{enr})^T \delta \bar{p}_a m B_u^{enr} \dot{\bar{a}} \, d\Omega \\
& + \int_{\Gamma_w} (N_p^{std})^T \delta \bar{p} \bar{q} \, d\Gamma + \int_{\Gamma_w} (N_p^{enr})^T \delta \bar{p}_a \bar{q} \, d\Gamma \\
& = 0
\end{aligned} \tag{A.38}$$

Assembling the test functions, it gives

$$\begin{aligned}
\delta \bar{p} \Big\{ & \int_{\Omega} (B_p^{std})^T k_F B_p^{std} \bar{p} d\Omega + \int_{\Omega} (B_p^{std})^T k_F B_p^{enr} \bar{p}_a d\Omega \\
& + \int_{\Gamma_w} (N_p^{std})^T \bar{q} d\Gamma + \int_{\Omega} (N_p^{std})^T m B_u^{std} \dot{\bar{u}} d\Omega \\
& + \int_{\Omega} (N_p^{std})^T m B_u^{enr} \dot{\bar{a}} d\Omega \\
& + \int_{\Gamma_d} (N_p^{std})^T c N_p^{std} \bar{p} d\Gamma \\
& + \int_{\Gamma_d} (N_p^{std})^T c N_p^{enr} \bar{p}_a d\Gamma \\
& - \int_{\Gamma_d} (N_p^{std})^T c N_{p_F}^{std} \bar{p}_F d\Gamma \Big\} \\
& + \delta \bar{p}_a \Big\{ \int_{\Omega} (B_p^{enr})^T k_F B_p^{std} \bar{p} d\Omega \\
& + \int_{\Omega} (B_p^{enr})^T k_F B_p^{enr} \bar{p}_a d\Omega + \int_{\Gamma_w} (N_p^{enr})^T \bar{q} d\Gamma \\
& + \int_{\Omega} (N_p^{enr})^T m B_u^{std} \dot{\bar{u}} d\Omega \\
& + \int_{\Omega} (N_p^{enr})^T m B_u^{enr} \dot{\bar{a}} d\Omega \\
& + \int_{\Gamma_d} (N_p^{enr})^T c N_p^{std} \bar{p} d\Gamma \\
& + \int_{\Gamma_d} (N_p^{enr})^T c N_p^{enr} \bar{p}_a d\Gamma \\
& - \int_{\Gamma_d} (N_p^{enr})^T c N_{p_F}^{std} \bar{p}_F d\Gamma \Big\} = 0
\end{aligned} \tag{A.39}$$

Arranging the terms into a matrix form, the following relation is obtained

$$\begin{aligned}
\begin{bmatrix} Q_{pu} & Q_{pa} \\ Q_{cu} & Q_{ca} \end{bmatrix} \begin{Bmatrix} \dot{\bar{u}} \\ \dot{\bar{a}} \end{Bmatrix} + \begin{bmatrix} H_{pp} + L_{pp} & H_{pc} + L_{pc} \\ H_{cp} + L_{cp} & H_{cc} + L_{cc} \end{bmatrix} \begin{Bmatrix} \bar{p} \\ \bar{p}_a \end{Bmatrix} + \begin{bmatrix} L_{pp_F} \\ L_{cp_F} \end{bmatrix} \{\bar{p}_F\} \\
= \begin{Bmatrix} q_p^{ext} \\ q_c^{ext} \end{Bmatrix}
\end{aligned} \tag{A.40}$$

where

$$Q_{pu} = \int_{\Omega} (N_p^{std})^T m B_u^{std} d\Omega \tag{A.41}$$

$$Q_{pa} = \int_{\Omega} (N_p^{std})^T m B_u^{enr} d\Omega \tag{A.42}$$

$$Q_{cu} = \int_{\Omega} (N_p^{enr})^T m B_u^{std} d\Omega \quad (A.43)$$

$$Q_{ca} = \int_{\Omega} (N_p^{enr})^T m B_u^{enr} d\Omega \quad (A.44)$$

$$H_{pp} = \int_{\Omega} (B_p^{std})^T k_F B_p^{std} d\Omega \quad (A.45)$$

$$H_{pc} = \int_{\Omega} (B_p^{std})^T k_F B_p^{enr} d\Omega \quad (A.46)$$

$$H_{cp} = \int_{\Omega} (B_p^{enr})^T k_F B_p^{std} d\Omega \quad (A.47)$$

$$H_{cc} = \int_{\Omega} (B_p^{enr})^T k_F B_p^{enr} d\Omega \quad (A.48)$$

$$L_{pp_F} = \int_{\Gamma_d} (N_p^{std})^T c N_{p_F}^{std} d\Gamma \quad (A.49)$$

$$L_{cp_F} = \int_{\Gamma_d} (N_p^{enr})^T c N_{p_F}^{std} d\Gamma \quad (A.50)$$

$$L_{pp} = \int_{\Gamma_d} (N_p^{std})^T c N_p^{std} d\Gamma \quad (A.51)$$

$$L_{pc} = \int_{\Gamma_d} (N_p^{std})^T c N_p^{enr} d\Gamma \quad (A.52)$$

$$L_{cp} = \int_{\Gamma_d} (N_p^{enr})^T c N_p^{std} d\Gamma \quad (A.53)$$

$$L_{cc} = \int_{\Gamma_d} (N_p^{enr})^T c N_p^{enr} d\Gamma \quad (A.54)$$

$$q_p^{ext} = \int_{\Gamma_w} (N_p^{std})^T \bar{q} d\Gamma \quad (A.55)$$

$$q_c^{ext} = \int_{\Gamma_w} (N_p^{enr})^T \bar{q} d\Gamma \quad (A.56)$$

Generalizing the equations and terms, it gives

$$[Q^T]\{\dot{\mathbb{U}}\} + [H + L1]\{\bar{\mathbb{P}}\} - [L2]\{\bar{\mathbb{P}}_F\} - q_{\mathbb{P}}^{ext} = 0 \quad (A.57)$$

$$H_{\delta\zeta} = \int_{\Omega} (B_p^{\delta})^T k_F B_p^{\zeta} d\Omega \quad (A.58)$$

$$L1_{\delta\zeta} = \int_{\Gamma_d} (N_p^{\delta})^T c N_p^{\zeta} d\Gamma \quad (A.59)$$

$$L2_{\delta p_F} = \int_{\Gamma_d} (N_p^\delta)^T c N_{p_F}^{std} d\Gamma \quad (\text{A.60})$$

$$q_\delta^{ext} = \int_{\Gamma_w} (N_p^\delta)^T \bar{q}_w d\Gamma \quad (\text{A.61})$$

For the continuity in the fracture region, the replacement of Eqs. (A.4) to (A.16) in Eq. (A.3) gives

$$\begin{aligned} & \int_{\Gamma_d} \frac{\partial \delta p_F}{\partial x'} k_{f_F} \cdot 2h \cdot \frac{\partial p_F}{\partial x'} d\Gamma + \int_{\Gamma_d} \delta p_F \cdot c(p_F - p) n_{\Gamma_d} d\Gamma \\ & + \int_{\Gamma_d} \delta p_F \cdot 2h \cdot \left\langle \frac{\partial \dot{u}_{x'}}{\partial x'} \right\rangle d\Gamma + \int_{\Gamma_d} \delta p_F \cdot \llbracket \dot{u}_{y'} \rrbracket d\Gamma \\ & = \int_{\Gamma_d} (B_{p_F}^{std})^T t_{\Gamma_d} \delta \bar{p}_F (2h) k_{f_F} \nabla \bar{p}_F t_{\Gamma_d} d\Gamma \\ & - \int_{\Gamma_d} (N_{p_F}^{std})^T \delta \bar{p}_F c N_p^{std} \bar{p} d\Gamma \\ & - \int_{\Gamma_d} (N_{p_F}^{std})^T \delta \bar{p}_F c N_p^{enr} \bar{p}_a d\Gamma \\ & + \int_{\Gamma_d} (N_{p_F}^{std})^T \delta \bar{p}_F c N_{p_F}^{std} \bar{p}_F d\Gamma \\ & + \int_{\Gamma_d} (N_{p_F}^{std})^T t_{\Gamma_d} \delta \bar{p}_F (2h) \langle \nabla \dot{u} \rangle t_{\Gamma_d} d\Gamma \\ & + \int_{\Gamma_d} (N_{p_F}^{std})^T \delta \bar{p}_F \llbracket \dot{u} \rrbracket n_{\Gamma_d} d\Gamma = 0 \end{aligned} \quad (\text{A.62})$$

Assembling the test functions, it gives

$$\begin{aligned} & \delta \bar{p}_F \left\{ \int_{\Gamma_d} (B_{p_F}^{std})^T t_{\Gamma_d} (2h) k_{f_F} \nabla \bar{p}_F t_{\Gamma_d} d\Gamma \right. \\ & + \int_{\Gamma_d} (N_{p_F}^{std})^T t_{\Gamma_d} (2h) \langle \nabla \dot{u} \rangle t_{\Gamma_d} d\Gamma \\ & + \int_{\Gamma_d} (N_{p_F}^{std})^T \llbracket \dot{u} \rrbracket n_{\Gamma_d} d\Gamma \\ & - \int_{\Gamma_d} (N_{p_F}^{std})^T c N_p^{std} \bar{p} d\Gamma \\ & - \int_{\Gamma_d} (N_{p_F}^{std})^T c N_p^{enr} \bar{p}_a d\Gamma \\ & \left. + \int_{\Gamma_d} (N_{p_F}^{std})^T c N_{p_F}^{std} \bar{p}_F d\Gamma \right\} \end{aligned} \quad (\text{A.63})$$

Arranging the terms into a matrix form, the following relation is obtained

$$[L_{p_F p} \quad L_{p_F c}] \left\{ \frac{\bar{p}}{p_a} \right\} + [H_{p_F p_F} + L_{p_F p_F}] \{\bar{p}_F\} = q_{p_F}^{int} \quad (A.64)$$

where

$$H_{p_F p_F} = \int_{\Gamma_d} (B_{p_F}^{std})^T t_{\Gamma_d} (2h) k_{Fd} \nabla \bar{p}_F t_{\Gamma_d} d\Gamma \quad (A.65)$$

$$L_{p_F p_F} = \int_{\Gamma_d} (N_{p_F}^{std})^T c N_{p_F}^{std} d\Gamma \quad (A.66)$$

$$L_{p_F p} = \int_{\Gamma_d} (N_{p_F}^{std})^T c N_p^{std} d\Gamma \quad (A.67)$$

$$L_{p_F c} = \int_{\Gamma_d} (N_{p_F}^{std})^T c N_p^{enr} d\Gamma \quad (A.68)$$

$$\begin{aligned} q_{p_F}^{int} = & \int_{\Gamma_d} (N_{p_F}^{std})^T t_{\Gamma_d} (2h) \langle \nabla \dot{\bar{u}} \rangle t_{\Gamma_d} d\Gamma \\ & + \int_{\Gamma_d} (N_{p_F}^{std})^T [\![\dot{\bar{u}}]\!] n_{\Gamma_d} d\Gamma \end{aligned} \quad (A.69)$$

Generalizing the equations and terms, it gives

$$-[L2^T] \{\bar{\mathbb{P}}\} + [H_F + L3] \{\bar{\mathbb{P}}_F\} - q_{\bar{\mathbb{P}}_F}^{int} = 0 \quad (A.70)$$

where

$$L2_{\delta P_F} = \int_{\Gamma_d} (N_p^\delta)^T c N_{p_F}^{std} d\Gamma \quad (A.71)$$

$$L3 = \int_{\Gamma_d} (N_{p_F}^{std})^T c N_{p_F}^{std} d\Gamma \quad (A.72)$$

$$H_F = \int_{\Gamma_d} (B_{p_F}^{std})^T t_{\Gamma_d} (2h) k_{Fd} B_{p_F}^{std} t_{\Gamma_d} d\Gamma \quad (A.73)$$

$$\begin{aligned} q_{p_F}^{int} = & \int_{\Gamma_d} (N_{p_F}^{std})^T t_{\Gamma_d} (2h) \langle \nabla \dot{\bar{u}} \rangle t_{\Gamma_d} d\Gamma \\ & + \int_{\Gamma_d} (N_{p_F}^{std})^T [\![\dot{\bar{u}}]\!] n_{\Gamma_d} d\Gamma \end{aligned} \quad (A.74)$$

The values related with velocity are defined as

$$\begin{aligned}
\langle \nabla \dot{\bar{u}} \rangle &= \frac{\nabla \dot{\bar{u}}^+ + \nabla \dot{\bar{u}}^-}{2} \\
&= \frac{1}{2} [(B_u^{std} \dot{\bar{u}} + B_u^{enr} \dot{\bar{a}})^+ + (B_u^{std} \dot{\bar{u}} + B_u^{enr} \dot{\bar{a}})^-] \\
&= \frac{1}{2} [2 \cdot B_u^{std} \dot{\bar{u}} + B_u^{std} (H^+ + H^-) \dot{\bar{a}}] \\
&= B_u^{std} \dot{\bar{u}} + B_u^{std} \langle H \rangle \dot{\bar{a}} \\
&= B_u^{std} \frac{(\bar{u}_n - \bar{u}_{n-1})}{\Delta t} + B_u^{std} \langle H \rangle \frac{(\bar{a}_n - \bar{a}_{n-1})}{\Delta t}
\end{aligned} \tag{A.75}$$

$$\begin{aligned}
\llbracket \dot{\bar{u}} \rrbracket &= \dot{\bar{u}}^+ - \dot{\bar{u}}^- \\
&= (N_u^{std+} \dot{\bar{u}} + N_u^{std+} H^+ \dot{\bar{a}}) \\
&\quad - (N_u^{std-} \dot{\bar{u}} + N_u^{std-} H^- \dot{\bar{a}}) = N_u^{std} \llbracket H \rrbracket \dot{\bar{a}} \\
&= N_u^{std} \llbracket H \rrbracket \frac{(\bar{a}_n - \bar{a}_{n-1})}{\Delta t}
\end{aligned} \tag{A.76}$$

Given that

$$N_u^{std+} = N_u^{std-} = N_u^{std} \tag{A.77}$$

$$N_u^{enr+} = N_u^{std+} H^+ = N_u^{std} H^+ \tag{A.78}$$

$$N_u^{enr-} = N_u^{std-} H^- = N_u^{std} H^- \tag{A.79}$$

$$B_u^{std+} = B_u^{std-} = B_u^{std} \tag{A.80}$$

$$B_u^{enr+} = B_u^{std+} H^+ = B_u^{std} H^+ \tag{A.81}$$

$$B_u^{enr-} = B_u^{std-} H^- = B_u^{std} H^- \tag{A.82}$$

Where H^+ and H^- represent the values of the enrichment function H in the fracture top and bottom faces, respectively. In $\bar{u}_n - \bar{u}_{n-1}$, n represents the current increment and $n-1$ the previous one.

Generalizing a number of degrees of freedom equal to $ndof$, it gives

$$\langle \nabla \dot{\bar{u}} \rangle = \sum_k^{ndof} \langle B_u^k \rangle \frac{(\bar{k}_n - \bar{k}_{n-1})}{\Delta t} \tag{A.83}$$

$$\llbracket \dot{\bar{u}} \rrbracket = \sum_k^{ndof} \llbracket N_u^k \rrbracket \frac{(\bar{k}_n - \bar{k}_{n-1})}{\Delta t} \tag{A.84}$$

with $\langle B_u^u \rangle = B_u^{std}$ and $\langle B_u^a \rangle = B_u^{std} \langle H_a \rangle$

Annex B

Newton-Raphson Algorithm

The Jacobian of derivatives is given by

$$\begin{aligned}
 J &= \begin{bmatrix} \frac{\partial \Psi_{\mathbb{U}}}{\partial \bar{\mathbb{U}}} & \frac{\partial \Psi_{\mathbb{U}}}{\partial \bar{\mathbb{P}}} & \frac{\partial \Psi_{\mathbb{U}}}{\partial \bar{\mathbb{P}}_F} \\ \frac{\partial \Psi_{\mathbb{P}}}{\partial \bar{\mathbb{U}}} & \frac{\partial \Psi_{\mathbb{P}}}{\partial \bar{\mathbb{P}}} & \frac{\partial \Psi_{\mathbb{P}}}{\partial \bar{\mathbb{P}}_F} \\ \frac{\partial \Psi_{\bar{\mathbb{P}}_F}}{\partial \bar{\mathbb{U}}} & \frac{\partial \Psi_{\bar{\mathbb{P}}_F}}{\partial \bar{\mathbb{P}}} & \frac{\partial \Psi_{\bar{\mathbb{P}}_F}}{\partial \bar{\mathbb{P}}_F} \end{bmatrix} \\
 &= \begin{bmatrix} K + \frac{\partial f_{\mathbb{U}}^{int}}{\partial \bar{\mathbb{U}}} & -Q + \frac{\partial f_{\mathbb{U}}^{int}}{\partial \bar{\mathbb{P}}} & \frac{\partial f_{\mathbb{U}}^{int}}{\partial \bar{\mathbb{P}}_F} \\ \frac{1}{\Delta t} Q^T & (H + L) & L \\ -\frac{\partial q_{\bar{\mathbb{P}}_F}^{int}}{\partial \bar{\mathbb{U}}} & L^T - \frac{\partial q_{\bar{\mathbb{P}}_F}^{int}}{\partial \bar{\mathbb{P}}} & (H_F + L_F) - \frac{\partial q_{\bar{\mathbb{P}}_F}^{int}}{\partial \bar{\mathbb{P}}_F} \end{bmatrix}
 \end{aligned} \tag{B.1}$$

Multiplying the second and third lines for Δt , it gives

$$\begin{aligned}
 J &= \begin{bmatrix} \frac{\partial \Psi_{\mathbb{U}}}{\partial \bar{\mathbb{U}}} & \frac{\partial \Psi_{\mathbb{U}}}{\partial \bar{\mathbb{P}}} & \frac{\partial \Psi_{\mathbb{U}}}{\partial \bar{\mathbb{P}}_F} \\ \frac{\partial \Psi_{\mathbb{P}}}{\partial \bar{\mathbb{U}}} & \frac{\partial \Psi_{\mathbb{P}}}{\partial \bar{\mathbb{P}}} & \frac{\partial \Psi_{\mathbb{P}}}{\partial \bar{\mathbb{P}}_F} \\ \frac{\partial \Psi_{\bar{\mathbb{P}}_F}}{\partial \bar{\mathbb{U}}} & \frac{\partial \Psi_{\bar{\mathbb{P}}_F}}{\partial \bar{\mathbb{P}}} & \frac{\partial \Psi_{\bar{\mathbb{P}}_F}}{\partial \bar{\mathbb{P}}_F} \end{bmatrix} \\
 &= \begin{bmatrix} K + \frac{\partial f_{\mathbb{U}}^{int}}{\partial \bar{\mathbb{U}}} & -Q + \frac{\partial f_{\mathbb{U}}^{int}}{\partial \bar{\mathbb{P}}} & \frac{\partial f_{\mathbb{U}}^{int}}{\partial \bar{\mathbb{P}}_F} \\ Q^T & \Delta t(H + L) & \Delta t.L \\ -\Delta t \frac{\partial q_{\bar{\mathbb{P}}_F}^{int}}{\partial \bar{\mathbb{U}}} & \Delta t \left(L^T - \frac{\partial q_{\bar{\mathbb{P}}_F}^{int}}{\partial \bar{\mathbb{P}}} \right) & \Delta t(H_F + L_F) - \Delta t \frac{\partial q_{\bar{\mathbb{P}}_F}^{int}}{\partial \bar{\mathbb{P}}_F} \end{bmatrix}
 \end{aligned} \tag{B.2}$$

Re-scaling the problem formulation for one standard u and one enriched degree of freedom a , the derivatives for the mechanical equation are

$$\begin{aligned} \frac{\partial f_{\mathbb{U}}^{int}}{\partial \bar{\mathbb{U}}} &= \left\{ \frac{\partial}{\partial \bar{\mathbb{U}}} \right\} \left\{ \begin{array}{c} 0 \\ \int_{\Gamma_d} \llbracket N_u^{enr} \rrbracket^T (D_F \bar{a} - p_F n_{\Gamma_d}) d\Gamma \end{array} \right\}^T \\ &= \begin{bmatrix} 0 & 0 \\ 0 & \int_{\Gamma_d} \llbracket N_u^{enr} \rrbracket^T D_F \llbracket N_u^{enr} \rrbracket d\Gamma \end{bmatrix} = \begin{bmatrix} 0 & 0 \\ 0 & T_a \end{bmatrix} \end{aligned} \quad (\text{B.3})$$

$$\frac{\partial f_{\mathbb{U}}^{int}}{\partial \bar{\mathbb{P}}} = \left\{ \frac{\partial}{\partial \bar{\mathbb{P}}} \right\} \left\{ \begin{array}{c} 0 \\ \int_{\Gamma_d} \llbracket N_u^{enr} \rrbracket^T (D_F \bar{a} - p_F n_{\Gamma_d}) d\Gamma \end{array} \right\}^T = 0 \quad (\text{B.4})$$

$$\begin{aligned} \frac{\partial f_{\mathbb{U}}^{int}}{\partial \bar{\mathbb{P}}_F} &= \frac{\partial}{\partial \bar{p}_F} \left\{ \begin{array}{c} 0 \\ \int_{\Gamma_d} \llbracket N_u^{enr} \rrbracket^T (D_F \bar{a} - p_F n_{\Gamma_d}) d\Gamma \end{array} \right\} \\ &= \left\{ - \int_{\Gamma_d} \llbracket N_u^{enr} \rrbracket^T n_{\Gamma_d} N_{p_F}^{std} d\Gamma \right\} = \left\{ -Q_{ap_F} \right\} \end{aligned} \quad (\text{B.5})$$

The derivatives for the continuity equation in the fracture are

$$\begin{aligned} \frac{\partial q_{\mathbb{P}_F}^{int}}{\partial \bar{\mathbb{U}}} &= \left\{ \frac{\partial}{\partial \bar{\mathbb{U}}} \right\} \left\{ \int_{\Gamma_d} (N_{p_F}^{std})^T t_{\Gamma_d} (2h) \langle \nabla \dot{u} \rangle t_{\Gamma_d} d\Gamma + \int_{\Gamma_d} (N_{p_F}^{std})^T \llbracket \dot{u} \rrbracket n_{\Gamma_d} d\Gamma \right\} \\ &= \left\{ \begin{array}{c} \int_{\Gamma_d} (N_{p_F}^{std})^T t_{\Gamma_d} (2h) \left(B_u^{std} \frac{1}{\Delta t} \right) t_{\Gamma_d} d\Gamma \\ \int_{\Gamma_d} (N_{p_F}^{std})^T t_{\Gamma_d} (2h) \left(B_u^{std} \langle H \rangle \frac{1}{\Delta t} \right) t_{\Gamma_d} d\Gamma + \int_{\Gamma_d} (N_{p_F}^{std})^T N_u^{std} \llbracket H \rrbracket \frac{1}{\Delta t} n_{\Gamma_d} d\Gamma \end{array} \right\} \\ &= \left\{ \begin{array}{c} \frac{1}{\Delta t} S_{p_F u} \\ \frac{1}{\Delta t} S_{p_F a} + \frac{1}{\Delta t} V_{p_F a} \end{array} \right\} \end{aligned} \quad (\text{B.6})$$

$$\begin{aligned} \frac{\partial q_{\mathbb{P}_F}^{int}}{\partial \bar{\mathbb{P}}} &= \left\{ \frac{\partial}{\partial \bar{\mathbb{P}}} \right\} \left\{ \int_{\Gamma_d} (N_{p_F}^{std})^T t_{\Gamma_d} (2h) \langle \nabla \dot{u} \rangle t_{\Gamma_d} d\Gamma \right. \\ &\quad \left. + \int_{\Gamma_d} (N_{p_F}^{std})^T \llbracket \dot{u} \rrbracket n_{\Gamma_d} d\Gamma \right\} = 0 \end{aligned} \quad (\text{B.7})$$

$$\begin{aligned} \frac{\partial q_{\mathbb{P}_F}^{int}}{\partial \bar{\mathbb{P}}_F} &= \frac{\partial}{\partial \bar{p}_F} \left(\int_{\Gamma_d} (N_{p_F}^{std})^T t_{\Gamma_d} (2h) \langle \nabla \dot{u} \rangle t_{\Gamma_d} d\Gamma \right. \\ &\quad \left. + \int_{\Gamma_d} (N_{p_F}^{std})^T \llbracket \dot{u} \rrbracket n_{\Gamma_d} d\Gamma \right) = 0 \end{aligned} \quad (\text{B.8})$$

Substituting the derivatives in the Jacobian, it gives

$$J = \begin{bmatrix} K_{uu} & K_{ua} & -Q_{up} & -Q_{uc} & 0 \\ K_{au} & K_{aa} + T_a & -Q_{ap} & -Q_{ac} & -Q_{ap_F} \\ Q_{pu} & Q_{pa} & \Delta t(H_{pp} + L_{pp}) & \Delta t(H_{pc} + L_{pc}) & \Delta t.L_{pp_F} \\ Q_{cu} & Q_{ca} & \Delta t(H_{cp} + L_{cp}) & \Delta t(H_{cc} + L_{cc}) & \Delta t.L_{cp_F} \\ -S_{p_{fu}} & -(S_{p_{fa}} + V_{p_{fa}}) & \Delta t.L_{p_{fp}} & \Delta t.L_{p_{fc}} & \Delta t(H_{p_{fpp}} + L_{p_{fpp}}) \end{bmatrix} \quad (B.9)$$

If both porous and fracture material constitutive behaviour are such that their matrices K and T are symmetric, the Jacobian may be symmetric if the following simplifications are considered:

- The lines relative to pore and fracture pressures (third, fourth and fifth lines) are multiplied by -1
- $S_{p_{fu}} = 0$
- $(S_{p_{fa}} + V_{p_{fa}}) = Q_{p_{fa}} = Q_{ap_F}^T$

The resulting Jacobian matrix is then given by

$$J = \begin{bmatrix} K_{uu} & K_{ua} & -Q_{up} & -Q_{uc} & 0 \\ K_{au} & K_{aa} + T_a & -Q_{ap} & -Q_{ac} & -Q_{ap_F} \\ -Q_{pu} & -Q_{pa} & -\Delta t(H_{pp} + L_{pp}) & -\Delta t(H_{pc} + L_{pc}) & -\Delta t.L_{pp_F} \\ -Q_{cu} & -Q_{ca} & -\Delta t(H_{cp} + L_{cp}) & -\Delta t(H_{cc} + L_{cc}) & -\Delta t.L_{cp_F} \\ 0 & -Q_{p_{fa}} & -\Delta t.L_{p_{fp}} & -\Delta t.L_{p_{fc}} & -\Delta t(H_{p_{fpp}} + L_{p_{fpp}}) \end{bmatrix} \quad (B.10)$$

Generalizing the terms, it gives

$$J = \begin{bmatrix} K + T & -Q & -Q_F \\ -Q^T & -\Delta t(H + L1) & \Delta t.L2 \\ -Q_F^T & \Delta t.L2^T & -\Delta t.(H_F + L3) \end{bmatrix} \quad (B.11)$$

Where the matrices are given by Eqs. (A.34), (A.35), (A.58) to (A.60), (A.71) to (A.73), and

$$T_{\beta\gamma} = \int_{\Gamma_d} \llbracket N_u^\beta \rrbracket^T D_F \llbracket N_u^\gamma \rrbracket d\Gamma \quad (B.12)$$

$$Q_{F\beta p_F} = \int_{\Omega} \llbracket N_u^\beta \rrbracket^T n_{\Gamma d} N_{p_F}^{std} d\Omega \quad (B.13)$$